Gerard Caneba

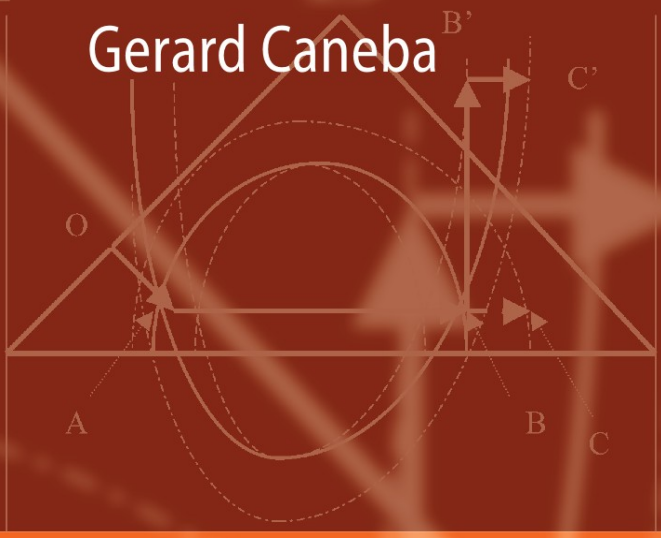

Free-Radical Retrograde-Precipitation Polymerization (FRRPP)

Novel Concept, Processes, Materials, and Energy Aspects

Springer

Free-Radical Retrograde-Precipitation Polymerization (FRRPP)

Gerard Caneba

Free-Radical Retrograde-Precipitation Polymerization (FRRPP)

Novel Concept, Processes, Materials, and Energy Aspects

Springer

Dr. Gerard Caneba
Michigan Technological
University
Dept. Chemical Engineering
1400 Townsend Drive
Houghton MI 49931-1295
USA
caneba@mtu.edu

ISBN 978-3-642-03024-6 e-ISBN 978-3-642-03025-3
DOI 10.1007/978-3-642-03025-3
Springer Heidelberg Dordrecht London New York

Library of Congress Control Number: 2009937716

Cover design: WMXDesign GmbH, Heidelberg

Printed on acid-free paper

Springer is part of Springer Science+Business Media (www.springer.com)

Dedicated to my loving wife, Mary Ann; my children, Christine, Richard, Benjamin, and Katherine; and to my parents, Doroteo and Saturnina Cañeba

Preface

The free-radical retrograde-precipitation polymerization (FRRPP) process was introduced by the author in the early 1990s as a chain polymerization method, whereby phase separation is occurring while reactive sites are above the lower critical solution temperature (LCST). It was evident that certain regions of the product polymer attain temperatures above the average fluid temperature, sometimes reaching carbonization temperatures. During the early stages of polymerization-induced phase separation, nanoscale polymer domains were also found to be persistent in the reacting system, in apparent contradiction with results of microstructural coarsening from constant-temperature modeling and experimental studies. This mass confinement behavior was used for micropatterning, for entrapment of reactive radical sites, and for the formation of block copolymers that can be used as intermediates, surfactants, coatings, coupling agents, foams, and hydrogels. FRRPP-based materials and its mechanism have also been proposed to be relevant in energy and environmentally responsible applications.

This technology lacks intellectual appeal compared to others that have been proposed to produce polymers of exotic architectures. There are no special chemical mediators needed. Control of conditions and product distribution is done by process means, based on a robust and flexible free-radical-based chemistry. Thus, it can readily be implemented in the laboratory and in production scale.

The FRRPP process is what the author calls a third-world method to produce multipolymers; and having spawned from the developing world, the author writes this monograph in appreciation of his beginnings that led to a life of discovery in new worlds. As for developed countries, this monograph offers insights into future energy independence and frontier intellectual explorations. It is not to say that the developed world can just sit on these insights; as the nature of the FRRPP technology suggests, even these advanced ideas can be exploited by others of limited resources.

This monograph contains a new dimensionless quantity, which the author believes to contain the sufficient-and-necessary condition for FRRPP behavior. It is symbolized as $C\tilde{n}$ (pronounced see-enye) and introduced in Section 2.2. In order to assure strict FRRPP behavior, computer simulation has established $C\tilde{n}$ to be less than -1000. This cutoff number could definitely be changed, if certain criteria for strict FRRPP behavior are relaxed. Experimental measurements seems to indicate

that *Cñ* should be a large enough negative number. The *Cñ* designation for the new dimensionless number is made in honor of the author's extended family name and Filipino–Hispanic heritage.

The FRRPP process involves a novel synergistic combination of various concepts. The author does not claim mastery of state-of-the-art understanding of the various fields it encompasses. He believes that even if these subareas may be imperfectly understood, the combination can yield novel discoveries. Over the history of science and technology, important discoveries were made this way. This is related to the recent discoveries of better performance from a group of persons of diverse backgrounds and perspectives working in a team or organization, even though individually they may not be the best in their positions.

Gratitude is expressed to Michigan Technological University for providing the intellectual atmosphere and isolation, as well as the pristine environment to carry out the research efforts that facilitated the development of the FRRPP concept. Crucial funding from various agencies and foundations are also appreciated, especially the National Science Foundation through Maria Burka of the Process Reaction Engineering Program and Norbert Bikales of the Polymers Program at the Division of Materials Research.

A significant amount of material from this monograph has been generated through the efforts and assistance of the author's former graduate and undergraduate students, post-doctoral associates, co-investigators in various projects involving the FRRPP process, and other supporters. The list includes Yadunandan Dar, Bo Wang, Rahul Saxena, Vijay Tirumala, Yi Zhao, Linhuo Shi, Anand Laxminarayan, Yuh-Ling Chen, Zhiyong Xu, Yuhao Cai, Anuj Aggarwal, Brian Ott, Michael Renier, Derrick Mancini, Douglas Gardner, Stephen Shaler, Pete Schlom, David Shonnard, Ghatu Subhash, David Johnson, Brooke Hatfield, Mitchell Zakin, Karel Solc, Jay Axland, Michael Crossey, Ahmed Bahabry, and many more with relatively minor roles. The author would also like to express appreciation to his mentors at the University of California – Berkeley: John Prausnitz, David Soong (now Soane), and Morton Denn, for all the intellectual discussions with them as a wide-eyed and inquisitive graduate student. A final gratitude is expressed to the University of the Philippines and UNESCO for providing the author the opportunity to start his studies in the United States.

The foregoing material in this monograph starts with background material in Chapter 1, which introduces the reader to the various components of the FRRPP process: phase equilibria thermodynamics, transport processes, phase separation kinetics, free-radical polymerization, and reactive phase separation. Then, in Chapter 2, the author introduces the FRRPP process and its various features. In Chapter 3, the FRRPP process is applied to polymerization processes, including statistical multipolymerizations and staged block copolymer formation. In Chapter 4, various applications of the FRRPP process developed by the author within his research group are presented. In Chapter 5, the author presents some of the energy-related applications of the FRRPP process, as they relate to his work in enhanced oil recovery. Finally, Chapter 6 involves a discussion of some future and more speculative uses of the FRRPP process and its conceptual underpinnings, in relation to nanotechnology, medical research, and control over other forms of energetic systems. It is suggested

that readers scan through the background material in Chapter 1 in order to obtain at least a cursory understanding of conventional fields related to the FRRPP process, before they embark on a reading adventure of the latter chapters. If there are problems understanding material beyond Chapter 1, careful reading of the background chapter (including some of the cited references) would be the required.

For those who are seasoned and practitioners in the field of polymerization processes, starting in Chapter 2 or even Chapter 3 could be worth the try. For technologists whose interest in this material is confined to products and applications, jumping into Chapter 4 onward could serve its purpose. For students of the art and science of polymer and energetic systems, it is a hope that their intellectual horizons will become more open after reading and absorbing the various ideas contained in this monograph.

Houghton, Michigan USA Gerard T. Caneba
September 2009

Contents

Chapter 1
Background

An adequate understanding of the FRRPP process can never be achieved without probing into its underlying concepts, since it is a synergistic combination of thermodynamic, transport, and polymer chain-reaction kinetics. The overall result is an unconventional polymerization and energetic behavior that requires the conceptual and mathematical understanding to link all FRRPP features into a coherent picture. Since its necessary condition is found in a phase behavior of polymer mixtures under equilibrium conditions, it is appropriate that the start of presentation of the technical aspects of the FRRPP process is in its relevant thermodynamic concepts.

Phase diagrams of polymer/small-molecule systems are used to determine concentrations or compositions of uniform phases (liquids or solids) at equilibrium. Equilibrium in the thermodynamic sense means that conditions of temperature, pressure, and component compositions do not change with time at a scale much larger than molecular dimensions. Also, the mixture is either a closed system or a representative sample of an overall system. If the system is made up of two components (i.e., a binary system), a typical phase diagram shown in Fig. 1.1.1(a) could have a lower concave-down curve and an upper concave-up curve in the composition–temperature plot (Saeki et al., 1973). The maximum of the concave-down curve is the upper critical solution temperature (UCST), whereas the minimum of the concave-up curve is the lower critical solution temperature (LCST). Outside the concave curves represents single-phase mixtures, just like honey or wine. Shaded regions inside the concave perimeter curves are areas that correspond to mixtures that permit coexistence of two phases. This means that immiscibility can occur if the temperature of the polymer solution is raised above the LCST or lowered below the UCST. The UCST and LCST envelopes display a roughly mirror-image view of each other (Casassa and Berry, 1989). By increasing the molecular weight of the polymer, the UCST is raised and LCST is lowered, thus shrinking the temperature region of complete miscibility. If a solvent of poor quality is chosen, the increase of molecular weight could cause the UCST and LCST to overlap, so that the two regions of limited miscibility merge into an hourglass-shape phase envelope (Siow et al., 1972) (Fig. 1.1.1(b)).

The LCST behavior has long been known to occur in polar small-molecule and polymer/small-molecule systems, and these temperatures can be close to room

G. Caneba, in: *Free-Radical Retrograde-Precipitation Polymerization (FRRPP)*,
Chapter DOI 10.1007/978-3-642-03025-3_1,

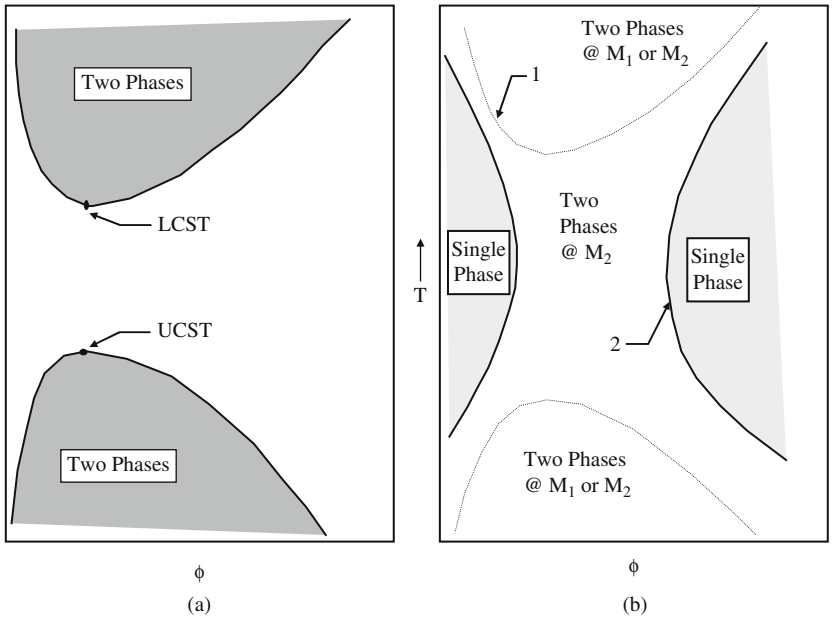

Fig. 1.1.1 Binary phase diagrams (polymer composition represented by the volume fraction, ϕ, vs temperature, T) of polymer/solvent systems exhibiting: (**a**) both LCST and UCST phase envelopes and (**b**) the hourglass-shape phase behavior, when the polymer 2 molecular weight is greater than that of polymer 1 (or $\bar{M}_2 > \bar{M}_1$)

temperature at or around atmospheric pressure. It has not been too long since nonpolar systems were first found to exhibit LCST behavior (Freeman and Rowlinson, 1960), although for most part it occurs at elevated temperatures and pressures. From a practical standpoint, it would be better if LCST values of nonpolar systems are close to small-molecule boiling temperatures; however, more and more data indicate that these values are closer to small-molecule critical temperatures instead. For nonpolar polymer/small-molecule systems, results seem to indicate that the LCST behavior is more of a rule than an exception (Saeki et al., 1973) and that usually there would also be UCST behavior. In fact, there have been cases wherein these systems may not show UCST behavior at all, because small-molecule components are good solvents for the polymer (Casassa and Berry, 1989). Thus, the LCST phenomenon may be quite unusual, but it is a prevalent behavior in polymer/small-molecule systems. It is just a matter of finding the right solvent or mixed solvent combination in the polymer one would like to work with.

From a molecular standpoint, the LCST behavior can be attributed to (**a**) strong polar interactions, including hydrogen-bonding interactions; and, (**b**) equation-of-state (compressibility) effects. In both cases, LCST phase separation is entropically driven (Sanchez and Panayiotou, 1993). Whenever strong interactions are important, they will decrease the entropy more than non-strong interactions,

because strong interactions induce more spatial orientation. At low temperatures, the potential energy gain in strong interactions offset the unfavorable entropy change. As the temperature increases, the unfavorable entropy change becomes more important and finally induces the LCST phase separation when this entropy change overwhelms the favorable energy change. In a nonpolar system, finite compressibility or equation-of-state effects dominate the LCST behavior. At high enough temperatures, unfavorable entropy changes associated with the densification of the mixture become prohibitive for a single-phase system (Sanchez and Panayiotou, 1993). Patterson et al. (1967) reported that the ratio of LCST-to-small-molecule critical temperature for many polyethylene (PE), polyisobutylene (PIB) and polydimethylsiloxane (PDMS) solutions with *n*-alkanes, lies between 0.8 and 0.98 K/K because of the difference in free volumes between the solvent and the polymer (Patterson, 1969; Somcynsky, 1982). Charlet and Delmas (1981) studied the LCST behavior for ethylene–propylene copolymer (EPM) in a wide range of solvents and found that for C_6 and C_7 alkanes, the LCST is 20–80°C less than the solvent critical temperature. They also correlated the LCST with the solvent density and solvent shape. The same results were obtained by Irani (1986) with both single solvent and mixed solvents for the EPM system. To lower the LCST, Irani et al. (1980) showed that dissolving a low-molecular weight hydrocarbon gas, such as ethylene or propylene, in an EPM solution considerably reduces the LCST. This makes the above explanation about the LCST more reasonable, because usually critical temperatures of low-molecular weight gases are much lower, and the system with such mixed solvents will be expected to show a lower LCST. For some systems, e.g., the PS/acetone solution, an hourglass-shape phase diagram was encountered at relatively high polymer molecular weight (Siow et al., 1972; Saeki et al., 1973). If specific energetic interactions were present (such as PEG/water solutions), a closed-loop behavior may be observed, where the LCST was found below the UCST (Casassa and Berry, 1989).

The fact that the LCST of nonpolar polymer/solvent systems was observed under pressure and close to the solvent critical temperature seemed to be a hindrance to its study and application. Phase separation above the LCST of polymer solution was first applied to the recovery of polymers produced from solution polymerization by Anolick and Goffinet (1966). Although this method potentially involved lower energy requirements compared to conventional solvent evaporation techniques, such as steam stripping, there were limitations for this technique to be widely adopted by industry. One of them was the relatively high LCST values for most of the systems. The addition of a low molecular weight gas into the system did not seem to be attractive enough because of the added component and the resulting increase in operating pressure. A more effective approach was the use of mixed solvents, especially polar and/or hydrogen-bonded types. For example, for polystyrene (PS), the LCST in *t*-butyl acetate was at around 98°C. However, with the addition of a small amount of water (1–2 wt% in the mixture), the LCST was lowered to around 55°C. In the various examples mentioned in this monograph, the reader will get a better sense of the various mixed solvents used in practical FRRPP systems.

1.1 Phase Separation Thermodynamics

The central thermodynamic quantity of interest to characterize phase separation behavior of polymer systems is the Gibbs free energy, G. In turn, the Gibbs free energy is related to the enthalpy, H, and the entropy, S, through the definition

$$G \equiv H - TS. \tag{1.1.1}$$

The enthalpy is associated with the energetic level of the system, while the entropy is related to the level of randomness of the system. Since the absolute Gibbs free energy cannot be determined, its relative value ΔG is used in various calculations and mathematical expressions. When the Gibbs free energy is relative to the weighted mole-average of those of the pure components that make up the mixture, it corresponds to the Gibbs free energy of mixing, ΔG_{M}. Thus,

$$\Delta G_{\mathrm{M}} \equiv G - \sum_i n_i G_{\mathrm{Pure}i}, \tag{1.1.2}$$

where G is the Gibbs free energy of the mixture and n_i is the number of moles of component i.

1.1.1 Thermodynamics of Polymer Solutions

Model equations that characterize component solubilities and phase compositions of polymer solutions range from simpler ones, such as the Flory–Huggins (FH) theory (Flory, 1942; Huggins, 1942), to more complicated ones based on equation-of-state (EOS) models (Prigogine, 1957; Flory, 1970; Patterson, 1968, 1982; Patterson and Delmas, 1970) and lattice fluid models (Sanchez and Lacombe, 1976, 1978; Panayiotou and Vera, 1982; High and Dinner, 1990). At the extreme end of the sophistication are complicated models, such as the Universal Quasi-Chemical or UNIQUAC (Prausnitz et al., 1986), Universal Functional Group Activity or UNIFAC (Fredenslund et al., 1977), perturbed hard sphere chain or PHSC (Prausnitz et al., 1986), and statistical associating fluid theory or SAFT (Condo and Radosz, 1996)]. In this monograph, only the Flory–Huggins and Flory–Prigogine–Patterson equation-of-state theories are presented, since they were the only ones used in subsequent computational efforts.

1.1.1.1 Flory–Huggins Theory

For a binary polymer–solvent solution, the simplest expression for the Gibbs free energy of mixing is based on the Flory–Huggins Theory (Flory, 1942; Huggins, 1942),

$$\Delta G_{\mathrm{M}} = RT\left[n_{\mathrm{S}} \ln \phi_{\mathrm{S}} + n_{\mathrm{P}} \ln \phi_{\mathrm{P}} + n_{\mathrm{S}} \phi_{\mathrm{P}} \chi\right], \tag{1.1.3}$$

where ϕ_P are ϕ_S the volume fractions of the polymer and solvent, respectively. The quantity χ is a dimensionless Flory–Huggins parameter and is initially assumed to be temperature dependent only. Note that Eq. (1.1.3) assumes that the polymer has at least a relatively narrow molecular weight distribution. There are extensions of the Flory–Huggins theory for polydisperse polymers (Guggenheim, 1952; Koningsveld, 1968a, 1968b), but they will not be needed for application to the FRRPP process, since products from the reaction system tend to be relatively narrow in their molecular weight distributions.

The original Flory–Huggins equation represents many of the essentials of polymer solution equilibria, but it is often not able to give a quantitative representation of experimental data. Some of the critical assumptions made for its development are (a) random mixing, i.e., polymer segments and solvent molecules show no preference in choosing nearest neighbors; and (b) rigid lattice without holes.

For a mixture that is applicable to the FRRPP process, one can write the multicomponent Flory–Huggins equation as

$$\frac{\Delta G_M}{N_r kT} = \sum_{i=1}^{n} \frac{\phi_i}{r_i} \ln \phi_i + \sum_{j=2}^{n} \sum_{i=1}^{j-1} g_{ij} \phi_i \phi_j, \tag{1.1.4}$$

where N_r is the total number of sites in the lattice and

$$N_r = \sum_i N_i r_i.$$

The quantity g_{ij} is the binary interaction parameter between species i and j and $g_{ij} = g_{ij}$ (T, P, r_i *or* r_j, ϕ_i *or* ϕ_j). The quantity ϕ_i is the volume fraction of component i with $\phi_i = N_i r_i / N_r$.

For a ternary mixture that usually applies to the FRRPP reaction fluid, the Gibbs free energy of mixing (Altena and Smolders, 1982; Boom et al., 1994) is

$$\frac{\Delta G_M}{RT} = \sum_{i=1}^{3} n_i \ln \phi_i + g_{12} n_1 \phi_2 + g_{13} n_1 \phi_3 + g_{23} n_2 \phi_3, \tag{1.1.5}$$

where subscripts 1 and 2 indicate solvents, and subscript 3 represents the polymer.

The above-mentioned deficiencies of the Flory–Huggins theory can be alleviated, in part, by using the local-composition concept based on Guggenheim's quasichemical theory for the random mixing assumption and replacing lattice theory with an equation-of-state model (Prausnitz et al., 1986). More sophisticated models are available, such as the perturbed hard sphere chain (PHSC) and the statistical associating fluid theory (SAFT) (Caneba and Shi, 2002), but they are too mathematically sophisticated that they are impractical for subsequent computational efforts.

Modified Flory–Huggins equations used different techniques to account for the concentration dependence of χ or g without considering the true cause of the deficiency of the theory; thus, their accuracy to represent experimental data must

rely on a curve-fitting procedure. Even though they cannot generate a universal theory with a physical meaning, they represent the most practical methods to numerically characterize LCST behavior for realistic FRRPP systems (Caneba and Shi, 2002).

The Flory–Huggins equation is one of the simpler models in polymer systems to accurately predict the phase behavior of a real system. In its original version with constant interaction parameters, it cannot even predict the LCST, a common phenomenon in polymer systems. However, its simple form and requirement for less number of parameters make it very suitable for more complex systems. Furthermore, parameters in the Flory–Huggins equation can be made a function of composition or even molecular weight to account for the deviation from experimental data. Thus, the Flory–Huggins model is still very useful and one of the most frequently used methods for polymer systems.

1.1.1.2 Flory–Prigogine–Patterson Equation-of-State Theory

The importance of coupling liquid state properties with the adequate solution theory to take into account the volume, the intermolecular enthalpy, and the intermolecular entropy (i.e., the entropy exclusive of ΔS_{comb}), and in particular the changes of these extensive quantities undergo upon mixing becomes apparent. Early attempts to take account of liquid state characteristics in the treatment of solution proceed along two main lines (Flory, 1970): exploitation of the cell model as a basis for formulating the properties of liquid mixtures and application of corresponding states methods to selected classes of liquid mixtures (Prigogine, 1957). Further development is due to Flory by expanding the partition function of van der Waals form to the solution theory. This development uses the approach without the lattice superposition.

Prigogine (1957), using corresponding states ideas, first emphasized the importance of equation-of-state effects on solution thermodynamics. Later, Patterson and his coworkers (Patterson, 1968, 1982; Patterson and Delmas, 1970) used and extended these ideas to polymer solutions. The brief review of Patterson (1982) based on lattice theory of corresponding states ideas is briefed here to give an intuitive insight into the polymer solution behaviors. According to Patterson, the three contributions to the Gibbs free energy of mixing are the combinatorial or positional entropy of mixing, the intermolecular interaction arising from the different forces surrounding the molecules, and the free-volume effect. The first two components correspond to the original FH equation and lead to the UCST phenomenon. Compared to polymer–polymer or low molecular systems, the difference in free volume becomes very important for polymer–solvent system because of significant difference in size and shape between the components. For example, in a polymer solution where a polymer has similar chemical structure as the solvent, there is little dissimilarity in the intermolecular interactions but the free-volume difference is significant. In this theory, free-volume effects (entropic effects) also contribute to the interaction parameter χ besides the enthalpic contribution as used in Flory–Huggins theory (Patterson and Delmas, 1970). As temperature rises, the free volume of the solvent increases; however, the free volume of the polymer is nearly constant. Since

the difference in free volume increases with temperature, this eventually induces the incipience of LCST. For polymer/polymer systems, the contribution from free-volume difference is often negligible, and the LCST can be achieved only by some specific interactions between the components. Specific interactions contribute to the negative ΔG_{M} (or χ), whereas the dispersion forces or random dipole-induced dipole interaction always leads to a positive contribution to ΔG_{M} (or χ). The total χ along with its contributions from intermolecular interactions (dispersion forces and specific interactions) and free volume is graphically depicted elsewhere (Patterson, 1982).

The quantitative description of the above results may be made from the Flory EOS, or Prigogine–Flory theory, which originated from Prigogine's concepts and was developed by Flory (Patterson, 1982). It was based on the generalized van der Waals partition function:

$$Q = Q_{\mathrm{comb}}(\gamma v^*)^{N_{rc}}\left(\tilde{v}^{1/3}-1\right)^{3N_{rc}}\exp\left(-\frac{U_o}{kT}\right) \quad \text{with} \quad -\frac{U_o}{kT} = \frac{N_{rc}}{\tilde{v}\tilde{T}}, \tag{1.1.6}$$

where γ is a geometric constant; v^*, the hard-core volume per segment; $\tilde{v}$, reduced volume v/v^*; v, volume per segment; r, number of segments per molecule; T^*, characteristic temperature which reflects the potential energy between two segments; $\tilde{T}$, reduced temperature T/T^*, and c, Prigogine's parameter per segment. The corresponding equation of state is

$$\frac{\tilde{P}\tilde{v}}{\tilde{T}} = \frac{\tilde{v}^{1/3}}{\tilde{v}^{1/3}-1} - \frac{1}{\tilde{v}\tilde{T}}, \tag{1.1.7}$$

where $\tilde{P}$ is the reduced pressure, which is equal to P/P^*, and P^* is the characteristic pressure. Normally, V^*, T^* and P^* are obtained in the literature, or they can be estimated from other fluid properties.

1.1.2 Liquid–Liquid Phase Equilibria of Polymer Solutions

1.1.2.1 Binodal Equations

The binodal compositions or compositions of liquid phases α and β in equilibrium can be obtained by solving the following equations:

$$\Delta\mu_i^{\alpha} = \Delta\mu_i^{\beta} \quad \text{for all component } i = 1,2,3,\ldots,m, \tag{1.1.8}$$

wherein the chemical potential difference, $\Delta\mu_i$, is defined as

$$\Delta\mu_i \equiv \left(\frac{\partial \Delta G_{\mathrm{M}}}{\partial n_i}\right)_{T,P,n_{j\neq i}} \tag{1.1.9}$$

Based on Eq. (1.1.4) for ΔG_M, corresponding chemical potential expressions for a multicomponent system are

$$\frac{\Delta\mu_i}{r_k RT} = \frac{1}{r_k}(\ln\phi_k + 1) - \sum_{i=1}^{n}\frac{1}{r_i}\phi_i + (1-\phi_k)\left(\sum_{i<k}^{n-1} g_{ik}\phi_i + \sum_{j>k}^{n} g_{kj}\phi_j\right) - \sum_{i\neq k}^{n-1}\sum_{j\neq k, j>i}^{n}\phi_i\phi_j g_{ij}. \tag{1.1.10}$$

For a ternary system, Eq. (1.1.10) can be written for the components as

$$\frac{\Delta\mu_1}{r_1 RT} = \frac{1}{r_1}(\ln\phi_1 + 1 - \phi_1) - \frac{1}{r_2}\phi_2 - \frac{1}{r_3}\phi_3 + (1-\phi_1)(g_{12}\phi_2 + g_{13}\phi_3) - g_{23}\phi_2\phi_3, \tag{1.1.11}$$

$$\frac{\Delta\mu_2}{r_2 RT} = \frac{1}{r_2}(\ln\phi_2 + 1 - \phi_2) - \frac{1}{r_1}\phi_1 - \frac{1}{r_3}\phi_3 + (1-\phi_2)(g_{12}\phi_1 + g_{23}\phi_3) - g_{13}\phi_1\phi_3, \tag{1.1.12}$$

$$\frac{\Delta\mu_3}{r_3 RT} = \frac{1}{r_3}(\ln\phi_3 + 1 - \phi_3) - \frac{1}{r_1}\phi_1 - \frac{1}{r_2}\phi_2 + (1-\phi_3)(g_{13}\phi_1 + g_{23}\phi_2) - g_{12}\phi_1\phi_2. \tag{1.1.13}$$

1.1.2.2 Spinodal Equations

The spinodal curve for an m-component system is obtained when the determinant of the (m–1)-ranked second-derivative matrix of ΔG_M is zero. Thus,

$$\det\left[\frac{\partial^2\Delta G_M}{\partial\phi_i\partial\phi_j}\right]_{m-1} = 0. \tag{1.1.14}$$

The reason why only (m–1)th rank is considered is the existence of the so-called Gibbs–Duhem equation in thermodynamic systems.

For a binary polymer–solvent mixture, the spinodal equation reduces to

$$\frac{1}{RT}\frac{\partial^2\Delta G_M}{\partial\phi_P^2} = \frac{1}{r\phi_P} + \frac{1}{1-\phi_P} - \left[2\chi - (1-2\phi_P)\left(\frac{\partial\chi}{\partial\phi_P}\right) - \phi_P(1-\phi_P)\left(\frac{\partial^2\chi}{\partial\phi_P^2}\right)\right] = 0. \tag{1.1.15}$$

Here, r is the average degree of polymerization or polymer chain length, and Eq. (1.1.17) accounts for composition-dependent χ-parameter. If the χ-parameter is composition independent, Eq. (1.1.15) in turn reduces to

$$\frac{1}{RT}\frac{\partial^2 \Delta G_{\mathrm{M}}}{\partial \phi_{\mathrm{P}}^2} = \frac{1}{r\phi_{\mathrm{P}}} + \frac{1}{1-\phi_{\mathrm{P}}} - 2\chi = 0. \tag{1.1.16}$$

For ternary polymer (3)/solvent (2)/non-solvent (1) systems which apply to the FRRPP fluid systems, the spinodal equation becomes (Altena and Smolders, 1982)

$$\left(\frac{\partial^2 \Delta G_{\mathrm{M}}}{\partial \phi_2^2}\right)\left(\frac{\partial^2 \Delta G_{\mathrm{M}}}{\partial \phi_3^2}\right) - \left(\frac{\partial^2 \Delta G_{\mathrm{M}}}{\partial \phi_2 \partial \phi_3}\right)^2 = 0, \tag{1.1.17}$$

where

$$\frac{1}{RT}\frac{\partial^2 \Delta G_{\mathrm{M}}}{\partial \phi_2^2} = \frac{1}{\phi_1} + \frac{1}{v_2\phi_2} - 2g_{12} + 2g_{12}(u_1 - u_2) + u_1 u_2 \left(\frac{\partial^2 g_{12}}{\partial u_2^2}\right), \tag{1.1.18}$$

$$\frac{1}{RT}\frac{\partial^2 \Delta G_{\mathrm{M}}}{\partial \phi_3^2} = \frac{1}{\phi_1} + \frac{1}{v_3\phi_3} - 2g_{13} + 2u_2^2(1+u_1)\left(\frac{\partial g_{12}}{\partial u_2}\right) + u_2^3 u_1 \left(\frac{\partial^2 g_{12}}{\partial u_2^2}\right), \tag{1.1.19}$$

$$\frac{1}{RT}\frac{\partial^2 \Delta G_{\mathrm{M}}}{\partial \phi_2 \partial \phi_3} = \frac{1}{\phi_1} - g_{13} + \frac{g_{23}}{v_2} - g_{12} - u_1 u_2 \left(\frac{\partial g_{12}}{\partial u_2}\right) - u_1 u_2^2 \left(\frac{\partial^2 g_{12}}{\partial u_2^2}\right), \tag{1.1.20}$$

$$u_1 = \frac{\phi_1}{\phi_1 + \phi_2}, \tag{1.1.21}$$

$$u_2 = \frac{\phi_2}{\phi_1 + \phi_2}, \tag{1.1.22}$$

and if g_{13} and g_{23} are composition independent. Note that from an FRRPP standpoint, the solvent becomes the monomer, while the non-solvent becomes the precipitant.

A representative plot of binodal and spinodal curves for ternary polymer/monomer/precipitant systems (which is similar to that of a polymer/solvent/non-solvent system) is shown in Fig. 1.1.2 at constant temperature and pressure. The phase envelope pertains to the region encompassed by the binodal curves, in which there exist two phases at equilibrium. Outside the phase envelope is the single-phase region. The so-called tie lines are straight lines that join the binodal compositions at equilibrium. If the system has an LCST, then the size of the phase envelope increases with increasing temperature. If the system has a UCST, then the size of the phase envelope decreases with increasing temperature.

1.1.2.3 Measurement of Binodal and Spinodal Curves

A number of phase curve measurement methods have been used in conjunction with FRRPP studies. Some of them will be described in various sections throughout this monograph. Briefly, they include the following:

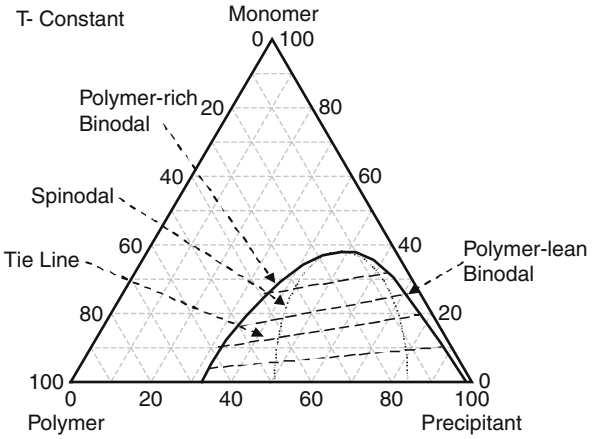

Fig. 1.1.2 Representative phase diagram in an equilateral triangular plot of a polymer/monomer/precipitant system showing binodal and spinodal curves and tie lines

1. Cloudpoint method, wherein the appearance and disappearance of another phase is detected through changes in turbidity of the fluid. Both binodal and approximate spinodal curves can be measured.
2. Time-resolved light scattering method, wherein the spinodal curve is measured based on vanishing mutual diffusivities.
3. Sorption method, wherein the spinodal curve is obtained when a swollen polymer membrane becomes incapable of further sorption due to vanishing mutual diffusivity.
4. Pulsed NMR method, which is used to determine binodal compositions based on differences in decay times of nuclear spins from polymer-rich and polymer-lean phases.

The cloudpoint method is the simplest and most reliable approach to measuring both binodal and spinodal curves. The cloudpoint apparatus is shown in Fig. 1.1.3. Usually, the method starts by loading the heavy walled tube container with the polymer and solvent. The temperature is raised to dissolve the polymer, at which point the solution is transparent. Then, the temperature is slowly changed until the mixture starts to appear cloudy. This indicates the formation of another liquid phase, and the onset of cloudiness can be interpreted as a spinodal point. To arrive at the binodal point corresponding to the fluid composition, the direction of temperature change is reversed until the mixture becomes clear again. The same measurement method is used for different compositions. However, for ternary polymer/monomer/precipitant systems, a more efficient method of traversing the phase diagram is used and presented in the next section.

Using the above-mentioned methods to measure phase curves, the following results are obtained for binary systems of interest. Figure 1.1.4 shows the result for polystyrene/cyclohexanol system, which has been a subject of early phase separation kinetics studies.

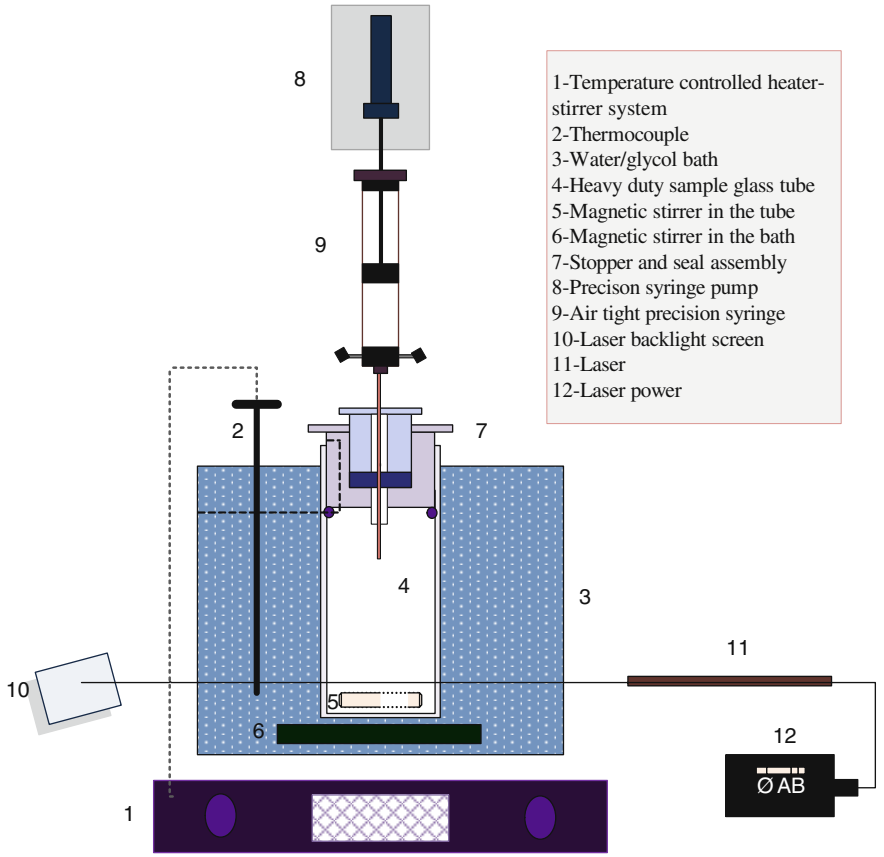

Fig. 1.1.3 Schematic experimental setup for generation of ternary phase diagrams using the cloudpoint method (Redrawn with permission from Wang et al., 1999)

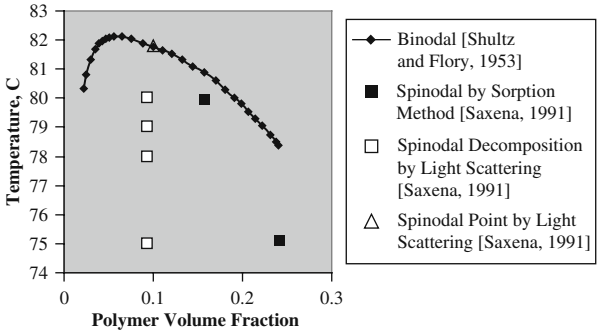

Fig. 1.1.4 Phase diagram-related results for polystyrene/cyclohexanol system

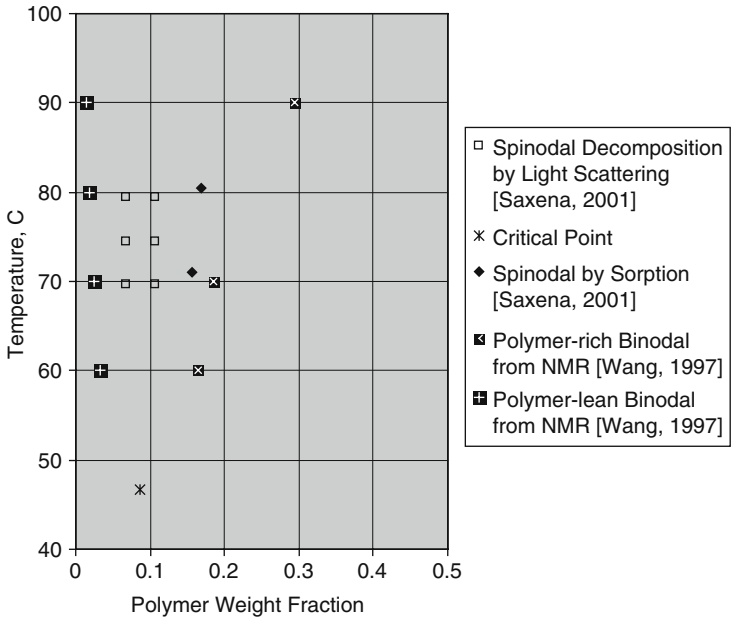

Fig. 1.1.5 Phase diagram measurement results for the PMAA/water system. The critical point (LCST) is obtained from the literature (Eliassaf and Silberberg, 1962). Spinodal decomposition-based points are used to analyze kinetics of phase separation deep inside the spinodal region

For the PMAA/water system that has become a prelude to studies of the PMAA/MAA/water reactive system, Fig. 1.1.5 shows phase curves and points that were obtained by our research group.

1.1.3 The LCST Phenomenon in Experimental Polymer/Small-Molecule Systems

Since it has not been easy to predict LCST data for polymer/solvent systems, an initial search was made for LCST data for mixed small-molecule systems. These were also considered "Universal" solvent systems, in which LCST behavior could be obtained with a wide variety of monomer/polymer systems. The following possibilities were obtained:

I. Mixed solvents – water/MEK, water/2-pentanone, water/other higher ketones, water/ethylene glycol methyl butyl ether, water/propylene glycol propyl ether, glycerol/guaiacol, glycerol/*m*-toluidine, glycerol/ethyl benzylamine, water/pyridines, water/piperidines (International Critical Tables, Volume III, 1928, pp. 386–398; Seidell and Linke, 1952)
II. Hydrocarbon gases – ethane, propane, and butane.

LCSTs have been known to occur 50–100°C below their critical temperatures (Freeman and Rowlinson, 1960; McHugh and Guckes, 1985).

Type I solvents form an LCST by themselves; they involve a variant of the currently understood FRRPP mechanism in polymer systems. As for Type II solvents, they offered good promise. It was believed that Freon® compounds are included in this class. The problem with these solvents is that they involve pressures in the 10–100 bar range.

1.1.3.1 LCST and the FRRPP Process

The free-radical retrograde-precipitation polymerization (FRRPP) process distinguishes itself from the conventional free-radical precipitation polymerization in both mechanisms and final product properties. In short, the FRRPP process proceeds above the LCST of the system, whereas the conventional-precipitation polymerization generally happens within the UCST region. For the different mechanisms of the UCST and LCST, one can expect that the polymerization process must be controlled by different schemes above the LCST and below the UCST. Furthermore, the product properties may possess some unique characteristics for the aforementioned reasons.

Since the discovery of the FRRPP process, research has been directed toward the study of the demixing polymerization mechanism (reaction kinetics, phase separation, morphology, product characterization, etc.). The FRRPP process relies heavily on the incipience of the LCST of the system. The fact that typical LCSTs of most nonpolar systems are much higher than normal operating temperatures for the free-radical polymerization process can make the FRRPP process infeasible. From a table that lists the LCST of polystyrene (PS) in some common solvents (Caneba, 1992a, b), the following observations and conclusions were drawn:

1. Most LCSTs lie between the boiling temperatures and the critical temperatures of the solvents, with notable exceptions for polystyrene in diethyl ether, acetone, and *t*-butyl acetate, wherein *T*/LCST (K/K) are 1.02, 1.03, and 1.08, respectively.
2. The similarities between the polarities and the shapes of the solvent and polymer have a significant effect on the LCST, and the more similar the polarities or the shapes of the solvent and the polymer, the higher the LCST.
3. The LCST has some relationship to the critical temperature of the solvent. The higher the critical temperature of the solvent, the greater the possibility that the system will possess a high LCST.

For the polystyrene/solvent systems listed (Caneba, 1992a, b), careful selection of the solvent(s) permitted the FRRPP process to be carried out at a relatively low temperature, which made this new polymerization method more promising. For high LCST systems, specially designed reactors can be used to carry out the FRRPP process. However the limitation is, the higher the temperature, the more likely the incipience of thermal degradation in the system. Additionally, running the free-radical

polymerization at relatively high temperature will result in more problems in process control, energy cost, and product quality. As far as the FRRPP process is concerned, the lower the LCST of the system, the easier the process control, and the better the product quality. Aqueous solutions of polar polymer systems could result in low LCST values. This makes FRRPP a very appropriate method for highly polar polymer systems, which can be at least be partially soluble in water. On the other hand, a few favorable cases, such as polystyrene–styrene–diethyl ether or polystyrene–styrene–acetone or polystyrene–styrene–*t*-butyl acetate, opened a new window for the application of the FRRPP process in nonpolar systems.

Efforts were also centered on the search for a practical solvent system that will exhibit an LCST with poly(methyl methacrylate) PMMA and poly(vinyl acetate) PVA. Results are recently being presented in the literature (Caneba et al., 2009). For the PVA/solvent system, no LCST data were reported in the literature, except for a citation on LCST behavior for partially hydrolyzed PVA in water. Cloudpoint experiments on PVA with mixtures of alcohol (ethanol, isopropanol, *n*-butanol, *t*-butanol) and water resulted in LCST behavior below 97ºC.

More recently, calculation of the LCST for polyethylene, polyvinylidene chloride, polychlorotrifluoroethylene, polystyrene, and polypropylene was undertaken using a theoretical method of atom connectivities for polymer and solvent (Liu and Zhong, 2005) (see Table 1.1.1). Some solvents of choice were water, butane, acetone, toluene, cyclopentane, *t*-butanol and methyl ethyl ketone, and THF. The LCST values for polyethylene, polyvinylidene chloride (PVDC), and polychlorotrifluoroethylene with the solvents are the same, because of the structure connectivity rules.

The determination of experimental LCST for the polymer–solvent mixtures was measured for PVDC–acrylonitrile (AN)–methyl methacrylate (MMA) 1 wt% in *t*-butanol; PVDC/AN/MMA 1 wt% in MEK; PVDC/AN/MMA 1 wt% in 50/50 wt% *t*-butanol/MEK mixture; PVDC/AN/MMA 1 wt% in 70% MEK/30% *t*-butanol mixture; polychlorotrifluoroethylene (PCTFE) 1 wt% in 70% MEK/30% *t*-butanol mixture; PVDC/VC in 70% MEK/30% *t*-butanol mixture; and polyvinyl methyl ketone

Table 1.1.1 LCST (*K*) values for various polymer/solvent pairs from theoretical calculations using connectivity rules (Liu and Zhong, 2005)

Solvent	Polyethylene	Poly(vinylidene chloride)	Polychlorotri-fluoroethylene	Polystyrene	Polypropylene
Water	361	361	361	–	–
Butane	386	386	386	–	429 (422)*
Acetone	396	396	396	352 (340)	–
MEK	401	401	401	357 (425)	–
Toluene	554	554	554	–	–
Cyclopentane	463	463	463	419 (428)	534 (540)
t-Butanol	436	436	436	–	–
THF	463	463	463	510 (552)	–

*Values in parentheses are experimental.

Table 1.1.2 LCST values of various polymers in azeotropic *t*-butanol/MEK

Polymer	LCST (°C)
PVDC–AN–MMA	112–123
PVDC–VC	105–114
PCTFE	97–107
PVMK	132–141

(PVMK) in 70% MEK/30% *t*-butanol. The PVDC/AN/MMA materials in *t*-butanol showed no cloudpoint transition, although PVDC/AN/MMA in MEK showed a cloudpoint of 145ºC. Further tests were done using mixtures of *t*-butanol and MEK to lower the cloudpoint from 145ºC. A test of 50/50% *t*-butanol and MEK showed no cloudpoint transition. A new set of experimental results using 70% MEK/30% *t*-butanol mixture is found in Table 1.1.2

1.1.3.2 Measurement of LCST-Based Ternary Phase Diagrams Using Cloudpoint Experimentation

Ternary (polymer/monomer/solvent) systems were investigated. The choice of the systems was based on the criterion that the systems should be suitable to run the FRRPP process.

Arbitrarily, the polymer/solvent system which has a relatively low LCST (i.e., LCST < 100ºC) is taken as the appropriate system to carry out the FRRPP process by using the corresponding monomer and free-radical initiator under moderate pressures. In practice, the FRRPP process should proceed at a temperature well above the LCST of the system to achieve a reasonably large two-phase envelope. Often, the molecular weight of the FRRPP polymer is not very high (as in solution polymerization), and this further requires a lower LCST system corresponding to the average molecular weight of the product. Usually, the aqueous polymer solution will give a LCST low enough to run the FRRPP process, and poly(methacrylic acid) (PMAA) polymerized in the water medium is chosen among these kinds of systems. For nonpolar polymer systems, the LCST is usually high and the appropriate system must be chosen to carry out the FRRPP process under suitable conditions. Polystyrene is one of the main commodity polymer products. The LCSTs of polystyrene in acetone and diethyl ether were cited to be equal to 67 and 42°C, respectively (Caneba, 1992a, b). Taking account of the actual molecular weight that can be achieved through solution polymerization under normal free-radical polymerization conditions, the styrene/diethyl ether system is the system that can display a significant phase envelope for the FRRPP process under 100°C and is mainly used in fundamental FRRPP efforts. Experiments show that both PMAA/MAA/water and polystyrene/styrene/diethyl ether systems have an applicable retrograde-precipitation behavior under the experimental conditions.

Materials

Methacrylic acid (MAA) was obtained from Aldrich Chemicals with 250 ppm inhibitor of methyl ethyl hydroquinone (MEHQ) without further purification. Styrene also came from Aldrich and was double distilled and inhibited with hydroquinone (HQ) before use. Diethyl ether (DEE) from Aldrich Chemicals was used as it is. Poly(methacrylic acid) (PMAA) made by the FRRPP process in our lab with different molecular weights and polydispersity indices (PDI) was used in the experiments. Polystyrene was bought from Pressure Chemicals Co. with different molecular weights and the same PDI of 1.06. The products through the FRRPP process in our lab were also used to determine the phase envelope.

Apparatus and Procedure

Ternary phase envelopes were determined with specially designed apparatus (Fig. 1.1.3) that consisted of a heavy-duty-wall tube with the outer diameter of 1.54 cm and effective length of 20.32 cm. Sometimes, a reference tube containing the solution with about the same polymer concentration of the sample, but with a composition in the homogeneous solution region, would also be used to double cross-check the cloudpoints. The sample tube had a tailored Teflon® stopper through which a channel with different diameters in different sections was cut to fit the requirement of a silicone rubber seal. The needle of a precision syringe could penetrate the silicone rubber without breaking the seal of the tube. Preweighed PS was transferred into the tube. The air in the tube was removed by vacuum before the experiment and the tube was mounted in the water bath. A small Teflon® coated magnetic stirrer was placed into the tube for stirring. The tube was capped with the specially designed Teflon® stopper and then subjected to vacuum. A clear water bath with magnetic stirrer was maintained within ± 0.1°C of the required temperature. A syringe pump was used to accurately meter the solvents into the tube. A He–Ne laser beside the bath was installed to facilitate the determination of the end point. Small-molecule fluids (MAA, water, styrene, and DEE) could be added from the precision air-tight syringes into the tube to change the compositions of the mixture in the sample tube. The cloudpoint curve (CPC) was determined by adding a monomer (MAA or styrene) to the point of clarity of the turbid solution. The end point was determined by comparing the laser beam passing the solution in the sample or reference tube. For high concentration of polymer sample, the CPC was determined by static method, where known composition samples in sealed bottles (prepared from the knowledge of the phase boundary) were placed into an isothermal bath for trial-and-error experiments until some of the samples began to turn a little cloudy. Usually, three samples gave the approximate phase boundary for this method, but the error was larger than the method shown in Fig. 1.1.3. Also, precipitant (water or DEE) was added to the transparent sample until the sample began to turn opaque; or monomer (MAA or styrene) added to the opaque sample until it became transparent. However, this procedure was time consuming; thus, solvents and non-solvents were added at a reasonable rate. The so-called

instantaneous precipitation point curve (IPPC)[1] was obtained by adding precipitant (water or DEE) to the homogeneous solution of the sample tube until the solution became totally cloudy. For high polymer concentration samples, the IPPC can be determined by the static method described above, or by the method shown in Fig. 1.1.3 with more intense stirring. The accuracy of the air-tight precision syringe was ±0.01 ml with one drop of the liquid equal to around 0.002 ml.

Measurement of Tie Line Compositions

Ends of tie lines in phase diagrams intersect phase curves and represent compositions of phases in equilibrium. The procedure to measure tie line compositions started by placing known composition samples into the capped vials. Then, the vials were immersed into a constant temperature bath for at least 4 h (usually for about 8 h) to ensure the phase separation nearly completed. To separate the two phases in equilibrium, different procedures were used for the PMAA/MAA/water and PS/S/ether systems. For the PMAA system, samples were taken out of the bath and the polymer-lean phase was poured into aluminum pans. Weights of both phases were obtained right after the separation. Also, the weight of the polymer-lean phase could be obtained from the difference between the weight of the original sample and that of the polymer-rich phase. After that, both the polymer-lean and polymer-rich phases were dried completely. Finally, the weighed polymer samples were used to calculate the polymer concentrations in both phases. For the PS/S/ether system, the procedure was a little different. Due to the pressure in the vials, the polymer-lean phase was not obtained by the above method. Carefully designed caps for the small vials were used. The caps were designed such that the polymer-lean phase was taken out by syringe easily after the phase separation. Usually, the PS in the polymer-lean phase was negligible, and almost no dry solid polymer could be seen in the aluminum pan after drying within the experimental error. The weight of the polymer-lean phase was then obtained by the difference between the weight of the original sample and that of the polymer-rich phase.

After calculating the concentration of the polymer in both polymer-rich and polymer-lean phases, the phase diagram obtained from the cloudpoint experiment was constructed with the tie lines. From polymer concentrations in both phases, tie lines were drawn in the ternary phase diagram, which would meet with the overall composition of the starting fluid. If the three points were not in a straight line, results from the determination of binodal or the tie line experiment were not correct. Only data with nearly straight tie lines were reported for both systems.

[1] The IPPC is neither the binodal nor the spinodal, but the phenomenon happens within the spinodal envelope. In our experiment, the spinodal can only be approximated. But, the IPPC may play a very important role in practical situations. Before the system enters the IPPC from the corresponding CPC curve, it will remain partially cloudy without precipitation with stirring for a very long time. After the composition change brings the system into the IPPC region, it will precipitate even with the stirring. That means, the IPPC is the boundary whereby the real system begins to precipitate rapidly.

Results and Discussion

Most of the phase diagrams shown here pertain to the PMAA/MAA/water system. For the PS/S/DEE system, more extensive results are shown in Caneba and Shi (2002), and its phase envelope orientation looked similar to that in Fig. 1.1.2. Figure 1.1.6 shows the cloudpoint curves (CPC) for the PMAA/MAA/water system at different temperatures. When the temperature of the system was raised, the two-phase region was enlarged, which corresponds to the LCST phenomenon. Figure 1.1.7 shows phase diagrams of different PMAA molecular weight samples in the mixture of MAA and water. It is clear that the higher molecular weight sample will have a larger two-phase region. Experimental data in the high polymer concentration region (above 8 wt% of PMAA for systems investigated) were determined from the static method described earlier. Results showed that the monomer, MAA, was a very good solvent for PMAA and the two-phase region was still kept below 8% of monomer concentration even at 90°C. The CPC flattened out at the highest monomer concentration for a relatively broad polymer concentration region until the polymer concentration passed around 10 wt%. Then, the monomer concentration in the system along the CPC started to go down. As discussed in the section about the LCST behavior, due to the strong intra- and intermolecular interactions, the liquid–liquid phase behavior of this system is different from the nonpolar systems, where the LCST often occurs between the boiling point and the critical point of the solvent.

For the PMAA/MAA/water system, water is also a solvent for PMAA to a certain degree; thus, the phase behavior is different from non-solvent/solvent/polymer systems. On the other hand, inter- and intra-association effects accompanying the

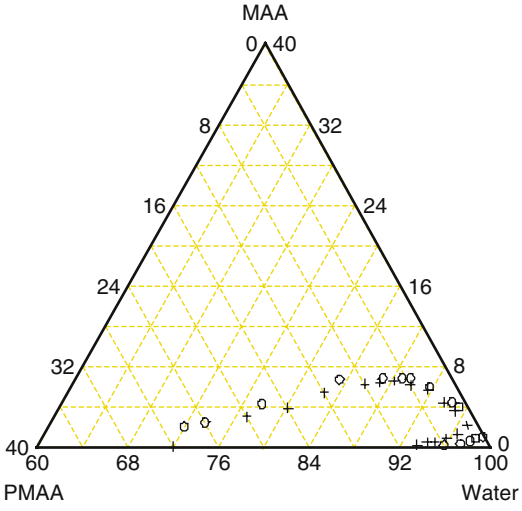

(M_n = 180,000 g/mol, *PDI* = 1.4; o: 90°C, +: 80°C)

Fig. 1.1.6 CPC (binodal points) of PMAA/MAA/water system at 80 and 90°C (Reproduced with permission from Shi, 1997)

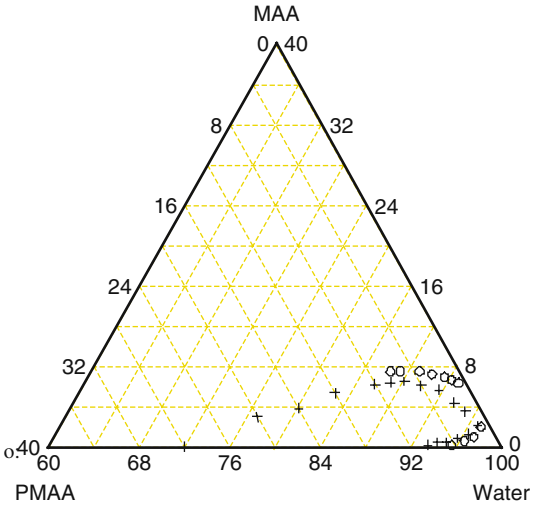

Fig. 1.1.7 CPC (binodal points) for PMAA/MAA/water systems of different PMAA molecular weights and at 80°C (Reproduced with permission from Shi, 1997)

(T = 80°C; + :M_n = 180,000, PDI = 1.4; o: M_n = 230,000, PDI = 1.41)

system make the liquid–liquid phase behavior more complicated. This was shown at the lower right corner of the ternary phase diagram where the CPC turns to the high polymer concentration again at a very low monomer concentration. This phenomenon is mainly attributed to the association effects between different components. In the vicinity of the pure water vertex when the polymer concentration is very low, the degree of the ionization of PMAA is relatively high, which is typically observed from a normal polyelectrolyte molecule. This enhances the solubility of the PMAA in water (Molyneux, 1984).

When MAA was added to such a system, the ionization of MAA was much stronger than that of PMAA, and the net effect was that the ionization of MAA prevented PMAA from ionizing in water. This changes the conformation of PMAA from expanded to a relatively compacted form, which in turn can reduce the solubility of PMAA in the system. If the monomer concentration in the system is high enough, the polymer will precipitate from the solution for the ionization suppression of the polymer molecules in water. This is the same as adding strong acid, such as hydrochloric acid, into the PMAA–water solution, which is often used to suppress the ionization of PMAA in water (Molyneux, 1984).

For PS/S/DEE systems, phase curves were measured by Wang (1997) at various temperatures and PS molecular weights. A replot of the data at 50 and 80°C at PS number average molecular weight of 25,000 g/mol is shown in Fig. 1.1.8. Note that Wang obtained tie lines that are horizontal for these systems. This means that both polymer-rich and polymer-lean phases have the same monomer composition at the same temperature. Based on the ternary Flory–Huggins equations (Eqs. 1.1.11–1.1.13), this corresponds to having the pairwise interaction parameter between S

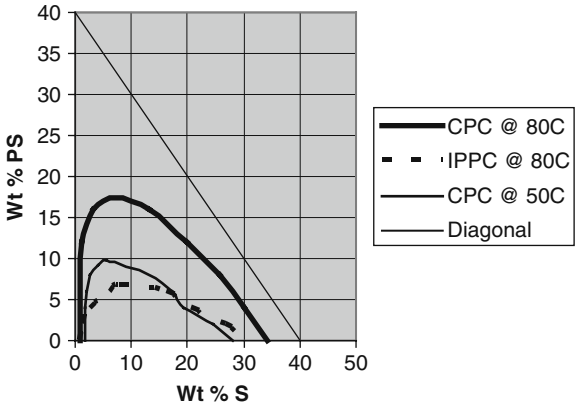

Fig. 1.1.8 Phase curves for LCST behavior of PS/S/DEE system. Note that tie lines should be considered horizontal, as verified experimentally

and PS to be approximately the same as the pairwise interaction parameter between S and DEE.

Figures 1.1.9–1.1.12 show more phase diagrams of the PMAA/MAA/water system. Figure 1.1.12 shows the CPC with several tie lines.

Figures 1.1.10–1.1.12 show the CPC and IPPC curves. For the system with PMAA number average molecular weight of 180,000 g/mol, the IPPC has been found to be very small. The spinodal curve is the theoretical boundary between the metastable and unstable regions, where the mutual diffusion coefficient is zero, whereas the IPPC corresponds to the sudden liquid–liquid phase separation under certain experimental conditions. The other difference is that the spinodal has a

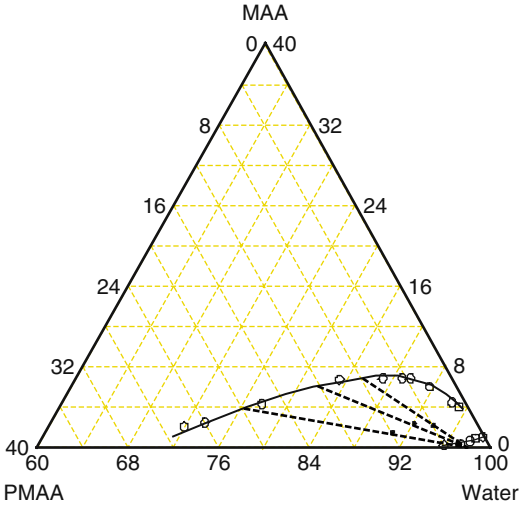

(PMAA: M_n = 180,000, PDI = 1.40; Temperature: 80°C)

Fig. 1.1.9 Phase diagram of the PMAA/MAA/water system at 80°C with tie lines (Reproduced with permission from Shi, 1997)

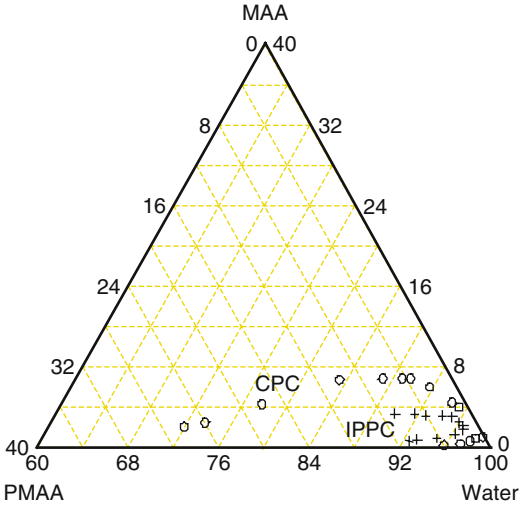

(PMAA: $M_n = 180{,}000$, $PDI = 1.4$)

Fig. 1.1.10 CPC and IPPC of the PMAA/MAA/water system at 90°C (Reproduced with permission from Shi, 1997)

common tangent point with binodal at the critical point, whereas the IPPC shares no common tangent point with binodal, as shown in the results. This may be caused by the fact that near the critical point, the composition difference between the two phases is relatively smaller compared with those at the points away from the critical point. The latter usually show large composition differences between the two

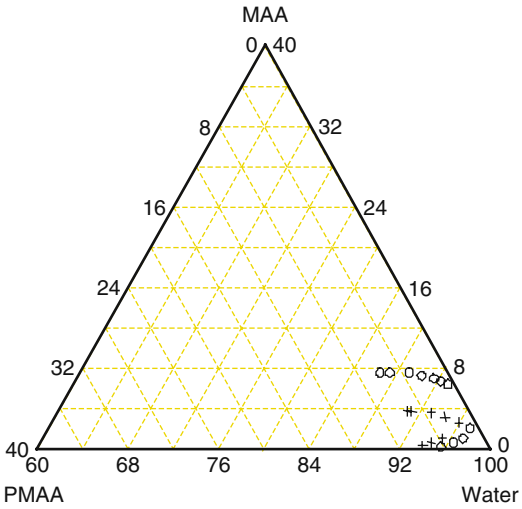

($M_n = 230{,}000$, $PDI = 1.4$; o: CPC, +: IPPC)

Fig. 1.1.11 CPC and IPPC for the PMAA/MAA/water system at 80°C (Reproduced with permission from Shi, 1997)

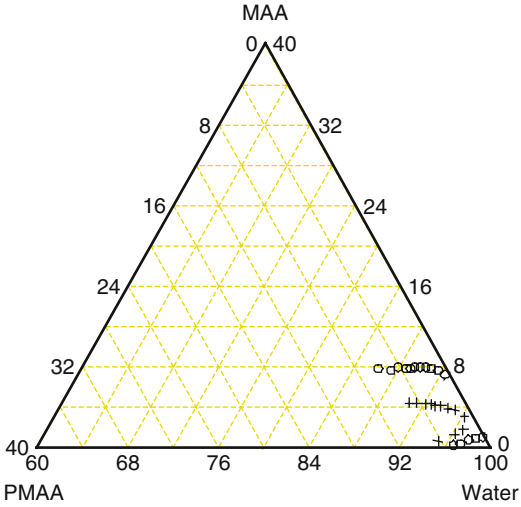

Fig. 1.1.12 CPC and IPPC for the PMAA/MAA/water system at 90°C (Reproduced with permission from Shi, 1997)

(M_n = 230,000, PDI = 1.4`; o: CPC, +: IPPC)

phases if phase separation presents. Therefore, it is reasonable to believe that the driving force for the phase separation between the two phases which have very similar compositions is not so significant, and the small composition difference between the two phases also results in the absence of IPPC points near the critical point. The common knowledge is that the critical point is the point where the two phases are undistinguishable. This also means that the points near the critical point within the two-phase region will bear some of these characteristics. Thus, the distinction between the two phases is small and time dependent, which induces more difference between the spinodal and the IPPC near the critical point. This phenomenon is confirmed by the experimental observations. To some degree, the spinodal is very important in both theory and practice, whereas the IPPC may be more important to industry.

1.1.4 Nomenclature

1.1.4.1 Alphabet Symbols

Upper Case

G – Gibbs free energy, J
H – enthalpy, J
$\bar{M}$ – average molecular weight, Da or g/mol
N_r – total number of sites in a lattice
Q – generalized van der Waals partition function, dimensionless
$\tilde{P}$ – reduced pressure (=P/P^*), dimensionless

P^* – characteristic pressure, bar
P – pressure, bar
R – universal gas constant
S – entropy, J
T – absolute temperature, K
T^* – characteristic temperature
$\tilde{T}$ – reduced temperature ($=T/T^*$)
U – internal energy per molecule
V^* – characteristic volume, cm^3/mol
V_1 – molar volume of solvent, cm^3/mol

Lower Case

c – Prigogine's parameter per segment (see Eq. 1.1.6)
g – interaction parameter for binary pairs, dimensionless
k –Boltzmann constant
n – Number of moles, mol
r – degree of polymerization or number of polymer segments
u – defined in Eqs. (1.1.12) and (1.1.22)

1.1.4.2 Subscripts

1, 2, 3, i,j – component label
M – property change upon mixing
S – solvent
P – polymer

1.1.4.3 Superscripts

α, β – phases in equilibrium

1.1.4.4 Greek Symbols

γ – geometric constant (see Eq. 1.1.6)
ϕ – volume fraction polymer, dimensionless
μ – chemical potential
χ – Flory–Huggins interaction parameter for binary polymer/solvent systems
v^* – hard-core volume per segment
$\tilde{v}$ – reduced volume ($= v/v^*$), dimensionless
v – volume per segment

1.2 Polymer Transport Processes

Polymer transport processes that are relevant to the FRRPP process are fluid flow, heat transport, and mass transfer. Fluid flow is evident during fluid conveying and mixing of reactor fluids. Heat transfer is always relevant not only for dissipation of the heat of polymerization but also in an unusual heat trapping effect found in FRRPP systems. Finally, mass transfer is relevant to the diffusion of reactants into polymerization reactive sites, in measurement of spinodal curves, and in study of the evolution of composition profiles during phase separation.

1.2.1 Fluid Flow

In FRRPP systems, pertinent fluid flow topics include pipe flow and fluid mixing in reactors. Since the main objective is usually a uniform distribution of components and fast conveying of materials, turbulent flow behavior is the aim. This flow pattern is traditionally characterized by the so-called Reynolds Number, *Re*, and defined as

$$\mathrm{Re} = \frac{D_\mathrm{P} v_\mathrm{av} \rho}{\mu}, \tag{1.2.1}$$

where D_P is the pipe diameter, v_av is the average velocity of the fluid in the pipe-length direction, ρ is the fluid density, and μ is the fluid viscosity (Geankoplis, 2003). Note that units of the various quantities in Eq. (1.2.1) should be adjusted in such a way that the Reynolds number becomes dimensionless. If the Reynolds number is greater than 4,000, then the fluid is flowing in turbulent behavior inside the pipe. If it is below 2,100, the flow is laminar. For normally viscous polymer solutions, it should not be a surprise that laminar flow conditions will persist, due to their relatively high viscosities. Under laminar flow conditions, the velocity distribution within the pipe is such that it is maximum at the center of the pipe cross-section and zero at the pipewall. From this, the average fluid velocity, v_av, can be obtained to be equal to one-half of the maximum fluid velocity. Finally, the average fluid velocity has been related to other quantities in the system through the so-called Hagen–Poiseuille equation:

$$v_\mathrm{av} = \frac{(-\Delta P)\, D_\mathrm{P}^2}{32 \mu L}, \tag{1.2.2}$$

where L is the pipe length, and $(-\Delta P)$ is the pressure drop across the flow direction of the pipe. If the flow is turbulent, the velocity profile is flat, i.e., the fluid has a uniform velocity within the pipe cross-section.

Fluid mixing inside reactor vessels is usually characterized through another type of Reynolds number:

$$\mathrm{Re}' = \frac{D_a^2 N \rho}{\mu}, \tag{1.2.3}$$

where D_a is the agitator blade diameter and N is the agitator angular speed. When *Re'* < 10, the fluid is being mixed in the tank under laminar flow conditions. Turbulent flow occurs when *Re'* > 10,000. For various tank and agitator geometries as well the types and measurements of tank baffles, *Re'* is used to determine the agitator power to maintain a given level of mixing.

Agitated tank scale-up is also a fluid flow consideration in polymerization systems, including the FRRPP process. Once the performance of the reactor system is obtained in a bench scale or laboratory unit, the proper conditions would have to be estimated in larger reactor units if larger amounts of material have to be produced. The first thing to satisfy is the so-called geometric similarity. This means that the larger-scale unit has to be made with the same shape as the laboratory unit. Then, the so-called scale-up ratio, *R'*, has to be determined, which can be based on the agitator diameter. A scale-up ratio $R = 100$ means that the larger-scale unit is 100 times longer, wider, and deeper than the laboratory unit. The purpose of the scale-up ratio is to determine the agitator speed N of the larger-scale reactor. This is based on the following equation:

$$N_{\text{large scale}} = N_{\text{small scale}} \left(\frac{1}{R'}\right)^{n'}. \tag{1.2.4}$$

Values of the scale-up exponent *n'* are used, based on the following considerations:

1. Same fluid velocity: $n' = 1$
2. Equal suspension of solids: $n' = {}^{3}/_{4}$
3. Equal mass transfer rate or equal power/volume: $n' = 2/3$

Viscosity of polymer/small-molecule systems depends on the shear rate, polymer concentration, solvent viscosity, polymer molecular weight, polymer functional groups, polymer chain stiffness, and polymer architecture in the solvent environment, among other things.

Usually, the shear rate is the first classification method used, and then the polymer concentration. At low shear rates, the solution has a constant relatively high viscosity, or this is called the upper Newtonian behavior. At higher shear rates, the viscosity is lower and follows a power-law relationship with shear rate, when the coiled polymer chains are deformed by the flow field; thus, this is called the power-law behavior. At still higher shear rates, the behavior is Newtonian at constant viscosity when the chains are almost entirely aligned with the flow field.

In the dilute regime at low shear rates, when the polymer molecules are isolated coils in space (up to around 1 wt% polymer), the system viscosity equation is similar to those of suspensions in the solvent. The viscosity, μ, of the fluid is classically expressed through the Einstein equation (Bird et al., 2007)

$$\mu = \mu_S [1 + 2.5\phi], \tag{1.2.5}$$

where μ_S is the viscosity of the solvent and ϕ is the volume fraction of the polymer. A more sophisticated expression is the Huggins equation, wherein

$$\frac{\mu}{\mu_S} = 1 + [\mu]c + k'[\mu]^2 c^2, \tag{1.2.6}$$

where *k*' is a temperature-dependent coefficient, *c* is the polymer concentration, and $[\mu]$ is the so-called intrinsic viscosity of the polymer/solvent system, defined as

$$[\mu] = \left[\frac{\mu - \mu_S}{c\mu_S}\right]_{c=0}. \tag{1.2.7}$$

For concentrated polymer solutions, the Martin equation is applicable:

$$\log\left[\frac{\mu - \mu_S}{c\mu_S}\right] = \log[\mu] + K''[\mu]c \tag{1.2.8}$$

where *K"* is a temperature-dependent coefficient. The point on all these expressions is that the polymer solution viscosity increases dramatically as the system goes from dilute (0–1 wt%) to semi-dilute (1–5 wt%), and finally to concentration (>5 wt%) solution. Also, for the same polymer concentration, more soluble polymers in the solvent have higher viscosities compared to less soluble polymers in the same solvent (Rodriguez et al., 2003).

Values of viscosities of polymer solutions range from those of the solvent to orders of magnitude higher. For example, water and small-molecule organic fluids at room temperature have viscosities in the order of 1 Centipoise, while polymer solutions can have viscosities of 10 or even 100 Centipoise. In contrast, polystyrene melt can have viscosities of 1,000 Pa s (100 Centipoise = 0.1 Pa s). This means that concentrated polymer solutions and certainly melts would have relatively high viscosities that they would tend to exhibit laminar flow behavior.

1.2.2 Heat Transfer

The generalized energy equation for a polymerization system in convective or non-convective domain is (Bird et al., 2007)

$$\rho C_P \frac{DT}{Dt} = k\nabla^2 T + \dot{q}, \tag{1.2.9}$$

where C_P is the heat capacity of the reacting mixture, *T* is the absolute temperature, *t* is the reaction time, *k* is the thermal conductivity, and $\dot{q}$ is the reaction source term. Note that *DT/Dt* is the substantial derivative of the temperature with time, which is the time derivative of the temperature as observed along the flow of the system. In

chain polymerization systems, the source term (positive quantity) can be expressed as the product of the heat of polymerization ($-\Delta H_P$) and the rate of consumption of the monomer, r_M:

$$S = (-\Delta H_P) \cdot r_M. \tag{1.2.10}$$

If the reaction domain is nonconvective, the substantial derivative becomes a partial derivative, or time derivative measured at each point in space. This approach is used for reactive spherical particulate systems in the next section.

An important limiting case of interest in this monograph is the purely diffusive case (no convection and chemical reaction) in the radial direction (radius = r_0) of a cylindrical geometry, which occurs when a fluid within a small tube is rapidly cooled. Thus, Eq. (2.2.9) reduces to

$$\frac{\partial T}{\partial t} = \frac{\alpha_T}{r}\frac{\partial}{\partial r}\left[r\frac{\partial T}{\partial r}\right], \tag{1.2.11}$$

where $\alpha_T = k/\rho C_P$ is the thermal diffusivity. For a fluid that is initially at a temperature T_0 and brought to a wall temperature T_1 at t=0, the solution of Eq. (1.2.11) is (Carslaw and Jaeger, 1959)

$$\Theta = 2\sum_{n=1}^{\infty} \frac{J_0\,(r\beta_n/r_o)}{\beta_n J_1\,(\beta_n)} \exp\left(-\beta_n^2\tau\right), \tag{1.2.12}$$

where the dimensionless temperature

$$\Theta = \frac{T - T_1}{T_0 - T_1}, \tag{1.2.13}$$

the dimensionless time

$$\tau = \frac{\alpha_T t}{r_0^2}, \tag{1.2.14}$$

and β_n are the zeroes of $J_0(\beta)$, i.e., $J_0(\beta_n) = 0$ for $n = 1,2,3,\ldots,\infty$. The functions J_0 and J_1 are zeroth and first-order Bessel functions of the first kind. Equation (1.2.12) is plotted (Carslaw and Jaeger, 1959), and the result for a 98% approach of the centerline temperature to the wall temperature, the dimensionless time should be equal to 0.8. For a concentrated polymer particulate with typical thermal diffusivity in the order of 10^{-3} cm^2/s (Middleman, 1977), the time it takes for a 1-μm radius is only 0.8×10^{-5} s. Thus from Eq. (1.2.14), for a constant thermal diffusivity, the time it takes for a particle centerline temperature to approach the wall temperature decreases proportionately to the square of the radius. Smaller particles would therefore dissipate heat relatively fast compared to larger ones.

1.2.3 Diffusional Mass Transfer

Figure 1.2.1 shows the general diffusion behavior of a penetrant in amorphous polymer (Hopfenberg and Frisch, 1969). At very low temperatures and/or penetrant activities, concentration-independent diffusion prevails, i.e., the diffusivity is constant. At temperatures above the effective glass transition (T_g) of the polymer–penetrant mixture, the diffusivity varies with local penetrant concentration. When the diffusivity is constant or varies only with penetrant concentration, the process is called Fickian diffusion. For temperatures well below the glass transition temperature and at high penetrant activities, case II transport is observed. In this case, the overall rate of penetrant transport is determined by polymer relaxation due to mechanical, structural, etc., modes of the polymer/penetrant system (Frisch, 1980). An extreme case of case II behavior occurs when there are local fractures in the material (as sometimes observed when the penetrant activity is close to 1.0). This condition is known as crazing. The remaining transport behavior indicated in Fig. 1.2.1 is anomalous diffusion, where both diffusion and relaxation occur at comparable rates. Thus, the region for anomalous diffusion is always between those of case II and Fickian diffusion.

If the penetrant is a supercritical gas, the general transport behavior is different from that shown in Fig. 1.2.1 (Frisch, 1980). At temperatures above the glass transition or at very low penetrant activities, diffusion is concentration independent. However, at temperatures below the glass transition and at moderate penetrant activities, the behavior becomes concentration dependent; the overall transport mechanism corresponds to those of dissolution of the penetrant in the polymer matrices and adsorption in microcavities.

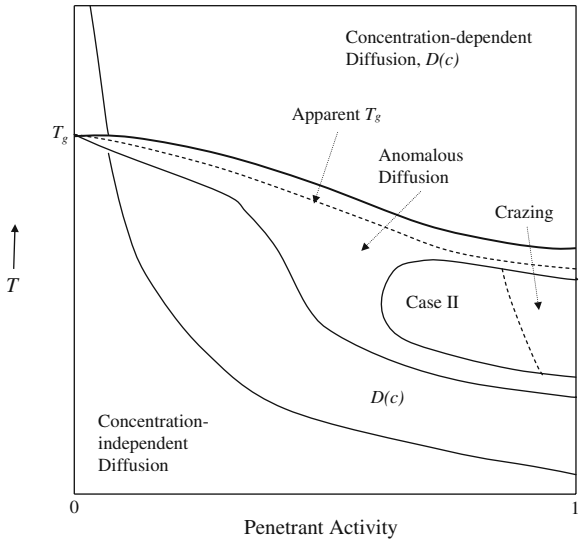

Fig. 1.2.1 Diffusion regimes for penetrant/polymer systems, where the penetrant activity usually means its pressure divided by its vapor pressure at the same temperature

The fundamental equation describing diffusion of a penetrant in the polymer system is Fick's first law

$$F = -D(\nabla c) \tag{1.2.15}$$

The quantities F and c are the flux and concentration of penetrant, respectively. When combined with the differential mass balance in the x-direction, Eq. (2.2.15) becomes

$$\frac{\partial c}{\partial t} = \frac{\partial}{\partial x}\left[D\left(\frac{\partial c}{\partial x}\right)\right]. \tag{1.2.16}$$

When D is constant, Eq. (1.2.16) reduces to the following special case:

$$\frac{\partial c}{\partial t} = D\left(\frac{\partial^2 c}{\partial x^2}\right). \tag{1.2.17}$$

Solutions to the three-dimensional form of Eq. (1.2.17) applied to different geometries and boundary conditions are summarized in a number of monographs (Crank and Park, 1968; Crank, 1970; Carslaw and Jaeger, 1959).

If we take a thin slab of polymer material of thickness, l, and expose both sides to a constant penetrant activity (sorption method), the weight of penetrant uptake, M_t after time t of exposure is obtained by solving Eq. (1.2.17). Thus,

$$\frac{M_t}{M_\infty} = 1 - \sum_{n=0}^{\infty} \frac{8}{(2n+1)^2\pi^2} \exp\left[-\frac{D(2n+1)^2\pi^2}{l^2}t\right] \tag{1.2.18}$$

or

$$\frac{M_t}{M_\infty} = 4\left(\frac{Dt}{l^2}\right)^{1/2}\left[\frac{1}{\pi^2} + 2\sum_{n=0}^{\infty}(-1)^n ierfc\frac{nl}{2(Dt)^{1/2}}\right]. \tag{1.2.19}$$

Equations (1.2.18) and (1.2.19) give identical numerical values. The former is obtained from separation of variables, while the latter from Laplace transforms. From Eq. (1.2.16), D can be obtained through the half-life method; at a relative uptake (right-hand side value) of 0.5,

$$\frac{t}{l^2} = -\left(\frac{1}{\pi^2 D}\right)\ln\left[\left(\frac{\pi^2}{l^6}\right) - \frac{1}{9}\left(\frac{\pi^2}{16}\right)\right]. \tag{1.2.20}$$

An alternate method to obtain D is given by approximating Eq. (1.2.19) at small times to give

$$\frac{M_t}{M_\infty} = 4\left(\frac{Dt}{\pi l^2}\right)^{1/2}, \tag{1.2.21}$$

which is valid for right-hand side values of 0 to about 0.6. Finally, when t approaches infinity, the series in Eq. (1.2.18) converges at $n = 0$ to give

$$\ln\left(1 - \frac{M_t}{M_\infty}\right) = -\frac{D\pi^2}{4\,l^2}t + \ln\left(\frac{8}{\pi^2}\right). \tag{1.2.22}$$

For any given D, Eqs. (1.2.18) and (1.2.19) indicate that a reduced plot of the relative uptake vs $(Dt)^{1/2}/l$ falls in a single master curve.

Concentration-independent diffusion results when inert gases diffuse in most polymers (Crank and Park, 1968; Duda and Vrentas, 1971) at sorbed concentrations of <0.2 wt%. In addition, this behavior is observed for water diffusing in some hydrophobic polymers, such as polyethylene and polypropylene (Rehage et al., 1970). Thus, only weak interactions exist between penetrant and polymer.

When the diffusivity is a function of concentration only, Eq. (1.2.16) describes concentration-dependent diffusion. Crank (1968) presents some mathematical formulations resulting in the following generalizations.

(a) Boltzmann transformation of Eq. (1.2.16) (when expressed in terms of $\varsigma = x/2t^{1/2}$) gives

$$-2\varsigma\frac{dc}{d\varsigma} = \frac{d}{d\varsigma}\left[D(c)\frac{dc}{d\varsigma}\right]. \tag{1.2.23}$$

Thus, for a certain value of $D(c)$, plots of M_t/M_∞ vs $t^{1/2}/l$ (or t/l^2) always fall on a single master curve.

(b) At the start of a sorption run, when the polymer matrix is a semi-infinite slab, we have

$$\frac{M_t}{M_\infty} = \frac{\int_0^\infty c\,dx}{c_o l} = \frac{2}{c_o}\left(\frac{t^{1/2}}{l}\right)\int_0^\infty c\,d\varsigma, \tag{1.2.24}$$

where c_o is the equilibrium penetrant concentration. At these times, the plot of M_t/M_∞ vs $t^{1/2}/l$ is a straight line with

$$Slope = \frac{2}{c_o}\int_0^\infty c\,d\varsigma,$$

Clearly, the integral quantity is not directly related to $D(c)$ at small times; thus, the aforementioned initial-times method (Eq. 1.2.21) cannot be used to deduce $D(c = 0)$ with sorption data taken near $t = 0$. In addition, if $D(c)$ increases with

c, the initial slope of the M_t/M_∞ vs $t^{1/2}/l$ plot is always higher for $D(c > 0)$ than for $D(c = 0)$. The opposite is true if $D(c)$ decreases with c.

For molecular interpretation, D (also called the mutual diffusion coefficient, or diffusion coefficient of the penetrant and polymer relative to the local enter of volume) has to be modified to take into account the bulk flow of the penetrant. Accordingly, a new coefficient, referred to as intrinsic diffusion coefficient, has been defined in terms of the rate of mass transfer relative to the center of mass. Crank (1968) shows that for negligible polymer mobility, the intrinsic diffusivity of the penetrant (designated as D_1', which is also the diffusivity of the penetrant based on the polymer frame of reference) is related to the volume-fixed mutual diffusion coefficient, D, by

$$D_1' = \phi^{-1} D, \tag{1.2.25}$$

where ϕ is the volume fraction of the polymer. With phenomenological arguments, Rehage and coworkers (1970) show that the intrinsic diffusivity of the penetrant, D_1, is the product of a hydrodynamic or transport factor (also called a mobility factor or intrinsic mobility), u_1, and a thermodynamic factor. Thus,

$$D_1' = u_1 \left(\rho_1 \frac{\partial \mu_1}{\partial \rho_1} \right), \tag{1.2.26}$$

where ρ_1 and μ_1 are the penetrant molar concentration and chemical potential, respectively. The thermodynamic factor is taken to be equal to RT at low penetrant concentrations. If not, it is established using polymer solution theories (see Section 1.1).

One of the simplest relationships (best regarded as semi-empirical) for the intrinsic mobility (Rogers, 1965), B, is

$$B = \frac{1}{\mu d}, \tag{1.2.27}$$

where μ is the viscosity and d is a length scale of the order of molecular dimensions. The quantity d is comparable to the jump length in the transition state (Glasstone et al., 1941) and zone (Cohen and Turnbull, 1959) theories. Although Eq. (1.2.27) describes the diffusion of tricresyl phosphate into poly(vinyl chloride) well, discrepancies observed with other systems are attributable to the fact that the effective "viscosity" of a penetrant molecule is not necessarily the same as the bulk viscosity of the medium. Nevertheless, the inverse relationship between viscosity and mobility has been used to relate mass transport and momentum transport mobilities.

Free-volume theories have been very successful in explaining concentration-dependent diffusion behavior of organic vapors in amorphous polymers, especially in cases where the penetrant is a good swelling agent for the polymer. The most significant free-volume theory is based on the works of Cohen and Turnbull (1959),

Fujita (Fujita and Kishimoto, 1961), and those of Vrentas and Duda (1977, 1982). They all consider the free volume per molecule as the volume within the "cage" of a molecule minus the volume of the molecule itself, i.e., as a "hole" opened up by density fluctuations of the molecules. According to Cohen and Turnbull (1959), diffusion occurs not as a result of activation in the ordinary sense, but as a result of redistribution of free volume within the liquid. With this, they derive an expression for mobility, similar to the Doolittle equation (1951, 1952):

$$B = A_{\mathrm{d}} \exp\left(-\frac{B_{\mathrm{d}}}{f}\right), \tag{1.2.28}$$

where B is the mobility, f is the fractional free volume, and A_{d} and B_{d} are constants. Fujita argues that Eq. (1.2.26) could be derived from the theory of Cohen and Turnbull if the mobility of a penetrant molecule depends primarily on the probability that a penetrant molecule finds itself adjacent to a hole large enough to permit a jump. In this case, A_{d} can be interpreted as a proportionality factor dependent primarily on the size of the penetrant molecule, and B_{d} a parameter proportional to the minimum value of the fractional free volume required for the penetrant molecule to undergo displacement. By assuming that the free volume is proportional to the volume fraction of the diluent (penetrant) added, Fujita obtains

$$\frac{1}{\ln\left(\frac{D_T}{D_{\varphi_1=0}}\right)} = \frac{f(0,T)}{B_{\mathrm{d}}} + \frac{\left[f(0,T)\right]^2}{B_{\mathrm{d}}\beta(T)}, \tag{1.2.29}$$

where D_T is the thermodynamic diffusion coefficient (also equal to the intrinsic diffusion coefficient, since Fujita totally ignored the thermodynamic factor), $D_{\phi_1=0}$ is the thermodynamic self-diffusion coefficient of the polymer, $f(0,T)$ is the fractional free volume of the polymer, ϕ_1 is the volume fraction of the penetrant, and $\beta(T)$ is the difference between the fractional free volume of the penetrant and polymer. Rogers and Machin (1972) discuss an extension of this theory by relaxing the linear dependence of $f(\phi_1,T)$ on ϕ_1. This is done by first relating $f(\phi_1,\mathrm{T})$ with the T_{g} (glass transition temperature) of the system. Then, various T_{g}–ϕ_1 relationships (Fox, 1956; Kelley and Bueche 1961; Kanig, 1963) were applied to get relationships similar to Eq. (1.2.27).

Even with this modification, the resulting equation was no better than Fujita's original equation, which only correlates data at $\phi_1 < 0.2$. These limitations seem to be absent in the free-volume theory of Vrentas and Duda, in which they obtained a general expression for the mutual diffusion coefficient, D, as

$$D = \frac{D_1 x_1 + D_2 x_2}{RT}\left(\frac{\partial \mu_1}{\partial \ln x_1}\right)_{\mathrm{T,P}}, \tag{1.2.30}$$

where x_i is the mole fraction of component i. Also, D_1 and D_2, the self-diffusion coefficients of the penetrant and polymer, respectively, are calculated from the free-

volume theory; and μ_1 is determined from Flory–Prigogine–Patterson theory (see Section 1.1). This formulation shows limited predictive capabilities; it breaks down for $\phi_1 > 0.8$ and at temperatures significantly higher than the T_g of at least one of the components in the binary mixture. A more modern free-volume expression for self-diffusivities of polymer and small-molecules in a mixture is the so-called Achilias–Kiparissides model (Achilias and Kiparissides, 1992), which is introduced in Section 2.4.

Other theories within the general framework of the free-volume concept have been advanced. They include the works of Kumins and Roteman (1961), Bueche (1953), Barrer (1957), DiBenedetto (1963), DiBenedetto and Paul (1964), Wilkens and Long (Wilkens, 1957; Wilkens and Long, 1957), and Vasenin (1960). Part of the reason that these theories are not so popular lies in the fact that their predictions of $D(c)$ were no better than those obtained by Fujita and Doolittle. In addition, most of these other theories concentrated on the temperature dependence of the intrinsic mobility, which is less important compared to its concentration dependence. In spite of the predictive limitations of the free-volume theory, it is applicable at the widest concentration range, and certainly it is the best theory to use for modeling diffusion limited behavior of polymerization systems.

In order to be able to analyze diffusion in multicomponent systems, we look into the phenomenological theory of irreversible processes (Fitts, 1962). At constant temperature and pressure, the diffusion current density j_i relative to the center of mass is obtained as

$$-j_i = \sum_{l=1}^{r} \Omega_{il} \nabla \mu_l \quad i = 1,2,\ldots,m, \tag{1.2.31}$$

where Ω's are phenomenological coefficients and m is the total number of components. Note that the sum of the diffusional fluxes j_i of all the components is equal to zero. The diffusion coefficient D_{ik} relative to the center of mass is

$$D_{ik} = \sum_{l=1}^{r} \Omega_{il} \frac{\partial \mu_l}{\partial \rho_k}, \tag{1.2.32}$$

where ρ_k is the partial mass density of component k. Equations (1.2.31) and (1.2.32) provide the generalized Fick's first law of diffusion, if the frame of reference is changed to the center of volume:

$$-j_i^{\mathrm{V}} = \sum_{k=1}^{m-1} D_{ik}^{\mathrm{V}} \nabla \rho_k \quad i = 1,2,\ldots,m, \tag{1.2.33}$$

where the superscript "V" corresponds to the use of the center of volume as the frame of reference. Note that the summation in Eq. (1.2.33) goes up to m–1 only,

because of the Gibbs–Duhem relation (Prausnitz et al., 1999). From the standpoint of experimental measurements, fluxes and diffusivities that are based on the center of volume (particle, rod, or layer) are more convenient to use.

An interesting situation occurs when the system is at the spinodal condition (Caneba and Soong, 1985b), wherein the determinant

$$\det\left[\frac{\partial \mu_i}{\partial \rho_j}\right] = 0 \quad i,j = 1,2,\ldots,m-1. \tag{1.2.34}$$

In matrix and vector notation, the volume frame of reference version of Eq. (1.2.32) means

$$\left[D^{\mathrm{V}}\right]_{m-1} = [M]_{m-1} \bullet \left[\frac{\partial \mu}{\partial \rho}\right]_{m-1}, \tag{1.2.35}$$

where the M-matrix (also called the mobility coefficient matrix) is uniquely related to the matrix of phenomenological coefficients; then for a positive-definite $[\Omega]$ (and consequently $[M]$), Eq. (1.2.34) implies that

$$\det\left[D^{\mathrm{V}}\right]_{m-1} = 0. \tag{1.2.36}$$

In matrix and vector notation, the volume frame of reference version of Eq. (1.2.32) becomes

$$\left[-j^{\mathrm{V}}\right]_{m-1} = \left[D^{\mathrm{V}}\right]_{m-1} \bullet [\nabla \rho]_{m-`1}. \tag{1.2.37}$$

Note that it is suffice to carry out the matrix operations for r–1 elements in Eqs. (1.2.34–1.2.37) because of the Gibbs–Duhem relation and the conservation of mass. If both sides of Eq. (1.2.37) are premultiplied by the transpose of $[\nabla \rho]_{r\text{-}1}$, then Eq. (1.2.37) becomes

$$[\nabla \rho]_{m-1}{}^{\mathrm{T}}\left[-j^{\mathrm{V}}\right]_{m-1} = [\nabla \rho]_{m-1}{}^{\mathrm{T}}\left[D^{\mathrm{V}}\right]_{m-1}[\nabla \rho]_{m-1}. \tag{1.2.38}$$

Application of Eq. (2.2.32) to (1.2.38) results in

$$-\sum_{i=1}^{m-1} j_i^{\mathrm{V}}\,(\nabla \rho_i) = 0. \tag{1.2.39}$$

Since the mutual diffusivity of component i relative to the center of volume (or could also be called effective diffusivity) is defined to be

$$D_i^{\mathrm{V}} = \frac{-j_i^{\mathrm{V}}}{\nabla \rho_i}, \tag{1.2.40}$$

combination of Eq. (1.2.40) with Eq. (1.2.39) results in

$$\sum_{i=1}^{m-1} D_i^{\mathrm{V}} (\nabla \rho_i)^2 = 0. \tag{1.2.41}$$

This means that if all $D_i{}^{\mathrm{v}}$ values are non-negative, then Eq. (1.2.41) holds only if for all i

$$D_i^{\mathrm{V}} = 0. \tag{1.2.42}$$

The consequence of Eq. (1.2.42) is very significant in the sense that for a multicomponent system, mutual diffusivities of all the components vanish at the spinodal curve. This has been clearly shown in binary (Caneba and Saxena, 1992) and even in ternary systems (Morral and Cahn, 1971) in the past.

1.2.4 Nomenclature

1.2.4.1 Alphabets

Upper Case

B – intrinsic mobility in Eq. (1.2.27), $\mathrm{Pa}^{-1}\ \mathrm{s}^{-1}\ \mathrm{m}^{-1}$
D – diffusivity based on fixed frame of reference and mutual diffusion coefficient, m^2/s
$\boldsymbol{F}$ – molar flux, $\mathrm{mol/m}^2\ \mathrm{s}$
L – pipe length, m
N – angular velocity, s^{-1}
P – pressure, bar
R – universal gas constant, J/mol K
T – absolute temperature, K

Lower Case

c – polymer concentration, mol/L or mol/ml
d – molecular interaction distance for viscosity and mobility, m
f – fractional free volume
k – thermal conductivity, $\mathrm{J/mol\ m}^2\ \mathrm{(K/m)}$
n – number of moles, mol
n' – scale-up exponent
r – radial distance, m
t – time, s

u – defined in Eqs. (1.1.21) and (1.1.22)
v – fluid velocity, m/s
x – spatial variable, m

1.2.4.2 Subscripts

av – average
1, 2, 3, *i, j, k* – component label
m – total number of components
n – dummy variable for infinite series
S – solvent

1.2.4.3 Superscripts

T – transpose operation of a matrix
V – corresponds to the use of the center of volume as the frame of reference

1.2.4.4 Greek Symbols

β_n – zeroes of $J_0(\beta)$, i.e., $J_0(\beta_n) = 0$ for $n = 1,2,3,\ldots,\infty$
ϕ – volume fraction polymer, dimensionless
μ – fluid viscosity, Pa s or Centipoise
μ_i – chemical potential of component i
ρ – fluid density, kg/m^3
τ – dimensionless time (Eq. 1.2.14)
Θ – dimensionless temperature, defined in Eq. (1.2.13)
ς – Boltzmann transformation associated with Eq. (1.2.23)

1.2.4.5 Other Symbols

α_{T} – thermal diffusivity, m^2/s
A_{d} – constant in Eq. (1.2.28)
B_{d} – constant in Eq. (1.2.28)
$\beta(T)$ – difference between the fractional free volume of the penetrant and polymer (Eq. 2.2.29)
c_o – equilibrium penetrant concentration, mol/L
C_{P} – heat capacity of the fluid
D_1 – self-diffusion coefficients of the penetrant
D_2 – self-diffusion coefficients of the polymer
D_{ik} – diffusion coefficient relative to the center of mass (Eq. 1.3.32)
D_1' , – diffusivity of the penetrant based on the polymer frame of reference

Da – agitator diameter, m
D_P – pipe diameter, m
D_T – thermodynamic diffusion coefficient (also equal to the intrinsic diffusion coefficient (Eq. 1.2.29)
$D_{\phi_1=0}$ – thermodynamic self-diffusion coefficient of the polymer (Eq. 1.2.29)
$(-\Delta H_P)$ – heat of polymerization (positive for exothermic reaction), J/mol
$f(0,T)$ – fractional free volume of the polymer (Eq. 1.2.29)
j_i – diffusion current density of component i relative to the center of mass
J_0 – zeroth-order Bessel function of the first kind
J_1 – first-order Bessel functions of the first kind
k' – coefficient in Eq. (1.2.6)
K'' – coefficient in Eq. (1.2.8)
M_t – weight of penetrant uptake at time t, kg
M_∞ – weight of penetrant uptake at equilibrium (infinite time), kg
$[M]$ – mobility coefficient matrix
$[\mu]$ – intrinsic viscosity, dl/g
∇ – Nabla operator
ρ_k – partial mass density of component k (Eq. 1.2.32)
ϕ_1 – the volume fraction of the penetrant (Eq. 1.2.29)
$\dot{q}$ - heat source term, energy/time volume
r_M – rate of monomer consumption, mol/L time
r_0 – radius of reacting particle or nonreactive fluid cylindrical tube, m
R' – scale-up ratio
Re – Reynolds number for pipe flow, dimensionless
Re' – Reynolds number for tank mixing, dimensionless
T_g – glass transition temperature, K
u_1 – thermodynamic factor for diffusivity (Eq. 1.2.26), m^2 mol/J s
x_i – the mole fraction of component i
Ω_{ij} – phenomenological coefficients of ij component pairs
$[\Omega]$ – phenomenological coefficient matrix, positive definite

1.3 Conventional Polymerization Kinetics and Processes

Polymers are macromolecules which are composed of smaller molecules linked by covalent bonds. In terms of the reaction kinetics, polymerizations are traditionally classified into several categories: stepwise polymerization, free-radical polymerization, ionic polymerization, ring-open polymerization, and coordination polymerization or polyinsertion. Each polymerization method has a combination of requirements for reaction conditions, and they exhibit certain types of product and process features (Caneba, 1992a, 1992b; Odian, 1991). Even though in principle, the FRRPP process can be implemented with a wide variety of polymerization mechanisms, its discovery and immediate implementation has occurred in conjunction with free-radical kinetics.

Free-radical polymerization normally involves monomers with double bonds, generally represented by the following structural formula:

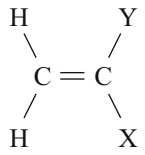

Specific monomers depend on the identities of functional groups X and Y. Examples are

1. Styrene: Y = H and X = Ø (phenyl or benzene group)
2. Vinyl chloride: Y = H and X = Cl
3. Ethylene: Y = H and X = H
4. Propylene: Y = H and X = CH_3
5. Acrylic ester: Y = H and X = (C=O)–O–C_mH_{2m+1}
   Methyl acrylate: $m = 1$
   Ethyl acrylate: $m = 2$
   Butyl acrylate: $m = 4$
6. Methacrylic ester: Y = CH_3 and X = (C=O)–O–C_mH_{2m+1}
   Methyl methacrylate: $m = 1$
   Ethyl methacrylate: $m = 2$
   Butyl methacrylate: $m = 4$
7. Acrylic acid: Y = H and X = COOH
8. Methacrylic acid: Y = CH_3 and X = COOH
9. Vinyl acetate: Y = H and X = O–(C=O)–CH_3

The double bond between the two carbon atoms in the above monomer molecular structure is the source of unsaturation and the reaction site, which is attacked by a free radical to form another free radical whose size is bigger by one monomer unit.

1.3.1 Free-Radical Kinetics

Free-radical polymerization is a chain reaction composed of three basic steps: initiation, propagation, and termination, as shown in Fig. 1.3.1.

Initiation can be accomplished by a variety of chemical, thermal, redox, and photochemical methods, during which the initiator decomposes at first into radicals and then attacks monomers to yield primary radicals. Most of the FRRPP efforts were done through the chemical initiation method, usually involving azobisisobutyronitrile (AIBN) or benzoyl peroxide (BPO).

When an AIBN molecule decomposes to form two radicals, N_2 gas is liberated. When a BPO molecule is decomposed, two radicals are formed and CO_2 is also produced. The molecular mechanism for initiator decomposition is unimolecular; thus, it follows the first-order kinetic rate expression

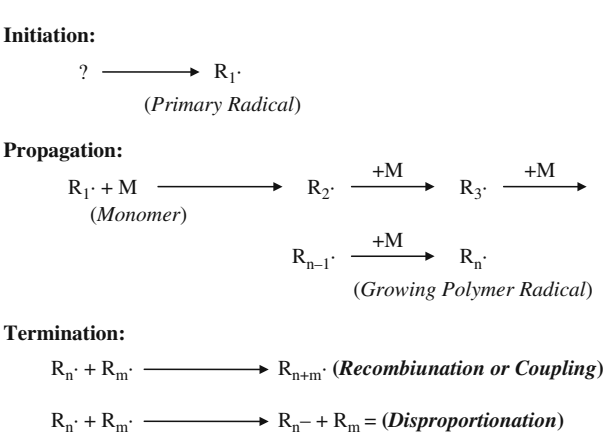

Fig. 1.3.1 Free-radical kinetics mechanism, which includes initiation to generate the primary radical, propagation to form the growing polymer, and termination to form the dead polymer chains

$$\frac{d[I]}{dt} = -k_{\mathrm{d}}[I], \tag{1.3.1}$$

k_{d} is the initiation rate coefficient and $[I]$ is the concentration of the initiator. With an initial initiator concentration of $[I]_{\mathrm{o}}$, Equation (1.3.1) can be integrated to obtain the algebraic form of the decay equation

$$[I] = [I]_{\mathrm{o}} \exp\left(-k_{\mathrm{d}} t\right). \tag{1.3.2}$$

The decomposition reaction proceeds when the initiator is placed in a high enough temperature environment. Thus, these materials are normally stored at relatively low temperatures and they have the property of having high enough activation energies for decomposition. This is evident when one looks into the Arrhenius expression normally used for the initiation rate coefficient

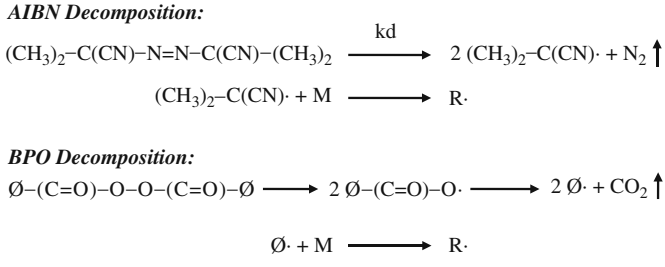

Fig. 1.3.2 Decomposition kinetics of AIBN and BPO to produce the primary radical R·

$$k_d = k_{do} \exp\left(-\frac{E_a}{RT}\right), \tag{1.3.3}$$

where k_{do} is the pre-exponential factor and E_a is the activation energy for initiator decomposition. Since the decomposition kinetics for chemical initiators is first order, another way of characterizing the rate of decomposition is through the half-life of reaction (or time it takes to decompose half of the starting amount of initiator molecules at a constant temperature), $t_{1/2}$, which is related to the rate coefficient by

$$t_{1/2} = \frac{0.692}{k_d}. \tag{1.3.4}$$

One of the nice features of free-radical polymerization is that values of the pre-exponential coefficients and activation energies (or alternately half-life values at various temperatures) can be obtained in the literature (such as in Odian (1991)) or from their manufacturers (such as Wako Chemical Corp.) for a variety of initiators, and these numbers do not normally change no matter what the fluid environment the initiator molecules are in. Thus, if we want to decompose more than 99% of the starting initiator material in the reactor, we just have to wait for the reaction to proceed up to five times the initiator half-life. The other attractive feature of free-radical polymerization is that free-radical reactions are well known and radical concentrations can be directly measured. Thus, we know, for example, that if we want to preserve radicals in solution, we should not allow oxygen gas (O_2) in our system, because reactive radicals will combine with oxygen gas to form a stable peroxy radical. That is why reaction fluids were bubbled with N_2, CO_2, Ar, or any inert gas, in order to displace O_2 gas that comes from the air. Finally, free-radical polymerization is not sensitive to atmospheric or process water, compared to other polymerization kinetic mechanisms.

During radical formation, the formation and liberation of N_2 or CO_2 gases prevent the reverse reaction from taking place to recover the initiator compounds. Instead, there is the possibility that the two radicals formed from a single initiator molecule can recombine into a stable molecule, especially if there is a scarcity of monomer molecules in the vicinity to start the formation of polymer chains. For this reason, an initiator efficiency is introduced into the equations to take into account the fraction of radicals formed from the initiator molecules that recombine and do not participate in further reactions.

In following propagation steps, monomers are successively added to the end of primary radicals to form polymer chains with high molecular weight ($R_n\cdot$ in Fig. 1.3.1). The propagation step can take place in quite a short time due to the high enough propagation rate coefficients and monomer concentration for most polymerization systems.

As two radicals ($R_n\cdot$ and $R_m\cdot$ in Fig. 1.3.1) collide and radical sites react, the propagating radical chains lose their active sites, and then terminate. This bimolecular reaction between radicals occurs either by recombination to form one dead polymer (R_{n+m} in Fig. 1.3.1) or by disproportionation leading to two dead polymer molecules (R_n^- and $R_m^=$ in Fig. 1.3.1); however, the latter is a less prevalent case.

Compared with the propagation rate coefficient, the typical termination rate coefficient is much higher, which keeps the concentrations of radical species very low. In addition to the three basic reactions, other side reactions such as chain transfer and degradation may occur as well. It is noted that each step can be diffusion controlled, in particular for termination reaction due to the involvement of long propagating chains.

The typical course of polymerization has three distinct stages: Stage 1 – the reaction rate is constant or moderately declines and could be characterized by an induction time; Stage 2 – the reaction rate grows rapidly with conversion; Stage 3 – the reaction rate flattens or decreases due to dead ending, monomer depletion, or end of radical production (see Fig. 1.3.3) (Odian, 1991). Stage 2 is the well-known characteristic of free-radical polymerization, which is ideally expressed through the following differential equation in a batch reactor:

$$R_{\mathrm{P}} = \frac{d[M]}{dt} = -k_{\mathrm{P}} \left(\frac{R_i}{2k_t} \right)^{1/2} [M], \tag{1.3.5}$$

where $[M]$ is the concentration of the monomer; R_p and R_i are the propagation and initiation rates, respectively; k_p and k_t are the propagation and termination rate coefficients, respectively. If initiation is based on the decomposition of an initiator material, I, such as a peroxide or azo compound, then the initiation rate becomes

$$R_i = -\frac{d[I]}{dt} = 2fk_{\mathrm{d}}[I], \tag{1.3.6}$$

where f is the fraction initiator molecules that becomes primary radicals or is also called the initiator efficiency. For peroxide initiators such as BPO, f is close to 1, while it is around 0.58 for AIBN.

Propagation involves the addition of monomer molecules one after another into the growing polymer radicals. This portion of the polymerization mechanism is exothermic, or it involves the generation of heat every time a monomer molecule is incorporated into the polymer radical. In order to fathom the extent of heat generation from free-radical chain polymerization reactions, we imagine the starting

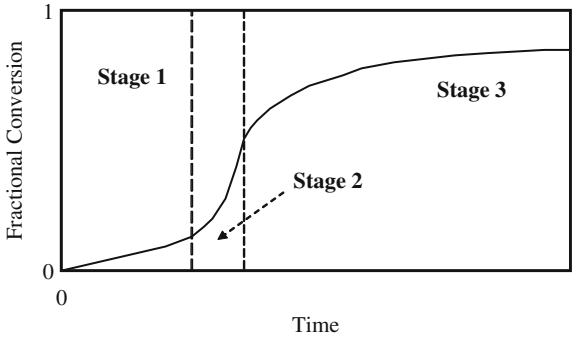

Fig. 1.3.3 Stages of conventional free-radical chain polymerization: 1 – induction period, 2 – growth period, 3 – period of dead ending, monomer depletion, or end of radical production

reaction fluid to be nothing but the monomer, such as ethylene or styrene, and such a fluid is thermally insulated from the environment. Then, we add initiator (in the order of 0.1 wt% of the fluid) to start the polymerization. Due to the inherent exothermic reactions during chain propagation, the temperature will rise to a certain maximum value. The maximum increase in temperature if all the monomer is converted to polymer is called the adiabatic rise temperature. Based on literature values given for the energy generated in these reactions (in the form of enthalpy of polymerization, in kJ/g) for specific monomers and typical fluid thermal properties, such as specific heat of 0.5 cal/g °C, adiabatic rise temperatures can be calculated and shown in Table 1.3.1.

Based on the table, these adiabatic rise temperatures can easily boil water and can melt softer metals, such as sodium and bismuth, or even harder ones, such as copper.

Another aspect of free-radical polymerization that is relevant to the FRRPP process is the molecular weight distribution (MWD) of product polymers. A polymeric material that is produced from a single monomer (such as styrene) will contain molecules of varying molecular weights, and there will be a distribution of these molecular weights. Just like other types of distributions, there will be a mean, a standard deviation, and other measures of the distribution. In polymers, we use averages based on number of moles (n_i) and weights (W_i) of polymer species i with a certain molecular weight M_i. The so-called number-average (M_n) and weight average (M_w) molecular weights are defined as

$$M_n \equiv \frac{\sum_{i=1}^{\infty} n_i M_i}{\sum_{i=1}^{\infty} n_i}, \tag{1.3.7}$$

$$M_w \equiv \frac{\sum_{i=1}^{\infty} W_i M_i}{\sum_{i=1}^{\infty} W_i} = \frac{\sum_{i=1}^{\infty} n_i M_i^2}{\sum_{i=1}^{\infty} n_i M_i}, \tag{1.3.8}$$

Table 1.3.1 Adiabatic rise temperatures, ΔT, of polymerization of various monomers, based on given enthalpies of polymerization, $(-\Delta H_p)$ (Rodriguez et al., 2003), and the assumption of fluid heat capacity of 0.5 cal/g °C.

Monomer	$(-\Delta H_p)$ (kJ/g)	ΔT (°C)
Ethylene	3.62	1730
Styrene	0.67	320
Vinyl chloride	1.54	721
Vinyl acetate	1.02	487
Acrylonitrile	1.42	678
Methyl acrylate	0.56	267
Ethylene oxide	2.15	1027

where we note that the weight of the polymer species i is related to its number of moles by

$$W_i = n_i M_i. \tag{1.3.9}$$

In order to determine the tightness of the molecular weight distribution, we calculate the polydispersity index (PDI) or the heterogeneity index (HI), based on the following simple equation:

$$\mathrm{PDI} = \frac{M_{\mathrm{w}}}{M_n}. \tag{1.3.10}$$

If all the polymer molecules that make up a product material have the same molecular weight, then PDI=1, or we have what we call a monodisperse MWD. The farther this number from 1, the broader is the molecular weight distribution. What would PDI values for an ideal free-radical polymerization system be? For systems with termination reaction solely based on recombination, PDI=2; if termination is solely based on disproportionation, PDI=1.5 (Rodriguez et al., 2003).

Following the influence of the polymerization medium on the reactions of propagation and termination, the occurrence of the three stages could be well explained (Odian, 1991). Termination and propagation may be diffusion controlled. Furthermore, a sequence of three steps for termination has been suggested: the first step is translational diffusion by which two terminating polymer chains move close to each other; then, the second step is segmental diffusion by which two neighboring chains rearrange their segments to make both active sites sufficiently close for the next reaction step. Since the last step is believed to have a high rate coefficient, any or both of the translational diffusion and segmental diffusion could limit termination reaction (Mahabadi and O'Driscoll, 1977a; Mahabadi and O'Driscoll, 1977b).

Diffusion is greatly affected by the viscosity of the reaction medium and the dissolving ability of the solvent. Both properties keep varying in the course of polymerization. At the initial period of polymerization, due to the increasing polymer concentration, the declining solubility of reaction medium shrinks the size of the growing polymer coils, which enhances the segmental diffusion but lowers the translational diffusion. As a result, reaction rate (Stage 1) may be constant or decline if the increase of segmental diffusion is greater than the decrease of translational diffusion. At Stage 2, due to the dramatically increasing viscosity of reaction medium, the decrease rate of translational diffusion is faster than that of segmental diffusion, which leads to a sharp decline of the termination rate, causing the occurrence of an autoacceleration phenomenon that can be accompanied by a sharp increase in reactor fluid temperature (also called Tromsdorff, Norrish, or gel effect [North, 1974]). It should be noted that at Stage 2 the propagation rate decreases as well, but much more slightly than the termination rate, because the propagation only involves one long propagating chain instead of two chains as in termination. At Stage 3 of high conversion, when the decrease of the propagation rate predominates over the

increase of the termination rate, and the initiation coefficient decreases, reaction rate flattens out or declines.

It should be noted that high polymer concentration normally results in the occurrence of autoacceleration, which makes the reaction fluid hard to mix. If the effective glass transition temperature of the system is reached by this increase in polymer concentration, then the autoacceleration behavior causes the fluid to vitrify in the reaction vessel. If there is no dispersant used when this happens, then a mixing catastrophe occurs, and the reaction vessel would just have to be dismantled for a messy cleaning job. A rule-of-thumb that we use to avoid the gel effect in undispersed reactor fluid systems is that we do not run the reaction beyond 20–25 wt% polymer composition, either by addition of a solvent (at least 75% by weight of total reactor fluid) or by allowing only 20 wt% of the monomer to react to form the polymer.

As suggested by above complications to ideal polymerization kinetics at high polymer concentrations, it should not be a surprise that the MWD would be affected by them. For a polymerization system undergoing termination by recombination, the gel effect results in PDI values greater than 2, such as 3, 4, 5, or greater. The significance of this observation is that even though we noted in the FRRPP process that regions around reactive sites are at relatively high polymer concentrations (based on phase equilibrium studies), PDI values have been observed to be reduced to 1.4, and even down to 1.1.

1.3.2 Polymerization Processes

Free-radical polymerization can be carried out both homogeneously (such as bulk polymerization and solution polymerization) and heterogeneously (such as suspension emulsion, and precipitation polymerization) (Odian, 1991). Bulk polymerization operating in a pure monomer medium leads to the product with minimal impurity; however, the rising viscosity and the reaction exotherm greatly increase the difficulty of controlling the temperature and product quality, which makes it less commercially feasible. Thus, solution polymerization is introduced to remove the main drawbacks of bulk polymerization by adding solvent(s) as the reaction medium. However, other new problems may arise such as undesirable chain transfer to the solvent, costly removal of the solvent, and the unfavorable effect of the solvent. Suspension polymerization is usually carried out in water, and the reaction takes place in suspending monomer droplets with the same kinetic behavior as that of bulk polymerization. Emulsion polymerization uses emulsifier to form reaction sites (micelles), and it has a distinct reaction mechanism compared to other polymerization processes.

Precipitation polymerization occurs when a poor solvent is used as the reaction medium in solution polymerization (such as acrylonitrile in water [Odian, 1991]), or the reacting monomer is not a good solvent for the corresponding polymer in bulk polymerization (such as vinyl chloride). At the initial stage of the polymerization,

the reaction system appears homogeneous; when the conversion increases over time, and the solution of the formed polymer in the solvent or monomer reaches saturation, the precipitation occurs. In the case that the employed solvent is totally insoluble in the polymer, the precipitation phenomenon may take place immediately.

In many aspects, the FRRPP process improves conventional free-radical polymerization processes (Carbaugh, 1991; Caneba, 1992a, 1992b).

In free-radical polymerization systems, despite the stable steady-state dynamic behavior, other various behaviors are also observed, such as oscillation (Schmidt and Ray, 1981), multiple steady states (Schmidt et al, 1984), and chaos (Teymour, 2004). These types of dynamic behavior have significant effects on final polymer product properties. Free-radical polymerizations under isothermal conditions are often characterized by autoacceleration of the polymerization rate as the reaction proceeds. Since most radical polymerizations are exothermic in nature, and since the rate of heat transfer from reaction decreases as the reaction proceeds and viscosity increases, heat accumulation is rapid when the system enters the autoacceleration stage. This will lead to thermal runaway, cause the reactor to be unstable, and negatively affect polymer product properties. Controlling the molecular weight (MW) and molecular weight distribution (MWD) is always important in the production of linear polymers. In conventional free-radical polymerization systems, relatively narrow MWD polymers can be obtained if (a) the molecular weight and monomer loading are relatively low (bulk and solution processes) and (b) the conversion is very low (precipitation process) (Louie, 1984). For commercial products, e.g., PMMA, PS, the most narrow MWD could approach 1.0 using the methods mentioned above (Wang, 1997).

From a macroscopic point of view, the FRRPP process is very similar to the conventional free-radical precipitation polymerization (CPP), in which the latter undergoes phase separation at some temperature (normally below the UCST), whereas the former is above the LCST. For the CPP process, phase separation occurs once a certain kinetic chain length is reached or the temperature is lowered. Entrapment of the reactive sites through precipitation will minimize the occurrence of the polymer radical termination reactions. Conventional-precipitation polymerization has been found to have problems associated with control of molecular weight distribution (Kumar, 1986)and autoacceleration effect. Even though free-radical CPP has already been used to produce polyolefins, polyacrylonitrile, and PVC, such an approach had never shown promise in competing with ionic and group-transfer methods as far as molecular weight control and block copolymer formation are concerned. On the other hand, using the FRRPP process, products with relatively narrow molecular weight distributions (MWD) can be obtained at reasonably high yields (Caneba, 1992a,b; Aggarwal, 1993), and block copolymers can also be readily synthesized without the rigorous control of the polymerization conditions associated with the anionic living-polymerization methods.

As a new kind of precipitation polymerization, the FRRPP process is claimed to differ from the conventional-precipitation polymerization mentioned above and has its own unique features. These process and product features will be discussed in subsequent sections.

1.3.3 Copolymerization Kinetics

If the reactor fluid contains two different monomers M_1 and M_2, both monomers can react with radical sites to form copolymer radicals. If there is no template for the monomer preference to react with the radical site, then the sequence of monomer addition will be based on monomer reactivity rules. Description of copolymerization kinetics differs from that in Fig. 1.3.1 (homopolymerization kinetics) during chain propagation, as shown in Fig. 1.3.4

Specifically, the copolymer mechanism expressed in Fig. 1.3.4 is the so-called terminal model, because identification and reactivity of copolymer radicals are solely based on which monomeric unit contains the radical site. Based on the rate coefficients shown above the reaction arrows, the following reactivity ratios are defined:

$$r_1 = \frac{k_{11}}{k_{12}} \; r_2 = \frac{k_{22}}{k_{21}}, \tag{1.3.11}$$

and values of reactivity ratios are given in the literature (Odian, 1991). Generally, it was found experimentally that $0 < r_1 r_2 \leq 1$. However, the following copolymer structures are special cases for various combinations of the reactivity ratios:

1. Alternating copolymers: $r_1 = r_2 = 0$
2. Block copolymers: $r_1 > 1$, $r_2 > 1$

In the first case, radical sites from a particular monomer have the preference of reacting with monomers of the other type; that is why the copolymer chain has an alternating sequence between the two monomers. In the second case, radical sites from a particular monomer prefer to react with monomers of the same type. Thus, once a particular monomer is incorporated, the same monomer is added into the copolymer chain in subsequent reactions as long as it is available. One note of caution here is that these copolymerization reactions are also based on statistical rules. For example, if $r_1 = 10$ and the copolymer radical site comes from monomer 1, then if monomer 2 in the vicinity of the radical site outnumbers monomer 1 by 10:1 there is an equal likelihood for either monomer type to be incorporated in the copolymer chain.

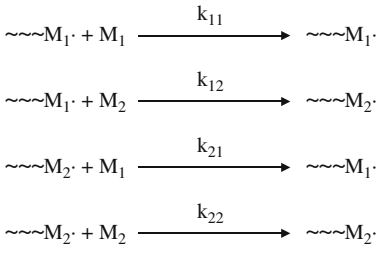

Fig. 1.3.4 Reaction kinetics mechanism of propagation for free-radical based copolymerization from monomers M_1 and M_1. Species $\sim\sim\sim M_1\cdot$ and $\sim\sim\sim M_2\cdot$ are copolymer radicals with end-groups coming from monomers M_1 and M_2, respectively

When we incorporate termination reactions into the analysis of monomer sequence formation in copolymerization kinetics, we note that in general the development of the copolymer sequence can be prematurely stopped. If one monomer sequence is being formed during propagation and the chain is terminated by disproportionation, then the result is more of a homopolymer than a copolymer. If the chain is terminated by recombination of a similar molecule, then the same type of homopolymer is formed. In fact, termination reactions usually prevent the formation of block copolymers when both monomers are present in the reactor fluid. With the radical trapping mechanism of the FRRPP process that will be discussed in the next chapter, formation of certain block copolymers becomes feasible in statistical-based radical copolymerizations. This is an apparent contradiction in terms, but the FRRPP process has been shown to break new ground in polymerization systems.

1.3.4 Nomenclature

1.3.4.1 Alphabets

Upper Case

M – molecular weight, g/mol
PDI – polydispersity index, dimensionless
R – universal gas constant, J/mol K
T – absolute temperature, K
W – weight, g

Lower Case

f – initiator efficiency coefficient ($0 < f < 1$)
n – number of moles, mol
r – reactivity ratio, dimensionless
t – time, s

1.3.4.2 Subscripts

i – component label of homologous polymer
n – number average
o – initial
w – weight average
$_{1/2}$ – half-life
1, 2 – monomer component labels

1.3.4.3 Superscripts

o – Pre-exponential factor

1.3.4.4 Greek Symbols

None

1.3.4.5 Other Symbols

ΔH_p – Enthalpy of polymerization, kJ/g
ΔT – adiabatic temperature rise, ºC
k_d – initiator decomposition rate coefficient, s^{-1}
k_t – termination rate coefficient, mol/l s
k_{ij} – propagation rate coefficient in statistical copolymerization, l/mol s
$[I]$ – concentration of initiator, mol/l
$[M]$ – concentration of monomer, mol/l
R_i – initiation rate, mol/l s
R_p – propagation rate, mol/l s

1.4 Phase Separation Kinetics in Nonreactive Polymer Systems

Even though the FRRPP process involves phase separation at a temperature above the lower critical solution temperature (LCST), analysis of relevant phase separation kinetics can be made through conventional upper critical solution temperature (UCST)-based phase separation starting from binary polymer/solvent system. Later, analysis is extended to ternary system at temperatures above the LCST.

1.4.1 Phase Separation Mechanisms

Figure 1.4.1 shows a representation of a typical phase envelope for an amorphous polymer/solvent system that exhibits a lower critical solution temperature (LCST) and an upper critical solution temperature (UCST). Outside the envelope is the homogeneous region, where the system is a true solution. Inside the binodal curve, the system is thermodynamically heterogeneous. The binodal curve provides the compositions of the phases in equilibrium at the temperature of interest. This is shown as c_α and c_β from the horizontal constant temperature line, i.e., c_α and c_β are compositions of the solvent-rich and polymer-rich phases. For systems wherein the polymer and solvent densities are assumed to be equal, these compositions are the same as the weight fractions. The region inside the spinodal curve is the unstable region, where the system will phase separate spontaneously. At the particular temperature of interest indicated by the horizontal line, c' and c" are the solvent-rich and polymer-rich spinodal compositions. Between the binodal and spinodal curves is the metastable region, wherein phase separation will occur only if the system is under a finite composition and/or temperature perturbation. This happens when nucleating sites are present; otherwise no phase separation will occur at a reasonable amount of time.

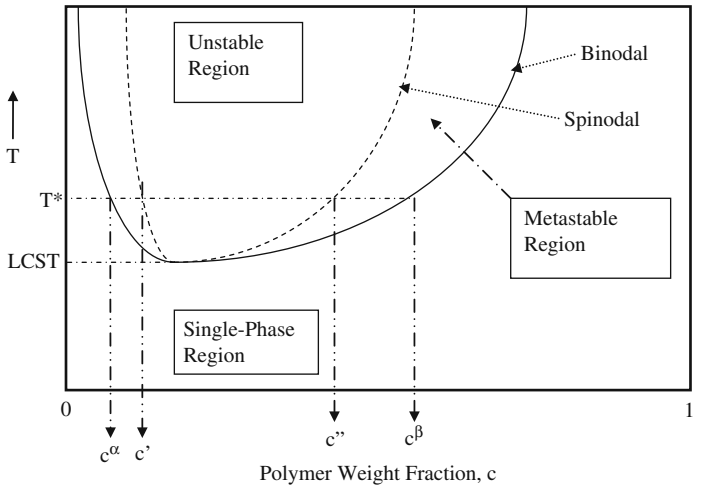

Fig. 1.4.1(a) Binary phase diagram of a binary amorphous polymer/solvent system undergoing phase separation above the lower critical solution temperature (LCST). The temperature of interest, T^*, intersects with the binodal curve at the composition (wt fraction) of α and β phases at equilibrium, c^{α} and c^{β}. On the other hand, T^* intersects with the spinodal at compositions (wt fraction) c" and c". Outside the binodal curve is the single-phase region, while inside it is the two-phase region

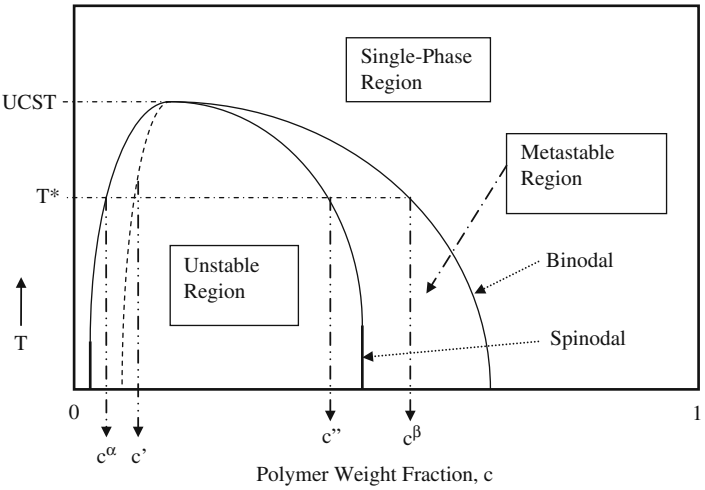

Fig. 1.4.1(b) Binary phase diagram of a binary amorphous polymer/solvent system undergoing phase separation below the upper critical solution temperature (UCST). The temperature of interest, T^*, intersects with the binodal curve at the composition (wt fraction) of α and β phases at equilibrium, c^{α} and c^{β}. On the other hand, T^* intersects with the spinodal at compositions (wt fraction) c" and c". Outside the binodal curve is the single-phase region, while inside it is the two-phase region

1.4.1.1 Nucleation and Growth

This is the kinetic mechanism when the system phase separates within the metastable region. Phase separation is rather slow and will only occur in the presence of nucleating sites or finite temperature perturbations. With nucleating sites, the concentration profile and its evolution is shown in Fig. 1.4.2 Here, it is evident that there is downhill movement of material, as seen in the direction of the arrows. Also, the spacing of domains is dictated by the composition distribution of the nucleating sites. For a rigorous mathematical treatment of nucleation and growth, one can look into the works of De Fontaine (1975), Cahn (1956, 1957), Cahn and Hilliard (1958, 1959), Hillert (1961), Coriell and Sekerka (1983), Rasmussen (1982); and Rasmussen et al., (1982).

1.4.1.2 Spinodal Decomposition

Figure 1.4.2 also shows the evolution of concentration profiles for a system undergoing spinodal decomposition, i.e., for systems that phase separate inside the spinodal curve. In contrast with nucleation and growth, one can see (based on the direction of the arrows) that material movement occurs from low to high composition. Also, the initial spacing between domains is dictated more by process conditions, unless there is already a well-developed pre-established composition profile. In terms of the rate of phase separation, spinodal decomposition can be quite fast. In Fig. 1.4.3 one can see an accelerated-growth regime after an initial induction period. The deeper the level of penetration of the system into the spinodal region, the smaller is the

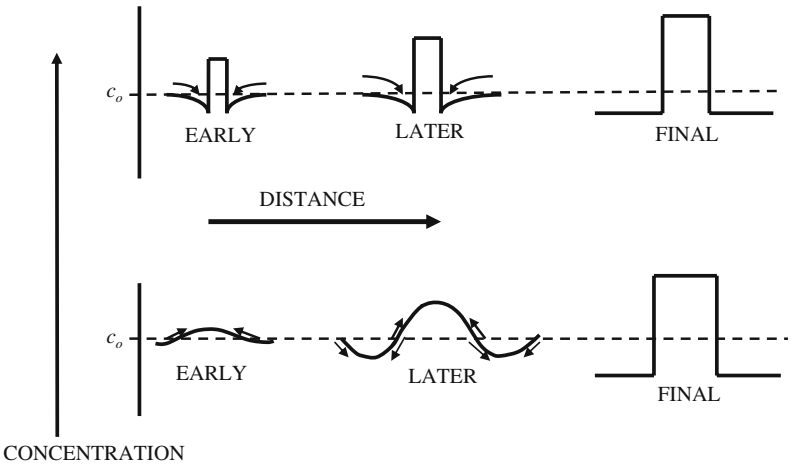

Fig. 1.4.2 Comparison of evolution of composition profiles for phase separation by nucleation and growth (*top*) and spinodal decomposition (*bottom*). Minimum and maximum levels of concentration (or composition) are binodal values

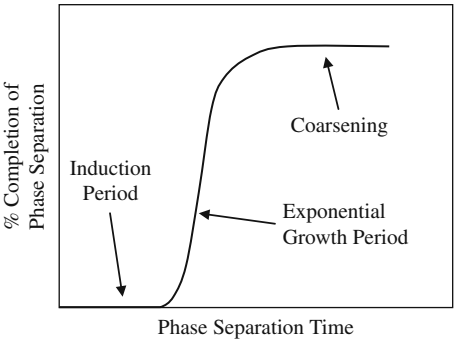

Fig. 1.4.3 Extent of phase separation by spinodal decomposition vs. time showing the various time regimes, starting with the induction period, followed by an accelerated-growth period, then the coarsening period (Redrawn with permission from Caneba and Saxena, 1996)

induction period and the time constant of the exponential accelerated-growth period (Laxminarayan and Caneba, 1991).

1.4.1.3 Coarsening

The end of the accelerated-growth regime in Fig. 1.4.3 corresponds to the increase in interdomain distance and domain size. This is the reason why it is called a coarsening regime. Actually, coarsening can occur through a number of mechanisms, sometimes at the same time or in sequence. At the early stages, the mechanism might be the continued increase in polymer composition of some of the domains, while the others are diminishing in polymer composition (Caneba and Saxena, 1996). This is due to the fact that the polymer-rich domains may not have reached their binodal composition, while the solvent-rich domains are already at their binodal composition. Another early-stage coarsening mechanism is the reduction of the surface-area-to-volume ratio of the domains due to interfacial tension. This is called the hydrodynamic flow mechanism. A third mechanism is the so-called Ostwald ripening (Shewmon, 1969), whereby microstructural changes occur (even though there is already equilibrium of the composition profile) that result in material from smaller droplets of precipitate migrating into larger droplets. Whatever the mechanism is, the effect is the increase in interdomain distance and/or domain size.

1.4.2 Mathematical Modeling of Structure Evolution in Phase Separating Polymer Systems

Mathematical modeling and computer simulation of early-stage phase separation applied to the FRRPP process is done through the spinodal decomposition mechanism. The reason is that nucleation and growth is normally not activated fast enough before the system goes inside the spinodal curve during polymerization. This is a similar situation during porous polymer membrane formation, either through sudden temperature changes or through introduction of a non-solvent. After the early stage,

coarsening occurs, first as an extension of spinodal decomposition wherein the composition profile is trying to attain the binodal compositions. Then, other mechanisms become dominant, such as Ostwald ripening, hydrodynamic, and gravity flows.

1.4.2.1 Binary Polymer/Solvent Systems

For a binary polymer/solvent system, the evolution of polymer composition (wt fraction) via spinodal decomposition has been derived by Caneba and Soong (1985b), resulting in the following equation:

$$\frac{\partial c}{\partial t} = \nabla \cdot \left[M(c) \nabla \left(f''(c) \nabla u - 2\kappa \nabla^2 c \right) \right], \tag{1.4.1}$$

where

$$f''(c) = \frac{\partial^2 \Delta G_{\mathrm{M}}}{\partial c^2}. \tag{1.4.2}$$

During the early-stage spinodal decomposition, it suffices that the mobility coefficient, $M(c)$, and the thermodynamic factor, $f''(c)$, to be constant at $c{=}c_{\mathrm{o}}$. In this case, Eqs. (1.4.1) and (1.4.2) reduce to

$$\frac{\partial c}{\partial t} = D_{\mathrm{o}} \nabla^2 c - 2M_{\mathrm{o}} \kappa \nabla^4 c, \tag{1.4.3}$$

where D_{o}, the mutual diffusion coefficient, is

$$D_{\mathrm{o}} = M_{\mathrm{o}} f_o''. \tag{1.4.4}$$

For a model system wherein the resulting composition profile can properly approach both binodal compositions, quadratic $D(c)$ and $M(c)$ are required, such as

$$D(c) = D_1 + D_2 c + D_3 c^2, \tag{1.4.5}$$

$$M(c) = M_1 + M_2 c + M_3 c^2. \tag{1.4.6}$$

Simulation results in binary amorphous polymer/solvent systems have been obtained for a poly(methyl methacrylate) (PMMA)/sulfolane system (Caneba and Soong, 1985b), which has a UCST of 51°C. For a polystyrene (PS)/cyclohexanol system with a UCST of 82°C, simulation results are presented by Caneba and Saxena (1996). Table 1.4.1 shows parameter values used in these systems.

Results of structure evolution for the one-dimensional PS/cyclohexanol system are shown in the subsequent figures. Figures 1.4.4(a–e) show structure evolution results for an almost symmetric composition profile system whereby the overall composition (polymer weight fraction), $c_{\mathrm{o}}{=}0.10$. This means that the composition profile that originally starts at the overall polymer weight fraction of 0.10 would have to travel almost equal weight fractions to reach both polymer-rich

Table 1.4.1 Parameter values for binary polymer/solvent systems used in the simulations

Parameter	PMMA/sulfolane system	PS/cyclohexanol system
T, °C	30	80
UCST, °C	51	82
D_1, cm^2/s	2.41×10^{-8}	9.858×10^{-10}
D_2, cm^2/s	-1.176×10^{-3}	-5.6×10^{-8}
D_3, cm^2/s	1.2583×10^{-3}	3.18×10^{-7}
M_1, cm^5/cal s	1.877×10^{-8}	0
M_2, cm^5/cal s	3.122×10^{-7}	1.68×10^{-7}
M_3, cm^5/cal s	-7.089×10^{-7}	-5.04×10^{-7}
κ, cal/cm	3.94756×10^{-9}	1.4409×10^{-11}
λ_m, cm for c_o=0.05		1.2735×10^{-4}
λ_m, cm for c_o=0.10	1.319×10^{-5}	1.37×10^{-4}
λ_m, cm for c_o=0.20	1.164×10^{-5}	
λ_m, cm for c_o=0.30	8.293×10^{-6}	
Spinodal c'	~0	0.0195
Spinodal c"	0.5204	0.155
Binodal c^α	~0	0.002
Binodal c^β	0.7069	0.207
D_o for c_o=0.05, cm^2/s		-1.0017×10^{-9}
D_o for c_o=0.10, cm^2/s	-9.4774×10^{-5}	-1.4342×10^{-9}

(c^β) and polymer-lean (c^α) binodal compositions of 0.207 and 0.002, respectively. Figure 1.4.4(a) is the plot of the percent completion vs dimensionless time, τ, defined by

$$\tau \equiv \frac{(-D_o)t}{\lambda_m^2}\theta. \tag{1.4.7}$$

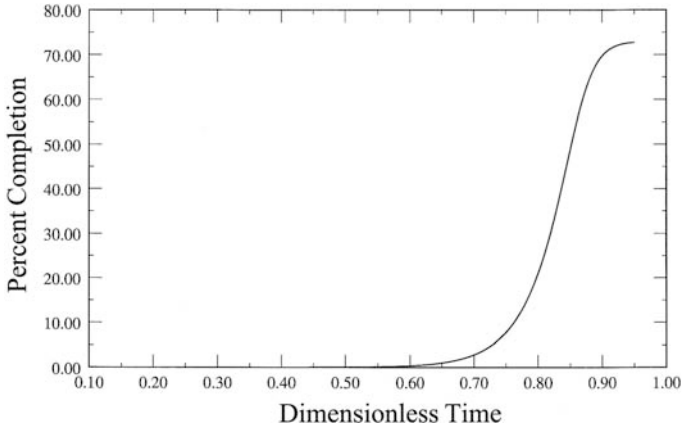

Fig. 1.4.4(a) Plot of the percent completion vs dimensionless time, τ, defined in Eq. (1.4.7), for a symmetric PS/cyclohexanol system ($c_o = 0.10$)

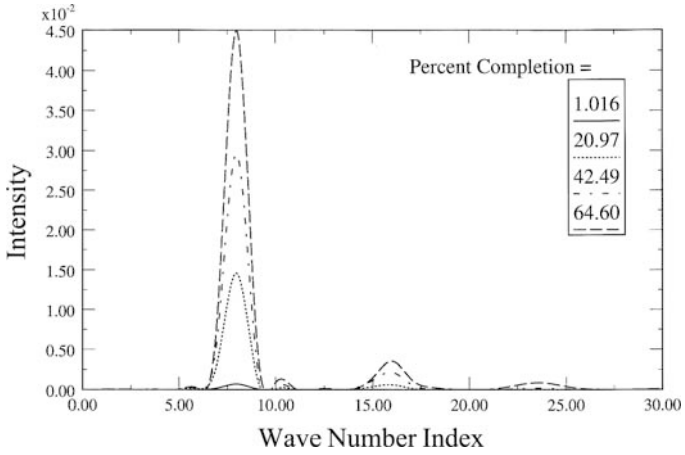

Fig. 1.4.4(b) Frequency spectra during the early-stage spinodal decomposition of a symmetric PS/cyclohexanol system (c_o=0.10)

The percent completion is the extent of phase separation relative to all domains reaching their corresponding binodal compositions, and it is derived elsewhere (Saxena, 2001). Note that Fig. 1.4.4(a) is similar to Fig. 1.4.3.

Figure 1.4.4(b) shows frequency spectra for corresponding composition profiles (Fig. 1.4.4(c)) at various percent completion values. Frequency spectra show a dominant peak at a wave number index value of around 8.0. Subharmonic peaks are also evident at wave number index values that integer factors of the wave number of the main harmonic; thus, there are subharmonics at wave number indices of 16, 24, etc. In Fig. 1.4.4(c), composition profiles are similar to the early-stage behavior for

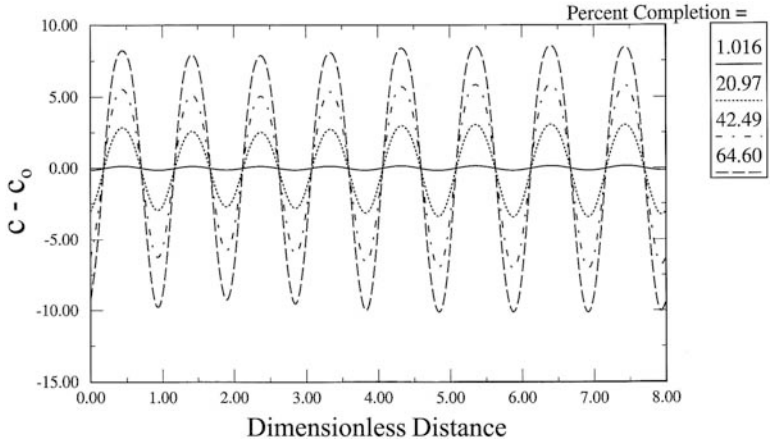

Fig. 1.4.4(c) Polymer weight fraction (c) profile during the early-stage spinodal decomposition of a symmetric PS/cyclohexanol system (c_o=0.10)

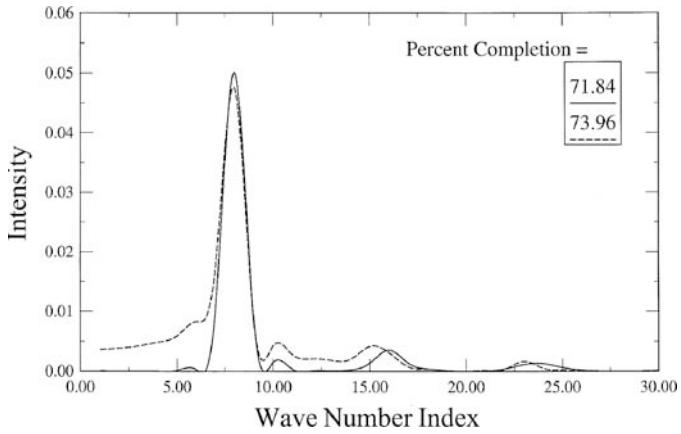

Fig. 1.4.4(d) Frequency spectra during the later-stage spinodal decomposition of an symmetric PS/cyclohexanol system (c_o=0.10)

spinodal decomposition shown in Fig. 1.4.2, wherein the profiles are evolving vertically. This means that the compositions of polymer-rich and polymer-lean phases are moving toward their binodal values without any dimensional shift; all polymer-rich domains are growing at the same rate, while all polymer-lean domains are also proceeding at the same rate. Note that the distance between polymer domains matches the interdomain distance, λ_m, shown in Table 1.4.1, which was calculated from theoretical equations.

In Fig. 1.4.4(d), frequency spectra of the same system are shown during the early portions of the later stage spinodal decomposition, in which the main harmonic is still dominant. Corresponding composition profiles (Fig. 1.4.4(e)) show a

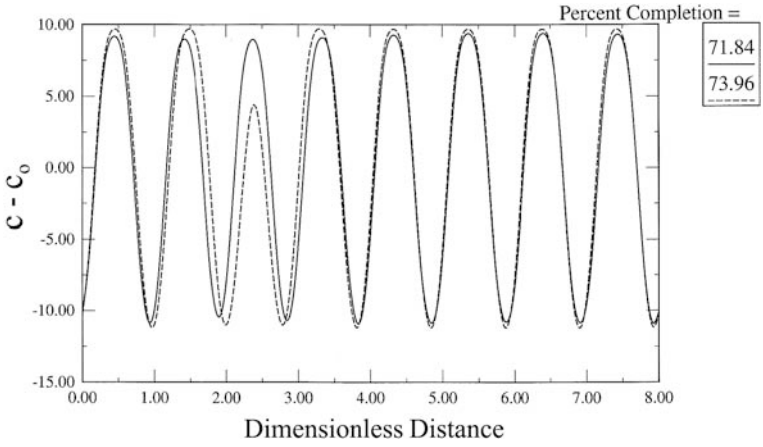

Fig. 1.4.4(e) Polymer weight fraction (c) profile during the later-stage spinodal decomposition of a symmetric PS/cyclohexanol system (c_o=0.10)

polymer-rich domain losing its polymer content, while other domains remain almost intact. This is probably reflective of an actual occurrence that could be construed as a defect in the structure. Still, they indicate the persistence of the early-stage domain structure, which is believed to later coarsen via Ostwald ripening, hydrodynamic flow, and finally, gravity flow.

Simulation results for $c_o = 0.05$ of the PS/cyclohexanol system at 80°C are shown in Fig. (1.4.5a–c). This is an asymmetric system, in which the composition profiles will reach the polymer-lean binodal composition first while the polymer-rich phase would just be halfway to its binodal composition. Beyond this would be the coarsening stages. In Fig. 1.4.5(a), the percent completion curve vs time for this system shows a multistep behavior that is totally different from just a single step in the symmetric case ($c_o = 0.10$ in Fig. 1.4.4(a)) (Caneba and Saxena, 1996). At the early stages of spinodal decomposition (dimensionless time of 0.85 in Fig. 1.1.5(b)), the frequency spectrum is similar to that for the symmetric case (c_o=0.10 in Fig. 1.4.4(b)) in which there is a dominant main harmonic at the wave number index of 8.0, while there are subharmonic peaks at wave number indices of 16, 24, etc. During the coarsening stage for dimensionless times of 1.3 and 5.0, other peaks showed up. In Fig. 1.4.5(c), the composition profile of the early-stage behavior at dimensionless time of 0.85 is similar to that for the symmetric case (c_o=0.10) in Fig. 1.4.4(c), in which the domains are uniformly spaced and sized. Figure 1.4.5(c) also shows the early portion of the coarsening stage when the dimensionless time is equal to 5.0. In this case, two of the peaks are losing polymer material at the expense of other growing peaks. At the later coarsening stage when the dimensionless time equals 185.0, four of the polymer-rich domains totally disappeared, and four of the other polymer-rich domains continued to grow. The reason for the behavior of the asymmetric system during coarsening has been

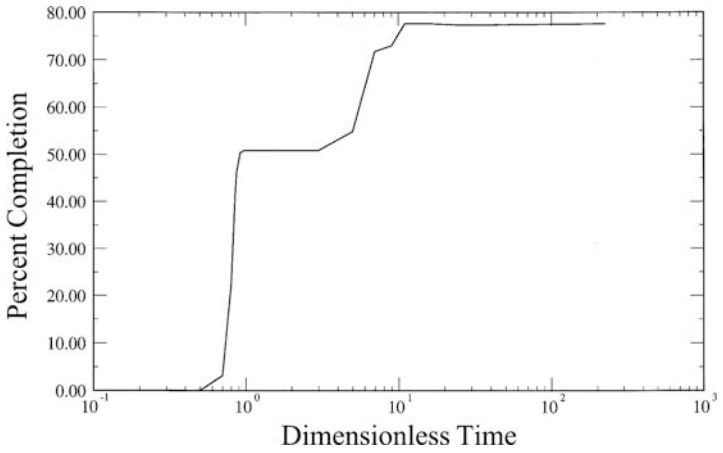

Fig. 1.4.5(a) Plot of the percent completion vs dimensionless time, τ, defined in Eq. (1.4.7), for an asymmetric PS/cyclohexanol system (c_o=0.05) (Replotted with permission from Caneba and Saxena, 1996)

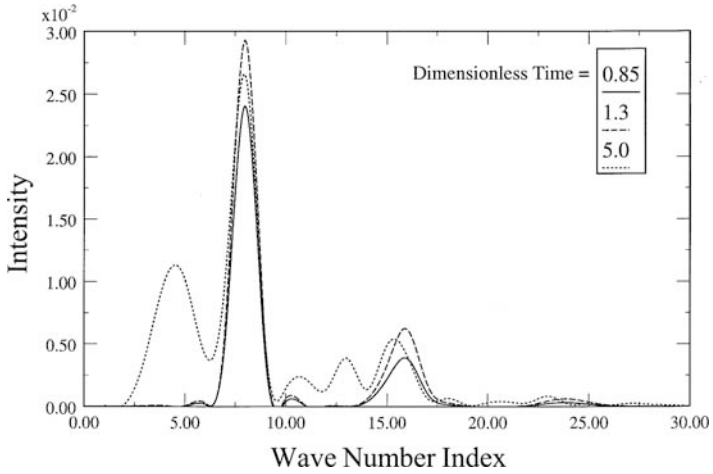

Fig. 1.4.5(b) Frequency spectra of early and later stages of spinodal decomposition for an asymmetric PS/cyclohexanol system (c_o=0.05)

articulated in Caneba and Soong (1985b), in which continued growth of the polymer-rich domains cannot occur with vertical movements in the composition profiles because the polymer-lean domains have already reached their binodal compositions. That is why some of the growing polymer-rich domains would have to take polymer material from other polymer-rich domains.

Two-dimensional (Chen et al., 1993) and three-dimensional simulations have also been done for the binary PMMA/sulfolane system at 30°C and overall polymer weight fraction, c_o=0.10. For this system, the one-dimensional simulation

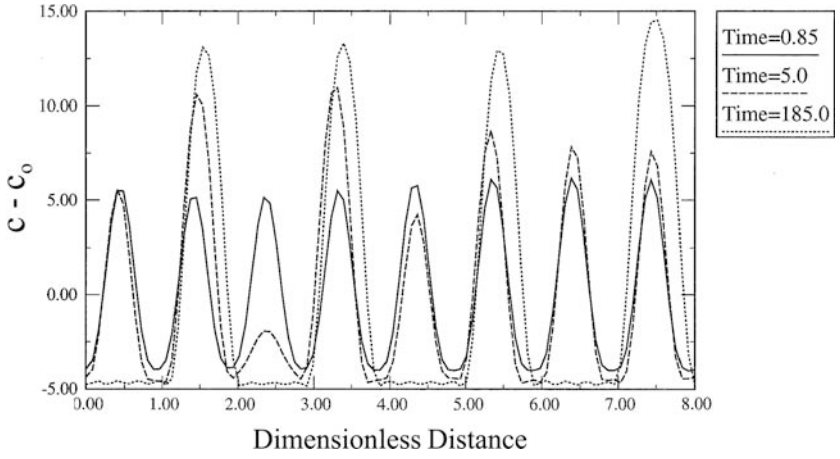

Fig. 1.4.5(c) Polymer weight fraction (c) profile during early and later stages of spinodal decomposition for an asymmetric PS/cyclohexanol system (c_o=0.05)

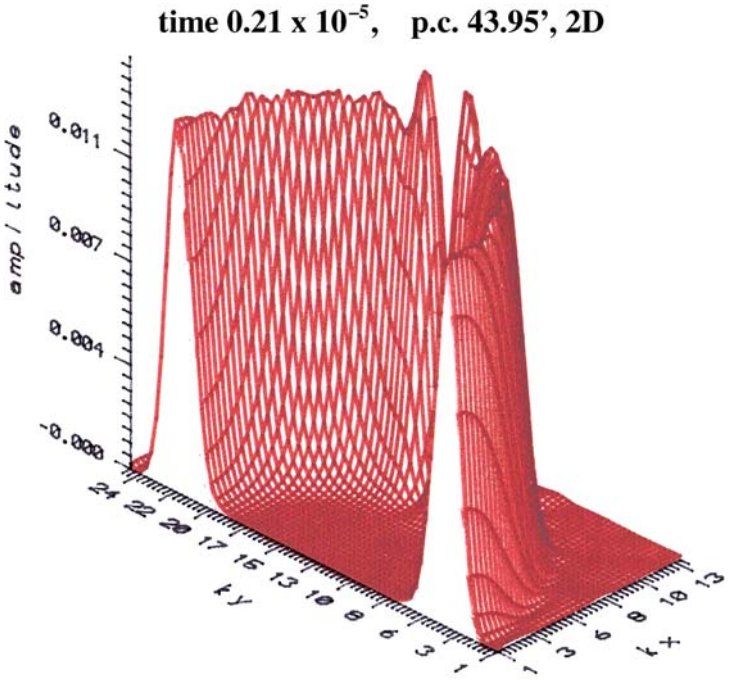

Fig. 1.4.6 Two-dimensional frequency spectrum for the early-stage spinodal decomposition of the PMMA/sulfolane system at 30°C, c_o=0.10

result is similar qualitatively to those of the PS/cyclohexanol system for c_o=0.05 (Figs. 1.4.5(a–c). In Fig. 1.4.6 frequency spectrum for the two-dimensional system is shown, which is shaped like open cups (only half of the "open cups" are plotted, because of symmetry). The plot is a logical extension of the one-dimensional frequency spectra for early-stage behavior shown in Figs. 1.4.4 and 1.4.5.

In Fig. 1.4.7 representative polymer composition profiles are shown from the two-dimensional simulation. Contour and isometric plots show co-continuous domain structures, which is indicative of spinodal decomposition. Also, note that distances between polymer domains match with interdomain distance, λ_m=0.13 μm, shown in Table 1.4.1. Coarsening from the two-dimensional composition profiles have been simulated (Oh and Rey, 2002), and qualitative results agree with our one-dimensional data.

Three-dimensional profiles were also obtained for the same system and conditions and results indicate similar plots from the two-dimensional simulations. Data are presented in Fig. 1.4.8 as a stack of two-dimensional contour plots.

Based on the results from these simulations from one dimensional to three dimensional, we note that the early-stage behavior involves the smallest possible structure that can be obtained in the system. Superimposition of a numerical structure from the three-dimensional calculation (Fig. 1.4.8) for the PMMA/sulfolane system

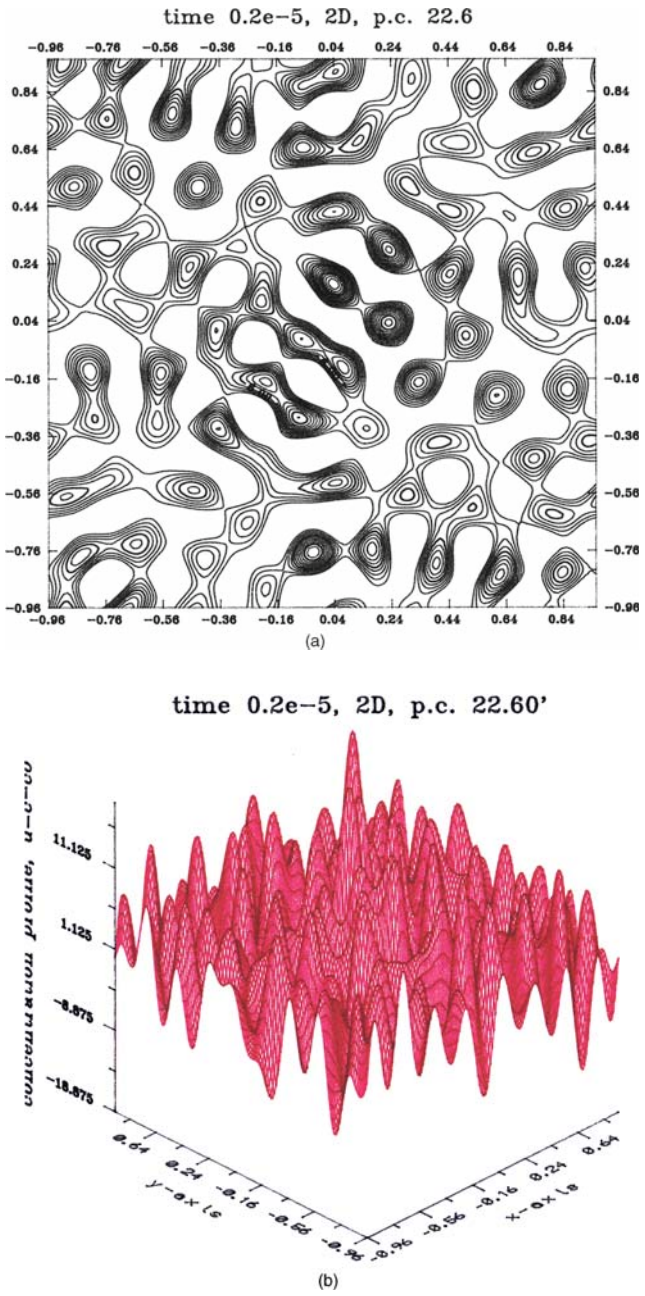

Fig. 1.4.7 Polymer composition profile: (**a**) contour view with 1 wt% polymer composition difference between adjacent curves and (**b**) isometric view of wt% polymer relative to overall wt% polymer of the early-stage spinodal decomposition of the PMMA/sulfolane system at 30°C, c_o = 0.10, time = 2×10^{-6} s, and percent completion = 21.6%. Distances are in micrometers

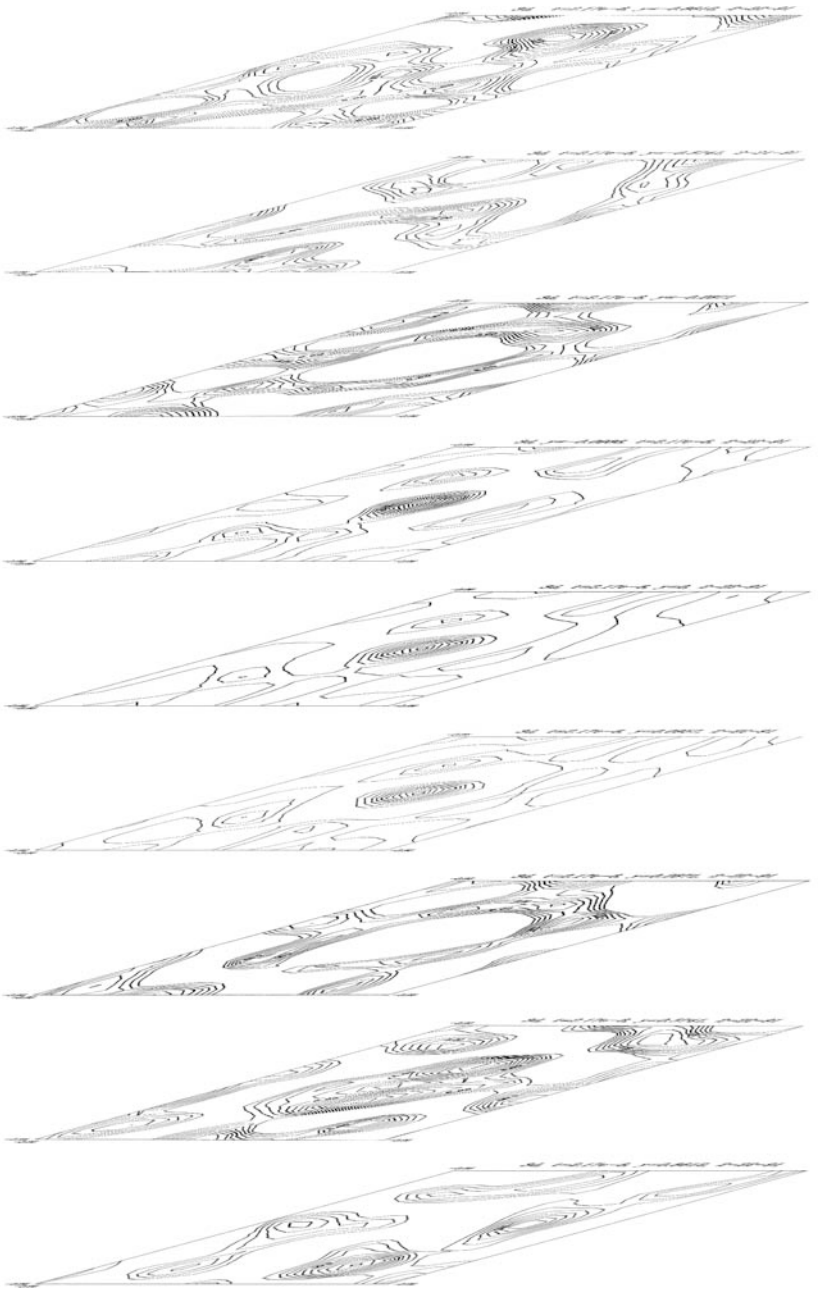

Fig. 1.4.8 Results of three-dimensional simulation of the PMMA/sulfolane system at 30ºC, as a stack in inclined view of two-dimensional contour plots. Two-dimensional domains are from −0.96 to +0.96 μm, while the vertical domain (top profile) starts at –0.86 μm and ends at the bottom profile at +0.86 μm

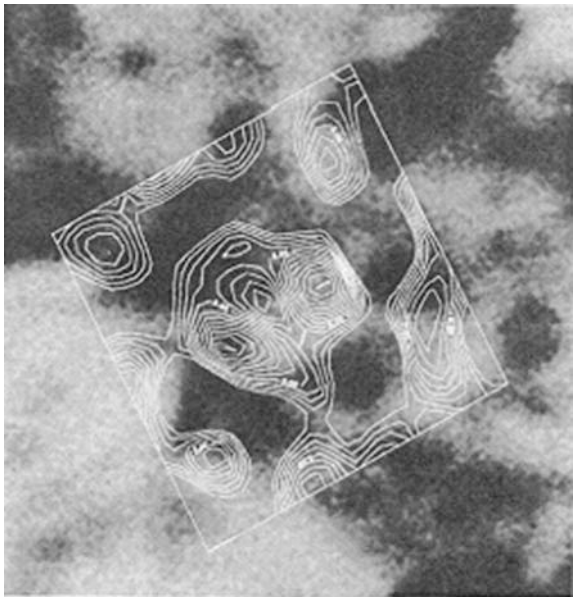

Fig. 1.4.9 Superimposition of numerical results of three-dimensional simulation of PMMA/sulfolane system at 30°C (shown in Fig. 1.4.8) with experimental data of a membrane portion showing early-stage pore structure (Caneba and Soong, 1985b)

matches with the overall structure obtained experimentally (Caneba and Soong, 1985b) (Fig. 1.4.9). Coarsening involves the formation of larger domains and interdomain distances.

1.4.2.2 Ternary System

Simulation of ternary systems is based on the poly(methacrylic acid) (PMAA)/methacrylic acid (MAA)/water system. In order to be able to determine some of the parameters for the model, the binary PMAA/water system was also analyzed.

Spinodal decomposition equations for ternary polymer systems have been derived in the Appendix. The equations are similar to those used for the above-mentioned binary polymer/solvent systems, except that there are two differential equations to solve, and there are four diffusion coefficients, mobilities, and gradient energy coefficients. This approach to modeling is suitable to experimentation, since some of the parameters can be obtained from various experiments. The rest of the parameters are obtained from reasonable assumptions.

For a binary system, D_{kj} is the binary mutual diffusion coefficient D_{AB}. The FRRPP process, however, is essentially a ternary system of the polymer/monomer/precipitant type (such as polystyrene/styrene/water or poly(methacrylic acid)/methacrylic acid/water). Let us designate the polymer (poly(methacrylic acid) or polystyrene) as component 1; precipitant (such as water or ether) as component 2; and the monomer (methacrylic acid or polystyrene) as component 3. Therefore, for the FRRPP process, we have four mutual diffusivities in the mixture: D_{11} is approximated as the mutual diffusivity of the polymer and precipitant; D_{22} is approximated as the mutual diffusivity of the monomer and the precipitant; D_{12} is the mutual diffusivity for the mass transfer of the polymer due to composition gradient of the monomer; and D_{21} is the mutual diffusivity for the mass transfer of the monomer

due to the composition gradient of the polymer. Similar definition applies for mobilities M_{ki} and gradient energy parameter κ_{ij}.

Derivation of the early-stage spinodal decomposition equations for a ternary system is presented elsewhere (Saxena, 2001). They reduce to the following:

$$\frac{\partial c_1}{\partial \tau} = \alpha^{\circ}_{11}\tilde{\nabla}^2 c_1 + \alpha^{\circ}_{12}\tilde{\nabla}^2 c_2 - (\delta^{\circ}_{11}\tilde{\nabla}^4 c_1 + \delta^{\circ}_{12}\tilde{\nabla}^4 c_2), \tag{1.4.8}$$

$$\frac{\partial c_2}{\partial \tau} = \alpha^{\circ}_{21}\tilde{\nabla}^2 c_1 + \alpha^{\circ}_{22}\tilde{\nabla}^2 c_2 - (\delta^{\circ}_{21}\tilde{\nabla}^4 c_1 + \delta^{\circ}_{22}\tilde{\nabla}^4 c_2), \tag{1.4.9}$$

where $\tilde{\nabla}(...)$ is the dimensionless form of $\nabla(...)$, or $\tilde{\nabla}(...) = \lambda_m \nabla(...)$, and

$$\begin{array}{ll} \tau = (-D^{\circ}_{11})t/\lambda^2_m & \alpha^{\circ}_{kj} = D^{\circ}_{kj}/(-D^{\circ}_{11}) \\ \delta^{\circ}_{kj} = 2M^{\circ}_{ki}\kappa_{ij}/(-D^{\circ}_{11})\lambda^2_m & \eta = x/\lambda_m \end{array}, \tag{1.4.10).}$$

Note that D and M are applied only to the overall or starting weight fractions; hence the superscript "o" applied on them. Also, note that D_{11} is a negative number, because the polymer phase separates from the solvent/precipitant. For simulation work, initial weight fraction of 7%/3%/90% were used for PMAA (component 1)/MAA (component 2)/water (component 3), respectively. The phase diagram, shown in Fig. 1.1.9 (Shi, 1997) for the PMAA/MAA/water system, indicates approximate values for the equilibrium compositions in the polymer-rich phase ($c^{\alpha}{}_1 = 12\%$, $c^{\alpha}{}_3 = 82\%$, $c^{\alpha}{}_2 = 6\%$) and polymer-lean phase ($c^{\beta}{}_1 = .5\%$, $c^{\beta}{}_3 = 97\%$, $c^{\beta}{}_2 = 0.5\%$).

A computer program was written in FORTRAN in order to solve Eqs. (1.4.8–1.4.10), which originally have eight unknowns. Prior work with the dimensionless system has shown that for a binary system, δ_{AB} can be approximated by the value of $1/8\pi^2$ (Laxminarayan and Caneba, 1991). For simplicity, factors of the same value were used for δ_{kj} 's (i.e., $\delta_{11}, \delta_{12}, \delta_{21}, \delta_{22}$). Thus, a design of experiments matrix was formulated and parameter values used in the calculations are shown in Table 1.4.2.

Based on the analysis of Morral and Cahn (1971), the set of parameters in Table 1.4.2 is just one of the possibilities of qualitative behavior for the signs of $\tilde{\alpha}_1, \tilde{\alpha}_2, \tilde{\delta}_1$, and $\tilde{\delta}_2$, based on the following definitions:

Table 1.4.2 Summary of design of experiment parameters for the simulation of spinodal decomposition of ternary polymer/monomer/solvent systems

Case	α_{11}	α_{12}	α_{21}	α_{22}	δ_{11}	δ_{12}	δ_{21}	δ_{22}	$\tilde{\alpha}_1$	$\tilde{\alpha}_2$	$\tilde{\delta}_1$	$\tilde{\delta}_2$
Binary3	−1.0	0	0	−1.0	$1/8\pi^2$	0	0	$1/8\pi^2$	−1	−1	$1/8\pi^2$	$1/8\pi^2$
qt1	−1.0	−0.1	0	−1.0	$1/8\pi^2$	0	0	$1/8\pi^2$	−0.9	−1.1	$1/8\pi^2$	$1/8\pi^2$
qt2	−1.0	0	−0.1	−1.0	$1/8\pi^2$	0	0	$1/8\pi^2$	−1	−1	$1/8\pi^2$	$1/8\pi^2$
qt3	−1.0	0	0	−1.0	$1/8\pi^2$	$1/8\pi^2$	0	$1/8\pi^2$	–1	−1	$1/8\pi^2$	$1/8\pi^2$
qt4	−1.0	0	0	−1.0	$1/8\pi^2$	0	$1/8\pi^2$	$1/8\pi^2$	−1	−1	$1/8\pi^2$	$1/8\pi^2$
qt5	−1.0	−0.1	−0.1	−1.0	$1/8\pi^2$	0	0	$1/8\pi^2$	−0.9	−1.1	$1/8\pi^2$	$1/8\pi^2$
qt6	−1.0	0	0	−1.0	$1/8\pi^2$	$1/8\pi^2$	$1/8\pi^2$	$1/8\pi^2$	−1	−1	$1/4\pi^2$	0
qt7	−1.0	−0.1	−0.1	−1.0	$1/8\pi^2$	$0.1/8\pi^2$	$0.1/8\pi^2$	$1/8\pi^2$	−0.9	−1.1	0.01393	0.00114

$$\tilde{\alpha}_1 = \frac{Tr(\alpha_{ij}) + \sqrt{\left[Tr(\alpha_{ij})\right]^2 - 4Det(\alpha_{ij})}}{2}, \tag{1.4.10}$$

$$\tilde{\alpha}_2 = \frac{Tr(\alpha_{ij}) - \sqrt{\left[Tr(\alpha_{ij})\right]^2 - 4Det(\alpha_{ij})}}{2}, \tag{1.4.11}$$

$$\tilde{\delta}_1 = \frac{Tr(\delta_{ij}) + \sqrt{\left[Tr(\delta_{ij})\right]^2 - 4Det(\delta_{ij})}}{2}, \tag{1.4.12}$$

$$\tilde{\delta}_2 = \frac{Tr(\delta_{ij}) - \sqrt{\left[Tr(\delta_{ij})\right]^2 - 4Det(\delta_{ij})}}{2}. \tag{1.4.13}$$

$Tr(\ldots)$ is the trace and $Det(\ldots)$ is the determinant of the corresponding matrices. As seen from Table 1.4.2 in all cases, both components 1 and 2 undergo spinodal decomposition due to their negative signs for $\tilde{\alpha}_1$ and $\tilde{\alpha}_2$, and positive signs for $\tilde{\delta}_1$ and $\tilde{\delta}_2$.

Figures 1.4.10–1.4.17 show frequency spectra of the cases, while Figs. 1.4.18–1.4.25 show their corresponding composition profiles.

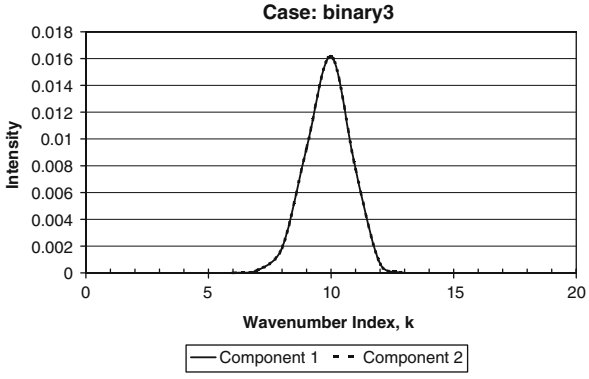

Fig. 1.4.10 Frequency spectra of components 1 and 2 for the ternary binary3 case, with parameters indicated in Table 1.4.2

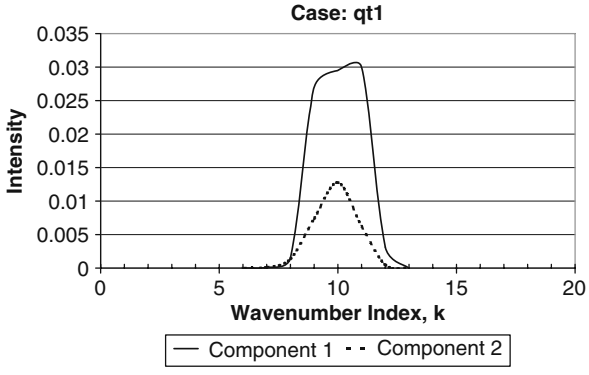

Fig. 1.4.11 Frequency spectra of components 1 and 2 for the ternary qt1 case, with parameters indicated in Table 1.4.2

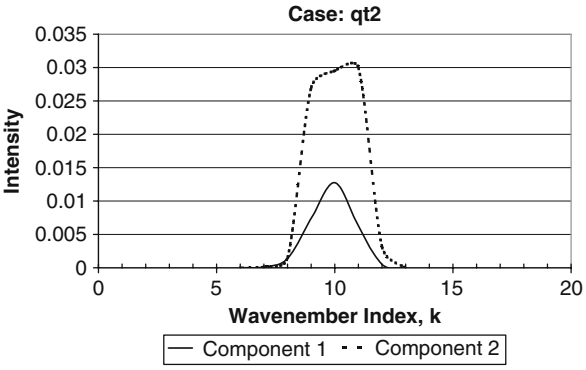

Fig. 1.4.12 Frequency spectra of components 1 and 2 for the ternary qt2 case, with parameters indicated in Table 1.4.2

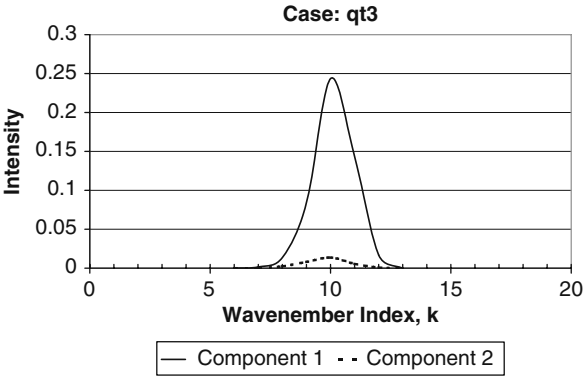

Fig. 1.4.13 Frequency spectra of components 1 and 2 for the ternary qt3 case, with parameters indicated in Table 1.4.2

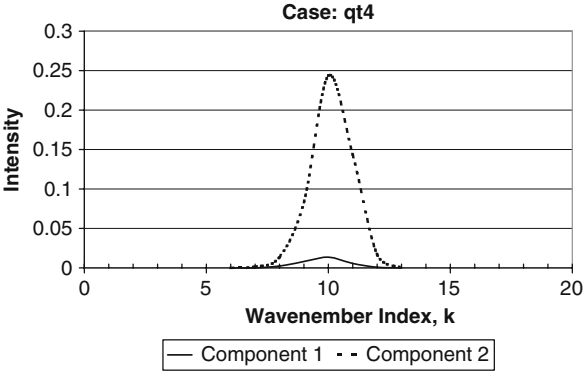

Fig. 1.4.14 Frequency spectra of components 1 and 2 for the ternary qt4 case, with parameters indicated in Table 1.4.2

1.4.3 Experimental Efforts

In this subsection, experimental efforts are presented to determine parameters for phase separation kinetics of polymer/solvent and polymer/monomer/precipitant systems. It is necessary to first apply these methods for polymer/solvent systems, since theoretical bases of experimental methods are well established for such systems. Later, they are applied to relevant ternary systems.

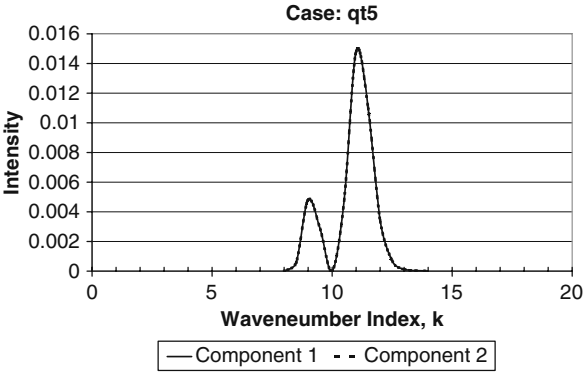

Fig. 1.4.15 Frequency spectra of components 1 and 2 for the ternary qt5 case, with parameters indicated in Table 1.4.2

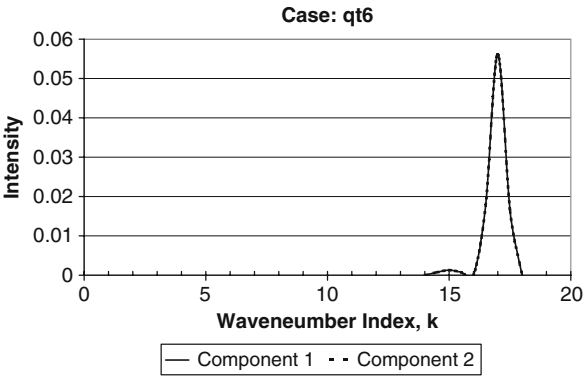

Fig. 1.4.16 Frequency spectra of components 1 and 2 for the ternary qt6 case, with parameters indicated in Table 1.4.2

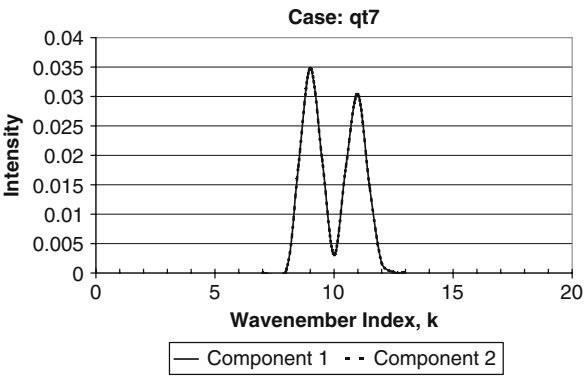

Fig. 1.4.17 Frequency spectra of components 1 and 2 for the ternary qt7 case, with parameters indicated in Table 1.4.2

1.4.3.1 Light Scattering Studies

Introduction

Light scattering techniques have been developed to determine the mobility, diffusion coefficient, and gradient-energy coefficient for phase separating polymer systems.

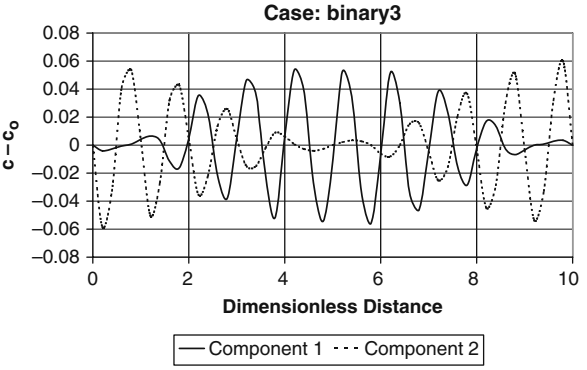

Fig. 1.4.18 Composition profiles of components 1 and 2 for the ternary binary3 case, with parameters indicated in Table 1.4.2

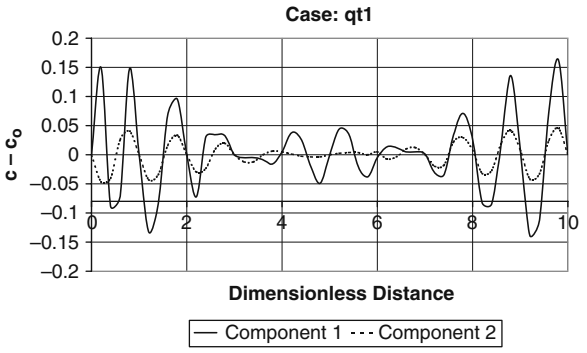

Fig. 1.4.19 Composition profiles of components 1 and 2 for the ternary qt1 case, with parameters indicated in Table 1.4.2

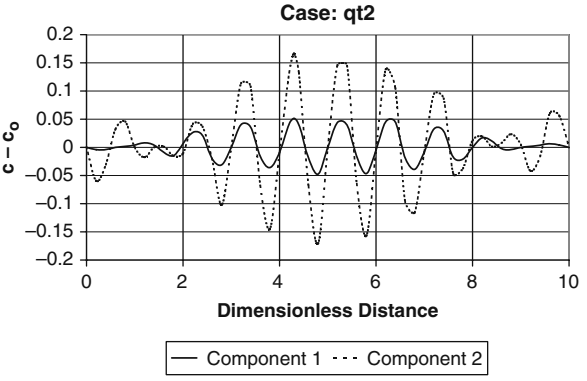

Fig. 1.4.20 Composition profiles of components 1 and 2 for the ternary qt2 case, with parameters indicated in Table 1.4.2

From these experimental studies (Hashimoto, et al., 1983, 1984, 1989; Inaba et al., 1986; Izumitani and Hashimoto, 1985; Kumaki and Hashimoto, 1986; Nojima et al., 1982, p. 225 and 907; Nose, 1987; Snyder et al., 1983; Snyder and Meakin, 1985; van Aartsen, 1970), it follows that the above-mentioned quantities can be obtained

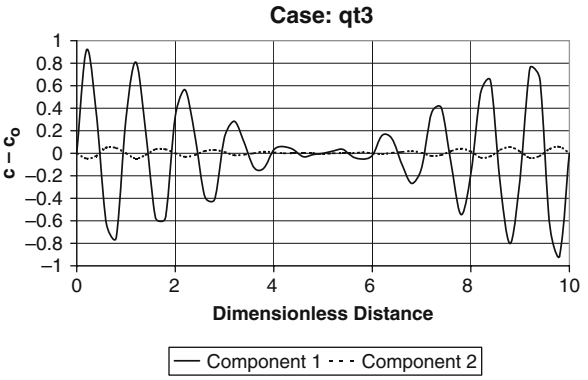

Fig. 1.4.21 Composition profiles of components 1 and 2 for the ternary qt3 case, with parameters indicated in Table 1.4.2

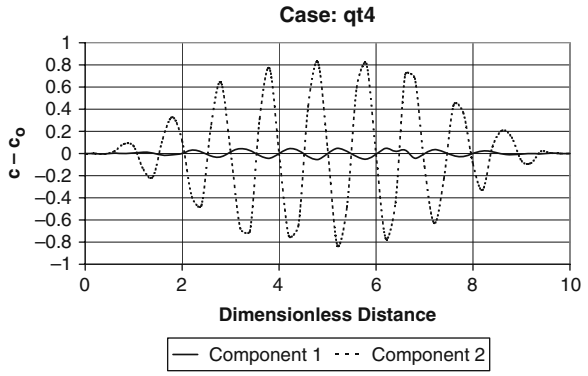

Fig. 1.4.22 Composition profiles of components 1 and 2 for the ternary qt4 case, with parameters indicated in Table 1.4.2

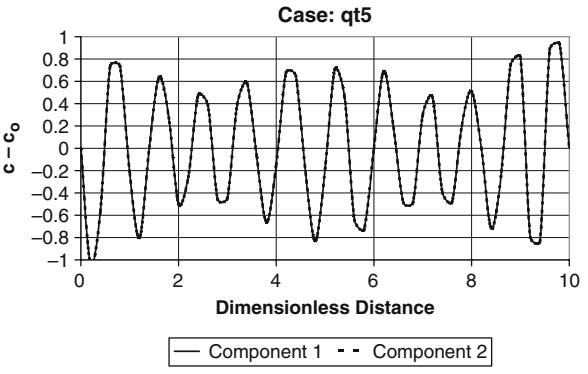

Fig. 1.4.23 Composition profiles of components 1 and 2 for the ternary qt5 case, with parameters indicated in Table 1.4.2

through intensity measurements and/or observation of the scattering pattern during the initial stages of spinodal decomposition (shown in Fig. 1.4.3 to comprise the induction period and the accelerated-growth period). Of great importance is the magnitude of the induction time for spinodal decomposition since it signifies a time lag prior to a relatively quick perceptible change in system properties. The period not only signifies a sudden change in system properties but also is associated with an open-cell morphology that may not persist in time (Caneba and Soong, 1985a, b).

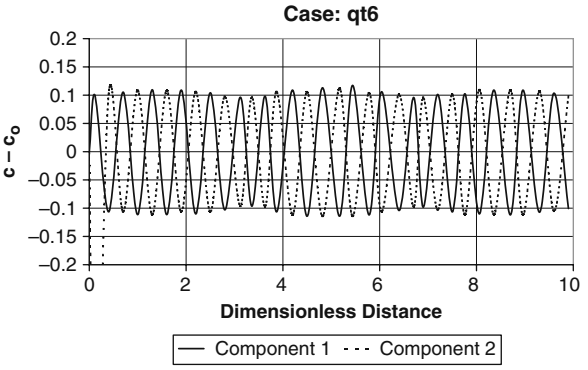

Fig. 1.4.24 Composition profiles of components 1 and 2 for the ternary qt6 case, with parameters indicated in Table 1.4.2

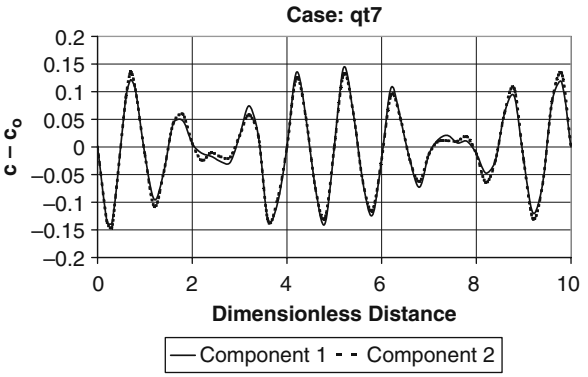

Fig. 1.4.25 Composition profiles of components 1 and 2 for the ternary qt7 case, with parameters indicated in Table 1.4.1

Theory for the Experimental Work

For an early stage of phase separation by spinodal decomposition, it has been shown (Hashimoto et al., 1983; Izumitani and Hashimoto, 1985; Sasaki and Hashimoto, 1984; Snyder, et al., 1983) that

$$Q_{\mathrm{SAL}}(t) \propto \exp\left[2R(\vec{q}_{\mathrm{m}})t\right] \tag{1.4.14}$$

where $Q_{\mathrm{SAL}}(t)$ is the total integrated intensity of the scattered light. A plot of $ln[Q_{\mathrm{SAL}}(t)]^{1/2}$ vs time should yield a straight line whose slope is equal to $R(\vec{q}_m)$. By measuring the time dependence of $Q_{\mathrm{SAL}}(t)$ at several temperatures within the spinodal, one can obtain the temperature dependence of $R(\vec{q}_m)$. Further, if the wave vector, $(\vec{q}_m)$, is known, one can also measure the temperature dependence of D using Eq. (1.4.4)

$$R(\vec{q}_{\mathrm{m}}) = -\frac{M\left(f''\right)(\vec{q}_{\mathrm{m}})^2}{2} = \frac{D(\vec{q}_{\mathrm{m}})^2}{2} \tag{1.4.15}$$

and $\left(\vec{q}_m\right)$ is determined from the angular dependence of the light scattering pattern (Hashimoto, et al., 1983; Izumitano and Hashimoto, 1985):

$$(\vec{q}_{\mathrm{m}}) = \left(\frac{4\pi}{\lambda}\right) \sin\left(\frac{\theta}{2}\right), \tag{1.4.16}$$

where λ is the wavelength of light and θ is the scattering angle in the medium.

Materials and Procedures

Slightly polydisperse polymethacrylic acid (PMAA) samples were also used in this study. The PMAA sample had molecular weight, M_{n}, of $\sim 2 \times 105$ g/mol and a polydispersity index, $M_{\mathrm{w}}/M_{\mathrm{n}}$, of 1.40. Methacrylic acid used was purchased from Aldrich Chemical Company. Binary mixtures of PMAA in water, as well as the ternary solutions of PMAA/MAA/water, were prepared in quartz cells with an interior thickness of 1 mm. The cells containing binary and ternary solutions were sealed and rotated at room temperature to provide mixing. The initial solutions were mixed for at least 2 days in this fashion to ensure a homogeneous system.

In order to obtain the molecular parameters that influence the early stage of spinodal decomposition, including the induction and the accelerated-growth period, our experiment focuses on the very first seconds of phase separation. This requires a very accurate and highly time-resolved monitoring of the process. Rather than getting a full picture by monitoring the total light scattering intensity with a power meter (Snyder et al., 1983; Snyder and Meakin, 1985) or a TV camera system (Hashimoto et al., 1983, 1989; Izumitano and Hashimoto, 1985), the scattering intensity was measured separately for different angles using a photodiode array detector. Details of the experiment applied to PS/cyclohexanol system are shown elsewhere (Saxena, 1991); the same apparatus and procedure were used in the PMAA/water as well as PMAA/MAA/water system.

In order to shift to PMAA/water and PMAA/MAA/water systems, phase separation is effected by starting the system at a lower temperature, and then placing it at a higher temperature. This is because such a system has an LCST, instead of a UCST. We note the plots in Figs. 1.1.5–1.1.7, which show points that were subject to light scattering studies.

Results

Figures 1.4.26 and 1.4.27 show plots of $ln[Q_{\mathrm{SAL}}(t)]^{1/2}$ vs the time for binary PMAA/water system at 70, 75, and 80°C, at 7 and 10 wt% PMAA, respectively. Note that $Q_{\mathrm{SAL}}(t)$ is the normalized integrated intensity of the scattered light.

Figure 1.4.28 shows plot of diffusion coefficient, $-D$, (mutual diffusivity between PMAA and water) vs temperature. This figure shows the temperature dependence of diffusion coefficient obtained from the slope of the lines in Figs. 1.4.26 and 1.4.27 and using Eqs. (1.4.14–1.4.16). Since diffusivity vanishes at the spinodal temperature, by extrapolating the linear relationship, the spinodal temperature was estimated to be 63°C for a 7% PMAA/water system and about 62°C for the 10% PMAA/water system.

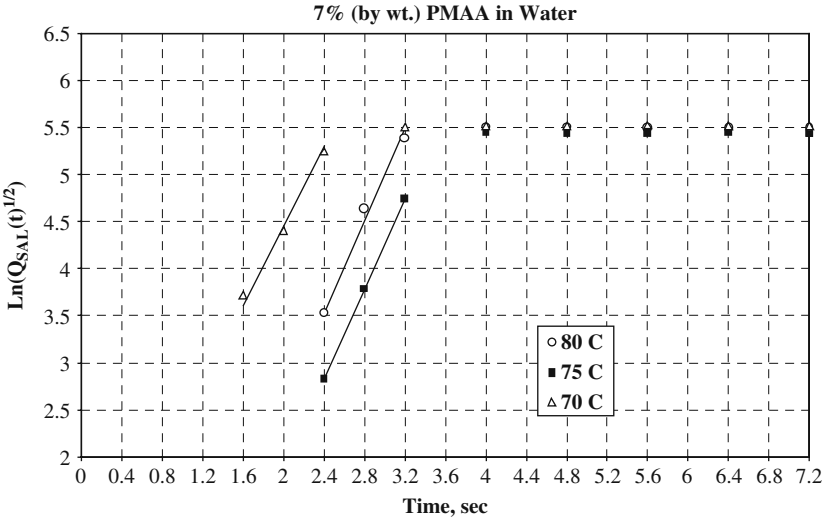

Fig. 1.4.26 Plots of $ln[Q_{SAL}(t)]^{1/2}$ vs the time for binary PMAA/water system at 70, 75, and 80°C, at 7 wt% PMAA (Reproduced with permission from Saxena, 2001)

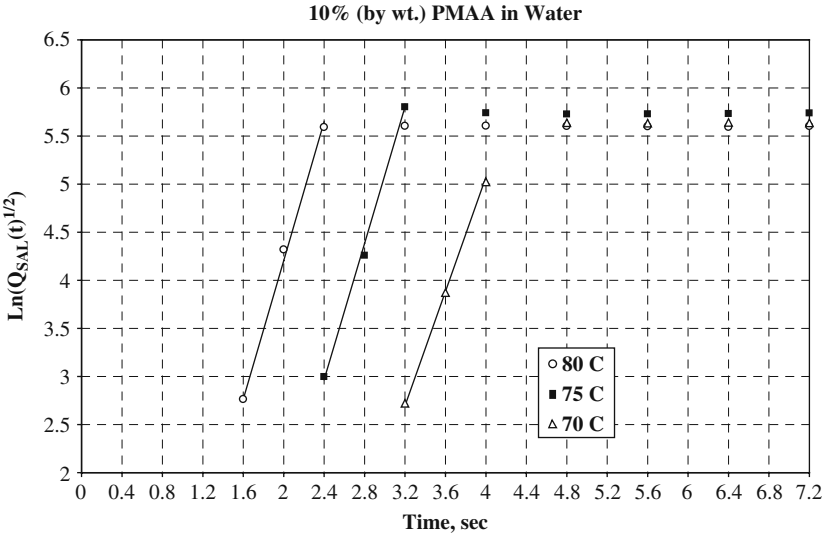

Fig. 1.4.27 Plots of $ln[Q_{SAL}(t)]^{1/2}$ vs the time for binary PMAA/water system at 70, 75, and 80°C, at 10 wt% PMAA (Reproduced with permission from Saxena, 2001)

Figures 1.4.29 shows plots of relative intensities $I(t)$ vs q for the ternary PMAA/MAA/water system (7 wt%/3 wt%/90 wt%) at 80°C. In Fig. 1.4.30, the plot of $ln[Q_{SAL}(t)]^{1/2}$ vs the time for the ternary PMAA/MAA/water system at 80°C is shown, whereby the straight-line section was used to determine diffusion coefficients and spinodal temperatures.

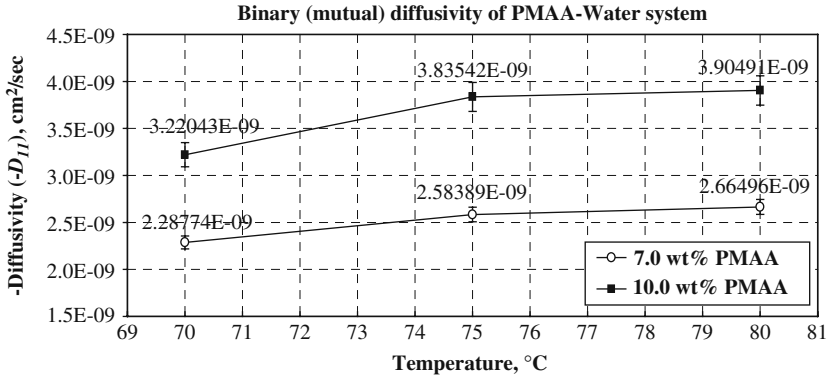

Fig. 1.4.28 Plot of diffusion coefficient, $-D$, (or $-D_{22}$) vs temperature (Reproduced with permission from Saxena, 2001)

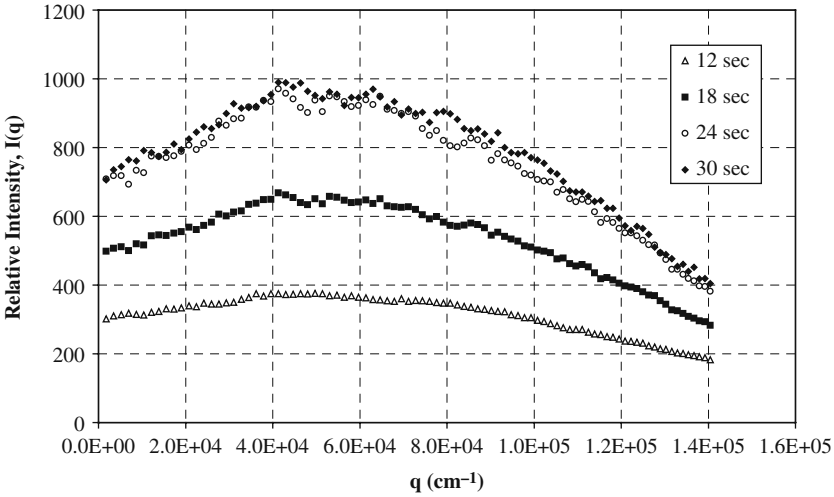

Fig. 1.4.29 Plot of $ln[Q_{SAL}(t)]^{1/2}$ vs the wavenumber q and time for the ternary PMAA/MAA/-water system at 75°C (Reproduced with permission from Saxena, 2001)

1.4.3.2 Morphological Studies

Phase separation phenomena of polymer solutions have been studied, and they were found to be relevant to membrane formation and to the study of the FRRPP process. Phase separation has been effected by removal of thermal energy from the homogeneous polymer solution. The polystyrene/cyclohexanol system is investigated. The final structure of these phase separated systems has been found to be a strong function of the quenching time. As processing time increases a shift from a highly interconnected open cell structure to a closed cell structure has been

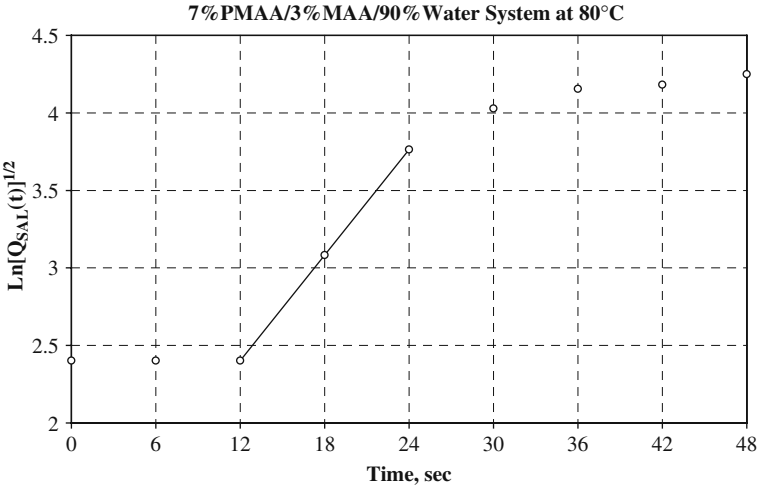

Fig. 1.4.30 Plot of $ln[Q_{SAL}(t)]^{1/2}$ vs the time for the ternary PMAA/MAA/water system at 80°C (Reproduced with permission from Saxena, 2001)

seen. This has been attributed to both coarsening and hydrodynamic effects in the polymer/solvent system.

Membranes were also prepared for the ternary (PMAA/MAA/water) system by first separating the system via spinodal decomposition and then freeze-drying to remove the solvent and non-solvent from the system. Freeze-drying technique was necessary since we are dealing with a non-equilibrium system. The structural variation of a membrane (such as pore size distribution) is influenced by processing and kinetic parameters such as chemical potential gradient and diffusivity. These parameters can change continuously during phase separation, which also constitutes the membrane formation process. In polymer systems, frozen states can then be obtained that are far from equilibrium and that are stable for a long period of time. Therefore, once these membranes were formed, they can be analyzed for pore sizes using a scanning electron microscope. The membrane formation investigation described in this chapter and the diffusion equation solved numerically both describe early stages of phase separation.

Introduction

The study of the morphological characteristics of polymeric membranes is of great interest in the area of membrane science (Kesting, 1971). It has been known that one of the keys to better membrane performance lies in the structure of the membrane itself. In turn the morphology of a particular membrane depends upon its processing conditions and the physical and chemical properties of the polymer system under consideration. Membranes from polypropylene (Porter, 1982), high-density polyethylene (Porter, 1982), polyvinylidene fluoride (Hiatt et al., 1984; Hiatt, 1985)

have been made via the thermal inversion process, and their structure investigated. The structure obtained in the case of suddenly quenched systems and systems where the temperature is dropped at a controlled rate have been reported in the above-mentioned references. In the case of systems which have been suddenly quenched below the spinodal temperature the membranes are seen to exhibit a highly interconnected fibrous structure characteristic of systems which have undergone spinodal decomposition (Porter, 1982; Hiatt et al., 1984; Hiatt, 1985). Systems which have been subjected to a controlled drop in temperature are seen to exhibit a cellular structure, characteristic of nucleation and growth.

The membranes formed in this investigation fall under a category of phase inversion membranes. Phase inversion refers to the process by which a polymer solution (in which solvent system is the continuous phase) inverts into a three-dimensional macromolecular network (where polymer is the continuous phase). The process typically begins with a homogeneous single-phase solution that undergoes a transition into heterogeneous liquid phases. The transition can occur in several ways including the thermal inversion process (TIPS).

Polymer membrane formation by thermal inversion process involves dissolution of the desired polymer in a suitable solvent at that temperature. For an LCST type of system, as the temperature of the system is increased inside the phase boundary, the system phase separates. For this investigation, a ternary phase diagram for a polymer/solvent/non-solvent system is similar to that of a polymer/monomer/precipitant system as shown in Fig. 1.1.2. If the temperature of the system is raised quickly to a point inside the phase boundary, the polymer solution will phase separate. Lets call this sudden rise in temperature as "quenching" (even though the regular meaning of this word may be opposite in general use). The rise in temperature is the same phenomenon referred to as the local heating in the FRRPP process albeit at a much smaller spatial scale or domain.

In this investigation, membrane formation conditions were selected based on the above-mentioned light scattering work. The starting mixture composition for the ternary PMAA/MAA/water system, and quench temperatures were identical to those used in the light scattering work. The scanning electron microscope (SEM) was used to observe the membranes made with various quench times and temperatures. The experiments were not of a dynamic mode in a sense that the evolution of the structure was not observed as a continuous function of time in one specimen. However, we were able to get an insight into the structure evolution by being able to test series of samples, all starting from the same parent mixture, and representing different stages of phase separation.

Theory

Early-stage spinodal decomposition has been extensively discussed in the early portions of this section. The discussion here pertains more to coarsening and other late-stage behavior.

One of the most extensive efforts in the area of late-stage phase separation is the work of Siggia (1979). It is also of great interest in the area of polymer blends

(Feke and Prins, 1974; Voight-Martin et al., 1986). Voight-Martin and coworkers (1986) adapted Siggia's findings and examined the phase separation kinetics of a polystyrene/polyvinylmethylether system. The same system has also been studied by Feke and Prins (1974). There are two theories to explain later-stage structure evolution, the applicability of either depending on the initial composition of the system. For compositions close to the critical composition, i.e., for systems with high-phase volume ratios, a high level of phase interconnectivity was observed at the end of the initial stages of phase separation. This and a unique periodicity in the spatial distribution of the two phases are two characteristics of spinodally decomposed systems (McMaster, 1975). On the other hand, concentrations away from the critical concentration resulted in a structure where there was a loss of phase interconnectivity. Such systems were characterized by the dispersion of one phase in an other and due to low-phase volume ratios.

Experimental

Polystyrene/Cyclohexanol System

Polystyrene used in the experiments was a primary standard (mol. wt. = 400,000 Da), purchased from Pressure Chemical Company. The solvent used was cyclohexanol obtained from Aldrich and was fractionally distilled before use.

The procedure for the study of membrane morphology consists of three stages:

1. Preparation of the polymer/solvent system at the desired elevated temperature.
2. Coagulation of a polymer solution layer at lower temperature.
3. Preparation of the solid membrane specimen and observation of the pore structure using a scanning electron microscope.

The polymer used in the thermal inversion process of making membranes was initially dissolved and maintained at a temperature above the critical point of the binary system under consideration. Solutions of 10 wt% polystyrene in cyclohexanol were prepared at 90°C and then placed in an oven at a temperature of 115–120°C. Note that the upper critical solution temperature of polystyrene/cyclohexanol system is about 82°C (Shultz and Flory, 1953). Also, the critical composition is at a polymer volume fraction of about 0.03, while the polymer-rich binodal composition is at a volume fraction of about 0.20. Thus, the cast solutions are expected to coagulate inside the spinodal curve, as we have verified using a diode-array time-resolved light scattering system similar to that used by Hashimoto and his coworkers (Inaba et al., 1986). Solid membranes were then made within 24 h, after the solutions were prepared. These membranes were then sputter-coated with gold–palladium and observed under the microscope.

The apparatus for making membrane-type structures (Fig. 1.4.31) essentially consists of a cell and an ethylene glycol bath whose temperature was controlled using a temperature controller. The cell (Fig. 1.4.32) includes a Teflon® cylinder, to the top of which is a Teflon® cover. The bottom of the cylinder is covered with

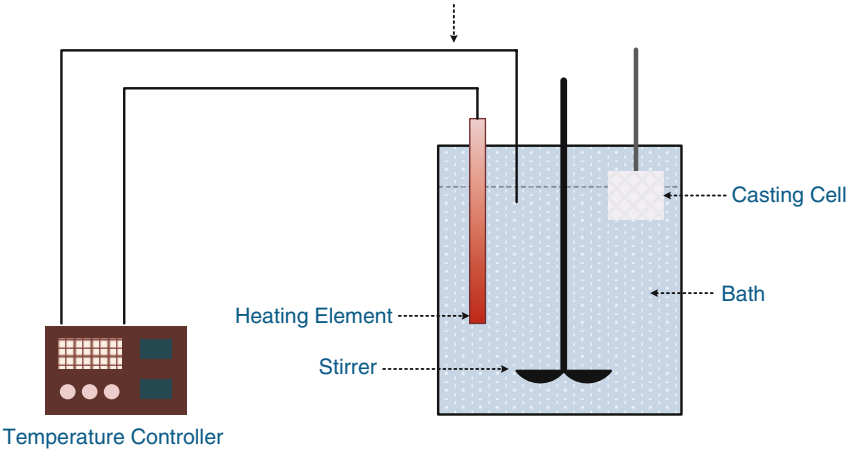

Fig. 1.4.31 Schematic diagram of the quenching system used in the formation of membrane-type structures through the thermal inversion process

an aluminum foil which is supported with a metal ring. Thus, the bottom of the cell has a good thermal conducting surface, while the air space above the aluminum foil is essentially insulating. After preheating the cell to the oven temperature, the homogeneous solution is poured into it so as to form as thin a layer as possible on the aluminum foil. The cover of the cell is replaced and the aluminum portion of the cell can now be quenched into the ethylene glycol bath, which in turn is maintained at any required temperature. Membranes have been made at different temperatures

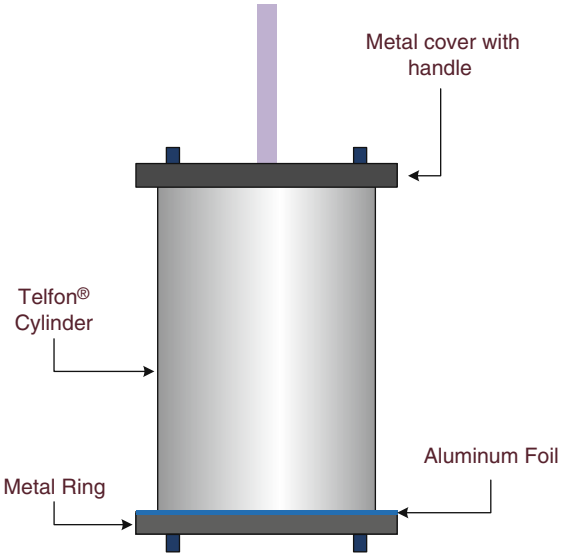

Fig. 1.4.32 Cross-sectional diagram of the casting cell used in phase separating a homogeneous polymer solution. The aluminum foil not only provides a seal for the material inside the cell but also acts as a cooling surface. The vapor space in the cell is assumed to act as a thermal insulator (Redrawn with permission from Guo et al., 1995)

and with different quenching times. Once a membrane is made, it is quenched in an ice bath to freeze its structure (the freezing point of cyclohexanol is 22°C). After this, the membrane is taken out and washed in cold water to leach the solvent out. Finally, solidification is done in a vacuum oven for 2 days.

The dried membranes are then broken in liquid nitrogen. A sample is then cut and placed on mounting cylinder with the cracked surface exposed for observation. It is coated with a gold–platinum sputter coater and observed using a scanning electron microscope.

PMAA/MAA/Water System

Membranes were prepared by first phase separating the polymer solution via spinodal decomposition. The criterion is to move the entire system into the spinodal region with minimum time delay. The solvents are then removed without affecting the polymer structure by freeze-drying. In this method, the system is frozen by lowering its temperature rapidly to below its freezing point. Vacuum is applied, while maintaining the low temperature, which removed the solvents from the system without significantly affecting the polymer pore structure.

Procedure. Two ternary polymer/solvent/non-solvent systems were prepared, one containing 7% PMAA, 3% MAA, 90% water and the other containing 10% PMAA, 3% MAA, 87% water.

The step-wise method for membrane preparation for this system is as follows:

1. A small glass bottle with flat bottom was immersed in a hot water bath at the phase separation temperature (within $\pm$0.2ºC), such that about $^1/_2$ to $^3/_4$ of the bottle was below the water level.
2. The bottle was allowed to equilibrate in the hot water bath for a minimum of 10 min. This ensured that the inside walls of the bottle were at the same temperature as the water. However, as one moves away from the wall, due to the heat capacity of the liquid, there will be temperature gradient inside the sample. There will be a delay, depending on the sample size, before the entire mixture reaches equilibrium. For this reason alone, when investigating membrane structure using SEM, we looked primarily at that cross-section of the membrane that was adjacent to the wall.
3. About 0.4 ml of the homogeneous polymer solution (in this case prepared at room temperature where it is outside the phase envelope) was added to the bottle. This resulted in a thin film of the polymer solution at the bottom of the bottle. The bottle was immediately covered with a rubber stopper with a glass rod to minimize any solvent loss. The timer was started.
4. The system was allowed to phase separate for a pre-determined length of time t_{ps}.
5. At the end of phase separation time, in order to stop the any further growth of the structure, the bottle was immediately removed and immersed in a liquid nitrogen bath. Note that the time taken to transfer the sample into liquid nitrogen bath in most cases was less than 1 s.

6. Once the entire system was frozen (it took a maximum of 1 second for the polymer solution in contact with the glass surface to freeze), the solidified MAA and water were removed from the system via freeze-drying process. Since the removal of solvents using conventional freeze-drying takes several days, we used a technique called "cold finger" to streamline and increase the efficiency of this process.

Freeze-Drying Procedure

1. Once the polymer system was frozen, the rubber stopper was replaced with another stopper containing a glass tubing which provided an opening into the bottle.
2. While the bottle was still inside the liquid nitrogen bath, the other end of the glass tubing was connected to one leg of the vacuum manifold. The vacuum manifold valve was opened and the system was allowed to pump-out for a few minutes.
3. Swiftly, the bottle was transferred to a dry ice bath that was maintained at –10°C or less at all times. This ensured that both MAA and water would not melt during drying. (The dry ice bath was prepared by slowly adding solid CO_2 [dry ice] pieces to 2-propanol till the mixture temperature was about 20–30°C below zero. A well-insulated system will maintain this temperature for several hours. In our case, it took almost 1 day before the dry ice bath warmed up to –10°C).
4. The bottle was left under vacuum and inside the dry ice bath till all MAA and water were removed from the system. This can be denoted as the drying time t_d.
5. After the drying period, the bottle was removed from the dry ice bath but further maintained under vacuum at room temperature for additional 2 days. This was done to ensure that all traces of solvent have been removed and that the membrane is absolutely dry.

Sample Preparation for SEM. Samples for the scanning electron microscopy (SEM: Model Joel JXA-8600) were prepared by first immersing the membrane into a liquid nitrogen. This made the membrane brittle. The membrane was broken into small pieces and some of the pieces were mounted on the metal cylinder that forms part of the stage inside the microscope. The membrane was mounted such that its cross-section (or the broken face) was perpendicular to the electron beam. This way we were able to study the pore structure of the membrane directly. Our focus was to study the edge that was in contact with the bottom wall of the bottle. All membranes were coated with carbon to make them conductive prior to any microscopy work.

Results and Discussion

PS/Cyclohexanol System

Figure 1.4.33 shows scanning electron micrographs of the cross-section of a polystyrene membrane that was coagulated at 80°C from a 10 wt% polystyrene solution in cyclohexanol. The left of Fig. 1.4.33(a) corresponds to the thermal conductor side (the side in contact with the aluminum foil of the coagulation cell shown

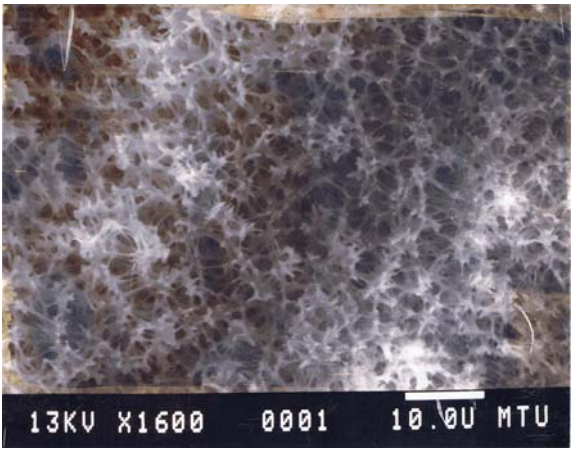

Fig. 1.4.33(a) Scanning electron micrograph of thermal conductor side of a polystyrene membrane that was cast at 80°C from a solution of 10 wt% polystyrene in cyclohexanol. For this quenching time of 5 min, pores are 0.4–1.2 μm, while cells are 1.2–4.0 μm

in Fig. 1.4.31) and the right side corresponds to the thermal insulator side. The morphological structure consists of spherical cells connected by circular pores, and the domains are in the form of an interconnected network. The high-magnification micrograph of the thermal conductor side of the membrane (Figs. 1.4.33(b)) shows pores of less than 1 μm and cells in the order of 1 μm. On the other hand, the high-magnification micrograph of the thermal insulator side (Fig. 1.4.33(c)) shows pores of 1–2 μm and cells of 5–10 μm.

Figures 1.4.34 and 1.4.35 represent the same experiment starting from other parent solutions, i.e., fresh solutions. All parent solutions are of the same weight percent. These pictures provide a closer look at the coarsening phenomenon, especially beyond the stage where the spherical cells are initially formed. Figures 1.4.34(a) and (b)provide a closer look at the stage where wall rupture is taking place, leading finally to the formation of closed cells. These closed cells are better represented by Fig. 1.4.35

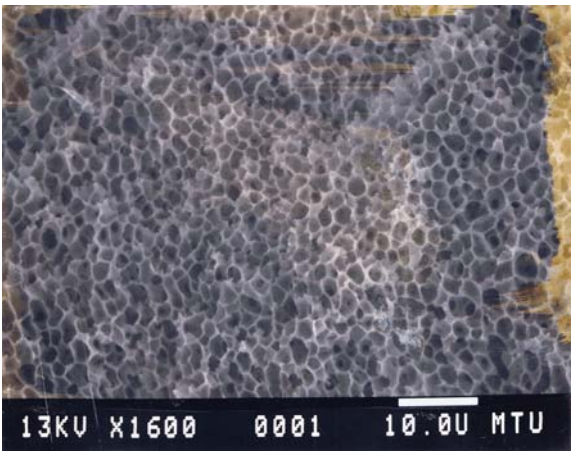

Fig. 1.4.33(b) Scanning electron micrograph of thermal conductor sides of a polystyrene membrane that was cast at 80°C from a solution of 10 wt% polystyrene in cyclohexanol. For the quenching time of 10 min, cells are 0.8–4.0 μm in diameter

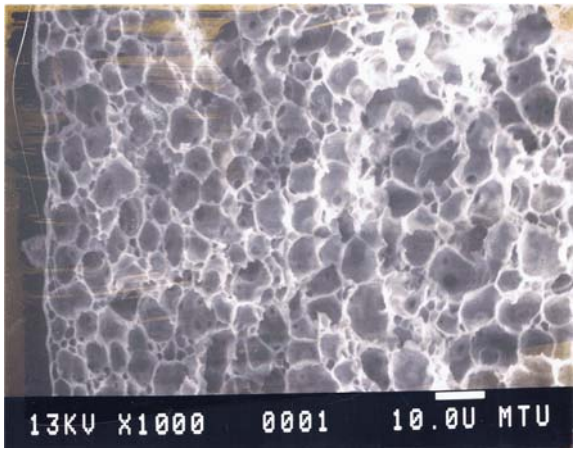

Fig. 1.4.33(c) Scanning electron micrograph of thermal conductor side of a polystyrene membrane that was cast at 80°C from a solution of 10 wt% polystyrene in cyclohexanol. For a quenching time of 25 min, small cells are greater than 0.6 μm, while larger cells are less than 9.6 μm

The observation of larger cell sizes at higher temperatures agrees with the prediction of the expression in the work of Hillert (1961) wherein the polymer interdomain distance was shown to be inversely proportional to the magnitude of the deviation of the quenching temperature from the spinodal temperature. On the other hand, the temperature dependence of the rate of formation of closed cells from open cells agrees with the foregoing proposed mechanism of morphology evolution.

With a great deal of certainty the observed evolution of structure in polystyrene/cyclohexanol system can be applied to other amorphous polymer systems undergoing thermally induced spinodal decomposition, which is the nonreactive analog of the FRRPP process for polymer/small-molecule systems.

It has been found that spinodal decomposition of a homogeneous polymer solution leads to a highly interconnected open network structure (Porter, 1982; Hiatt et al., 1984; Hiatt, 1985). Theoretically, this structure is represented by a single predominant composition wave number (Cahn, 1961). Later stage behavior resulting

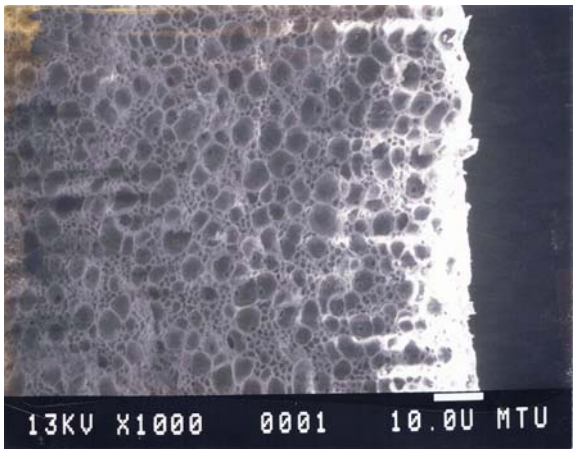

Fig. 1.4.33(d) Scanning electron micrograph of thermal conductor side of a polystyrene membrane that was cast at 80°C from a solution of 10 wt% polystyrene in cyclohexanol. For a quenching time of 55 min, small cells are greater than 0.6 μm, while larger cells are less than 10.5 μm

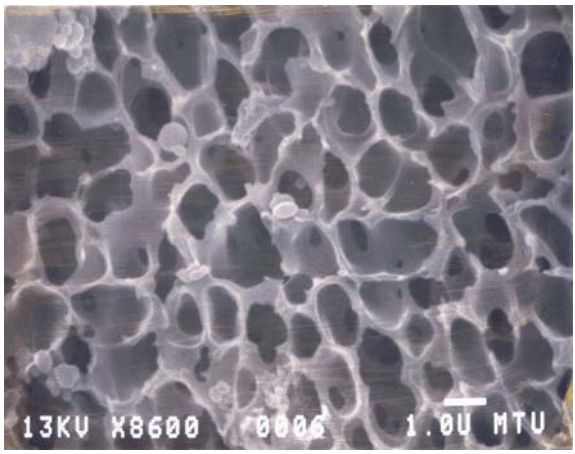

Fig. 1.4.34(a) SEM picture of a material similar to that in Fig. 1.4.33, except that it came from a different parent solution and at a quenching time of 10 min

in the coarsening of structure has been cited to involve open cell domain disappearance, closed cell formation (Caneba and Soong, 1985a), hydrodynamic flow (Siggia, 1979), and gravity flow (Siggia, 1979). Based on these cited structure formation processes and our experimental observations, we think that after thermal quenching an interconnected fibrous structure occurs. The end of this stage is the point in time wherein the solvent-rich domains reach the binodal composition. If the polymer-rich domains have not yet reached the binodal composition, continued increase in the polymer composition has been cited to occur at the expense adjacent polymer-rich domains (Cahn, 1961) (asymmetric system shown in Fig. 1.4.5). On the other hand, a symmetric system (shown in Fig. 1.4.4) will involve simultaneous attainment of bimodal compositions in polymer-rich and polymer-lean phases. For the polystyrene/cyclohexanol experimental system, this latter process is likely

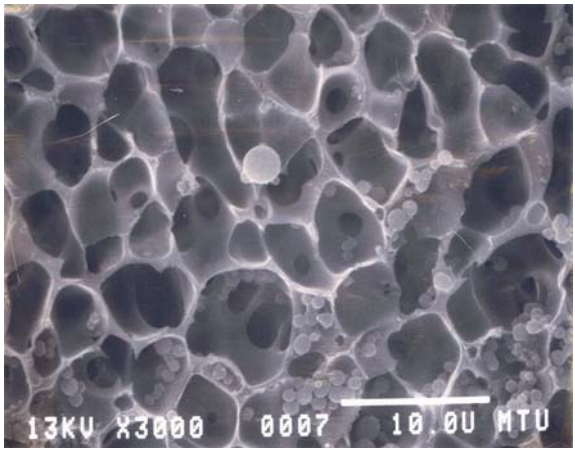

Fig. 1.4.34(b) SEM picture of a material similar to that in Fig. 1.4.33, except that it came from a different parent solution and at a quenching time of 20 min

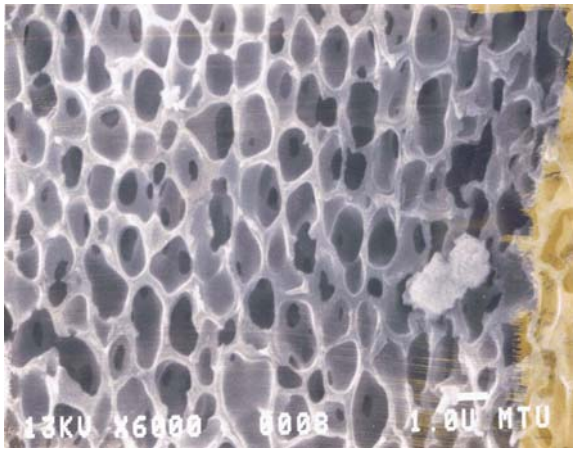

Fig. 1.4.34(c) SEM picture of a material similar to that in Fig. 1.4.33, except that it came from a different parent solution and at a quenching time of 40 min

to occur because the solvent-rich polymer composition is at a volume fraction close to zero and the polymer-rich polymer composition is at a volume fraction of about 0.20, while the overall composition is at a weight fraction (almost the same as volume fraction) of 0.10. In fact, from a rough approximation of negligible volume change upon mixing, a certain polymer composition asymmetry ratio, $R_{\alpha\beta}$, can be defined as

$$R_{\alpha\beta} = \frac{c^{\beta} - c_{\mathrm{o}}}{c_o - c^{\alpha}}, \tag{1.4.17}$$

where c_{o} = the overall polymer wt fraction, c_{α} = the solvent-rich polymer wt fraction, and c_{β} = the polymer-rich polymer wt fraction.

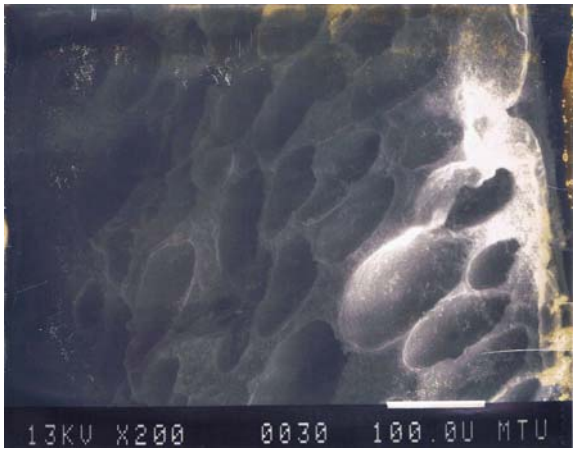

Fig. 1.4.35(a) SEM picture of a material similar to that in Fig. 1.4.33, except that it came from a different parent solution and at a quenching time of 60 min

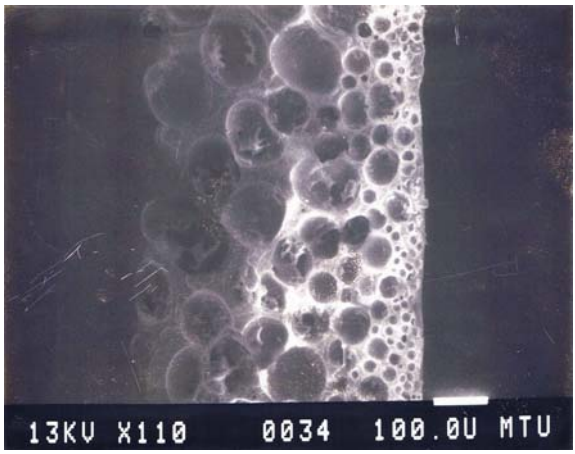

Fig. 1.4.35(b) SEM picture of a material similar to that in Fig. 1.4.33, except that it came from a different parent solution and at a quenching time of 70 min

For the polystyrene/cyclohexanol system, $R_{\alpha\beta} = 1.0$. This means that the polymer-rich domains will have to travel a "composition distance" that is equal to that of the solvent-rich domains in order to reach its binodal composition (symmetric case in Fig. 1.4.4). However, if the polymer composition asymmetry ratio is equal to about 2 (such as in Fig. 1.4.5), then half of the polymer-rich domains is believed to migrate to adjacent domains in order for the rest of the polymer-rich domains to continue to approach the binodal composition (Cahn, 1961). Since there is equal competition for polymer-rich material from every domain, then the position of the resulting holes (or cells) will be in a regular lattice position. Continued growth of structure should be based on the belief that the domains that are eaten up are those that are contiguous to the most number of polymer-rich domains. Also, as implied by the presence of distinct dominant frequencies for spinodal decomposition mechanism, the disappearance of contiguous polymer-rich domains should occur uniformly in space.

After the solvent-rich and polymer-rich domains attain binodal composition values, structure evolution is proposed to occur based on interfacial-tension-induced flow or hydrodynamic flow (Siggia, 1979). The driving force here is the differences in curvature in various locations in the interfacial boundaries. Since the migration of polymer molecules does not result in an increase in polymer concentration, the volume of the areas of migration should increase in the process. Ultimately, these areas of migration will have enough polymeric material to fill up open pores; thus, resulting in closed cell lattice structure. If this flow process evolves from a regular open cell structure, then we should expect the resulting closed cell structure to be regular as well. This is because areas of high and low curvature are regularly spaced as well. After these spherical closed cells are formed, further coarsening primarily takes place through wall rupture between the cells. Otherwise, walls that are not completely closed are good starting points for continued coarsening.

Wall rupture would have to be preceded by wall thinning. The following factors can be identified as contributing to wall thinning:

1. The cells observed in these membranes obviously have nonuniform curvature, i.e., the cells are not perfectly spherical. This nonuniform curvature leads to a flow process which results in the migration of material from cell walls to cell junctions.
2. The second factor contributing to wall thinning is based on the hypothesis of Castro (1981). This deals with the possibility that the polymer upon precipitation could still be swollen with some solvent. This solvent would slowly start diffusing out of the polymer causing the walls to thin.

The movement of material from cell wall to cell junctions is believed to occur due to perturbations of closed cell geometry from that of perfect sphere. Since the material inside the closed cells (solvent-rich material) has better wetting properties than that around the cells (polymer-rich material), these perturbations are unstable. The tendency of the system is to form larger spherical domains from the smaller solvent-rich spherical cells (as in the case of gas bubble coalescence in a liquid medium). Clearly, as a first step toward this process, closed cells would coalesce with one another; the smaller cells tending to coalesce with the bigger ones. During the removal of the solvent to form the solid product, the wall thinning and rupture processes continue to occur. The extent of this second mechanism depends on how efficient is the solvent removal process.

In the polystyrene/cyclohexanol system, the formation of closed cells from open cell network structure is not quite complete. Since some cells are in fact completely closed, it is reasonable to expect that the tendency is toward the formation of closed cells. In our systems, this process cannot be completed because of the coalescence of the cells to form larger ones. Once the larger cells are formed, smaller cells would tend to coalesce with the larger ones due to curvature differences between these cells. As the large cells become larger, there is more driving force for the smaller cells to coalesce with the larger cells compared to the driving force for the smaller cells to coalesce with the smaller ones. The result is the formation of macrovoids which are large closed cells. The formation of closed cells from open cells could still occur even if there is very little size difference between the cells. This is due to the fact that the driving force for the coalescence of cells also depends on the magnitude of the interfacial tension. It is possible that coalescence of smaller open cells into closed cells can effectively occur in systems with relatively large interfacial tensions. For these latter systems, it may even be possible to have hydrodynamic flow even though the polymer-rich domains have not yet reached their binodal compositions.

PMAA/MAA/water system.
Table 1.4.3 lists the specifications about each membrane prepared from the ternary PMAA/MAA/water system.

Table 1.4.3 Recipes and processing variables used in the preparation of membranes from the ternary PMAA/MAA/water system (Reproduced with permission from Saxena, 2001)

PMAA/MAA/ water composition	Phase separation temperature, T_{ps} (°C)	Phase separation time, t_{ps}	Drying time, t_d (h)	Smallest pore size (μm)	Comment (type of structure, etc.)
10%/3%/87%	75	30 s	40	1.5	Fibrous, interconnected network
10%/3%/87%	75	1 min	48	2	Fibrous, interconnected network
10%/3%/87%	80	30 s	50	1	Shallow open cells as well as interconnected network
10%/3%/87%	80	1 min	80	1.5	Shallow open cells as well as interconnected network
10%/3%/87%	80	1 min 30 s	80	2	Larger open cells that are interconnected by pores
10%/3%/87%	80	2 min	80	2	Larger open cells that are interconnected by pores
10%/3%/87%	80	2 min 30 s	80	2	Larger interconnected network of pores and deep cavities
10%/3%/87%	80	3 min	50	2	Three-dimensional, interconnected network of pores
10%/3%/87%	80	5 min	50	2	Three-dimensional, interconnected network of pores
7%/3%/90%	80	30 s	40	2	Open cells that are interconnected by pores
7%/3%/90%	80	1 min	40	3	Open cells that are interconnected by pores. Fibrous structure also visible
7%/3%/90%	80	1 min 30 s	40	2	Large interconnected network of pores
7%/3%/90%	80	2 min	40	1	Interconnected network of pores and deep cavities
7%/3%/90%	80	2 min 30 s	40	3	Three-dimensional interconnected network of pores
7%/3%/90%	80	3 min	40	4	Three-dimensional interconnected fibrous network with pores

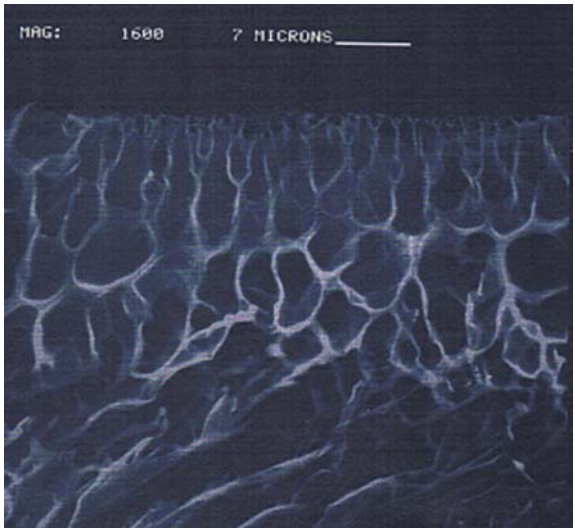

Fig. 1.4.36 Scanning electron micrograph of the pore structure of the PMAA membrane from a starting composition of 7%/3%/90% PMAA/MAA/water and quenched at 80ºC for 2 min (Reproduced with permission from Saxena, 2001)

Figure 1.4.36–1.4.38 shows SEM micrographs of the PMAA membranes formed via thermal inversion process starting with a 7%/3%/90% solution of PMAA/MAA/water at room temperature and quenched at 80°C. The micrographs show fibrous, interconnected network, with open pores, indicative of spinodal decomposition. As phase separation time increases to about 2 min, a cellular

Fig. 1.4.37 Scanning electron micrograph of the pore structure of the PMAA membrane from a starting composition of 7%/3%/90% PMAA/MAA/water and quenched at 80ºC for 2 min and 30 s (Reproduced with permission from Saxena, 2001)

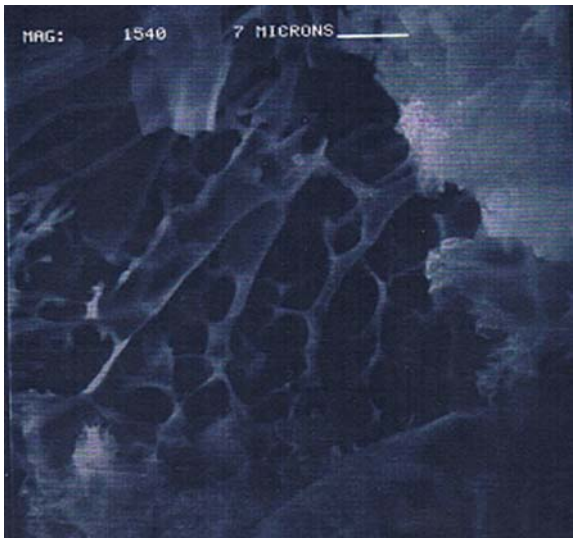

Fig. 1.4.38 Scanning electron micrograph of the pore structure of the PMAA membrane from a starting composition of 7%/3%/90% PMAA/MAA/water and quenched at 80ºC for 3 min (Reproduced with permission from Saxena, 2001)

structure consisting of pores is seen to evolve. Other membranes in Table 1.4.3 show similar micrographs and are presented elsewhere (Saxena, 2001).

The above data reveal a structure similar to those obtained from PS/cyclohexanol binary systems in Section PMAA/MAA/Water System. Network structures are generally larger in the ternary PMAA/MAA/water system, and the smallest structure or pore size obtained here is in the order of 1–2 μm. In further calculations, the interdomain distance of 1 μm was used as a result of this experimental study.

1.4.4 Determination of Phenomenological Diffusivities from Numerical and Experimental Data

Even with limited experimental data, it was possible to estimate all eight phenomenological coefficients needed to fully characterize spinodal decomposition of a nonreactive ternary PMAA/MAA/water system undergoing phase separation above the LCST. Out of the eight coefficients, it was possible to assume that regular solution applies for estimating all paired dimensionless gradient energy coefficients (β_{ij}) to be equal to $1/8\pi^2$, based on the work of Laxminarayan (Laxminarayan and Caneba, 1991). This is justifiable because all components that make up the ternary system are polar and hydrogen bonded. Simulations using the set of parameter values in Table 1.4.2 and accompanying frequency spectra as well as composition profile plots also indicate that numerical differences in gradient energy coefficients could result in similar behavior, as seen from the qt3, qt4, and qt6 cases.

In order to determine the remaining four phenomenological diffusivity parameters, four types of measurements were performed. One is the interdomain distance

of 1 μm during early-stage spinodal decomposition, which was obtained from morphological studies (Section 1.4.3.2). The other measurement is the induction time, which was matched between numerical simulation and time-resolved light scattering studies. The last type of measurement was a comparison between polymer-rich and polymer-lean compositions based on numerical simulation and the tie line from phase equilibria studies. For one particular case of a starting composition of 7 wt% PMAA, 3 wt% MAA, and 90 wt% water at 80ºC, a similar approach was done by Saxena (2001) using a factorial analysis, except that he assumed the first phenomenological diffusivity, D_{11}, to be equal to that of the equivalent binary PMAA/water system at the same temperature (Fig. 1.4.28). Note that subscript 1 corresponds to the PMAA and subscript 2 corresponds to MAA. Still, Saxena's approach only shifted all diffusivities proportionately by the ratio of induction times between numerical simulation and ternary light scattering experiments. This is justifiable since the experimental system and Saxena (2001) showed that induction times can be drastically reduced by higher initial composition perturbations. Timescales for numerical simulation were made to coincide with ternary light scattering experiments. Finally, the value of D_{22} (mutual diffusion coefficient of MAA and water) used by Saxena will be maintained, and it was estimated from the Wilke–Chang equation (Bird et al., 1960).

Based on Saxena's efforts (Saxena, 2001) and the adjustment on the timescales of phase separation to make numerical simulation data coincide with light scattering results, the following phenomenological diffusion coefficients for the ternary PMAA/MAA/water (7 wt%/3 wt%/90 wt%) system at 80ºC were obtained:

$$D_{11} = 1.306 \times 10^{-11}\text{cm}^2/\text{s}; \text{ or } \alpha_{11} = D_{11}/(-D_{11}) = 1 \text{ and } \beta_{11} = 1/8\pi^2$$
$$D_{12} = 4.18 \times 10^{-9}\text{cm}^2/\text{s}; \text{ or } \alpha_{12} = D_{12}/(-D_{11}) = 320.06 \text{ and } \beta_{12} = 1/8\pi^2$$
$$D_{21} = 1.121 \times 10^{-5}\text{cm}^2/\text{s}; \text{ or } \alpha_{12} = D_{21}/(-D_{11}) = 1.624 \times 10^{6} \text{ and } \beta_{21} = 1/8\pi^2$$
$$D_{22} = 3.35 \times 10^{-5}\text{cm}^2/\text{s}; \text{ or } \alpha_{22} = D_{22}/(-D_{11}) = 1.565 \times 10^{7} \text{ and } \beta_{22} = 1/8\pi^2$$

Predictions of these dimensionless parameters result in the following frequency spectra (Fig. 1.4.39) and composition profiles (Fig. 1.4.40).

Frequency spectra in Fig. 1.4.39 can be seen to be qualitatively the same as those of qt3 and qt4, and almost the same as that of qt6 (Table 1.4.2). This is expected since values of β_{ij} are all the same. However, composition profiles in Fig. 1.4.40 are more qualitatively the same as those of qt1, qt2, qt5, and qt7 due to the combination of phenomenological diffusion coefficients obtained from experimental data. They indicate higher concentrations of MAA in the polymer-rich phase domains, which should result in more polymerization reaction and enhanced coarsening from those domains in the corresponding reactive system.

Figure 1.4.40 also indicates that the interdomain distance during the early stages of spinodal decomposition is around 1 μm. Relevant binodal compositions for this system at the operating conditions were mentioned in Section 1.4.2.2.

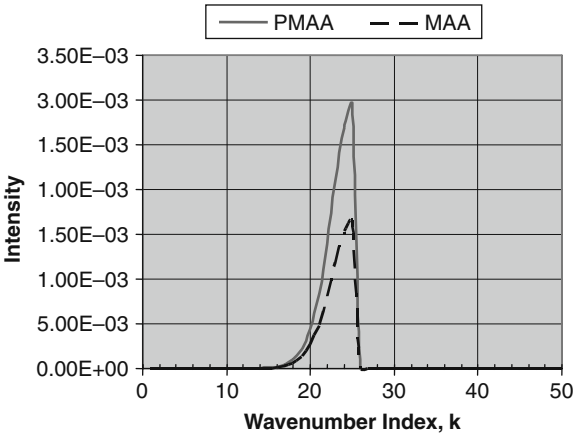

Fig. 1.4.39 Frequency spectra for the early-stage spinodal decomposition of the ternary PMAA/MAA/water (7 wt%/3 wt%/90 wt%) system at 80ºC, based on parameter values in Eq. (1.4.18) (Replotted with permission from Saxena, 2001)

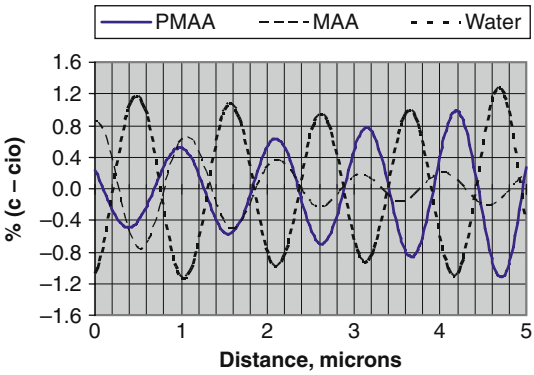

Fig. 1.4.40 Evolution of composition profiles for PMAA, MAA, and water in the early-stage spinodal decomposition of the ternary PMAA/MAA/water (7 wt%/3 wt%/90 wt%) system at 80°C, based on parameter values in Eq. (1.4.18) (Replotted with permission from Saxena, 2001)

1.4.5 Nomenclature

1.4.5.1 Alphabets

Upper Case

T – absolute temperature, K
D – mutual diffusion coefficient, cm^2/s
M – mobility coefficient, $cm^5/cal\ s$

Lower Case

c – polymer weight fraction, dimensionless
k – wave number index, dimensionless
t – time, s

1.4.5.2 Subscripts

o – overall
1, 2, 3, *i, j, k* – component label

1.4.5.3 Superscripts

‘,” – pertains to spinodal compositions
α, β – pertains to binodal compositions
o – overall

1.4.5.4 Greek Symbols

α – diffusivity ratio (Eq. 1.4.10), dimensionless
δ – defined in Eq. (1.4.10), dimensionless
κ – gradient energy coefficient, cal/cm
λ – wavelength of laser light, cm
η – dimensionless interdomain distance (Eq. 1.4.10)
θ – scattering angle in the medium
τ – dimensionless time (Eq. 1.4.7)

1.4.5.5 Other Symbols

f” – thermodynamic factor, cal/cm^3
T^* –absolute temperature of interest, K
ΔG_{M} – Gibbs free energy of mixing, cal/cm^3
λ_{m} – polymer interdomain distance, cm
∇ – Nabla operator
$Q_{\mathrm{SAL}}(t)$ – total integrated intensity of the scattered light vs time, dimensionless
$R(\bar{q}_m)$ – defined in Eq. (1.4.14)
$R_{\alpha\beta}$ – polymer composition asymmetry ratio (defined in Eq. 1.4.17)
$\bar{q}_m$ or $\mathbf{q}$ – wave number, cm^{-1}

1.5 Phase Separation Kinetics in Reactive Polymer Systems

In order to attempt to quantitatively analyze the kinetics of phase separation of the reactive ternary PMAA/MAA/water system, the derivation in the Appendix was initially used, starting with Eq. (A.1) up to Eq. (A.39). For the continuity equation, a more general form was used:

$$\frac{\partial c_k}{\partial t} = -\nabla J_k + q_k, \tag{1.5.1}$$

where q_k ($= q_k(\underline{r},t)$) is the reaction source term for the kth component. Upon substituting Eq. (A.5) into Eq. (1.5.1), we obtain the simultaneous partial differential equation governing the behavior of composition variation in an n-component system.

$$\frac{\partial c_k}{\partial t} = \sum_{i=1}^{n-1} \nabla \left[M_{ki} \nabla(\varphi_i - \varphi_n)\right] + q_k \qquad k = 1, \ldots, n-1. \tag{1.5.2}$$

Equation (1.5.2) describes early-stage as well as late-stage behaviors of a spinodal decomposition process in any coordinate system.

1.5.1 Derivation of the Spinodal Decomposition Equation with the Reaction Term

The system under consideration follows the free-radical chain polymerization, which has been mathematically derived in Section 1.3. From Eqs. (1.3.5) and (1.3.6), the resulting equation is

$$R_\mathrm{p} = -\frac{d[M]}{dt} = \left(\frac{f k_\mathrm{d} k_\mathrm{p}^2}{k_\mathrm{t}}\right)^{1/2} [I]^{1/2}[M] \tag{1.5.3}$$

or

$$-\frac{d[M]}{dt} = \boldsymbol{k}'[M], \tag{1.5.4}$$

where $\boldsymbol{k}$' is the overall first-order reaction rate coefficient given by

$$\boldsymbol{k}' = \left(\frac{f k_\mathrm{d} k_\mathrm{p}^2}{k_\mathrm{t}}\right)^{1/2} [I]^{1/2}. \tag{1.5.5}$$

Equation (1.5.4) has to be modified before it can be used with the spinodal decomposition equation derived in Section 1.4. Let us define $[S]$, $[M]$, and $[P]$ as concentrations in mol/cc of the solvent (water), monomer (MAA), and polymer (PMAA), respectively. Let, M_m, M_s, and M_p be the molecular weights and C_m, C_s, and C_p be the concentrations in g/cm^3 of the monomer, solvent, and the polymer, respectively. Then, by definition

$$C_\mathrm{m} = [M] \cdot M_\mathrm{m} \qquad C_\mathrm{s} = [S] \cdot M_\mathrm{s} \qquad C_\mathrm{p} = [P] \cdot M_p. \tag{1.5.6}$$

Let, c_m, c_s, and c_p be the weight fractions of monomer, solvent, and the polymer, respectively. Then, by definition

$$c_m = \frac{C_m}{C_m + C_s + C_p} \quad c_s = \frac{C_s}{C_m + C_s + C_p} \quad c_p = \frac{C_p}{C_m + C_s + C_p} \tag{1.5.7}$$

By combining Eqs. (1.5.4), (1.5.6), and (1.5.7), we get

$$-\frac{d}{dt}\left[\frac{(C_m + C_p + C_s)c_m}{M_m}\right] = \boldsymbol{k}'\frac{(C_m + C_p + C_s)c_m}{M_m}. \tag{1.5.8}$$

Since the molecular weight M_m of the monomer does not vary with time, Eq. (1.5.8) reduces to

$$\left[\frac{dC_m}{dt} + \frac{dC_p}{dt} + \frac{dC_s}{dt}\right]c_m + (C_m + C_p + C_s)\frac{dc_m}{dt} = -\boldsymbol{k}'(C_m + C_p + C_s)c_m. \tag{1.5.9}$$

The quantity $dC_s/dt = 0$ since the concentration of the solvent does not change, i.e., it is neither produced nor consumed. Also, we make the assumption that for a dilute system ($\geq$85% solvent) the overall density of the system does not change over time, i.e., the concentration in g/cm^3 of the polymer produced is the same as the amount in g/cm^3 of the monomer consumed. In that case

$$\frac{dC_m}{dt} + \frac{dC_p}{dt} = 0 \quad or \quad \frac{dC_m}{dt} = -\frac{dC_p}{dt} \tag{1.5.10}$$

Thus, Eq. (1.5.9) reduces to

$$\frac{dc_m}{dt} = -\boldsymbol{k}'c_m. \tag{1.5.11}$$

In general, Eq. (1.5.11) can be written as

$$\frac{\partial c_k}{\partial t} = -\psi_k^* c_k, \tag{1.5.12}$$

where ψ^*_k is zero for solvent, equal to $\boldsymbol{k}'$ for monomer, and normally equal to $-\boldsymbol{k}'$ for the polymer. Equation (1.5.12) can be converted into dimensionless form by using the definition of τ given in Eq. (1.4.10) and by defining

$$Da_k = \frac{\psi_k^* \lambda_m^2}{(-D_{11})}. \tag{1.5.13}$$

Here, Da_k is an overall dimensionless reaction rate coefficient for the k th component or the second Damkohler number of the k th component. Since, $u_k = c_k - c_k{}^o$, Eq. (1.5.12) reduces to the following dimensionless form:

$$\frac{\partial u_k}{\partial \tau} = -Da_k(u_k + c_k^o). \tag{1.5.14}$$

The reaction term can be combined with the phase separation diffusion equation resulting in an expression for the relevant reactive phase separation process. The spinodal decomposition expression that defines the FRRPP process for constant mobilities and diffusivities is given below

$$\frac{\partial u_k}{\partial \tau} = \sum_{j=1}^{n-1} (\alpha_{kj}\nabla^2 u_j - \delta_{kj}\nabla^4 u_j) - Da_k(u_k + c_k^o) \quad k = 1, \ldots, n-1. \tag{1.5.15}$$

The computer simulation of the phase separation part of Eq. (1.5.15) is discussed in the next section. It was solved in the Fourier or reciprocal space and then the inverse of the Fourier transform was applied to obtain the solution in the real space. The reaction part was solved in the real space using as initial condition the composition profile that was obtained at the beginning of the time step in the phase separation part. The reaction part was then solved at a full time step and composition profiles for the phase separation and reaction part were added. In order to solve the reaction part, an explicit Euler type of numerical scheme was adopted

$$u_k(\eta,\tau + \Delta\tau) = u_k(\eta,\tau) + \Delta\tau(-Da_k(u_k(\eta,\tau) + c_k^o)). \tag{1.5.16}$$

1.5.2 Numerical Simulation for Reactive Polymer Phase Separation Systems

Since that FRRPP process was developed as the sum of phase separation term and the reaction term, the phase separation term was solved through the methods presented in Section 1.4. The reaction part was derived in Section 1.5.1 and resulted in Eq. (1.5.14). Its closed form solution is given by

$$u_k + c_k^o = c_k^o \exp(-Da_k\tau). \tag{1.5.17}$$

For the experimental system extensively analyzed in Section 1.4, concentrations of 7 wt%/3 wt%/90 wt% were used for PMAA/MAA/water, respectively. However, for the FRRPP process, simulation was started with only MAA and water, at 10 wt% MAA ($c_2^o = 0.10$) in water ($c_3^o = 0.90$). The MAA polymerized to form of PMAA due to the decomposition of the initiator molecules. The final composition, assuming that all monomers reacted, was 10 wt% PMAA in water. Here, it was assumed that the specific gravity of MAA is almost equal to that of PMAA.

Figure 1.5.1 shows the graphical representation for the reaction term based on analytical solution described by Eq. (1.5.17). Several reaction rate coefficients ψ_1 were used. Note that $Da_3 = 0$ since it refers to water, which was neither produced nor removed from the system. Also, Da_1 was assumed to be zero due to the asymp-

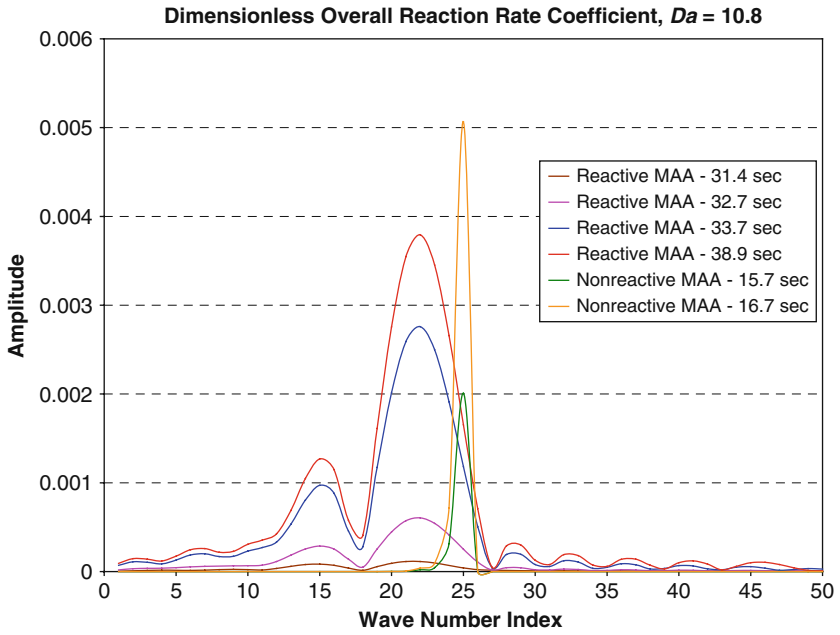

Fig. 1.5.1 MAA frequency spectra for the reactive phase separation of the ternary system starting with 10 wt% MAA and 90 wt% water at a dimensionless reaction rate coefficient $Da = Da_2 = 10.8$. Nonreactive data are included starting from a composition of 7 wt% PMAA, 3 wt% MAA, and 90 wt% water

totic polymer conversion levels for the FRRPP system after an initial fast rise in conversion. Equation (1.5.15) will be solved for different values of Da_2, i.e., the dimensionless reaction rate coefficient for the monomer, and this quantity will simply be called Da. In Section 1.4, the phase separation part of Eq. (1.5.1) was solved. The appropriate values for α_{kj} and δ_{kj} from Section 1.4 were obtained and used throughout this section.

The extent of percent completion, p_k, for the reaction process was defined as

$$p_k = 100\frac{u_k}{c_k^{\mathrm{o}}}. \tag{1.5.18}$$

Composition profiles for the FRRPP process, $u_{k_{\mathrm{total}}}$, were obtained as

$$u_{k_{\mathrm{total}}}(\vec{r},\tau) = u_{k_{\mathrm{phaseseparation}}}(\vec{r},\tau) + u_{k_{\mathrm{reaction}}}(\vec{r},\tau), \tag{1.5.19}$$

and was also written as

$$u_{k_{\mathrm{total}}}(\vec{r},\tau) = \sum_{k_1=1}^{n}\sum_{k_2=1}^{n}\left(B_{k,\vec{k}}\cos(\vec{\beta}\cdot\vec{r}) - C_{k,\vec{k}}\sin(\vec{\beta}\cdot\vec{r})\right). \tag{1.5.20}$$

Implementation of the calculations involving Eqs. (1.5.16)–(1.5.20) was not straightforward, because during microstructural (microscopic) development of the composition profile, overall compositions were also changing. Thus, a macroscopic calculation was also performed to determine overall compositions with time. In turn, results of the macroscopic calculation at every time step were used in the microscopic calculation in the subsequent time step. It was evident that at time $t = 0$ when the system has 10 wt% MAA and 90 wt% water, the computational procedure starts with the macroscopic calculation, because the system was not phase separated yet. As soon as the system acquired a composition that places it inside the spinodal curve, the microscopic calculation is ran alongside the ongoing macroscopic calculation method. Details of these two methods are presented below.

1.5.2.1 Microscopic Calculation

The diagram below shows one iteration for the technique used to solve for the FRRPP process:

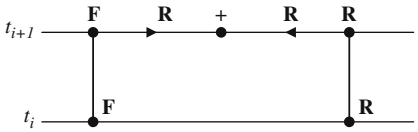

The phase separation part was solved in the Fourier space (F), and the reaction part was solved in the real space (R). At time t_i, the concentration profile for the phase separation part is available both in the reciprocal space and in the real space. The reaction part was incremented to time t_{i+1} using for the initial condition the real space concentration profile. The phase separation part was also incremented to time t_{i+1} in the Fourier space and then converted into the real space by applying the inverse of the Fourier transform. The two concentration profiles were then added in the real space. This constitutes one iteration for the time step. The summed up concentration profile is again converted into the Fourier space, and the two concentration profiles then become input for the next iteration.

1.5.2.2 Macroscopic Calculation

It was assumed that the diffusivity values obtained for the 7%/3%/90% PMAA/MAA/water system were applicable over the entire concentration range, i.e., from monomer concentration of 10 wt% to zero. The diagram below shows one iteration for the technique used to solve for the FRRPP process:

The phase separation part was solved in the Fourier space (F) and the reaction part in the real space for equal time step. The initial conditions for each step were different as shown in the above diagram. At the end of the time step, the two concentration profiles were added to obtain overall concentration. Prior to the next time step, however, in order to conserve mass, the amount of the monomer concentration that had depleted due to the reaction process (R–ΔR) was subtracted from the phase separation part.

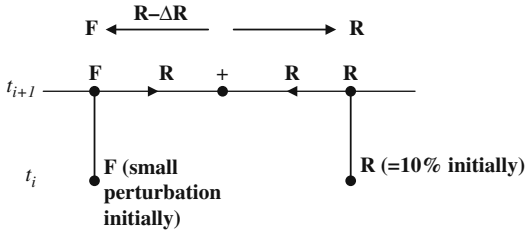

1.5.3 Results and Discussion

Figures 1.5.1–1.5.3 show component frequency spectra for the reactive phase separation of the ternary system starting with 10 wt% MAA and 90 wt% water at a dimensionless reaction rate coefficient for the monomer, $Da = 10.8$. For comparison, the nonreactive phase separation simulation result is also shown in the figures.

It is evident from these figures that coarsening occurs even at the early stages of spinodal decomposition in the reactive system. Figure 1.5.4 shows their corresponding composition profiles at indicated phase separation time values.

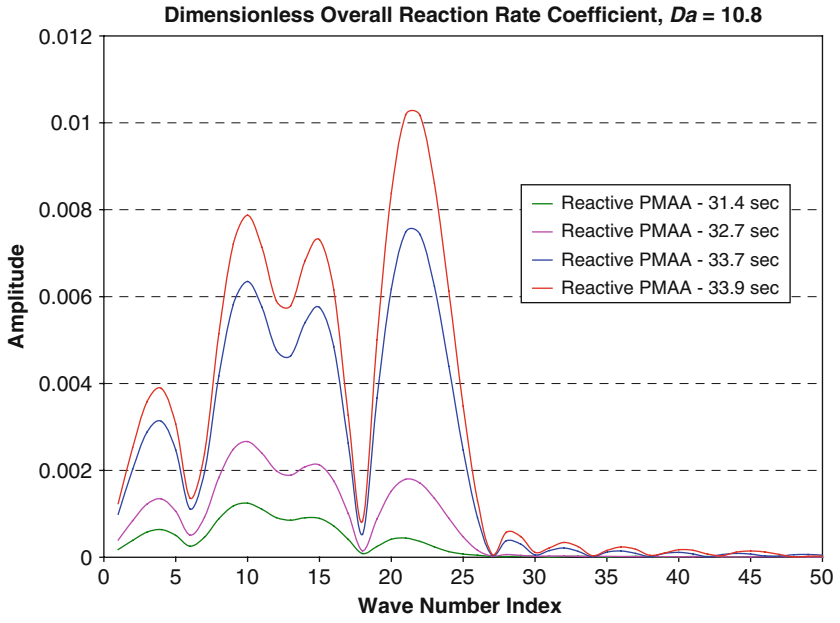

Fig. 1.5.2 PMAA frequency spectra for the reactive phase separation of the ternary system starting with 10 wt% MAA and 90 wt% water at a dimensionless reaction rate coefficient $Da = Da_2 = 10.8$

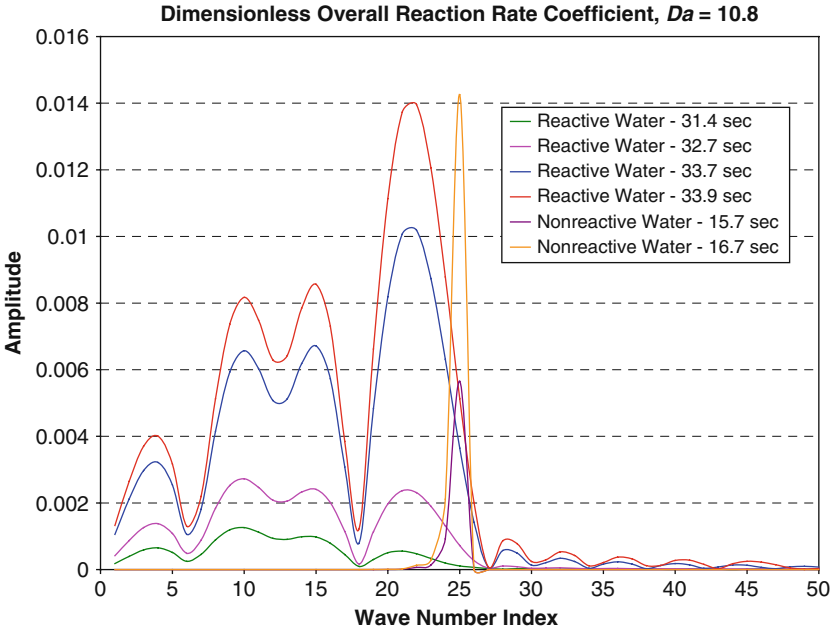

Fig. 1.5.3 Water frequency spectra for the reactive and nonreactive phase separation of the ternary system starting with 10 wt% MAA and 90 wt% water at a dimensionless reaction rate coefficient $Da = Da_2 = 10.8$

Disappearance of polymer-rich domains is beginning to be seen from the figure even at the early stages of the phase separation of the reactive system, although there is no evidence of this happening with MAA and water in the reactive system.

It should therefore be no surprise that the reactive phase separation system would exhibit advanced coarsening even at the equivalent early stages of phase separation in nonreactive analog systems.

1.5.4 Nomenclature

1.5.4.1 Alphabets

Upper Case

C – concentration in g/cm^3
D – mutual diffusion coefficient, cm^2/s
J – diffusion flux used in Eq. (1.5.1), cm^2/s
M – mobility coefficient, cm^5/cal s

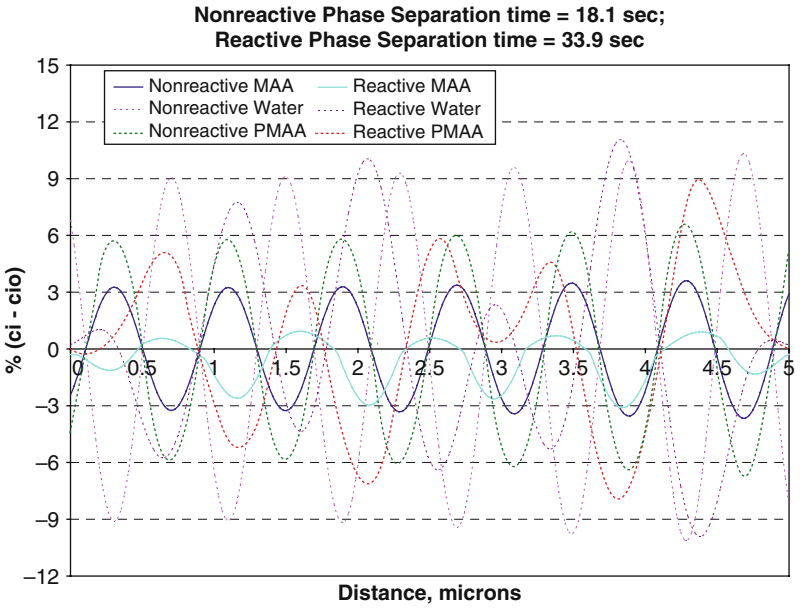

Fig. 1.5.4 Composition profiles representing frequency data from Figs. 1.4.1–1.4.3

Lower Case

c – weight fraction, dimensionless
f – initiator efficiency coefficient ($0 < f < 1$)
P – percent completion of development of composition profile
q – mass source term, 1/s
t – time, s
u – weight fraction at any time and position minus overall weight fraction, dimensionless

1.5.4.2 Subscripts

1, 2, 3, i, j, k – component label
n – total number of components
m – monomer
p – polymer
s – solvent

1.5.4.3 Superscripts

o – overall

1.5.4.4 Greek Symbols

ϕ – thermodynamic potential associated with mass transfer, defined in Eq. (1.5.2)
τ – dimensionless time
α – diffusivity ratio (Eq. 1.4.10), dimensionless
δ – defined
η – dimensionless interdomain distance (Eq. 1.4.10)

1.5.4.5 Other Symbols

$\vec{\beta}$ – wave number vector, cm^{-1}
Da – Damkohler number, dimensionless
$[I]$ – concentration of initiator, mol/l
k_d – initiator decomposition rate coefficient, s^{-1}
k_t – termination rate coefficient, mol/l s
k_p – propagation rate coefficient, l/mol s
k' – effective polymerization rate coefficient (defined in Eq. 1.5.4), s^{-1}
λ_m – polymer interdomain distance, cm
M_m – molecular weight of monomer, g/mol
M_p – molecular weight of polymer, g/mol
M_s – molecular weight of solvent, g/mol
$[M]$ – concentration of monomer, mol/l
R_p – propagation rate, mol/l s
$\vec{r}$ – generalized spatial variable, cm
Ψ^* – defined in Eq. (1.5.12), s^{-1}

References

Achilias, D. S., and Kiparissides, C., 1992. *Macromolecules, 25*, 3739–3750.
Aggarwal, A., 1993. M.S. Thesis, Michigan Technological University.
Altena, F. W., and Smolders, C. A., 1982. *Macromolecules, 15*, 1491–1497.
Anolick, C., and Goffinet, J. S., 1966. U.S. Patent No. 3,553,156.
Barrer, R. M., 1957. *J. Phys. Chem., 61*, 178.
Bird, R. B., Stewart, W. E., and Lightfoot, E. N., 1960. Transport Phenomena, John Wiley and Sons, New York, p. 350.
Bird, R. B., Stewart, W. E., and Lightfoot, E. N., 2007. Transport Phenomena, 2nd Ed., John Wiley and Sons, New York.
Boom, R. M., Van den Boomgaard, Th., and Smolders, C. A., 1994. *Macromolecules, 27*, 2034–2040.
Bueche, F., 1953. *J. Chem. Phys., 21*, 1850.
Cahn, J. W., 1956. *Acta Metall., 4*, 449.
Cahn, J. W., 1957. *Acta Metall., 5*, 169.

Cahn, J. W., 1961. *Acta Metall., 9*, 795.
Cahn, J. W., and Hilliard, J. E., 1958. *J. Chem. Phys., 28*, 258.
Cahn, J. W., and Hilliard, J. E., 1959. *J. Chem. Phys., 31*, 688.
Caneba, G. T., 1992a. *Adv. Polym. Technol., 11*, 277.
Caneba, G. T., 1992b. U.S. Patent No. 5,173,551, December 22.
Caneba, G. T., and Saxena, R., 1992. *Proceedings of the A.I.Ch.E. Annual Meeting*, Miami, FL, November 1–6.
Caneba, G. T., and Saxena, R., 1996. *Polym. Eng. Sci.*, *55*, 753.
Caneba, G. T., and Shi, L., 2002. "Lower critical solution temperature of polymer-small molecule systems: a review", in: Phase Separation in Polymer Solutions and Blends, P. K. Chan (Ed.), *Research Signpost*, ISBN #81-7736-097-3, Chapter 4, pp. 63–104.
Caneba, G. T., and Soong, D. S., 1985a. *Macromolecules, 18*, 2538.
Caneba, G. T., and Soong, D. S., 1985b. *Macromolecules, 18*, 2545.
Caneba, G. T., Xu, Z., and Dar, Y. L., 2009. *J. Appl. Polym. Sci. 113*, 3872–3882.
Carbaugh, D. C., 1991. Presented at the Engineering Foundation Conference in Polymer Reaction Engineering, Santa Barbara, CA, March 10–15.
Carslaw, H. S., and Jaeger, J. C., 1959. Conduction of Heat in Solids, Oxford University Press, London.
Casassa, E. F., and Berry, G. C., 1989. "Polymer solution", in: Comprehensive Polymer Science, G. Allen et al. (Ed.), Elsevier Science Inc., USA, Vol. 2, Chapter 3, pp. 105–106.
Castro, A. J., 1981. U.S. Patent No. 4,247,498, January 27.
Charlet, G., and Delmas, G., 1981. *Polymer, 22*, 1181–1189.
Chen, Y.- L., Solc, K., and Caneba, G. T., 1993. *Polym. Eng. Sci., 33*, 1033–1041.
Cohen, M. H., and Turnbull, J., 1959. *J. Chem. Phys*., *31*, 1164.
Condo, P. D., and Radosz, M., 1996. *Fluid Phase Equilib., 117*, 1–10.
Coriell, S. R., and Sekerka, R. F., 1983. *J. Crystal Growth*, *61*, 499.
Crank, J., 1970. Mathematics of Diffusion, Oxford University Press, London.
Crank, J., and Park, G. S., 1968. Diffusion in Polymers, Academic Press, New York.
De Fontaine, D., 1975. "Phase changes", in: Treatise on Solid State Chemistry, N. B. Hannay (Ed.), Plenum Press, New York, Vol. 5, pp. 129–178.
DiBenedetto, A. T., 1963. *J. Polym. Sci., A1*, 3459, 3477.
DiBenedetto, A. T., and Paul, D. R., 1964. *J. Polym. Sci., 2*, 1001.
Doolittle, A. K., 1951. *J. Appl. Phys*., *22*, 1471.
Doolittle, A. K., 1952. *J. Appl. Phys., 23*, 236.
Duda, J. S., and Vrentas, J. L., 1971. *AIChE J.*, *March*, 464.
Eliassaf, J., and Silberberg, A., 1962. *Polymer (London), 1962*(3), 555–564.
Feke, G. T., and Prins, W., 1974. *Macromolecules*, *7*, 527.
Fitts, D. D., 1962. Nonequilibrium Thermodynamics, McGraw-Hill, New York, Chapter 8.
Flory, P. J., 1942. *J. Chem. Phys., 10,* 51–61.
Flory, P. J., 1970. *Disc. Faraday Soc., 49,* 7–29.
Fox, T. G., 1956. *Bull. Am. Phys. Soc., 1*, 123.
Fredenslund, Aa., Gmeling, G., and Rasmussen, 1977. Vapor-Liquid Equilibria using UNIFAC, Elsevier, Amsterdam.
Freeman, P. I., and Rowlinson J. S., 1960. *Polymer, 1*, 20.
Frisch, H. L., 1980. *Polym. Eng. Sci., 20*, 2.
Fujita, H., 1961. *Fortschr. Hochpolym. Forsch., 3*, 1.
Fujita, H., and Kishimoto, A., 1961. *J. Chem. Phys., 34*, 393.
Geankoplis, G. J., 2003. Transport Processes and Separation Process Principles, 4th ed., Prentice-Hall, New Jersey, pp. 34–234.
Glasstone, S., Laidler, K. J., and Eyring, H., 1941. Theory of Rate Processes, McGraw-Hill, New York.
Guggenheim, E. A., 1952. Mixtures, Oxford University Press, Oxford.
Guo, H.-F., Laxminarayan, A., Caneba, G. T., and Solc, K., 1995. *J. Appl. Polym. Sci., 55*, 753–759.

Hashimoto, T., Kumaki, J., and Kawai, H., 1983. *Macromolecules, 16*, 641.
Hashimoto, T., Susaki, K., and Kawai, H., 1984. *Macromolecules, 17*, 2812.
Hashimoto, T., Takenaka, M., and Izumitani, T., 1989. *Polymer Commun., 30*, 45.
Hiatt, W. C. 1985. Materials Science of Synthetic Membranes, D. R. Lloyd (Ed.), *ACS Symp. Ser.* No. 269, pp. 229–244.
Hiatt, W. C., Vitzthum, C. H., and Wagener, K. B. 1984. *Polym. Mater.*, *50*, 161.
High, M. S., and Dinner, R. P., 1990. *A.I.Ch.E. J., 36*(11), 1625–1632.
Hillert, M., 1961. *Acta Met.*, *9*, 525, 179.
Hopfenberg, H. B., and Frisch, H. L., 1969. *J. Polym. Sci.*, *B7*, 405.
Huggins, M. L.,1942. *Ann. NY. Acad. Sci*., *43*, 431–443.
Inaba, N., Sato, K., Suzuki, S., and Hashimoto, T., 1986. *Macromolecules, 19*, 1690.
Irani, C. A., 1986. *J. Appl. Polym. Sci*., *31*, 1879–1899.
Irani, C. A., Cozewith, C., and Kasegrande, S., 1980. U.S. Patent No. 4,319,021.
Izumitani, T., and Hashimoto, T., 1985. *J. Chem. Phys., 83(7)*, 1.
Kanig, G., 1963. *Kolloid-Z., 190*, 1.
Kelley, F. N., and Bueche, J., 1961. *J. Polym. Sci.*, *50*, 549.
Kesting, R. E., 1971. Synthetic Polymeric Membranes, McGraw-Hill Book Co., New York.
Koningsveld, R., 1968a. *J. Polym. Sci*., Part A-2*, 6*, 305–323.
Koningsveld, R., 1968b. *J. Polym. Sci*., Part A-2*, 6*, 325–347.
Kumaki, J., and Hashimoto, T., 1986. *Macromolecules, 19*, 763.
Kumar, S. K., 1986. D. Sc. Thesis, Massachusetts Institute of Technology, MA.
Kumins, C. A., and Roteman, J., 1961. *J. Polym. Sci*., *55*, 663–699.
Laxminarayan, A., and Caneba, G. T., 1991. *Polym. Eng. Sci.*, *31*, p.1597.
Lifshitz, I. M., and Slyozov, V. V., 1961. *J. Phys. Chem. Solids, 19*, 35.
Liu, H., and Zhong, C., 2005. *Ind. Eng. Chem. Res., 444*, 634–638.
Louie, B. M., 1984. M.S. Thesis, University of California-Berkeley, CA.
Mahabadi, H. K., and O'Driscoll, K. F., 1977a. *J. Polym Sci.: Polym. Chem. Ed., 15*, 283.
Mahabadi, H. K., and O'Driscoll, K. 1977b. *J. Macromol. Sci.–Chem., AII(5)*, 967.
McHugh, M. A., and Guckes, T. L.**,** 1985. *Macromolecules, 18*, 674.
McMaster, L. P., 1975, *Adv. Chem. Ser.*, No. 142, N. A. Platzer (Ed.), pp. 43–65.
Middleman, S., 1977. Fundamentals of Polymer Processing, McGraw-Hill Book Co., New York, p. 360.
Molyneux, P., 1984. Water - Soluble Synthetic Polymers: Properties and Behavior, CRC Press, Inc., Boca Raton, Vol. 1, pp. 92–95.
Morral, J. E., and Cahn, J. W., 1971. *Acta Met., 19*, 1037.
Nojima, S., Tsutsumi, K., and Nose, T., 1982. *Polym. J., 14*, 225.
Nojima, S., Ohyama, Y., Yamaguchi, M., and Nose, T., 1982. *Polym. J., 14*, 907.
North, A. M., 1974. "The influence of chain structure on the free radical termination reaction". in: "Reactivity, Mechanism and Structure in Polymer Chemistry," A.D. Jenkins and A. Ledwith (Eds.), Wiley-Interscience, New York.
Nose, T., 1987. *Phase Transitions, 8*, 245.
Odian, G., 1991. Principles of Polymerization, John Wiley and Sons, New York.
Oh, J., and Rey, A. D., 2002. "Computer simulation of functional polymeric materials formation via polymerization-induced phase separation under a temperature gradient", in: Phase Separation in Polymer Solutions and Blends, P. K. Chan (Ed.), Research Signpost, Trivandrum, India.
Panayiotou, C., and Vera, J. H., 1982. *Polym. J., 14*, 681–694.
Patterson, D., 1969. *Macromolecules, 2*(6), 672–677.
Patterson, D., 1982. *Polym. Eng. Sci., 22*(2), 64–73.
Patterson, D., and Delmas, G., 1970. *Disc. Faraday Soc., 49*, 98–105.
Patterson, D., Delas, G., and Somcynsky, T., 1967. *Polymer, 8,* 503–516.
Porter, M. C. 1982. Harnessing Theory Pract. Appl., World Filtr. Congr., 3rd Ed., Vol. II, p. 451.
Prausnitz, J. M., Lichtenthaler, R. N., and Azevedo, E. G. D., 1986. Molecular Thermodynamics of Fluid Phase Equilibria, Prentice-Hall, Englewood Cliffs, NJ.

Prausnitz, J. M., Lichtenthaler, R. N., and Azevedo, E. G. D., 1999. Molecular Thermodynamics of Fluid Phase Equilibria, 3rd ed., Prentice-Hall, Englewood Cliffs, NJ.
Prigogine, I., 1957. The Molecular Theory of Solutions, North Holland Publishing Co., Amsterdam.
Rasmussen, D. H., 1982. *J. Crystal Growth, 56*, 45.
Rasmussen, D. H., Sivaramakrishnan, M., and Leedom, G. L., 1982. *A.I.Ch.E. Symp. Ser.,* Crystallization Process Engineering, 1.
Rehage, G., Ernst, O., and Fuhrmann, J., 1970. *Disc. Faraday Soc., 49*, 208.
Rodriguez, F., Cohen, C., Ober, C., and Archer, L. A., 2003. Principles of Polymer Systems, Taylor and Francis, New York, p. 178.
Rogers, C. E., 1965. Physics and Chemistry of the Organic Solid State, D. Fox, M. M. Labes, and A. Weissberger (Eds.), Interscience, New York, Chapter 6, Vol. 2.
Rogers, C. E., and Machin, D., 1972. CRC Critical Reviews in Macromolecular Science, *April*, 245.
Saeki, S., Kuwahara, N., Konno, S., and Kaneko, M., 1973. *Macromolecules, 6*(2), 247–51.
Sanchez, I. C., 1979. *Macromolecules, 12*(5), 980–988.
Sanchez, I. C., and Lacombe, R. H., 1976. *J. Phys. Chem., 80*(21), 2352–2362.
Sanchez, I. C., and Lacombe, R. H., 1978. *Macromolecules, 11*(6), 1145–1156.
Sanchez, I. C., and Panayiotou, C. G., 1993. "Equations of state thermodynamics of polymer and related solutions", in: Models for Thermodynamics and Phase Equilibria Calculations, Chapter 3, S. I. Sandler (Ed.), Marcel Dekker, Inc., New York, pp. 187–286.
Sasaki, K., and Hashimoto, T., 1984. *Macromolecules, 17*, 2818.
Saxena, R., 1991. M.S. Thesis, Michigan Technological University.
Saxena, R., 2001. Ph.D. Dissertation, Michigan Technological University.
Schmidt, A. D., and Ray, W. H., 1981. *Chem. Eng. Sci., 36*, 1401–1410.
Schmidt, A. D., Clinch, A. B., and Ray, W. H., 1984. *Chem. Eng. Sci., 39*, 419–432.
Seidell, A., and Linke, W. F., 1952. Solubilities of Inorganic and Organic Compounds, Supplement to the Third Edition, D. Van Nostrand Co. Inc., New York, pp. 578–673.
Shewmon, P. G., 1969. Transformations in Metals, McGraw-Hill, New York.
Shi, L., 1997. M.S. Thesis, Michigan Technological University.
Shultz, A. R., and Flory, P. J. 1953. *J. Am. Chem. Soc., 75*, 3888.
Siggia, E. D. 1979. *Phys. Rev., A20*, 595.
Siow, K. S., Delmas, G., and Patterson, D., 1972. *Macromolecules, 5,* 29.
Snyder, H. L., and Meakin, P., 1985. *J. Polym. Sci. Polym. Symp., 73*, 217.
Snyder, H. L., Meakin, P., and Reich, S., 1983. *Macromolecules, 16*, 757.
Somcynsky, T., 1982. *Polym. Eng. Sci., 22*(2), 58–63.
Teymour, F., 2004. *AICHE Journal, 43*, 145–156.
Van Aartsen, J. J., 1970. *Eur. Polym. J., 6*, 919.
Vasenin, R. M., 1960. *Vysokomol. Seodin., 2*, 861.
Voight-Martin, I. G., Leister, K. H., Rosenau, R., and Koningsveld, R. 1986. *J. Polym. Sci. B: Polym. Phys., 24*, 723.
Vrentas, J. S., and J. L. Duda, 1977. *J. Polym. Sci.: Polym Phys. Ed.*, *15*, 417–439.
Vrentas, J. S., and Duda, J. L., 1982. *A.I.Ch.E. J., 28*, 229.
Wang, B., 1997. Ph.D. Dissertation, Michigan Technological University.
Wang, B., Dar, Y., Shi, L., and Caneba, G. T., 1999. *J. Appl. Polym. Sci., 71*, 761.
Wilkens, J. B., 1957. Ph.D. Thesis, Cornell University.
Wilkens, J. B., and Long, F. A., 1957. *Trans. Faraday Soc.*, *53*, 1146.

Chapter 2
The FRRPP Concept

From a first impression, the concept behind the FRRPP process is nothing special compared to polymerization-induced phase separation processes (PIPS) (Oh and Rey, 2002), wherein polymer formation induces conventional phase separation at temperatures below the upper critical solution temperature (UCST). What people fail to take into account are the effects of the polymerization reaction exotherm (heat generation) in the accompanying phase separation process. It is noted from Section 1.3 that adiabatic temperature rises from free-radical chain polymerizations are in the order of hundreds of degrees Celsius. Also, from Section 1.1, it is noted that at these temperature rises, polymer-small molecule mixtures can shift from a true solution to a phase separated system above the lower critical solution temperature (LCST). Based on the discussion in using Eqs. (1.2.9–1.2.14), we note that high-temperature domains dissipate heat faster as they become smaller, unless the mechanism of heat dissipation becomes inherently inefficient, such as conduction through gases or heat transfer via radiation.

Just like a lot of other discoveries, the technological/applied aspects of the FRRPP process were developed before its science. In the age of template-based polymerizations and chemistries that produce relatively clean products, the FRRPP process has been seen to lack a high level of intellectual appeal. It does not help that its conceptual underpinnings are derived from a number of mature fields, such as free-radical polymerization and statistical copolymerization, exothermic chain polymerization, liquid–liquid phase equilibria of polymer solutions, conventional transport processes, and phase transition kinetics. This monograph aims to establish the unique nature of the FRRPP process and attempts to advance its conceptual basis. The author believes that with its understanding, one will be able to use the concept in the formation of new products and in controlling runaway energetic systems, in order to harness these high energy density sources.

2.1 Connection to Nanotechnology

The field of nanotechnology has captured the imagination of scientists, engineers, and policy makers, as a means of obtaining biology-based organization and self-assembly in application areas that are relevant to current and future technologies.

G. Caneba, in: *Free-Radical Retrograde-Precipitation Polymerization (FRRPP)*,
Chapter DOI 10.1007/978-3-642-03025-3_2,

It pertains to operations that occur in the 100-nm scale or below and also invoked possibilities of current micromachines and even macroscopic devices that are somehow reduced to this size scale. To scientists and engineers who have been doing research in heterogeneous catalysis, high surface area-per-volume sorbents, and macromolecular chemists, reality has been far from perception, because these earliest practitioners of nanotechnology were hardly able to overcome the statistical behavior of molecules and macromolecules at that level. This was vividly pointed out by the late Nobel Laureate Richard Smalley (CENEAR, Vol. 81, No. 48, Dec. 1, 2003, pp. 37-42), who correctly asserted that there are no set of fingers with enough dexterity that can assemble nanoscale machines; thus, originated the term "Smalley's fingers." Still, the emphasis in nanotechnology research has been most welcome, because of the various theoretical and experimental techniques that are being discovered to be useful in these conventional nanotechnology fields. As new types of nanoscale materials are being discovered, such as fullerenes, carbon nanotubes, nanogold, nanofibers, DNA structures, quantum dots, nanotechnology research has been mostly involved in the determination of the properties of these nanomaterials. Very little research is being done in reaction and even transport processes in the nanoscale. If ever, what is becoming apparent is that the usual continuum mechanics-based analysis of material interactions with its environment is no longer applicable in nanoscale processes. There is now the need to address the analysis of nanoscale processes using molecular and even quantum mechanical-based concepts. This need is heightened by discoveries of contrary types of behavior in nanoscale processes, such as reduced pressure drops of gas flow through nanofiber beds, compared to microfiber beds.

Based on a variety of experimental results, it seems that the FRRPP process is one of those nanoscale processes that involve transport and chemical reaction processes. Even though the analysis of the FRRPP process is still based on continuum concepts, at least it is now possible to show that it is a nanotechnology, if not, a nanoscience system, as discussed below.

2.1.1 Formation of Reactive Polymer Nanoparticles

With the discovery of the FRRPP of methacrylic acid (MAA) in water at temperatures below the boiling point of the mixture, it has become possible to carry out in situ polymerization experiments in glass and quartz containers. Small-angle X-ray scattering (SAXS) experiments using the synchrotron X-ray source of the MAA/water reactive system (Fig. 2.1.1) showed persistence of Gaussian coil nanoscale domains (Tirumala et al., 2003a,b,c).

Table 2.1.1 shows radii of gyration of poly(methacrylic acid) in reactive FRRPP PMAA/MAA/water systems that are in the nanometer scale. Based on the phase diagram for PMAA/water system (Fig. 1.1.5), the experimental reactive system at 60°C barely makes it above the LCST, and yet the domain sizes are still relatively small. It seems that the polymer domains at 80°C have been into coarsening

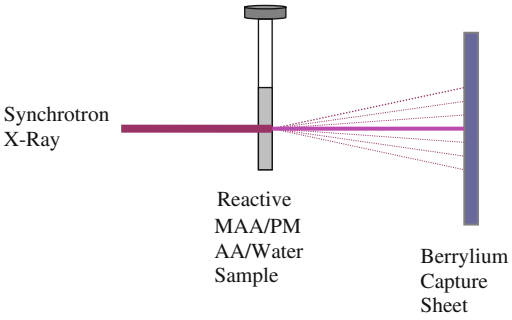

Fig. 2.1.1 Diagram depicting the synchrotron X-ray scattering system. When the polarized synchrotron X-ray beam passes through the sample, it interacts with the material and scattered X-rays are captured into a Beryllium sheet detector. The scattering pattern is analyzed to fit into various geometric models of nanometer and micrometer structures

behavior rather quickly, if it were nonreactive. However, this is likely due to the fact that even within these nanosized domains, polymer chains are being produced because of the presence of monomer and initiator molecules. The persistence of these nanosized domains seems to be unique with the FRRPP process, because reactive conventional-precipitation analogs did not show such behavior; the polymer material formed large domains that easily settled to the bottom of the container. This advanced coarsening effect for conventional reactive precipitation polymerization was predicted by simulation studies shown in Section 1.5. With the FRRPP system, there is some visible settling of agglomerated domains, but at a much longer time (30 min or more).

Comparing radii of gyration with conversion data, the relatively high conversion at 60°C and lower molecular sizes mean that more of the polymer settled to the bottom of the vessel. The opposite was observed for conversion and molecular size data at 80°C. Even the prereacted sample resulted in progressively lowering

Table 2.1.1 Radius of gyration, R_g, obtained from the SAXS data fits for the different FRRPP systems. Starting formulation is at 0.06 g/12 g/120 g V-50/MAA/water ratio. Conversion values are indicated in parenthesis (Data taken with permission from Tirumala et al., 2003)

	R_g (% conversion)		
System	1.5 min	15 min	30 min
Methacrylic acid/water system, reacting @ 60°C	6 nm	5 nm (50%)	5 nm (58%)
Methacrylic acid/water system, reacting @ 80°C	11 nm	13 nm (17%)	12 nm (32%)
Methacrylic acid/water system, prereacted for 15 min @ 60°C and continued reacting @ 80ºC	13 nm	10 nm	10 nm

values of molecular sizes with time after resumption of the polymerization reaction. It should also be no surprise that for the 80°C system, molecular sizes did not really go down until after around 30 min of reaction. It just took that long for the system to start showing polymer settling at the bottom of the glass cell container. Since at this temperature the system would be at least in the semi-dilute regime if it were in solution, persistence of nanoscale domains in the fluid is not a natural consequence of macromolecular isolation due to dilution.

Subsequently, a more direct verification of formation of persistent nanoscale domains was done by running the FRRPP of MAA/water in a quiescent fluid, and then doing a morphological analysis of the product polymer material from liquid samples that were "frozen" to preserve the polymer structure from the liquid before drying. The result is a picture from the atomic force micrograph (AFM) of nanoparticles from a polystyrene/ether reactive FRRPP system, shown in Fig. 2.1.2.

Nanoparticles have also been obtained and viewed with an AFM from other FRRPP recipes (Tirumala et al., 2003a,b,c; 2004, 2005a,b), such as

1. Polystyrene crosslinked with ethylene glycol dimethacrylate (EGDMA) in ether.
2. Polystyrene that is polymerized in *t*-butyl acetate/water (TBA/water).
3. Poly(*N*-isopropyl acrylamide) (PNIPAM) in water.

Similar nanoscale particles were obtained in these systems as those in above-mentioned PMAA and PS systems.

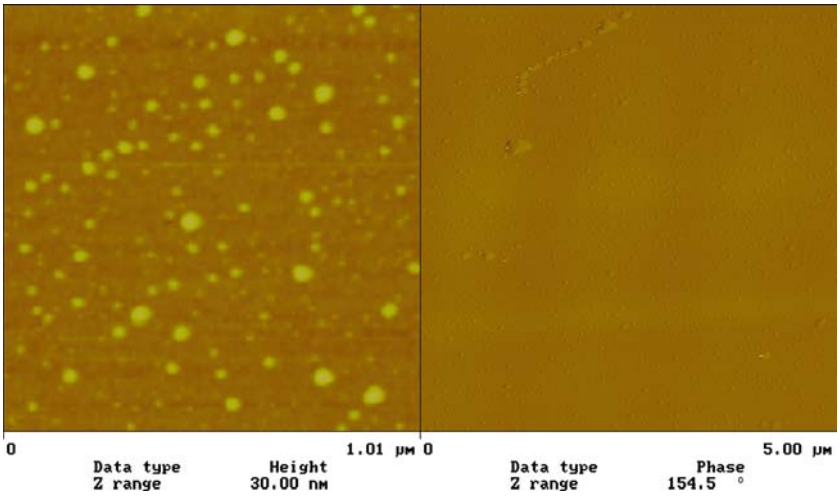

Fig. 2.1.2 AFM image of styrene nanoparticles polymerized in ether and deposited onto an aluminum pan. The *left pane* shows the particles in a height mode, while the *right pane* is the amplitude phase image of the surface (V.R. Tirumala personal communication)

2.1.2 Agglomeration of Nanoparticles in a Stirred Vessel

In a continuously stirred vessel, it should be obvious that nanoscale particulates would be agglomerating into larger ones. What is unique about the FRRPP process is that mixed fluid systems ended up to be very manageable dispersions up to the effective glass transition temperature. This has been validated in all of the FRRPP formulations that were tried in a mixed-vessel system. In contrast, conventional-precipitation polymerization formulations of the same monomer % charge at the same operating temperature and pressure have produced relatively large agglomerates that even resulted in polymer materials in the same size scale as the reactor.

In the 0.6 g/12 g/120 g V-50/MAA/PMAA FRRPP system at 80°C, the following sampling procedure was used by Dar (1999):

(1) Samples were drawn from the reactor into a cold (liquid nitrogen temperature) tube using a vacuum apparatus. The tube was immediately immersed in liquid nitrogen to freeze the sample solid.
(2) The samples taken were stored in a freezer at temperatures below −30°C
(3) They were freeze dried by freezing them to temperatures below −70°C by immersing them in an isopropanol-dry ice bath and subjecting them to vacuum.
(4) The temperature was gradually brought up to room temperature over a period of 48–72 h.
(5) The sample tube was removed without opening and placed inside a dessicator within a freezer to maintain it in a water-free environment.
(6) A small amount of sample was carefully mounted on an SEM sample mount using a thin layer of conductive carbon paste just prior to the procedure.
(7) The sample was coated with a thin layer of gold to make it conductive.
(8) The samples mounted were observed in the SEM (JEOL-72C) and micrographs of representative particle populations were obtained.

With the above-mentioned procedure, micrographs of resulting polymer samples show particle sizes ranging from 50 μm to several hundred μm (Fig. 2.1.3) in the initial stages of polymerization (15 min after start of reaction). For samples taken at a later time (75 min after start of reaction), this morphology had coarsened to give particle sizes ranging from 100 μm to the mm range (Fig. 2.1.4). Particles in the initial stages still displayed the co-continuous structure typical of spinodal decomposition with relatively small primary particulates (as small as 10–50 nm) that are agglomerated into the 50–100 s of micrometer. The latter stage showed a coarsened structure with no apparent porosity. The particles seemed to be solid chunks of polymer.

It can therefore be said that there is agreement of morphological results between quiescent-fluid and mixed-vessel FRRPP studies in the reactive MAA/PMAA/water system.

A similar morphological analysis was tried with the reactive S/PS/ether system in a continuously stirred reactor. However, due to the relatively low conversion values,

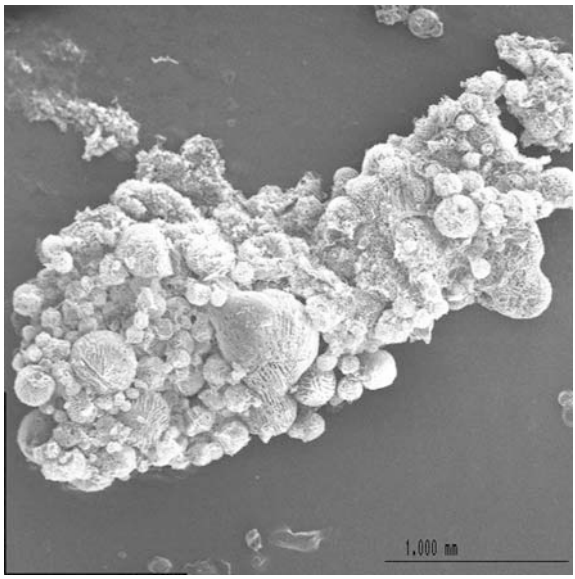

Fig. 2.1.3 Agglomerated particulate material taken from a 0.6 g/12 g/120 g V-50/MAA/PMAA reactive FRRPP system at 80°C sampled 15 min from start of reaction. The scale bar is 1 mm (Reproduced with permission from Wang, 1997)

it has not been possible to observe any primary nanoscale particulates and their co-continuous pore structure. The experimental reactor fluid was bluish in color and quite transparent. The fact that the dispersion is stable again shows the unique characteristic of FRRPP reactor fluids.

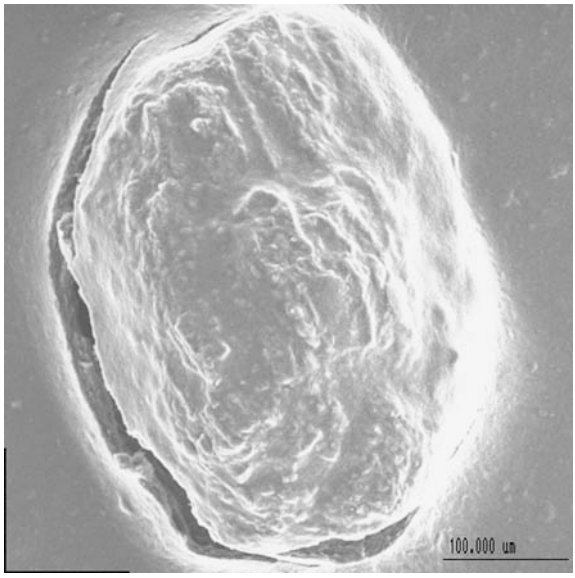

Fig. 2.1.4 Agglomerated particulate material taken from a 0.6 g/12 g/120 g V-50/MAA/PMAA reactive FRRPP system at 80°C sampled 75 min after start of reaction. The scale bar is 1 mm (Reproduced with permission from Wang, 1997)

Experiments were done to at least capture particulate structures in the mixed S/PS/ether system with the addition of 10 wt% crosslinker (EGDMA) relative to the monomers (Tirumala et al., 2003a). Specifically, it involved a reactor 2.5 in. in diameter, with 1.5-in. diameter turbine blades rotating at 300 (50% speed) and 500 (80% speed) rpm. Fluid samples were taken and gelled polymer particulates were observed using an optical microscope. Upon removal of the product, 350-micron polymer-rich particles were observed from the experiment at 300 rpm. Initial 1–2 nm particles agglomerated into 350-micron particles due to the mixing action of the agitator. At this size scale, the level of mixing has a lot to do with the size of the agglomerated polymer-rich domains.

2.1.3 Light Scattering

Agglomeration and large particle sizes were observable in such a system even before phase separation using in-house time-resolved laser light scattering system, as described in Section 1.4.3.1. Since the software for data collection was limited by its ability to take only 120 scans per sample, a dual sample scanning strategy was used. The scanning interval was set to 1 s, and 110 scans were taken (from $t = 0$ to $t = 110$ s). The next 110 s were used to store data into the hard disk and the sample (Sample A) was scanned for a further 110 s ($t = 220$–330 s). This was done until macroscopic phase separation was observed in the sample. The gaps in the scan were filled up using another sample (Sample B) of the same starting composition. The resulting data were analyzed based on total integrated intensity and intensity at the pixel element showing maximum intensity at the start of the experiment; jumps in the data were a reflection of the changing of the samples after every 100 s. In the study, we also tried to find the extent of error in the system due to the limitations of the apparatus and setup used. To do this, several scans were taken of a sample cell which contained just water under operating conditions. The result is an error range of $\pm 3\%$ in the intensity readings.

In the study done by Dar et al. (1995) on the PMAA water system, a He–Ne laser beam passing through the sample showed an angular shift of the peak of the transmitted laser light (Fig. 2.1.5). Before phase separation (after around 700 s), the shift was by about 2° and there was no significant variation in the total intensity of scattered light, aside from the square wave type jumps attributed to identical sample changes. This indicates that the particle in the path of light was smaller than the wavelength of the incident light (672.8 nm). On visual inspection, both the MAA–water and the styrene–ether systems showed bluish gray blobs settling very slowly through the sample cell. This indicates the presence of agglomerated polymer domains in the system which are much larger than the size of individual polymer globules (of the order of several nanometers) even before the onset of large-scale phase separation. When phase separation started to occur after 700 s, it is natural to expect dramatic shifts in the central maximum of the scattering peak, due to developing cloudiness in the system. As reflected in theoretical and experimental

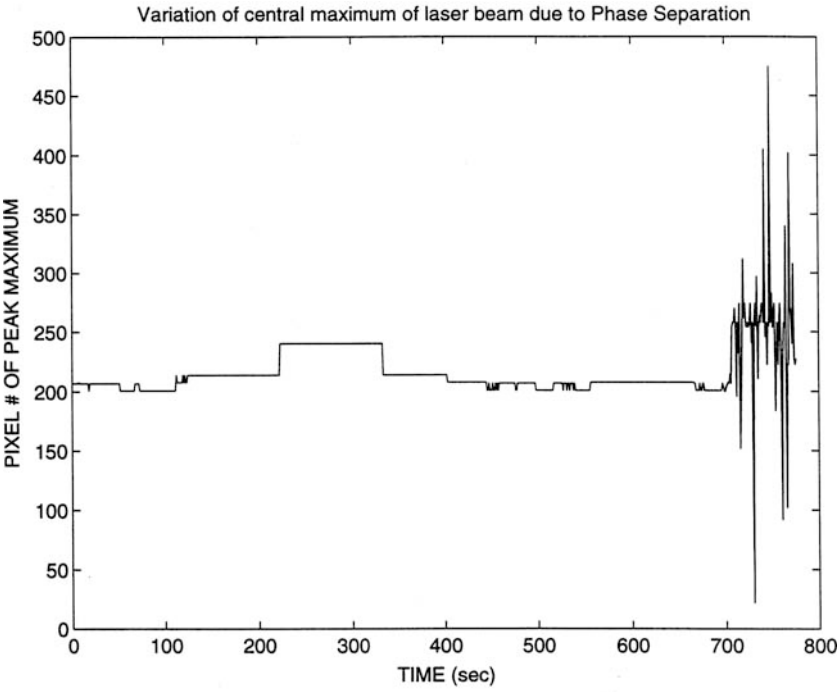

Fig. 2.1.5 Location of the central maximum of the scattered laser beam for the reactive V-50/MAA/PMAA/water system. Small square-function jumps are artificially caused by identical samples changes

results in Section 1.4, the scattering profile at the start of phase separation is low and relatively flat. That is why in Fig. 2.1.5, there seems to be the dramatic shift in scattering peak with time. Finally, Fig. 2.1.5 indicates that it takes around 70 s for the system to equilibrate thermally and electronically.

In Fig. 2.1.6, the integrated intensity vs time is plotted, showing the dramatic lowering of the integrated scattered light when phase separation started after 700 s. Observations in Figures 2.1.5 and 2.1.6 are consistent with above-mentioned persistent nanoscale domain formation from morphological studies and synchrotron X-ray scattering results.

2.1.4 Proton and ^{13}C-NMR Studies

The reactive MAA/PMAA/water system was analyzed during in situ NMR spectroscopy (Wang, 1997). Similar studies with nonreactive MAA/PMAA/water analogs have resulted in nothing unusual in terms of chemical shift and nuclear spin relaxation behavior.

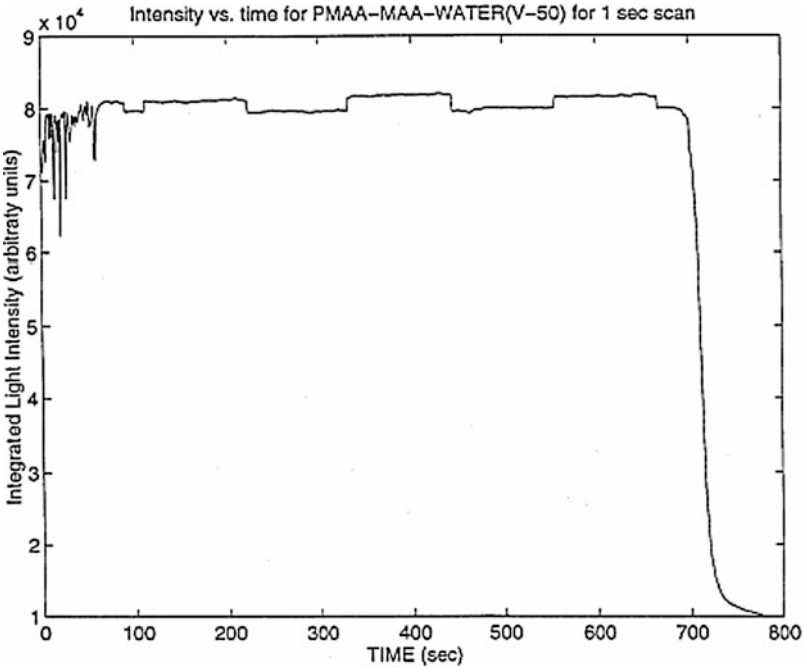

Fig. 2.1.6 Integrated intensity of scattered light for the reactive V-50/MAA/PMAA/water system. Small square-function jumps are artificially caused by identical sample changes

Figures 2.1.7 and 2.1.8 show evolution of proton methyl and ^{13}C methyl peaks of the MAA and PMAA in the reactive system, respectively. In both plots, peak broadening was observed as the polymer was being formed, which would indicate increased polymer viscosity. This is not unusual since polymer conversion is increasing with time. However, with the MAA, peak broadening from viscosity increase is quite unusual even after taking into account reduction in monomer concentration in the polymer domains.

What is also unusual was the evolution of the proton peak from water in the reactive system (Fig. 2.1.9). Again, there seems to be peak broadening and shifting with the water as time increases. This is indicative of increasing viscosity of water, which can happen if water molecules are entrapped within relatively high-viscosity polymer domains. Also, note the narrowing of the peak at very long reaction time of almost 15 h. This indicates that the water viscosity has somehow decreased as more polymers have been formed. It seems that the local heating of the polymer domains during polymerization is responsible for peak broadening.

The NMR sample that resulted in Fig. 2.1.9 was then cooled to room temperature for 8 h in order to terminate the polymer radicals and redistribute the polymer. Then, it was placed in the NMR probe chamber that was preheated to 80°C and allowed to heat for 10 min. After the proton NMR spectrum was taken (Fig. 2.1.10(a)), the sample was removed from the NMR probe chamber and allowed to cool again.

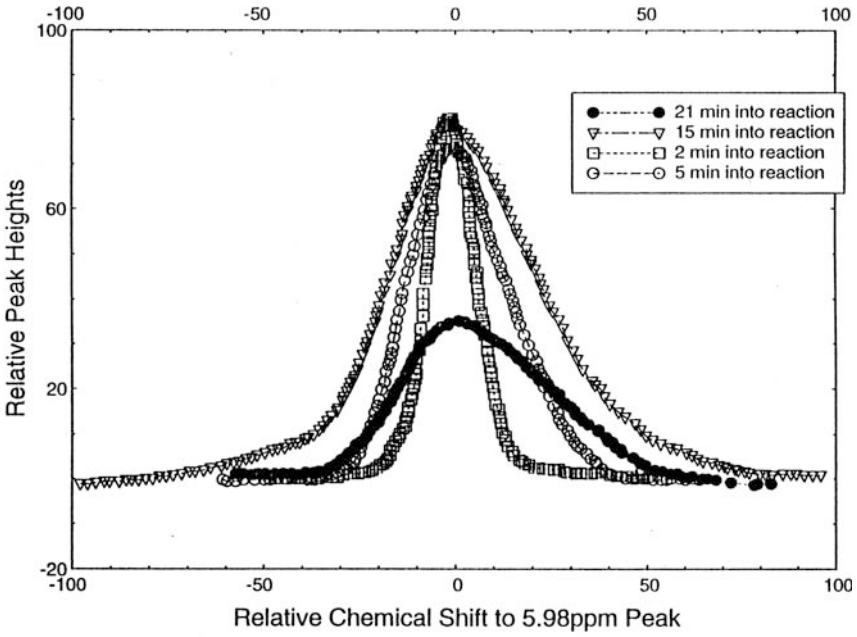

Fig. 2.1.7 Evolution of proton methyl NMR peaks in MAA relative to the chemical shift of 5.98 ppm for in situ FRRPP of 0.009 g/1 g/10 g V-50/MAA/D_2O at 80°C. Peak broadening is observed even at lowered peak intensities due to consumption of the polymer (Reproduced with permission from Wang, 1997)

When the NMR chamber has been preheated to 90°C, the sample was inserted into the preheated NMR probe chamber and the proton spectrum (Fig. 2.1.10(b)) taken after 10 min. Again, the sample was removed and allowed to cool to room temperature, while the NMR probe chamber was preheated to 100°C. Finally, the sample was reinserted in the preheated NMR probe chamber and the spectrum is taken (Fig. 2.1.10(c)) after 10 min. What can be observed from the water sub-spectra is that at higher temperatures, similar peak broadening was observed as that in the reactive FRRPP system at 80°C.

These NMR studies show that polymer domains in the reactive FRRPP system are at higher temperatures than the average, validating a basic foundation of the FRRPP concept. The question to be answered now is how hot are these polymer domains compared to systems under solution polymerization processes.

2.1.5 IR Imaging Study

An infrared (IR) imaging study was done by Dar et al. (1995), for the purpose of determining residual heat generation from reactive MAA/PMAA FRRPP system compared to its solution and nonreactive counterparts. For the FRRPP system, the

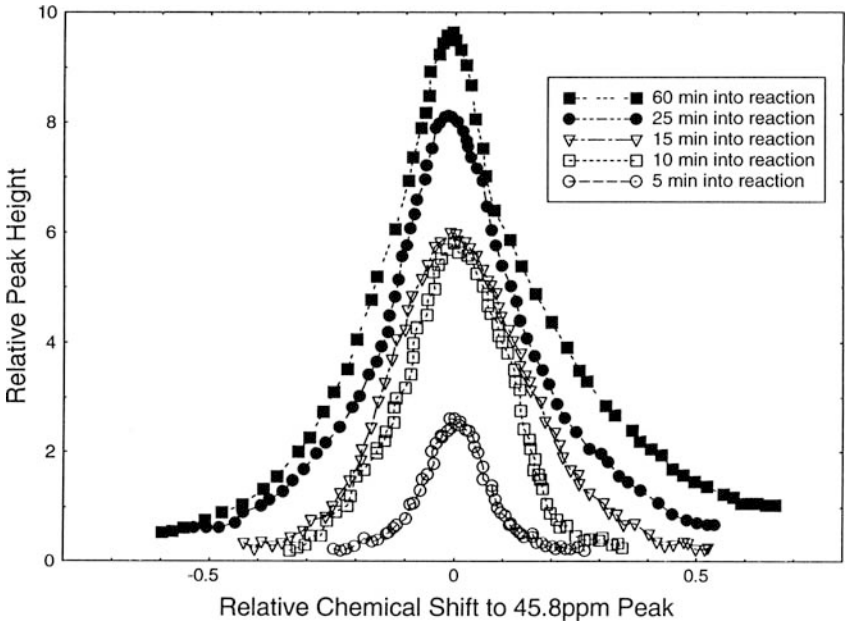

Fig. 2.1.8 Evolution of ^{13}C-NMR methyl peaks in PMAA relative to the chemical shift of 45.8 ppm for in situ FRRPP of 0.009 g/1 g/10 g V-50/MAA/D_2O at 80°C. Peak broadening is observed due to increased viscosity of the polymer as it is being produced (Reproduced with permission from Wang, 1997)

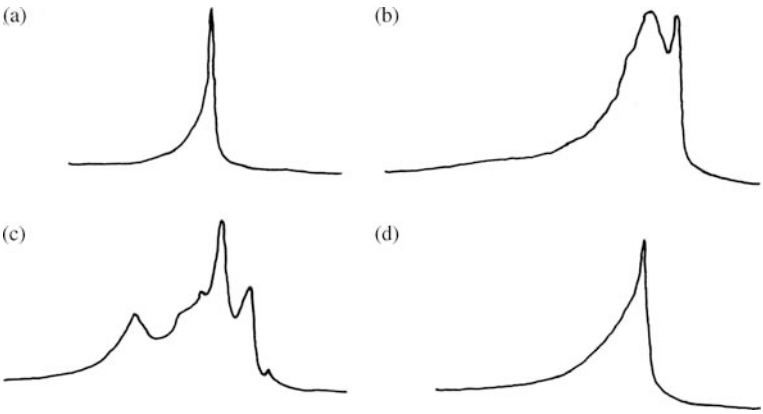

Fig. 2.1.9 Evolution of proton NMR water peak for in situ polymerization of MAA in water at 80°C. Starting reaction composition is 0.005 g/1 g/10 g V-50/MAA/water. Vertical scale of peaks is adjusted automatically to be based on the highest peak in the sub-spectrum. Reaction times are (h:m:s) (**a**) 00:3:16–00:3:56; (**b**) 00:28:00–00:28:40; (**c**) 01:45:20–01:46:00; and (**d**) 14:48:30–14:49:10 (Reproduced with permission from Wang, 1997)

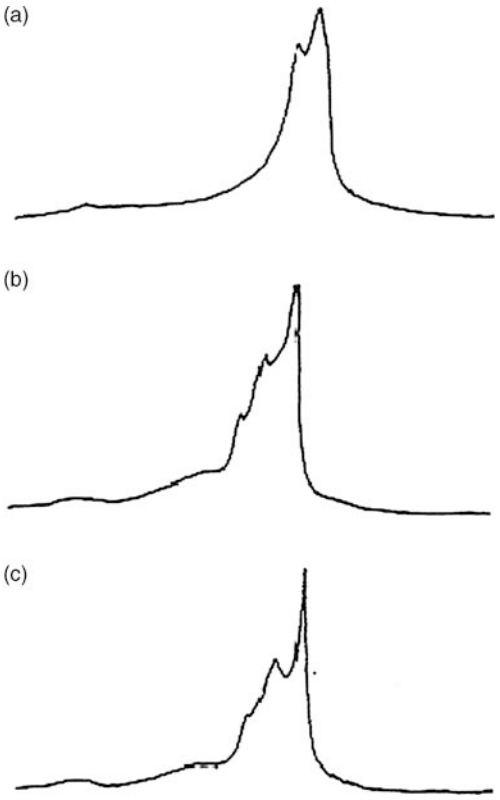

Fig. 2.1.10 Proton NMR sub-spectra of water at various temperatures after the sample of Fig. 2.1.9(d) was taken out of the NMR probe chamber which was preheated at 80°C. The proton NMR spectrum was taken 10 min later (**a**). Then, the sample was removed from the NMR chamber and cooled to room temperature. The sample was placed into the preheated probe chamber at 90°C, and the spectrum taken after 10 min (**b**). During the final cooldown and heatup cycle, the NMR probe chamber was preheated to 100°C. The spectrum was taken 10 min after the sample was placed in the probe chamber (**c**) (Reproduced with permission from Wang, 1997)

solvent was water and initiator was V-050. For the solution system, the solvent was DMF and the initiator was AIBN. For the nonreactive system, solvent was water and various polymer concentrations were used. The solutions were charged into closed test tubes and immersed in an ethylene glycol bath at 80°C. At given times, they were removed from the bath, placed on a line, and then line-scanned for 1 min with the IR imaging device. What was observed was the persistence of higher temperatures on the glass surfaces of the samples, based on color differences from IR imaging sensor.

The FRRPP tube had a highest heat persistence at the beginning (<30 min), i.e., it maintained higher temperature the longest. The solution system was next in heat persistence, and the nonreactive system was last. At 60–90 min after the start of reaction, the heat persistence of the FRRPP system is roughly the same as that of the solution system, i.e., the solution system caught up in the heat persistence scale. Then, a little beyond 90 min, the solution system had a higher heat persistence than the FRRPP process. All this time, there was no heat persistence change with the nonreactive systems; they were all at the lowest levels.

This IR imaging study indicates the relatively hot FRRPP nanodomains, especially at the early stages (<30 min) of reaction, as suspected in the proton NMR tests. The way the heat persistence compared between the FRRPP and solutions systems

mirrors the conversion–time plot between the two (Aggarwal et al. 1996). It should not be a surprise that the conversion directly correlates with the heat persistence level. As it can be seen from prior work (Aggarwal et al., 1996), the FRRPP system clearly had a higher conversion than the solution system up to around 30 min. Then, the solution system started catching up and overtook the conversion level of the FRRPP system at 60–90 min. From this pattern, the FRRPP system would remain hotter relative to the solution system when the next conversion crossover occurs after 100 min.

What is the effect of the reaction exotherm with this thermodynamic condition of phase separation above the LCST for the FRRPP process? Here and at this point, the author will start to integrate concepts and experimental results into a cohesive and plausible picture. As shown in a ternary composition–temperature reaction trajectory plot (Fig. 2.1.11), when the polymer-rich domains are formed (Point B), its local temperature would increase due to the reaction exotherm. This places the reactive polymer-rich domains at Point B' in the vertical temperature projection of Fig. 2.1.11 where diffusional fluxes drop to zero due to the approach of the system toward the spinodal curve at a higher temperature T_2. Note that in Section 1.2, it was shown that all component mutual diffusion coefficients are zero at the spinodal. Then, the polymer-rich domains attain the binodal composition at C' and at the higher temperature T_2. If new chains are initiated and propagated at T_2, then the reaction trajectory can go on, until a certain ceiling temperature is reached.

The drop in the mutual diffusion coefficients of all the components would explain theoretically why even at such high temperatures the monomer and solvent would seem to be frozen in the system, as seen from NMR studies. This would have a profound effect on reactivity of the system, because it would also mean a reduction in conversion rate for the FRRPP system, which was indeed observed. One thing to note is that the explanation here applies to the point when the FRRPP system has already phase separated. Nanoscale domain formation at the early stages of FRRPP process requires a dilute regime explanation.

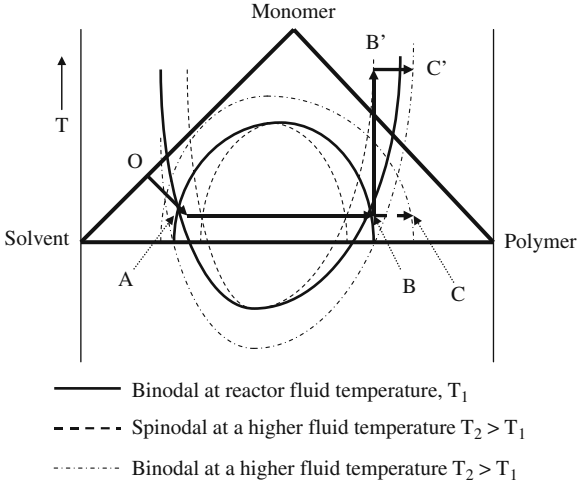

Fig. 2.1.11 Temperature-ternary composition diagram showing the proposed reaction pathway OABB'C' for an FRRPP system, in which the BB' segment occurs due to local heating. Segment ABC is the tie line. The segment OACB is in the basal ternary composition triangular diagram plane. Vertically oriented phase envelopes at T_1 and T_2 intersect with the tie line

2.1.6 Coil-to-Globule Transition

For a while, it was a big mystery why nanoscale polymer domains at the early stages of polymerization would remain relatively hot in FRRPP systems. Intuition formalized by arguments in Section 1.2 tells us that with this small size scale, heat dissipation will be relatively fast. One plausible answer to this mystery is the so-called coil–globule transition for isolated polymer macromolecules.

Since the polymer molecules at this point exist as in a poor solvent environment, they assume the form of highly collapsed polymer globules (Doi, 1996). For dilute systems, the internal volume fraction of the globule is independent of the bulk concentration of polymer in the system and is a function of polymer–polymer, polymer–solvent, and solvent–solvent interactions.

For typical nonpolar organic liquids, interaction forces are dispersive or London-type forces (Olabisi et al., 1979). The physics of the globular state is not well understood, although it has been studied extensively both experimentally (Nishio et al., 1982, Nierlich et al., 1978) and theoretically (Sanchez, 1979, Kholodenko and Freed, 1984, Raos and Allegra, 1996).

The globular state is an excellent example of the peculiarity of polymer/diluent systems. A globule, in its collapsed state, is a single molecule. However, along with the enclosed molecules of the diluent, it forms a system that is very different in composition and properties than the bulk macroscopic system, which it is a part of. A region within the globule seems to satisfy all the requirements of belonging to a different phase than a region that lies outside the macromolecule. This leads to the peculiar concept of a "polymer-rich phase" made up of a single polymer molecule, which would be capable of trapping radical sites.

A schematic diagram showing the collapse of a polymer coil into a dense globule with decreasing quality of solvent is shown in Fig. 2.1.12. R_G and $R_{G\theta}$ refer to the radii of gyration of the coil/globule and the coil/globule at θ-conditions, respectively.

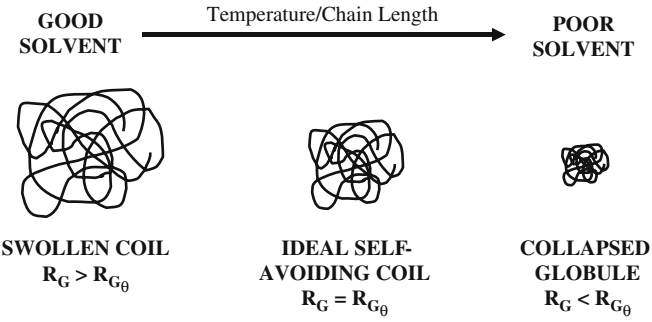

Fig. 2.1.12 A schematic depiction of the polymer collapse from a swollen coil to a collapsed globule with the intermediate θ-condition. $R_G/R_{G\theta}$ is the radius of gyration of the coil/globule (Reproduced with permission from Dar, 1999)

What happens beyond the coil–globule transition is the reason for the mystery of reaction control of the FRRPP process. It so happens that this would also require a change in analysis methods, going from macromolecular to a continuum method. If what is happening in nanoscale does not have a strong influence on the macroscopic behavior of the reactive FRRPP system, then delving into this transition would not be needed. Also, nanoscale materials have become interesting in their own ways. For example, if nanoparticles from these polymers can be efficiently produced, then they would be useful in a number of applications, as it will be shown in Chapters 4–6. Another thing to realize is that the mechanistic underpinnings of the FRRPP process involves a reaction-transport behavior in the nanoscale. This area of nanoscience is a part of the next generation of research in nanotechnology, one that involves efficient self-assembly in that scale. Therefore, the author believes that the FRRPP process and its conceptual underpinnings can result in new and useful materials and applications in the future.

At A and A", the system phase separates until the polymer-rich phase reaches B and B". If the polymer-rich domains undergo gel effect, their temperature will increase to C.

What happens beyond the coil–globule transition is the reason for the mystery of reaction control.

2.2 Local Heating and Energy Analysis of the FRRPP Process

This section pertains to the attempt to push the frontier in the time–space control and coherency effects in precipitating reactive polymer particles.

2.2.1 Notional Concept

The free-radical retrograde-precipitation polymerization (FRRPP) process has been shown to involve a complicated interaction of a chain-reaction kinetics with reaction exotherm, a phase separation behavior occurring as the temperature of the system increases and changes in transport properties with polymer concentration (Caneba, 1992a, b; Aggarwal et al., 1996; Wang et al., 1999; Dar and Caneba, 2002, 2004). An apparent consequence is the trapping of radical sites due to the collapse of nonreactive polymer segments around them; the greater the tendency for system conditions to lead to faster reaction and heat release, the more the radical sites become temporarily entrapped. Thus, this type of polymerization process has been shown to possess a self-regulating thermally induced characteristic behavior. For the purpose of materials synthesis, its ability to maintain live polymer radicals has been exploited for the production of block copolymers (Caneba and Dar, 2005) including a new class of halogenated block copolymers (Caneba, 2007a).

More recently, it has been shown that the early-stage behavior of the FRRPP process involves the persistence of nanoscale structures, which were shown through microscopy (SEM, AFM) and synchrotron X-ray scattering studies (Tirumala et al., 2003b), especially in quiescent fluid systems. Moreover these nanostructures were observed to be persistently occurring and lasting in the order of the half-life of the initiator used (30 min–1 h). Subsequently, the nanostructures would coalesce into larger domains via a coarsening mechanism, but in a mixed system their dispersion can be maintained to be stable until the effective glass transition temperature is reached.

As far as this section is concerned, thermal aspects of the FRRPP process are of most interest, based on the manner at which it was able to "store" the exotherm locally and apparently able to release it to temperatures much higher than the adiabatic temperature rise in a coherent fashion (Cases 1–2) or catastrophically (Case 3) in micro-, meso-, and macroscales. The following case studies detail such behavior.

2.2.2 Case Studies

2.2.2.1 Case 1 – Pressure Control Stirred-Tank Batch Reactor

Experimental Setup

Figure 2.2.1 shows the setup used in this experiment. The reactor is a 300-ml high-pressure vessel (from Parr Instruments, Inc.) that has an electric heater. The pressure is controlled by the heater and 3-way solenoid valve for cooling water. Temperature is read using a digital readout or strip chart recorder.

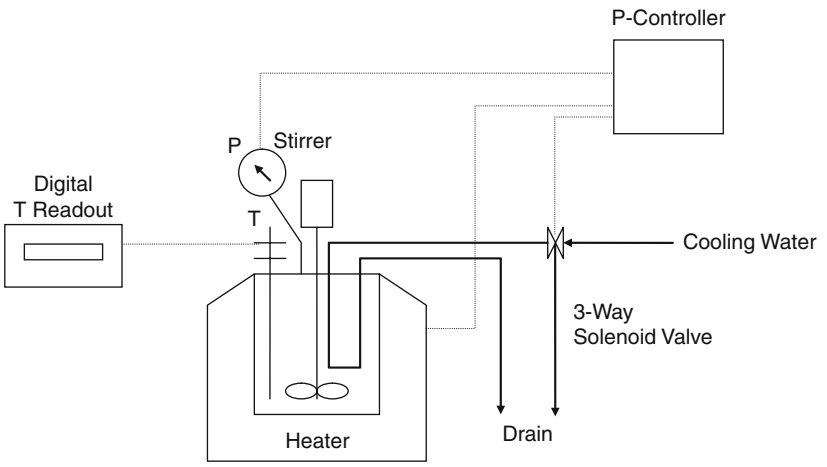

Fig. 2.2.1 Setup of pressure-controlled reactor system used in the experiment

Procedure

Reagent grade ether and styrene monomer were rid of dissolved gases by vacuum freeze-thaw cycles. The ether was distilled, while the styrene was used as is. Thus, styrene still contained nonvolatile inhibitor. The reactor was initially charged with 1 ml styrene, 100 ml ether, and AIBN (equivalent to 0.3 wt% in the system). The setpoint pressure in the reactor was slowly increased and the reactor temperature was recorded.

Results and Discussion

Table 2.2.1 shows a typical thermal history of the polymerization reaction system. We can depict the comparison between the reactive ("reactor temperature" data column) and the nonreactive ("initiator-free temperature" data column) system in Fig. 2.2.2, from which various time regimes can be inferred (Caneba, 1992a): start-up (Region I); solution polymerization (Region II); and, precipitation (Regions III–V). Other experiments also establish a constant-temperature (Region IV) and a dead-ending (Region V) period. At the start of Region II, the temperature of the pressure of the reactor was maintained at 90 psig, in which case the corresponding saturation temperature (initiator-free temperature) for pure ether was 101℃.

Table 2.2.1 Time log of a typical pressure control FRRPP stirred-tank reaction run

Time (min:s)	Reactor temp. (°C)	Init.-free temp. (°C)	Pressure (psig)	Comment(s)
0	24		0	Start
5:00	36		4	
6:07	40		7	
7:30	50	51	12.5	
8:41	60	59	20	
9:30	66	64	25.5	
10:55	74	72	35.5	
12:00	82	78	45.5	
13:05	88	84	55	
14:00	94	90	66	
15:12	100	96	78	Maintain at 100°C Hotspots at 104, 102°C
19:52	100	98	81	Increase setpoint P
23:10	103	101	90	
33:00	101	101	90	Hotspots at 111°C
42:00	99	101	90	
53:00	97	101	90	
67:00	95	101	90	
125:00	93	101	90	
155:00	92	101	90	Shutdown
168:00	18		0	

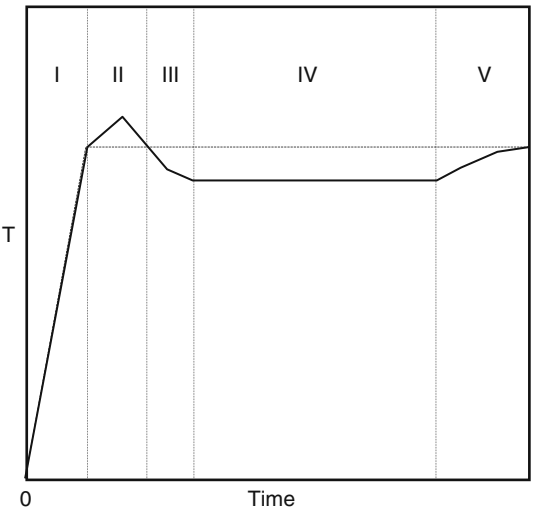

Fig. 2.2.2 Temperature evolution of the FRRPP reactor (*solid curve*) under pressure control. Region I is the heat-up regime. Region II is the solution polymerization regime. Regions III–IV are the FRRPP regimes. During Regions II–IV, the pressure is maintained to a constant value. The behavior of the reactive system is compared with the nonreactive system represented by the *dashed curve*

During the start-up phase (Region I), very little reaction was occurring, as evidenced by the coincidence of the vapor pressure data with that for pure ether. In Region II, there was an increase in measured temperature for the reactive system. This was the period when the system was reacting, but the polymer was formed in a homogeneous solution. The polymer depressed the boiling temperature; thus, the measured temperature increased beyond that of pure ether at constant pressure. As time went by, the reactor fluid temperature started to decrease to the point that it coincided once again with the equivalent saturation temperature of pure ether at the start of Region III. As the system entered Region III, the reactor fluid temperature dropped even further. This means that if we maintained the temperature to a constant value, the reactor fluid vapor pressure would actually be actually increasing! An explanation for this behavior is that the reaction exotherm cannot be completely dissipated within the reactor fluid. At a later time, the reactor fluid attained a thermal pseudo-steady state, and the temperature remained constant with time (Region IV). At a very long time (Region V), the temperature of the reactor returned to the saturation temperature of pure ether. This corresponds to dead-ending of the polymerization reaction system.

A detailed look at the temperature readings in Table 2.2.1 shows that higher temperature flashes were also obtained. For example, when the temperature was generally at 100°C, readings of 102 and 104°C can be seen momentarily from the digital display.

Inside the reactor, formation of carbon particles was obtained. The frequency of the higher temperature flashes increased with the amount of carbon particles. It is therefore evident that the exotherm in polymer formation can result in the degradation of the polymer into carbon particles.

2.2.2.2 Case 2 – Mathematical Modeling of Hot Spots in Precipitation Polymerization Systems

Background

It has been observed that features of the FRRPP process include relatively narrow molecular weight distributions, persistence of live polymer radicals, and gradual change in conversion with time (Caneba, 1992a). A local heating concept has been developed here to explain the above features. It was thought that in the FRRPP process local heating (or hot spots) in the vicinity of the radical sites effectively causes choking of the propagating reaction and minimization of the radical–radical termination reaction. Therefore, it is very important to develop a simple and effective model to estimate the temperature profile around the reacting site and within the precipitated particle, because the direct measure of such temperature is too difficult to achieve using current technologies.

Quasi-static/Pseudo-steady-State Model

The model was based on the assumption that each polymerization site was a spherical particle of radius r_0 immersed in a fluid (as shown in Fig. 2.2.3). A steady-state differential energy balance along with Fourier's Law of heat conduction with a source term (from Eq. 1.2.9) gave

$$k\frac{1}{r^2}\frac{d}{dr}\left(r^2\frac{dT}{dr}\right)+\dot{q}=0, \tag{2.2.1}$$

where T is the absolute temperature, k is the thermal conductivity, r the radial distance, and $\dot{q}$ the energy source term. As seen in Fig. 2.2.4, T_s is the absolute temperature at the surface of the spherical particle, while T_b is the absolute temperature of the bulk fluid. The boundary conditions are

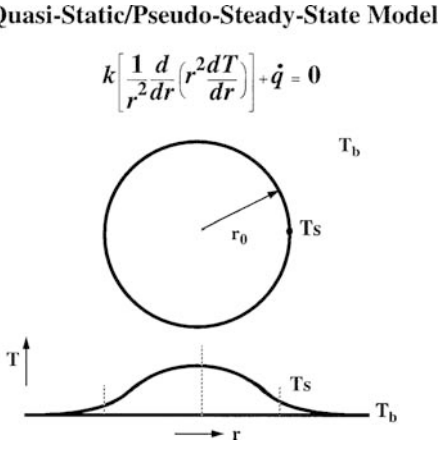

Fig. 2.2.3 The model used for the analysis of the effect of exotherm when polymerization occurs within a spherical particle for a phase separating system

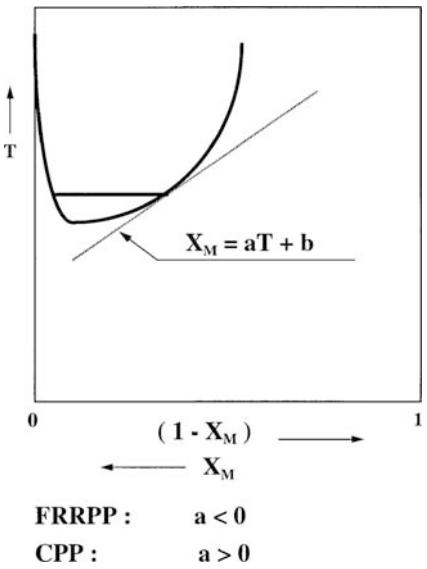

Fig. 2.2.4
Temperature-monomer composition phase diagram, wherein the relationship was obtained to decouple the heat transfer equation (Eq. 2.2.1) from its dependence with composition

$$
\begin{aligned}
&@\ r = 0,\ dT/dr = 0 \\
&@\ r = r_0,\ T = T_s \\
&@\ r = r_0 - K(dT/dr) = h(T_s - T_b)
\end{aligned}
\tag{2.2.2}
$$

where h is the convective heat transfer coefficient of the fluid that the particle is immersed in. If the kinetic rate expression was based on the propagation reaction and that the radical concentration does not change with time (quasi-steady-state assumption), then $\dot{q}$ can be expressed as

$$
\begin{aligned}
\dot{q} &= (-\Delta H_p) k' X_M \\
k' &= k'_0 \exp(-E_a/RT),
\end{aligned}
\tag{2.2.3}
$$

where ΔH_p is the heat of polymerization, E_a is the activation energy of polymerization, X_M is the monomer weight fraction, and $k_0{}'$ is a factor that includes the radical concentration. This model also assumed no density change in the system. Since the rate of mass transfer is quite small in the system, it was assumed that the monomer composition at any point in the spherical particle was related to its temperature based on the equilibrium phase diagram (shown in Fig. 2.2.4). This quasi-static assumption means that the polymer-rich portion of the precipitated particle will have a T-vs-X_M relationship which would trace the phase curves. In this case, it was assumed that a linear portion of the polymer-rich phase curve defines this relationship, thus,

$$
X_M = aT + b, \tag{2.2.4}
$$

where a and b are assumed to be constants. Based on the sign of a, one can deduce that precipitation above the lower critical solution temperature (or FRRPP process) corresponds to $a < 0$, while precipitation below the upper critical solution temperature (or conventional-precipitation polymerization, CPP, process) corresponds to $a > 0$. Although Eq. (2.2.4) was based on a binary polymer–solvent thermodynamic system, it was believed that it was useful in predicting qualitative behavior of precipitating polymerization systems.

Nondimensionalization of Eqs. (2.2.1–2.2.4) resulted in

$$\frac{1}{\eta^2}\frac{d}{d\eta}\left(\eta^2\frac{d\theta}{d\eta}\right) + (\alpha\theta + \beta)\exp(-\gamma/\theta) = 0 \tag{2.2.5}$$

with the following boundary conditions:

$$\begin{aligned} &@\ \eta = 0,\ \mathrm{d}\theta/\mathrm{d}\eta = 0 \\ &@\ \eta = 1,\ \theta = 1 \\ &@\ \eta = 1,\ -d\theta/\mathrm{d}\eta = (1/2)Nu(1-\upsilon) \end{aligned} \tag{2.2.6}$$

where Nu is the Nusselt Number. The dimensionless quantities were related to the various dimensional quantities by the following:

$$\begin{array}{ccc} \eta = r/r_0, & \theta = T/T_\mathrm{s}, & \alpha = \gamma_0^2 A/k = \gamma_0^2(-\Delta H_\mathrm{p})k_0\text{'}a/k \\ \gamma = E_\mathrm{a}/RT_\mathrm{s}, & Nu = h(2r_0)/k, & \beta = r_0^2 B/kT_\mathrm{s} = r_0^2(-\Delta H_\mathrm{p})k_0\text{'}b/kT_\mathrm{s}. \\ A = (-\Delta H_\mathrm{p})k_0\text{'}a, & B = (-\Delta H_\mathrm{p})k_0\text{'}b & \upsilon = T_\mathrm{b}/T_\mathrm{s} \end{array} \tag{2.2.7}$$

Equation (2.2.5) was solved by transforming it into an initial-value problem with the initial condition at the center of the particle ($\eta = 0$). A guess for the value of θ at $\eta = 0$ is made and the trajectory was solved using a predictor–corrector numerical method (relative tolerance of 10^{-6}). When the correct guess was made, the value of q at $\eta = 1$ should be equal to 1.000.

Results and Discussion

Computer simulated results of the temperature profile at different values of the dimensionless parameters are shown in Table 2.2.2.

In general, as γ increases, the temperature profile becomes relatively flat. This is seen from the value of θ @ $\eta = 0$ approaching 1.0, and the value of $d\theta/d\eta$ @ $\eta = 1$ approaching zero. Note that a value of $\theta = 1.05$ @ $\eta = 0$ already implies a temperature difference of about 15°C between the surface and the middle of the particle. The temperature profile also becomes more flat when α and/or β decreases, and/or γ increases. Finally, for the same values of β and γ, the temperature within the particle is more uniform when $\alpha < 0$.

This calculation only concludes that the particle temperature profile is relatively flat for a system undergoing FRRPP polymerization because of the $\alpha < 0$ condition. Also, the need for a small value of β means that particle sizes have to be small

Table 2.2.2 Simulated results of temperature profile inside precipitated particles

α	β	γ	θ @ η= 0	$d\theta/d\eta$ @ η=1	Φ_0=[$\alpha\theta(0)+\beta$]exp(-$\gamma/\theta(0)$)
−0.1	0.5	0.5	1.0407	−0.0812	0.245
−0.1	0.5	2.0	1.009	−0.0182	0.055
−0.1	2.5	0.5	1.26	−0.5055	1.60
−0.1	2.5	2.0	1.058	−0.1131	0.362
0.2	0.5	1.0	1.0446	−0.0878	0.272
0.2	0.5	2.0	1.0162	−0.032	0.0983
0.2	2.5	1.0	1.1874	−0.3561	1.18
0.2	2.5	2.0	1.0668	−0.1285	0.416
0.4	0.5	0.5	1.0967	−0.1885	0.595
0.4	0.5	2.0	1.021	−0.0414	0.128
0.4	2.5	0.5	1.3325	−0.6314	2.084
0.4	2.5	2.0	1.0725	−0.1388	0.454

and/or polymer-rich phase curves have to be relatively steep for a system exhibiting LCST behavior (see Fig. 2.2.4). If these particles are producing thermal energy, then their temperatures will be much higher than the bulk fluid temperature, as seen in Eq. (2.2.2). Much of it depends on the convective heat transfer coefficient, *h*, which might be a misnomer because of the increased importance of radiation heat transfer mechanism compared to heat transport by convection.

2.2.3 Energy Analysis of Cases 1–2

2.2.3.1 Adiabatic Temperature Rise

From the phase diagram for S/PS/ether system, the polymer-rich phase had a composition of about 27 wt% PS (Wang et al., 1999) at 15% conversion (Dar and Caneba, 2004). The adiabatic temperature rise can be obtained from the following calculations:

From reactor data,
Volume of styrene charge = 1 ml
Density of styrene = 0.906 g/ml
Weight of styrene charge = (1 ml) (0.906 g/ml) = 0.906 g
Volume of ether charge = 100 ml
Density of ether = 0.7134 g/ml
Weight of ether charge = (100 ml) (0.7134 g/ml) = 71.34 g
Weight AIBN initiator charged = 0.22 g

From the literature (Rodriguez et al., 2003),
Heat of polymerization of styrene = 670 J/g
Heat capacity of polymer-containing fluid = 0.5 cal/g °C (assumption)

Adiabatic temperature rise = heat of polymerization/heat capacity= (670 J/g)/(4.186 J/cal)/0.5 cal/g °C) = 320°C

With a bulk polymerization adiabatic temperature rise of 320°C, the 15% conversion translates to a maximum of (320°C) (0.15) = 48°C adiabatic temperature rise. If the starting temperature is the operating temperature of 100°C, then the average adiabatic temperature rise of the particles is at 148°C.

2.2.3.2 Actual Overall Reactive Particle Temperature

Bulk fluid temperature = 100°C = T_0
Mixer RPM = 300 rpm = 5 rev/s
Fluid velocity = 60 cm/s
Temperature flashes (hot spots as indicated in Table 2.2.1 of Case 1) recorded at 102–111°C = T
Thus, T–T_0 = 2–11°C

Polymer particle diameter = 1–2 mm = 1–2/10 cm = 0.1–0.2 cm
Thermocouple diameter = 1/8 in. = 0.16 cm
Mean contact time of polymer particle to thermocouple = 0.2 s

Thermocouple metal is assumed to be stainless steel. From the literature,
Thermal conductivity of steel, k = 25 Btu/h ft^2(°F/ft) = 42.3 W/m K
Density of stainless steel, $\rho = 7830\,\text{kg/m}^3$
Heat capacity of steel, $C_P = 500\,\text{J/kg K}$
Thermal diffusivity of stainless steel, $\alpha = k/\rho C_P = 42.3/(7830)(500) = 1.1 \times 10^{-5}\ \text{m}^2/\text{s} = 0.11\ \text{cm}^2/\text{s}$

For R_0 = radius or hemispherical tip of the thermocouple, t = contact time, $\alpha t/R_0{}^2 = (0.11)(0.2)/(0.16)^2 = 0.86$

From unsteady-state heat transfer into a sphere (Bird et al., 1960), $\Theta = (T–T_0)/(T_1–T_0) = 0.99$ at the center where the thermocouple is located. If T–T_0 = 2–11°C, then $T_1 = T_0 + (T–T_0)/\Theta = 100 + (2–11)/(0.99) = 102–111$°C, which is also equal to the polymer surface particle temperature or the average polymer particle temperature.

2.2.3.3 Carbonization Temperatures

Carbonization temperatures start at 300°C up to as high as 2000°C (Hiroaki et al., 2008).

2.2.3.4 Data Interpretation

The best way to interpret these temperature values is to follow the reaction and its morphological features. At the start, small molecules exist in solution at the operating temperature of 100°C. With the presence of the free-radical initiator (such as AIBN), initiation events take place to form oligomers (short polymer chains at molecular weights below around 10,000 g/mol). In fact, in this case,

molecular weights are around 2,000 g/mol only. While polymer chains are being formed, reaction exotherm kicks in to raise nanometer scale local temperatures and form polymer-rich domains. These local temperatures are at the low end of the 102–111°C range. Relatively hot nanoscale reactive polymer-rich domains continue to grow due to the reactor fluid mixing. As the domains grow in size, they get hotter and reach the upper end of the 102–111°C. Each particle attains a relatively flat temperature profile (based on Case 2 results); the larger the particle, the higher its temperature. While all this is happening, initiation events are occurring from the hot particles forming even hotter regions within the hot particles. What keeps these hot regions from dispersing is the thermodynamic-based tendency to confine them due to phase separation as the temperature increases. Again, hotter regions within the hot particles easily agglomerate. This keeps on going forming a "tower" effect with the temperature profile, in which higher temperature domains are supported by larger lower temperature domains. This is how the hottest regions can reach carbonization temperatures of 300–1000°C – way above the adiabatic temperature rise of 148°C. What sustains all these reaction exotherm effects? It is the fact that at this point only 10–20% of the monomer charge is converted to polymer and volume confinement accompanying the energy confinement keeps the active sites from being terminated. Of course, at a later time when the base of the temperature profile is no longer hot enough, these cooler regions of the polymer particle dissolve away leaving behind the hot regions around carbonized polymer. This would then correspond to a tower temperature profile that later crumbles to expose only the carbonized regions, as we observed on long-term reaction runs. In fact, phase diagram studies indicated that with the 1,000–2,000 g/mol polymer products, they would have been dissolved in the reactor fluid if they were nonreactive at the reactor fluid operating temperature (Wang et al., 1999). This is depicted in Fig. 2.2.5.

2.2.4 Glass Tube Reactor Experiment with Release of Reaction Fluid

2.2.4.1 Experimental Setup

Another set of polymerizations was carried out in a small-scale glass tube reactor within an ethylene glycol bath (Fig. 2.2.6). The tube was sealed with a Teflon® cap after the reactants mixture was added in and bubbled with N_2.

2.2.4.2 Procedure

The pressure glass tube was to be filled with a 5 ml MEK/4.75 water mixture, since according to the International Critical Tables, this mixture has an LCST of about −16°C. About 0.4 ml of vinyl acetate (VA) was to be incorporated into the mixture. The actual sequence used was the addition of 5 ml MEK into the pressurized glass tube followed by the 0.4 ml VA, and then finally injecting in the 4.75 ml water which resulted in a cloudy mixture. Then, the glass tube was sealed using the Teflon®

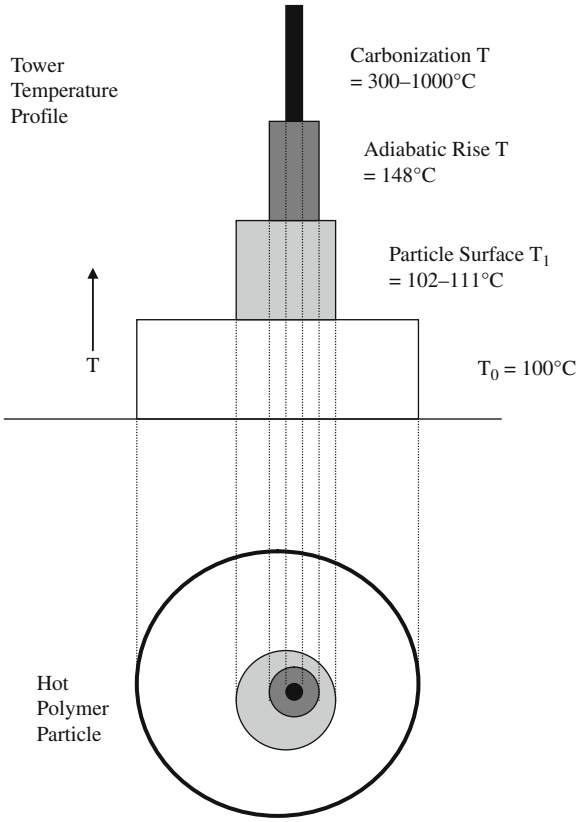

Fig. 2.2.5 Depicted temperature profile within an agglomerated polymer reactive particle, based on the above-mentioned quantitative energy analysis

cap. The mixture was continuously mixed while the controller temperature was set at 25°C for several hours to see what will happen when the VA monomer self-polymerized.

2.2.4.3 Results and Discussion

After at least 24 h, the following observations were made:

- The Teflon® cap on the tube was partially charred/melted, as if burnt Teflon® had ran down the side of the glass tube.
- The rubber o-ring that was used to seal the Teflon® cap became brittle.
- There was a solid black mass at the bottom of the tube, which included remnants of the stirrer magnet.
- A glass thermometer that was also used to indicate the bath temperature was broken and about one fifth of the lower part was molten and misshapen. The plastic of the clamp used to hold it was charred.
- All the bath fluid (1,800–2,000 ml) disappeared and seemed to have vaporized.

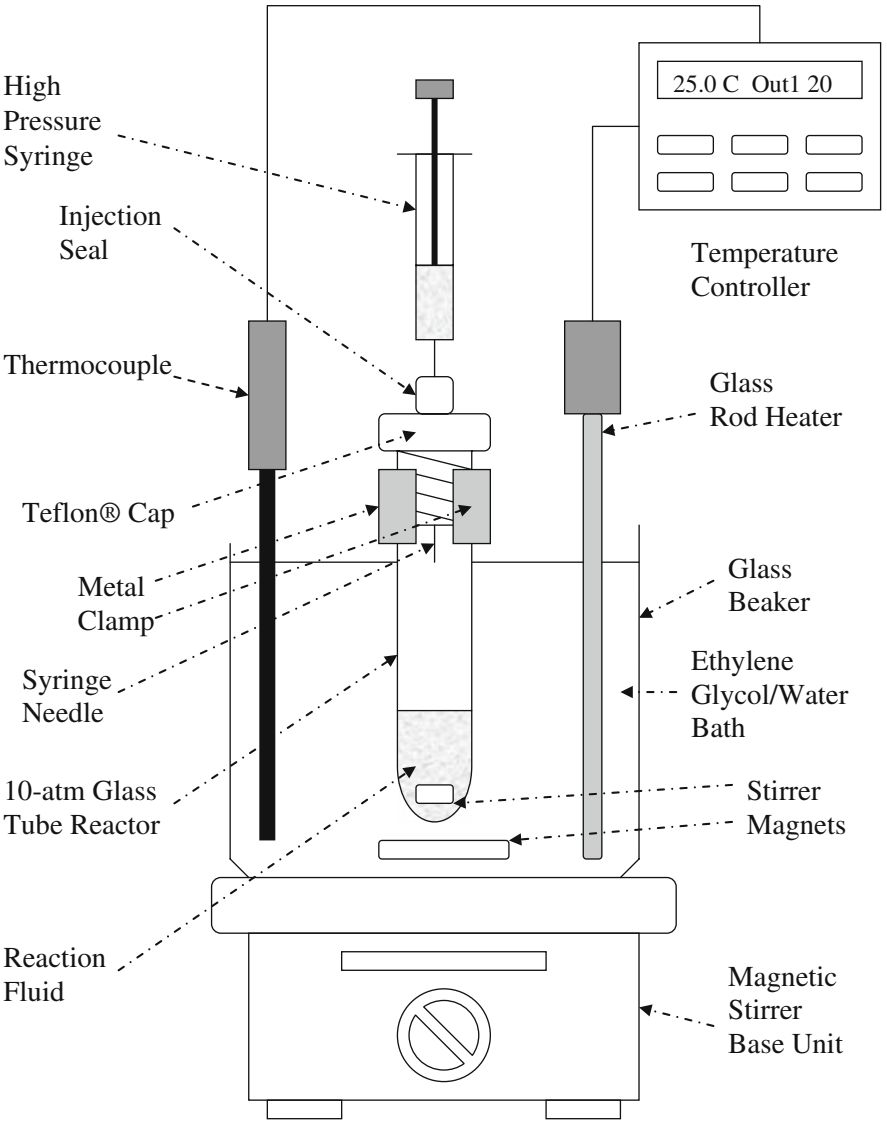

Fig. 2.2.6 Pressure (10 atm maximum pressure) glass tube reactor used to obtain catastrophic release of reaction exotherm from self-polymerization of vinyl acetate in MEK/water mixtures

- The metal clamp holding the pressurized glass tube was damaged. The plastic on the clamp was charred completely. The metal part was deformed quite severely due to melting, and phase separated the copper from the alloy.
- Part of the wire of the power supply to the heating rod was charred at the point where it touched the beaker holding the bath.
- The rod heater had some scale-like deposits on it but no sign of heat damage at all.

- The big Teflon® stirrer used to mix the ethylene glycol bath was completely charred from one end and partially charred from the other end.
- The glass microsyringe attached to the top of the tube was broken. The glass part had broken off at the point of attachment. There was no break in the glass. It seemed to have come off due to melting of whatever attachment it had to the needle assembly.
- The thermocouple had some carbon deposit on the tip.
- Both thermocouple and temperature controller were working at the time the accident was discovered, and the controller was still working afterward.
- There was blackening of both glass tube and glass beaker.

A duplicate run was made, and part of what happened was observed before too much safety concern was felt. In the repeat run, the bath was replaced with 50/50 v/v ethylene glycol/water. Still what was observed is the formation of a quiescent flame emanating from the surface of the bath fluid, which slowly consumed the entire bath. Upon throwing a large amount of water on the flame, a large amount of steam was produced. Also, it became clear that the heat source of the surface flame from the bath was the material from the pressurized glass tube, which escaped through the Teflon® cap while charring its way through. Electrical-based fire or energy release was ruled out, although it was hard to believe that there was any other source of heat to deform the metal clamp. It was concluded that an autoacceleration reaction occurred, although it is hard to imagine it happening at less than 10 wt% monomer loading. Taken into consideration the char formation in the previous FRRPP experiment, both experiments are concluded to be related by the fact that polymerization occurred above the LCST. In the previous stirred-tank pressurized reactor experiment, the thermal effects were under control, while here it was under control for awhile and then went out of control to unleash its full exotherm. Early victims were materials around the reactor fluid (Teflon® coating on stirrer magnet), followed by anything in its pathway out of the pressurized glass tube (Teflon® cap, syringe, plastic cover of the metal clamp, metal clamp), and finally the surface of the bath fluid to start a quiescent flame. What this also means is that temperatures went to relatively high values, as evidenced by the fact that the autoignition temperature of ethylene glycol is 410°C (from online Wikipedia), and the melting points of Al and Cu are 600 and 1083°C, respectively (Cahen and Trielle, 1961). Some of the damaged materials were collected and pictures of the remnants are shown in Fig. 2.2.7.

It is clear that the FRRPP process resulted in the discovery of new nanoscale polymers, and other materials will still be discovered from it. The above-mentioned thermal effects have not been the subject of a more systematic study, and yet understanding it is a key to its application to more energetic systems. If a mere few grams of a monomer can release enough exothermic energy and result in char formation of Teflon®, metal deformation, metal alloy phase separation, the initiation of an intense localized surface combustion that slowly consumes a bath material a few thousand times its weight, then what can more energetic materials do especially around other more energetic materials/systems? The search for the answer to this question is the subject of our continuing efforts and should be an intriguing but challenging undertaking.

Fig. 2.2.7 Remnants of the glass tube reactor FRRPP experiment showing deformed metal clamp showing the reddish phase separated inner part (*center*), carbonized plastic samples in bottles, partially charred Teflon® cap (*left center*), syringe remains (*lower left side*), and pressurized glass tube container with carbonized material (*right side*)

2.2.5 Nomenclature

2.2.5.1 Alphabets

Upper Case

A – dimensionless version of a, defined in Eq. (2.2.7)
B – dimensionless version of b, defined in Eq. (2.2.7)
T – absolute temperature, K
R – universal gas constant, J/mol K
R_0 – radius of the hemispherical tip of the thermocouple, m

Lower Case

a, b– constants for Eq. (2.2.4)
h – convective heat transfer coefficient of the fluid, W/m^2 K
k – thermal conductivity, J/mol m^2 (K/m)
r – radial distance, m
t – time, s

2.2.5.2 Subscripts

b – bulk fluid
s – surface

2.2.5.3 Superscripts

None

2.2.5.4 Greek Symbols

α – dimensionless version of a from Eq. (2.2.4)
β – dimensionless version of b from Eq. (2.2.4)
γ – dimensionless activation energy, defined in Eq. (2.2.7)
η– dimensionless radius, defined in Eq. (2.2.7)
υ – dimensionless bulk fluid temperature, defined in Eq. (2.2.7)
θ – dimensionless temperature, defined in Eq. (2.2.7)
Θ – dimensionless temperature ($=(T–T_0)/(T_1–T_0)$)

2.2.5.5 Other Symbols

ΔH_P – heat of polymerization, J/mol
E_a – activation energy of polymerization, J/mol K
k'– effective rate coefficient of polymerization, mol/m^{3}s
k_o – pre-exponential factor for effective rate coefficient of polymerization, mol/m^{3}s
$\dot{q}$ – energy source term, W/m^3
Nu – Nusselt number, defined in Eq. (2.2.7)
r_0 – particle radius, m
Φ_0 – dimensionless energy source term, defined in Table 2.2.2
X_M – weight fraction monomer
T_0 – initial particle temperature, K
T_1 – surface particle temperature, K

2.3 FRRPP Polymerization Kinetics

This section pertains to studies made to delineate the kinetics of the FRRPP process involving polystyrene (PS) and poly(methacrylic acid) (PMAA) systems.

2.3.1 Polystyrene/Styrene-Based FRRPP Systems

Most of the systematic studies done on the FRRPP kinetics for the formation of polystyrene is through the use of diethyl ether (or simply ether) as precipitant. Some of the work involving acetone is also presented.

2.3.1.1 Phase Diagram Results

Using the cloudpoint method described in Section 1.1.2.3, ternary phase diagrams for PS/S/ether systems at various temperatures are presented. Note that the

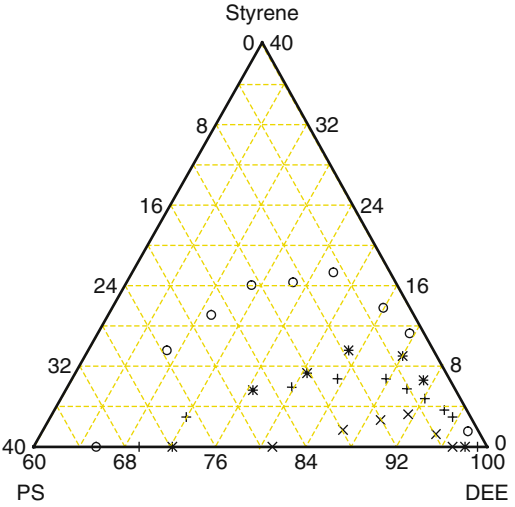

Fig. 2.3.1 PS/S/ether system phase diagrams at different temperatures. PS: M_n = 25,000, PDI = 1.06. 80°C: o – CPC; + – IPPC; 50°C: ∗ – CPC, x – IPPC (Reproduced with permission from Shi, 1997)

LCST of at least 42°C for PS/ether system is presented in the literature (Caneba, 1992a). Figure 2.3.1 shows the cloudpoint curve (CPC representing the binodal) and the instantaneous precipitation point curve (IPPC, or approximately representing the spinodal) for polystyrene with a number-average molecular weight of 25,000 g/mol. Phase boundaries are bigger at 80°C compared to those at 50°C; thus, the ternary system exhibits an LCST behavior. In Fig. 2.3.2, CPCs and IPPCs are plotted at a number-average molecular weight of 400,000 for ternary systems at 50°C and 80°C. Here, the phase boundaries are shown to be larger for the system with larger polystyrene molecular weight, compared to the phase curves in Fig. 2.3.2. This observation is based on the fact that the system is more likely to phase separate when the polymer has a higher molecular weight. In Fig. 2.3.3, the CPC for the system at 80°C with PS number-average molecular weight of 400,000 g/mol is shown with measured tie line. Tie line measurements were done using the method described in Section Measurement of Tie Line Compositions. Note that the tie lines are horizontal, which indicate that styrene has equal affinity to PS compared to ether. Tie lines for other PS molecular weights have also been shown to be horizontal (Wang, 1997). This is in contrast with tie lines obtained for the PMAA/MAA/water system (Fig. 1.1.9), wherein MAA distributes itself more with the PMAA than with water. A higher monomer content for the polymer-rich phase indicates a potentially faster chain extension during polymerization.

2.3.1.2 Conversion and Molecular Weight Distributions

Styrene monomer was purchased from Aldrich Chemicals, and they contain the usual amounts of inhibitor. It was purified with a double distillation technique under

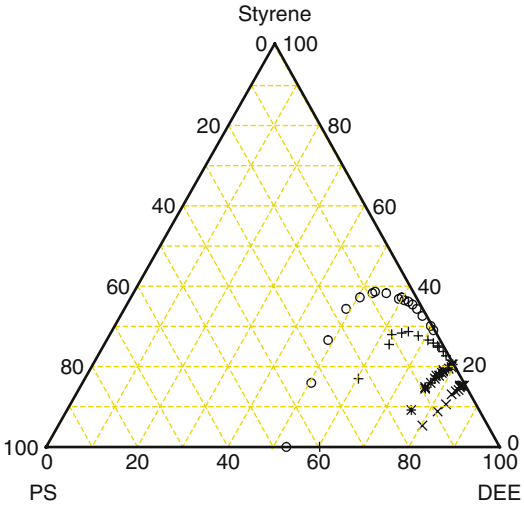

Fig. 2.3.2 Phase diagram of PS/S/ether at different temperatures. PS: M_n = 400,000, PDI = 1.06. o: 80°C, CPC; +: 50°C, CPC; ∗: 80°C, IPPC; x: 50°C, IPPC (Reproduced with permission from Shi, 1997)

reduced pressure. Analytical grade ether was purchased from Fisher Scientific and used as is. Initiators, 4,4′-azobis(4-cyanopentanoic acid) (V-501) and V-65 were obtained from Wako Chemicals and used without further purification.

Polymerization Setup and Procedure

Because the polymerization reaction took place at a temperature above the boiling point of the solvent, the vapor pressure will be high during the course of reaction. Therefore, a high pressure reactor was desirable for polymerization of styrene in ether. The setup is shown in Fig. 2.3.4. Here, a 300-ml mantle heated at high-pressure reactor vessel (purchased from Parr Instruments, Inc.) was used, and two

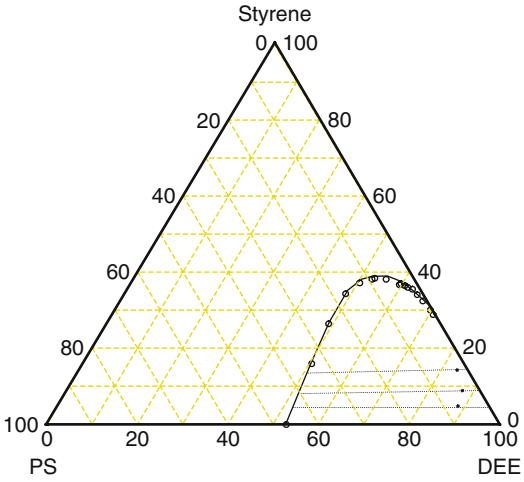

Fig. 2.3.3 CPC of the PS/S/ether system at 80°C and PS number-average MW = 400,000 g/mol with tie lines. *Solid points* on the tie lines represent overall compositions where the samples are prepared (Reproduced with permission from Shi, 1997)

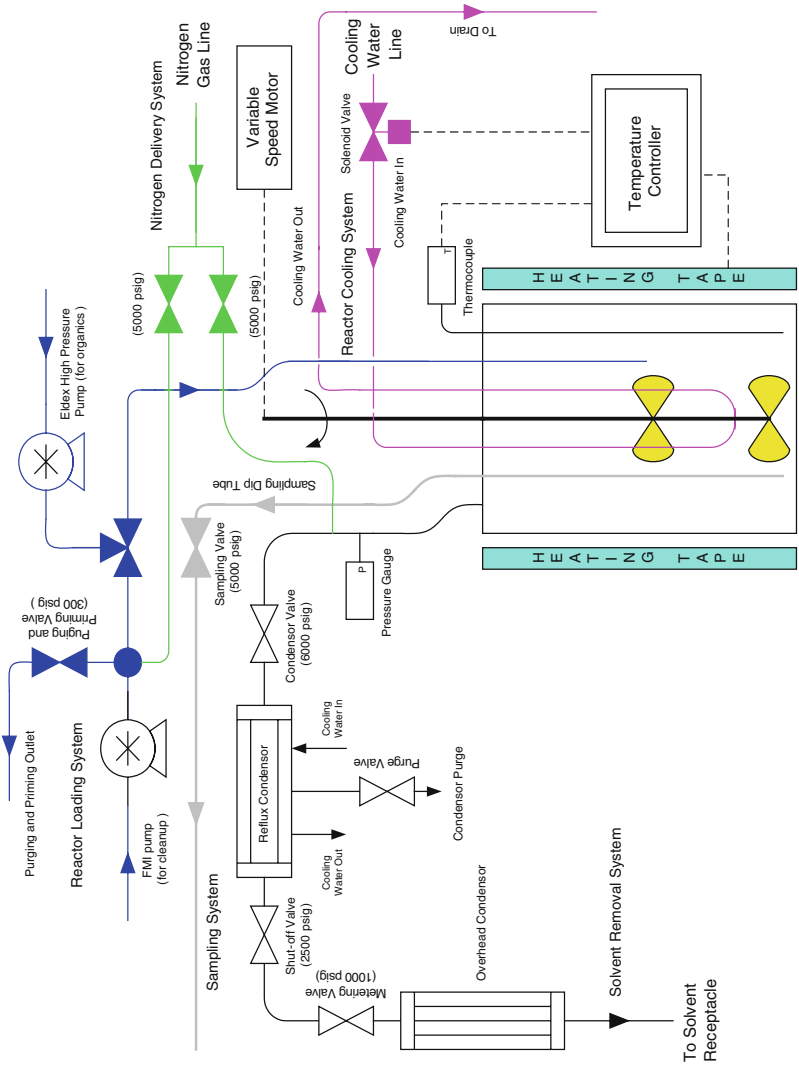

Fig. 2.3.4 Pressurized 300-ml Parr reactor system used in FRRPP work (Reproduced with permission from Dar, 1999)

Table 2.3.1 Range of chemical compositions for styrene polymerization (Reproduced with permission from Wang et al., 1999)

Chemicals	Amount
Styrene	15–40 ml
Ethyl ether	65–120 ml
V-501 or V-65	0.1–0.684 g

high pressure metering pumps (purchased from Fluid Metering, Inc.) were used. The range of recipes for polymerization of styrene in ether is given in Table 2.3.1. Half of nitrogen-bubbled solvent was charged into the reactor first, and the temperature was ramped to 80°C in 30 min. The reactor was then pressurized to 70 psig with the nitrogen gas before the rest of the nitrogen-bubbled reactant mixture was pumped into the reactor in about 2 min. Samples were withdrawn at known times, cooled with dry ice, and purged with air to stop further polymerization reaction. Samples were then dried to constant weight for computation of conversion. Dried samples used for further analysis were purified by dissolving in toluene and washing them with water to get rid of residual initiator fragments.

The molecular weights of the dried polymer samples from the reactor fluid were measured using a size exclusion chromatograph. The chromatography system had refractive index and multi-angle light scattering detectors (Wyatt Technologies, Inc.). Thus, measured molecular weights were absolute, and there was no need to calibrate molecular weights after injecting a few samples. For the analysis of the polystyrene samples, a silica column (Supelco, Inc., LC-1 Supelcosil Column) with HPLC grade toluene was used as a carrier fluid.

Results

Figure 2.3.5 shows the conversion–time data for the batch reactor polymerization of styrene in ether and acetone under FRRPP conditions (80°C). The half-life of the V501 initiator used in the ether system is about 130 min (Wako Chemicals, 1987). It is evident that there is a sharp rise in conversion at the beginning, followed by a period of reduced conversion rate. The onset of reduced conversion rate occurs at around 25%.

Corresponding number-average molecular weight (Fig. 2.3.6) as well as polydispersity index (Fig. 2.3.7) data show asymptotic values with time. What is quite remarkable is that the asymptotic value of the polydispersity index was at 1.7–1.8.

Figure 2.3.8 shows conversion–time plot for polymerization of styrene in ether (15 wt% styrene charge) at 80°C, using V-65 as initiator. The time axis was based on the number of initiator half-lives. From the product literature of Wake Chemical Co., initiator half-lives at 60 and 80°C were calculated to be equal to 200 and 20 min, respectively. It was noted from Figs. 2.3.8 and 2.3.9 that the slowdown period at 80°C corresponded to conversion values of 12.4% and a number-average MW of

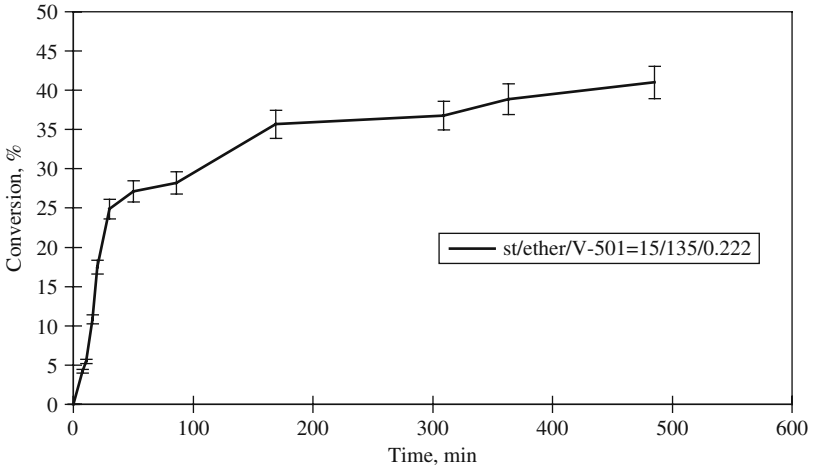

Fig. 2.3.5 Conversion–time plot for polymerization of styrene in ether at 80°C. Starting reactor composition is 14 g/135 g/0.222 g for styrene/ether/V-501 (Replotted with permission from Wang et al., 1999)

3 kD. This is in contrast to the 30–35% conversion range and 6–8 kD number-average MW for an equivalent system using AIBN as initiator. In addition to data at 80°C, some were obtained at 60°C, although it was based on half the amount of initiator. At the lower temperature of 60°C, the final conversion was higher at 18.9%, while the molecular weight jumped to 10.06 kD. Also, PDI values seemed to be smaller than at 80°C. Finally, when the initiator was doubled at 80°C, the conversion increased from 12.4% to about 15% only. Thus, lowering the temperature seemed to be an effective way of increasing the conversion values, but more at a square root level as predicted by Eqs. (1.3.5) and (1.3.6).

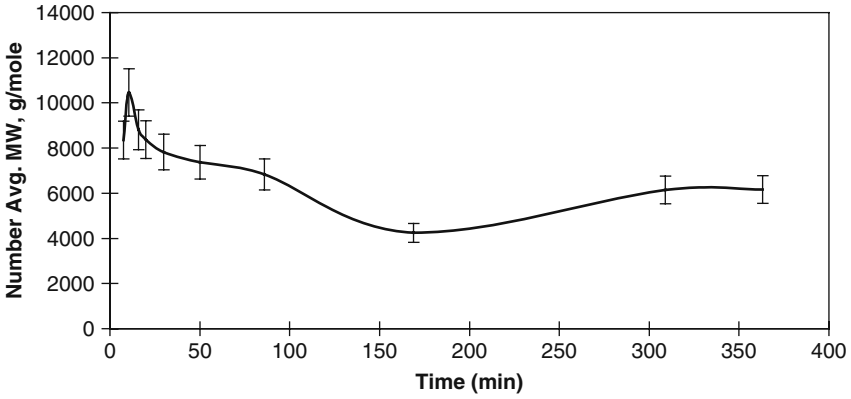

Fig. 2.3.6 Number-average molecular weight for the ether-based FRRPP system at 80°C. Starting reactor composition is the same as in Fig. 2.3.5 (Replotted with permission from Wang et al., 1999)

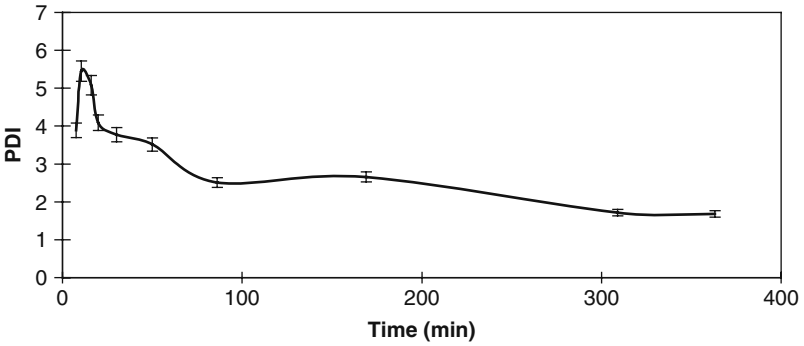

Fig. 2.3.7 Polydispersity index for the ether-based FRRPP system at 80°C (Replotted with permission from Wang et al., 1999)

Figure 2.3.10 is a replot of Fig. 2.3.8 in log–log scale. It is evident that a linear plot of conversion vs. time relative to initiator half-life is a key kinetic feature of the FRRPP process, especially when all initiator molecules have been exhausted (time greater than four times initiator half-life).

A look at the evolution of the molecular weight distribution (Fig. 2.3.11) resulting in Figs. 2.3.6 and 2.3.7 indicates a bimodal distribution at the beginning, in which the lower molecular weight peak was relatively sharp compared to the higher molecular weight one. As time went on, the higher molecular weight peak became more and more dominant, and the sharp low molecular weight peak seemed to be diminishing. Also, the positions of the peaks barely changed with time. In the end, when almost all initiator molecules have been exhausted, the higher molecular weight peak became so dominant that the effect of the lower molecular weight peak became

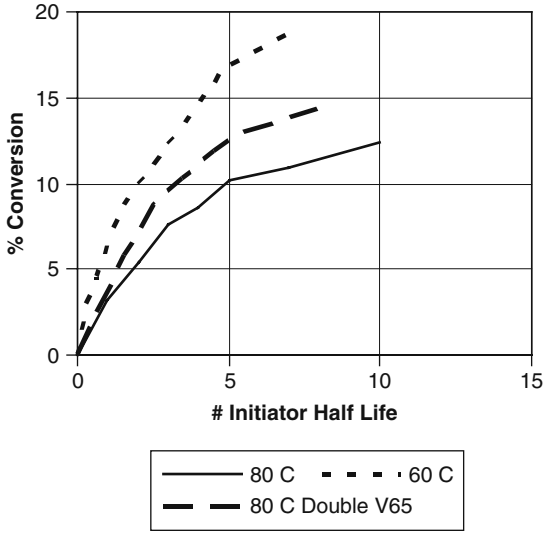

Fig. 2.3.8 Conversion–time data for polymerization of 16.7 g styrene in 100 g ether using 0.17 g V-65 as initiator at 80°C, and 30 g styrene in 100 g ether using 0.15 g V-65 at 60°C (Replotted with permission from Caneba et al., 2003)

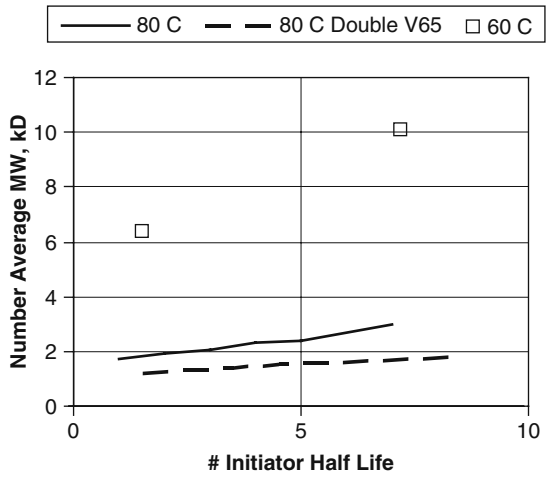

(a) Number Average MW

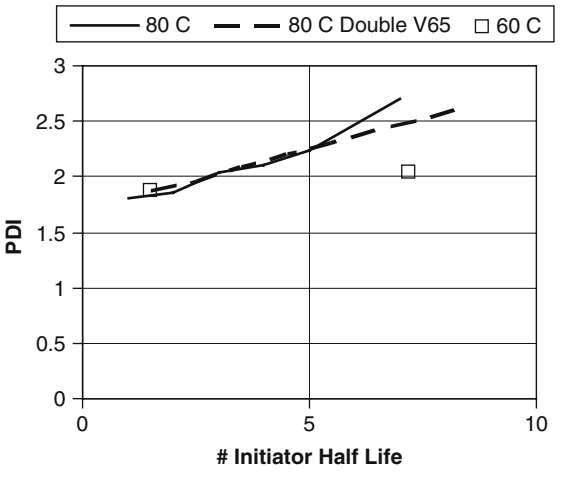

(b) Polydispersity Index

Fig. 2.3.9 MWD properties of samples from Fig. 2.3.9 (Replotted with permission from Caneba et al., 2003)

relatively insignificant. Also, as time went on, there seemed to an appearance of a third even smaller lower molecular weight peak.

Discussion of Results

As seen from phase equilibria and polymerization results, the entry of the FRRPP system in the phase envelope can be linked with the reduction in conversion rate. From conversion–time data alone, it was evident that the FRRPP system had better reaction control after the onset of phase separation, even though it might have a greater tendency to go into autoacceleration at the beginning of the reaction.

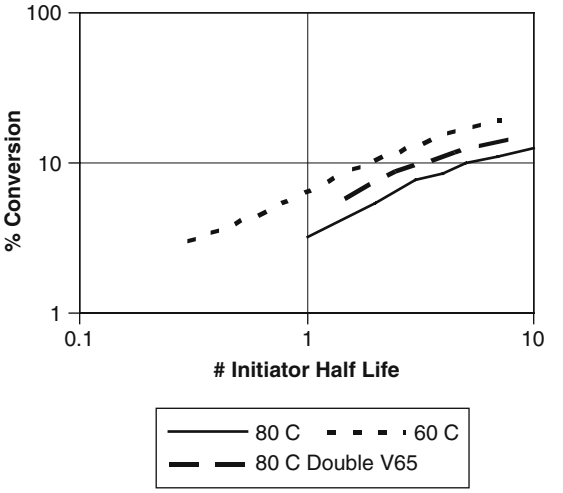

Fig. 2.3.10 Replot of Fig. 2.3.8 in log–log scale (Replotted with permission from Caneba et al., 2003)

The initial overshoot in number-average molecular weight (Fig. 2.3.6) and polydispersity index (Fig. 2.3.7) at low conversions seems to be consistent with the initial OA line segment of the system trajectory as depicted in Fig. 2.1.11, wherein the system follows a solution polymerization process during the first 10 min (based on Figs. 2.3.5–2.3.7). Subsequently, when the polymer-rich phase was being formed as the system traversed the OB line segment of the reaction trajectory in Fig. 2.2.5, the tendency for this phase was to go into gel effect, as seen from the sharper rise

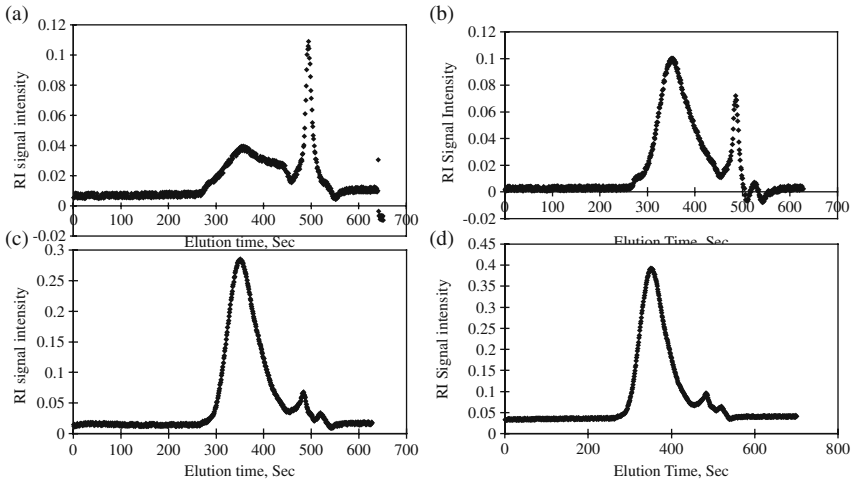

Fig. 2.2.11 Size exclusion chromatograms for the polymer samples at various times in the reactor: (**a**) 16 min; (**b**) 86 min; (**c**) 300 min; and (**d**) 360 min (Reproduced with permission from Wang, 1997)

in conversion (Fig. 2.3.5). However, instead of having increasing number-average molecular weight and polydispersity index as a consequence of the gel effect for higher polymer composition (Balke and Hamielec, 1973, Louie, 1984), the opposite was happening. Before the gel effect, bulk and solution systems closely followed the quasi-steady-state approximation (Odian, 1991), whereby the rate of formation of radicals from decomposition of initiator molecules is almost balanced by the rate of termination. In the FRRPP system, deviations from this approximation were already observed even at low conversions. Since phase separation might have already been occurring, then the propagating radicals could actually be within high polymer concentration domains.

This means that these domains could be at their gel effect condition. However, this may not be entirely true because the end of the rise in conversion–time data may not coincide with the glass effect of the reactor system. In the polystyrene/styrene/ether system, the polymer-rich phase can be conservatively taken to contain about 28 wt% polystyrene, 7 wt% S, with the rest as ether (Fig. 2.3.1). This corresponds to a glass transition temperature of −80°C, which is well below that of the operating temperature of 80°C. In the calculations, T_g or T_m values are 100°C for polystyrene (Fried, 1995), −31°C for styrene (Fried, 1995), and −116°C for ether (Dean, 1985).

If there is a possibility that the polymer-rich domains were assumed at a higher temperature, then phase behavior could force them into a high polymer concentration. This can explain the reduction of the termination rate coefficient, but not the propagation rate coefficient. However, it is well known that adjacent to the boundary of the phase envelope for liquid–liquid phase separation in amorphous systems is a spinodal curve (McMaster, 1975). In this case, polymer-rich domains that were originally in the phase boundary will be driven toward the spinodal curve by local heating (Fig. 2.2.5). From past modeling (Caneba and Soong, 1985b) and experimental (Caneba and Saxena, 1992) work in binary polymer systems, it was found that a system in the spinodal curve had a vanishing mutual diffusivity. In a ternary system, this translates to vanishing concentration-gradient-based diffusional mass fluxes for all the components. Thus, while there was ample Brownian motion of the various small molecules and polymer segments, radical sites that were starved of the monomer cannot propagate much further because monomer molecules did not move away from their high-concentration regions. This resulted in reductions of propagation and termination rate coefficients, but it may not end there. Was it possible that within the polymer-rich phase, even higher polymer concentration domains can form? This means that in Fig. 2.1.11, Point B can find itself in a higher temperature phase envelope and phase separate into another polymer-rich phase at Point C or C'. Further reaction can keep this going at even higher polymer compositions and even more exponentially lower reaction rates due to even lower diffusion rates. This is consistent with the linear conversion–time plots in the log–log scale in Fig. 2.3.10, as well as the conclusions from local heating and energy analysis section (Section 2.2).

Further calculations supporting this hypothesis have been facilitated by the following radical population measurements.

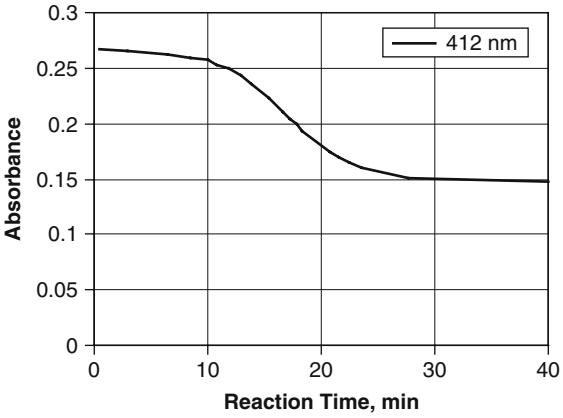

Fig. 2.3.12 Spectrophotometer intensity vs time for the determination of concentration of polystyrene radicals from the FRRPP system (Replotted with permission from Wang et al., 1999)

2.3.1.3 Studies of Radical Populations

Spectrophotometric Analysis of PS Radicals

Spectrophotometer, Spec 20D (from Milton Roy, Inc.), was used for the determination of radical concentrations of PS samples produced through the FRRPP process. A 1-ml DPPH/toluene solution of concentration 5.16×10^{-6} mol/ml was used to react with 1 ml PS samples in ether and acetone. Changes in transmitted light intensities (at 412 nm) were recorded as a function of time (Fig. 2.3.12).

Radical concentrations were then calculated from the light intensity differences using a calibration curve obtained from direct determination of PS radical concentration using an electron spin resonance spectrometer vs light absorbance at 412 nm (Fig. 2.3.13).

End-group Analysis of PS in Reactor

Purified PS samples were dissolved in chloroform. Then, the carboxylic end-groups of the PS sample were titrated with 0.02 N NaOH/ethanol solution using 0.5% phenolphthalein–ethanol solution (color changes from colorless to pink at pH > 8)

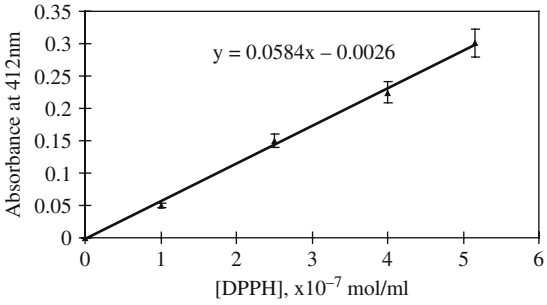

Fig. 2.3.13 Radical concentration calibration curve for determining the polystyrene radical concentration using a spectrophotometer approach. The maximum light absorbance occurs at 412 nm for DPPH/DMF solution (Reproduced with permission from Wang, 1997)

at room temperature. The NaOH/ethanol solution was standardized with pre-dried potassium acid phthalate (KHP). The carboxylic group concentrations were calculated from the amount of NaOH/ethanol solutions used.

A Mattson FT-IR (Galaxy-3000) was used to measure the amount of C=O and C–O groups in PS samples prepared from acetone and ether, and their characteristic peaks of 1711 and 1120 cm^{-1} were chosen, respectively. The purified PS powder samples were mixed with KBr crystal powder, pressed into transparent thin films, and placed into the FT-IR machine for spectrum scan. Calibration lines were constructed by measuring spectra of standard PS/adipic acid and standard PS/*n*-butyl ether mixtures at different levels.

Polystyrene Radical and End-Group Measurements

Figure 2.3.14 shows the evolution of radical concentration for the polymerization of styrene in ether under FRRPP conditions. It can be seen that the radical concentration goes up, overshoots a little, and then reaches an asymptote. At the asymptote, most of the initiator molecules have already been exhausted.

Figure 2.3.14 shows evolution of [COOH], [C=O], and [C–O] species in polystyrene samples that were polymerized using carboxy-functional V-501 initiator and ether as solvent. Very low [C–O] readings imply that there was practically no radical attack on ether to produce new growing radicals, such as chain transfer.

In order to determine the amount of polymer radical compared to live and dead polymer species, we used the results of end-group analyses of carboxylic acid from the initiator, carbonyl group from the carboxylic end-group of the initiator and from acetone by chain transfer, and C–O bond from ether group by chain transfer. The following possible product polymer species have been identified after all initiator fragments have already been removed:

[*A*]: HOOC–PS–COOH
[*B*]: HOOC–PS·
[*C*]: HOOC–PS–solvent

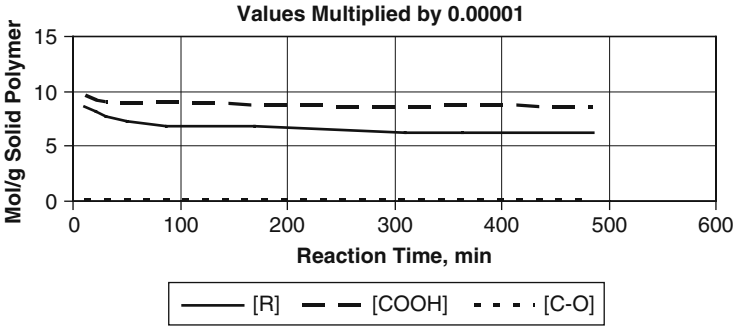

Fig. 2.3.14 Evolution of radical concentration [R], [COOH], and [C–O] for polymerization of styrene in ether at 80°C. Starting reaction compositions are 14 g/81 g/0.222 g S/ether/V501 (Replotted with permission from Wang et al., 1999)

[*D*]: Solvent–PS·
[*E*]: Solvent–PS–solvent

Note that the "solvent" end-group contained [C–O] species. If there was no chain transfer, then a unique functional group in the solvent will not be detected by subsequent infrared spectroscopy of the polymer materials. In general, the radical concentration, [*R*], would be

$$[R] = [B] - [D]. \tag{2.3.1}$$

The object was to determine the fraction of live polymer radical relative to all polymer species, X, noting that the C–O concentration in polystyrene is negligible (Fig. 2.3.14). Thus, if chain transfer to solvent was neglected, i.e., [*C*]=[*D*]=[*E*]=0. Alternately,

$$X = \frac{[R]}{[A] + [B]}, \tag{2.3.2}$$

$$[B] = [R] \tag{2.3.3}$$

and from the [COOH] balance,

$$[\text{COOH}] = 2[\text{A}] + [\text{B}]. \tag{2.3.4}.$$

Thus,

$$X = \frac{2[\text{R}]}{[\text{COOH}] + [\text{R}]}. \tag{2.3.5}.$$

With the plots of [R], [COOH], [C=O], and [C–O] vs time (Fig. 2.3.14), values of X vs time were obtained and shown in Fig. 2.3.15. It is therefore worth noting that for this system, the proportion of polymer radical compared to all polymeric species can be as high as 84%. Also, the value of X seems to have reached an asymptote at 80–85% levels, when almost all initiator molecules have already decomposed into radicals. Asymptotic behavior with time for X (Fig. 2.3.15) and for [R] (Fig. 2.3.14)

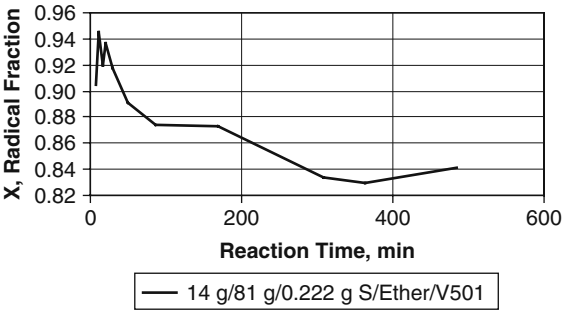

Fig. 2.3.15 Time evolution of X defined in Eq. (2.3.5), the fraction polymer radical compared to all polymeric species, for the ether-based FRRPP system (Replotted with permission from Wang et al., 1999)

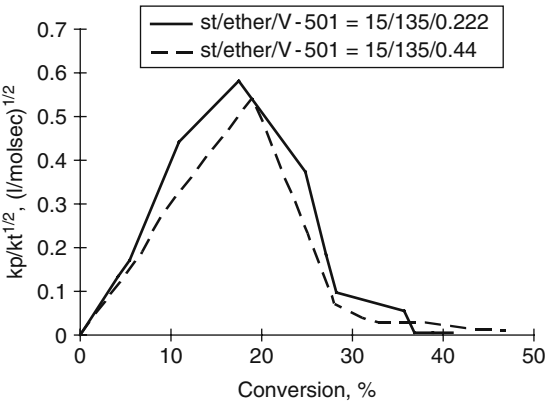

Fig. 2.3.16 Plot of $k_p(f/k_t)^{1/2}$ vs conversion for the ether-based FRRPP system at 80°C showing the drop in ordinate values during the period when the system exhibited a decrease in conversion rate starting at 30% conversion (Replotted with permission from Wang et al., 1999)

indicates a living radical aspect of the FRRPP process. Also, the fact that this occurs at values of X closer to 100% than 50% indicates the potential of the FRRPP process in the generation of high yields of block copolymers from free-radical chemistry.
Based on measurements of radical concentrations, conversions, end-groups, and molecular weight distributions, it has become possible to determine the values of $k_p(f/k_t)^{1/2}$. In Fig. 2.3.16, the plot of $k_p(f/k_t)^{1/2}$ vs conversion shows the extent of the reduction of the propagation rate coefficient compared to the termination rate coefficient for the ether-based system. The calculation procedure for ordinate values was based on the use of quasi-steady-state approximation to our conversion and molecular weight data (Aggarwal, 1993). In the slowdown period starting at 30% conversion, the drop in ordinate values was another way of looking into the effect of vanishing mass fluxes in the system. Since it happened to be the opposite of the rise in ordinate values for a gel effect situation, we called the physico-chemical mechanism of our work an anti-gel effect phenomenon. Similar calculations for acetone-based styrene and the water-based methacrylic acid reaction systems all resulted in a similar drop of the ordinate values as in Fig. 2.2.16.

2.3.2 Poly(Methacrylic Acid)/Methacrylic Acid/Water System

Since polymerization conditions for this system occur below the boiling temperature, an atmospheric version of the reactor system shown in Fig. 2.3.4 was used. Materials preparation and procedures were similar to those for PS/S FRRPP systems.

2.3.2.1 Results

Relevant phase envelopes for the PMAA/MAA/water system are shown in Section 1.1. Also, kinetics of phase separation results are presented for this system in Sections 1.4 and 1.5.

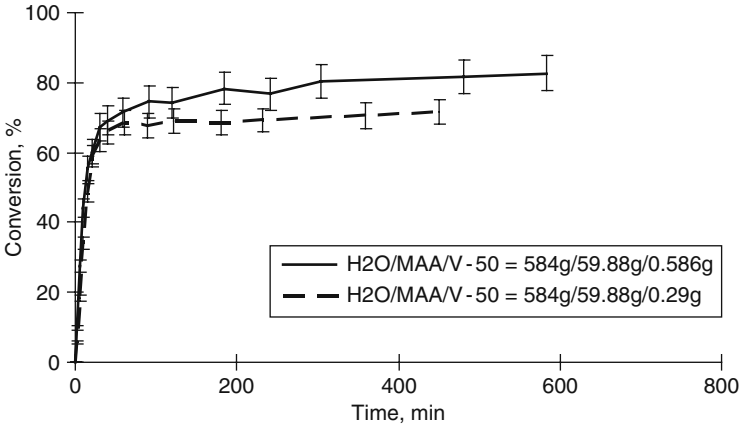

Fig. 2.3.17 Conversion–time plots for batch polymerization of methacrylic acid in water with different levels of initiator (V-50) at 90°C. The starting compositions are given in the plots (Replotted with permission from Wang et al., 1999)

Figure 2.3.17 shows conversion–time plots for polymerization of MAA in water at 90°C, for two starting compositions with different initiator (V-50) levels. This is contrasted with similar plots in Fig. 2.3.18, which is also at 90°C, but at two amounts of monomers. In Fig. 2.3.19, a lower proportion of initiator was used at the same reactor temperature compared to that used in Fig. 2.3.18. More plots (Figs. 2.3.19–2.3.21) show the adherence of the system to FRRPP behavior. Finally,

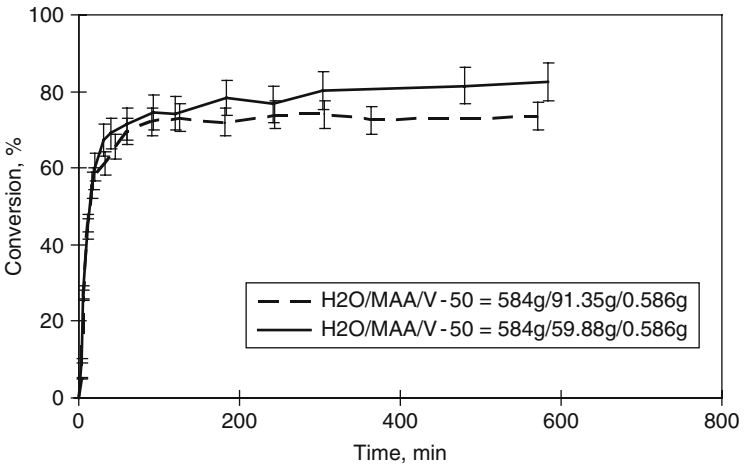

Fig. 2.3.18 Conversion–time plots for batch polymerization of methacrylic acid with V-50 initiator in different levels of water at 90°C. The starting compositions are given in the plots (Replotted with permission from Wang et al., 1999)

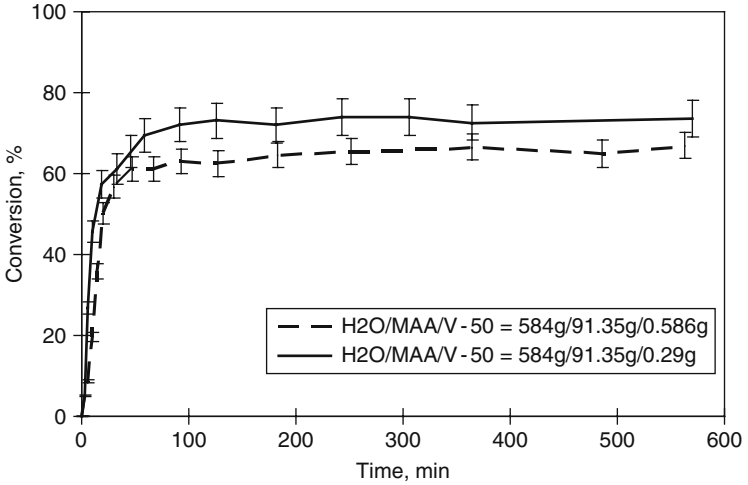

Fig. 2.3.19 Conversion–time plots for batch polymerization of methacrylic acid are less than what were used in Fig. 2.2.18, with different levels of initiator (V-50) at 90°C. The starting compositions are given in the plots (Replotted with permission from Wang et al., 1999)

in Fig. 2.3.22, a culminating comparison was made between FRRPP process and other conventional polymerization processes from MAA (DMF was used for the equivalent solvent system). The persistent polymer radical level at reaction times greater than five times the initiator half-life illustrated the uniqueness of the FRRPP process.

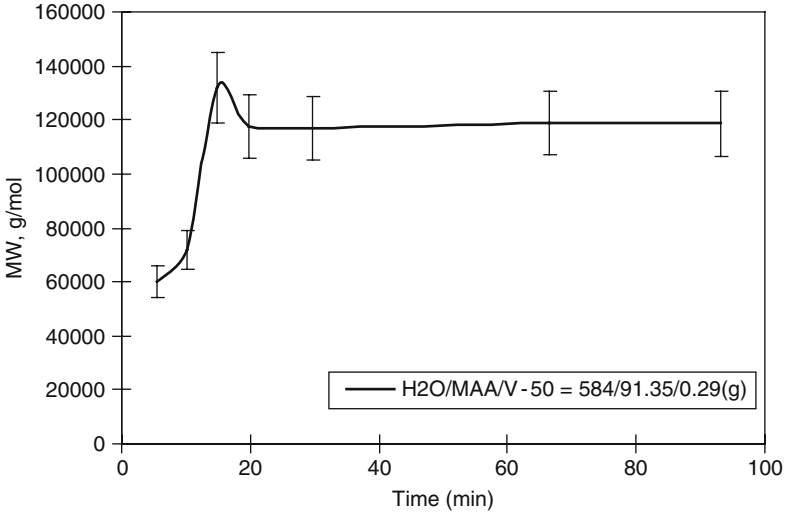

Fig. 2.3.20 Number-average molecular weight vs reaction time for samples from batch polymerization of MAA in water at 90°C. The starting composition is MAA/water/V-50 = 584 g/91.35 g/0.29 g (Replotted with permission from Wang et al., 1999)

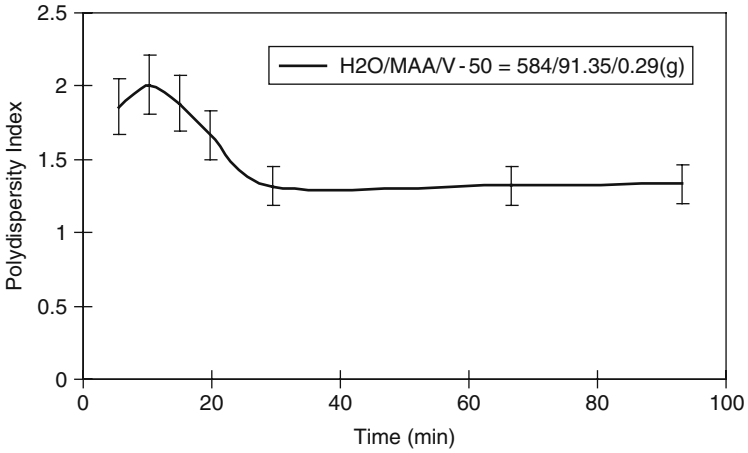

Fig. 2.3.21 Polydispersity index vs time for samples from batch polymerization of MAA in water at 90°C. The starting composition is MAA/water/V-50 = 584 g/91.35 g/0.29 g (Replotted with permission from Wang et al., 1999)

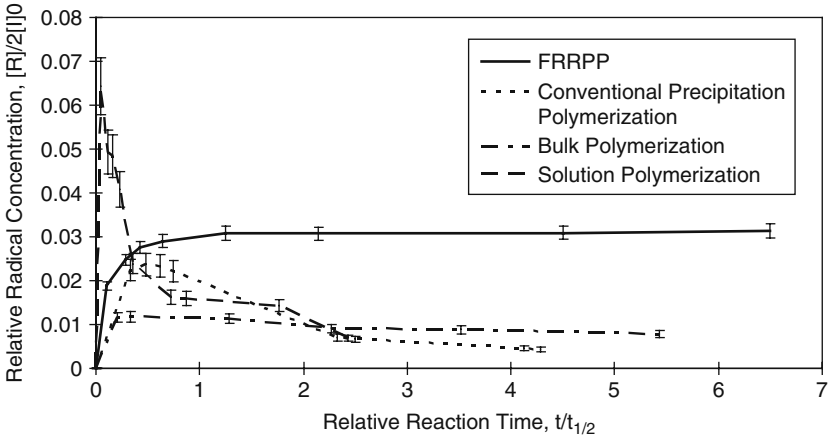

Fig. 2.3.22 Comparison of evolution of experimentally measured radical concentrations for different modes of polymerization of methacrylic acid. Note that the radical concentration stays almost constant for the FRRPP process. Reactions were done at 80ºC and at the same starting monomer concentration of 10 wt%, except for the bulk polymerization process (Replotted with permission from Wang et al., 1999)

2.3.2.2 Discussion of Results

Coupled with the necessity of the free-radical polymerization conditions, Caneba (1992a, b), Aggarwal (1993), and Wang (1997) studied systems with retrograde-precipitation behavior at convenient temperatures and pressures, including

PS/S/ether, PS/S/acetone, and PMAA/MAA/water systems. The following key features were observed and summarized for the FRRPP process (Aggarwal et al., 1996):

- gradual increase of conversion vs time even under gel effect conditions;
- local heating around the radical site;
- reduced rate of propagation, as well as the rate of radical–radical termination;
- relatively narrow molecular weight distributions;
- the existence of live radicals that could be exploited for production of block copolymers.

Initially, the reactive system follows the solution polymerization mechanism until the system reaches the phase envelope of inverse phase separation (LCST) and starts to separate into polymer-rich and polymer-lean phases. The polymer-lean phase follows solution polymerization kinetics, because there is often a very low polymer concentration. Whereas, the incipience and formation of the polymer-rich phase follows a new mechanism, which originates from the concept of a hot radical and has been detailed by Caneba (1992a, 1992b). In brief, during the propagation of the polymer radical, the net result of the conflict between the accelerating effect of the relatively high temperature around the radicals due to the exothermic reaction nature and the vanishing component diffusivities resulting from retrograde phase separation is a self-regulated propagation reaction. Another notable thing is that the relatively high polymer concentration around the radical sites reduces the radical–radical termination reaction, which ensures the preservation of certain amount of living radicals. Finally, the self-regulated propagation could result in polymer products with relatively narrow molecular weight distributions (MWDs).

2.4 Predictions of FRRPP Behavior Through the Coil–Globule Transition

In the previous section, conversion–time data indicate that for the FRRPP of styrene in ether, practical asymptotic values of 15 or 40% conversion were achieved for starting monomer compositions of 10 or 14.3 wt% (Figs. 2.3.5 and 2.3.8). From the phase envelopes shown in Fig. 2.3.1, these data correspond to overall polymer compositions in the reactor to be up to 2 or 4 wt% only. It should also be noted that number-average PS molecular weights were only up to 6,000 Da (Fig. 2.3.6) or 3,000 Da (Fig. 2.3.9), while thermodynamic data in Fig. 2.3.1 went down to PS molecular weight of only 25,000 Da. This means that the polymer may not have entered the polymer-rich regions in the phase diagram if it is required to cross the IPPC or spinodal, from a nonreactive standpoint. Indeed, reactor fluids have been shown to exhibit viscosities close to that of the solvent than a polymer solution at these conditions of FRRPP of styrene in ether. If the polymer macromolecules

tended to heat up on during chain polymerization and the phase envelope indicated macromolecular shrinking at higher temperatures, then there was a possibility that for this type of system, the polymer chains were not expanded enough to be considered in a semi-dilute configuration.

What might be anti-intuitive was the observation of extreme temperature rises in Section 2.2, when the starting styrene composition was in the order of 1 wt% in ether. This was a recurring observation in FRRPP systems. The explanation is that in dilute starting monomer concentrations, polymer molecules are scarce to the point that thermal sensors did not detect their temperatures. Thus, temperature control acted on the solvent material, which left the polymer molecules to heat up on their own, agglomerate, and form nucleated hot spots. This was made worst in a pressure-controlled reactor operation shown in Section 2.2, because in order to keep the pressure constant in a volatile medium, the reacting particles could now take advantage of the phase change to absorb the thermal effect of the exothermic reaction. At the same time, the vapor that was formed around the reacting domains would lower the convective heat transfer coefficient; thus facilitating more temperature rises within the particles.

It was fortuitous that the coil–globule transition had been advanced and validated in recent years. It was believed that for FRRPP of styrene in ether, what was occurring was a modified version of this phenomenon (Fig. 2.4.1). If one looks into the results in Section 2.1, the same can be said with the PMAA/MAA/water system. However, it was harder for this to be accepted, due to the relatively high conversions obtained in this type of FRRPP system. Still, a modification of the coil–globule transition picture was presented to involve a collection of chains in isolated domains for FRRPP systems, before they agglomerated into larger domains. The underlying reason is the fact that initiation of new chain polymerization events can occur within these domains.

In this section, effects of the current nonreactive version coil–globule transition in the FRRPP process was introduced using thermodynamic, transport phenomena, and kinetic concepts. Mathematical modeling efforts were applied to the polystyrene/styrene/ether system. This involved a probe into the model predictions

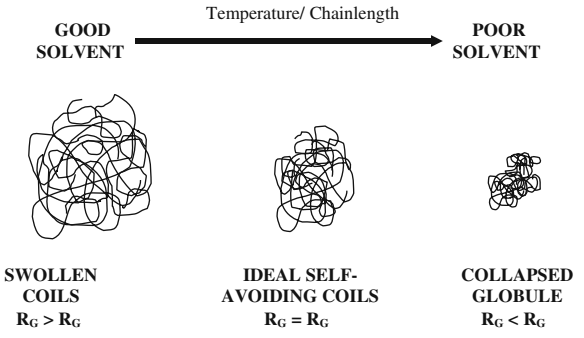

Fig. 2.4.1 A schematic depiction of the modified version of the coil–globule transition occurring in dilute FRRPP systems, whereby assembly of polymer swollen coils became collapsed globule through the intermediate θ-condition. $R_G/R_{G\theta}$ is the radius of gyration of the coil/globule of an individual polymer chain within the polymer domains

of the polymerization system starting in the dilute regime as isolated polymer chains that undergo coil–globule transition. Once a critical condition was reached whereby the molecular weight and polymer concentration (based on polymerization conversion and initial monomer charge) showed a slowdown in conversion rate from experimental data, the model was shifted to polymerizations in polymer-lean and polymer-rich phases.

2.4.1 Thermodynamics of Ternary Polystyrene/Styrene/Ether System

Dar (Dar, 1999; Dar and Caneba, 2002) calculated Flory–Huggins interaction parameters from the Flory–Prigogine equation-of-state theory (Eq. 1.1.7), which adequately represented the experimental system. From the work of Patterson and coworkers, the following expression for the Flory–Huggins interaction parameter, χ, was obtained:

$$\chi = \frac{c_1 \tilde{\nu}^2}{1 - \tilde{\nu}_1^{-\frac{1}{3}}} + \frac{c_1 \tau^2}{2\left[\frac{4}{3}\tilde{\nu}_1^{-\frac{1}{3}} - 1\right]}, \tag{2.4.1}$$

where

$$c_1 = \frac{P_1^* V_1^*}{R T_1^*} \tag{2.4.2}$$

and

$$\tau = 1 - \frac{T_{\text{ms}}^*}{T_{\text{polymer}}^*}. \tag{2.4.3}.$$

The reference temperature for polystyrene, T_{polymer}^*, was obtained in the literature, while T_{ms}^*, the reference temperature for the mixed styrene(1)–ether(2) is expressed from the Flory EOS theory as

$$T_{ms}^* = \frac{\left(\frac{\varphi_1 p_1^* T_1^* + \varphi_2 p_2^* T_2^*}{\varphi_1 p_1^* + \varphi_2 p_2^*}\right)}{\left(1 - \frac{\varphi_1 \theta_2 X_{12}}{\varphi_1 p_1^* + \varphi_2 p_2^*}\right)}. \tag{2.4.4}$$

In turn,

$$\theta_2 = \frac{\varphi_2}{\varphi_2 + \varphi_1 \left(\frac{s_1}{s_2}\right)},$$

$$X_{12} = p_1^* \left[1 - \left(\frac{s_1}{s_2} \right)^{\frac{1}{2}} \left(\frac{p_2^*}{p_1^*} \right)^{\frac{1}{2}} \right]^2 . \tag{2.4.5}$$

The quantity s_1/s_2 is the ratio of the molecular surface areas of contact per segment and can be estimated as (Abe and Flory, 1965)

$$\frac{s_1}{s_2} = \left(\frac{V_2^*}{V_1^*} \right)^{\frac{1}{3}} . \tag{2.4.6}$$

Abe and Flory (1965) did not use this expression for X_{12} but instead chose to fit excess enthalpy data. Since excess enthalpy data for the styrene/ether system were not readily available, this equation was used to estimate X_{12}. Dar (Dar, 1999; Dar and Caneba, 2002) validated the resulting value of X_{12} by comparing calculated excess molar enthalpy for the system using the Flory EOS (Abe and Flory, 1965, Howell et al., 1971) and the regular solution theory with solubility parameters obtained from the literature (Immergut and Brandrup, 1989). For the styrene/ether system, the two methods did not deviate by more than 10% for the entire composition range.

Parameters used for the calculated values of χ are summarized in Table 2.4.1.

2.4.2 Mass Transport Phenomena

In order to determine the various diffusion-controlled rate coefficients, monomer and polymer diffusivities were estimated. In general, the free-volume theory is the accepted model for the determination of these quantities. In this model, diffusion is

Table 2.4.1 Parameters and results of calculation of the Flory–Huggins χ-parameter at 80 and 90°C (Dar, 1999; Dar and Caneba, 2002; with permission)

Parameter	Value @ 80°C	Value @ 90°C
T	353 K	363 K
P	0.584 MPa	0.584 MPa
T^*_{styrene}	5349.42 K	5349.42 K
T^*_{ether}	4074.24 K	4074.24 K
$T^*_{\text{polystyrene}}$	8,191 K	8,191 K
$P^*_{styrene}$	542.5389 MPa	542.5389 MPa
P^*_{ether}	481.2829 MPa	481.2829 MPa
$V^*_{styrene}$	93.3144 ml/mol	92.3144 ml/mol
V^*_{ether}	76.1915 ml/mol	76.1915 ml/mol
c_{styrene}	1.138	1.138
c_{ether}	1.083	1.083
$s_{\text{styrene}}/s_{\text{ether}}$	0.9347	0.9347
τ	0.4892	0.4892
χ	0.8283	0.89

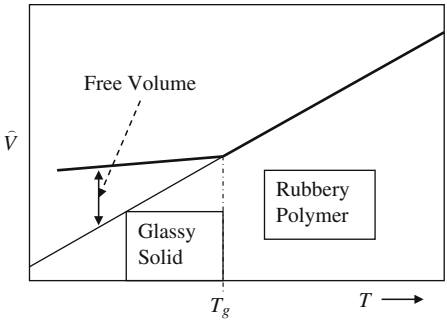

Fig. 2.4.2 Free volume of the polymer as the excess specific volume relative to extrapolated specific volume from the rubbery polymer behavior

based on the availability of an adjacent "hole" wherein the polymer or monomer can jump into. In turn, the "hole" is formed due to the presence of free volume within the system. The free volume is the excess specific volume of the glassy system compared to the specific volume behavior of the rubbery polymer extrapolated into the glassy solid region (Fig. 2.4.2).

Using the free-volume theory, the following polymer diffusivity expression attributed to Achilias and Kiparissides (1992) was used, which in turn was based on the scaling theory predications of De Gennes (1979)

$$D_2 = \left(\frac{D'_{02}}{M_W^2}\right)\exp\left[\frac{1}{\xi}\left(\frac{-\left(\omega_1\hat{V}_1^* + \omega_2\xi\hat{V}_2^*\right)}{\omega_1\left(\frac{K_{11}}{\gamma}\right)\left(K_{21} - T_{g1} + T\right) + \omega_2\left(\frac{K_{12}}{\gamma}\right)\left(K_{22} - T_{g2} + T\right)}\right)\right] \tag{2.4.7}$$

where

D_2 self-diffusivity of the polymer
D'_{02} constant pre-exponential factor
M_W - weight-average molecular weight
$\hat{V}_i^*$ specific critical hole free volume of component *i* required for a jump
ω_i weight fraction of component *i*
T_{gi} glass transition temperature of component *i*
γ overlap factor
K_{1i} free-volume parameter 1 for component *i*
K_{2i} free-volume parameter 2 for component *i*
ξ ratio of molar volumes for solvent and polymer jumping units and
T absolute temperature

The self-diffusion coefficient of the polymer in the limit of zero polymer concentration can be used to cancel the D'_{02} pre-exponential constant

$$D_{2_{\omega_1\to 1}} = \left(\frac{D'_{02}}{\left(M_W^2\right)_{\omega_1\to 1}}\right) \exp\left[\frac{1}{\xi}\left(\frac{-\left(\hat{V}_1^*\right)}{\left(\frac{K_{11}}{\gamma}\right)\left(K_{21}-T_{g1}+T\right)}\right)\right]. \tag{2.4.8}$$

Dividing Eq. (2.4.7) by Eq. (2.4.8) results in

$$D_2 = (D_2)_{\omega_1\to 1}\left(\frac{\left(M_W^2\right)_{\omega_1\to 1}}{M_W^2}\right) \exp\left[\frac{1}{\xi}\left(\frac{-\left(\omega_1\hat{V}_1^*+\omega_2\xi\hat{V}_2^*\right)}{\omega_1\left(\frac{K_{11}}{\gamma}\right)\left(K_{21}-T_{g1}+T\right)+\omega_2\left(\frac{K_{12}}{\gamma}\right)\left(K_{22}-T_{g2}+T\right)}\right) + \left(\frac{1}{\xi}\right)\left(\frac{\hat{V}_1^*}{\left(\frac{K_{11}}{\gamma}\right)\left(K_{21}-T_{g1}+T\right)}\right)\right]. \tag{2.4.9}$$

It is possible to estimate the self-diffusion coefficient at zero polymer concentration ($(D_2)_{\omega 1\to 1}$) using the Stokes–Einstein equation as

$$(D_2)_{\omega_1\to 1} = \frac{k_B T}{6\pi\eta_S R_H}, \tag{2.4.10}$$

where

k_B Boltzmann constant
η_S solvent viscosity, and
R_H hydraulic radius of the polymer molecule

The hydraulic radius of the polymer molecule (R_H) was estimated using the mean end-to-end distance calculations for a polymer globule as (Strobl, 1997)

$$R_H = \frac{2}{3}\frac{R_P}{\sqrt{6}}. \tag{2.4.11}$$

The size of the globule, R_P, was estimated by De Gennes (1979) as

$$R \cong \frac{aN^{\frac{1}{3}}}{\left(\chi-\frac{1}{2}\right)^{\frac{1}{3}}}, \tag{2.4.12}$$

where a is the effective length per unit, N is the number of repeat units, and χ is the Flory–Huggins interaction parameter. Data used to determine R_P were gathered for polystyrene (number-average molecular weight, M_n = 7,600 g/mol or Da) in cyclohexane (Nierlich et al., 1978).

For the diffusivity of the monomer, the following pseudobinary expression attributed to Vrentasand Duda (1977) was used (Dar and Caneba, 2002):

$$D_1 = D_{01}\exp\left(\frac{-E}{RT}\right)\exp\left(\frac{-\left(\omega_1\hat{V}_1^* + \omega_2\xi\hat{V}_2^*\right)}{\omega_1\left(\frac{K_{11}}{\gamma}\right)\left(K_{21}-T_{g1}+T\right)+\omega_2\left(\frac{K_{12}}{\gamma}\right)\left(K_{22}-T_{g2}+T\right)}\right), \tag{2.4.13}$$

where

D_1 self-diffusivity of monomer–solvent mixture
D_{01} constant pre-exponential factor, and
E activation energy for a jump per mole

Specifically, the styrene–ether small-molecule mixture was used as a mixed solvent in Eq. (2.4.12). The resulting diffusivity value of the mixed solvent was assumed to be valid for styrene in the subsequent calculation of the propagation rate coefficient. This is a valid assumption since ether and styrene have enough polarity in them.

Values of the polymer and monomer diffusivities as well as intermediate quantities are presented in Table 2.4.2.

Table 2.4.2 Parameters and results for free-volume theory calculations of polymer and solvent self-diffusivities at 80°C (Dar, 1999; Dar and Caneba, 2002; with permission)

Parameter	Value @ 80°C	Value @ 90°C
T	353 K	363 K
V_1^*	1.0223 ml/g	1.0223 ml/g
V_2^*	0.8296 ml/g	0.8296 ml/g
K_{12}/γ	4.1037×10^{-4}	4.1037×10^{-4}
$K_{22}-T_{g2}$	−311	−311
D_0	1.7806×10^{-7} m^2/s	1.7806×10^{-7} m^2/s
K_{11}/γ	1.0051×10^{-3}	1.0051×10^{-3}
$K_{21}-T_{g1}$	−14.8161 K	−14.8161 K
ξ	0.57486	0.57486
$\omega_{polystyrene}$	0.5457	0.625
$\omega_{styrene}$	0.0591	0.033
ω_{ether}	0.3952	0.342
M_w	8,000 Da	8,000 Da
$(M_w)_{\omega 1=1}$	8,000 Da	8,000 Da
$(D_2)_{\omega 1=1}$	3.027×10^{-9} m^2/s	3.2598×10^{-9} m^2/s
$(D_1)_{\omega polystyrene}$	2.1352×10^{-9}m^2/s	1.5698×10^{-9}m^2/s
$(D_2)_{\omega polystyrene}$	2.5784×10^{-10}m^2/s	1.4474×10^{-10}m^2/s
$(D_1)_{\omega 2=0.95}$	4.7802×10^{-14} m^2/s	4.7802×10^{-14} m^2/s
$(D_2)_{\omega 2=0.95}$	2.4995×10^{-18} m^2/s	2.4995×10^{-18} m^2/s

2.4.3 Calculation of Kinetic Parameters and Polymer Formation Behavior

The Achilias–Kiparissides (AK) model (1992) for propagation and termination rate coefficients, which is based on the CCS model (Chiu et al., 1983), was used by Dar (Dar and Caneba, 2002) to calculate the propagation and termination rate coefficients for the FRRPP of styrene in ether. Expressions for the k_p and k_t given below were based on a molecular picture whereby the terminating polymer chains had to undergo translational motion toward each other, before radical sites underwent segmental motion. As such, the rate limiting step was segmental diffusion of radical sites for termination; thus, polymer self-diffusivity was considered. Propagation was based on monomer diffusion into the reactive radical sites.

$$\frac{1}{k_t} = \frac{1}{k_{t0}} + \frac{r_t^2}{3}\frac{\lambda_0}{D_{pe}} \tag{2.4.14}$$

$$\frac{1}{k_p} = \frac{1}{k_{p0}} + \frac{r_m^2}{3}\frac{\lambda_0}{D_m} \tag{2.4.15}$$

where

k_t effective termination rate coefficient
k_{to} intrinsic termination rate coefficient
k_p effective propagation rate coefficient
k_{po} intrinsic propagation rate coefficient
r_t minimum distance of approach for a termination reaction to take place
r_m minimum distance of approach for a propagation reaction to take place
D_{pe} effective polymer self-diffusivity
D_m monomer self-diffusivity, and
λ_0 concentration of polymer radicals

The termination radius r_t or the minimum distance between radical sites for termination to occur can be obtained from

$$r_t = \frac{\left[\ln\left(\frac{1000\tau^3}{N_A\lambda_0\pi^{\frac{3}{2}}}\right)\right]^{\frac{1}{2}}}{\tau}, \tag{2.4.16}$$

where τ is a constant given by

$$\tau = \left(\frac{3}{2j_c\delta^2}\right)^{\frac{1}{2}} \tag{2.4.17}$$

and

j_c entanglement spacing between polymer chains
δ average root mean square end to end distance for a polymer chain per square root of the chain length

The quantity, j_c, can be calculated based on the work of Soh and Sundberg (1982):

$$j_c = \frac{X_{c0}}{2\varphi_p}, \tag{2.4.18}$$

where

X_{co} critical degree of polymerization for the entanglement of polymerchains
ϕ_p volume fraction of polymer

and

$$\delta = \frac{R}{\sqrt{N}}. \tag{2.4.19}$$

Table 2.4.3 shows parameter values used for the calculation of the rate coefficients and for subsequent computer simulation efforts.

In order to simulate the kinetic behavior of the system and compare results to experimental data, the method of moments was used (Dar, 1999). At the start, the system was in a dilute solution, whereby the polymer was in the form of globules. At some critical conversion, the system split into a polymer-rich phase and a polymer-lean phase. The critical conversion was obtained from experimental conversion–time data, wherein the conversion rate slowed down after its initial fast rise. This is usually close to the spinodal curve or IPPC in Fig. 1.1.8 for the particular temperature of interest (80°C). The relative amounts of polymer-rich and polymer-lean phases were obtained from the lever-arm rule in the phase diagram along the tie line. In the initial dilute system and in the polymer-lean phase, intrinsic propagation rate coefficient (k_{po}) and intrinsic termination rate coefficient (k_{to}) were used. When splitting of the phases occurred, kinetic simulations were done for each phase independently. Overall conversion, average molecular weights, polydispersity indices, radical concentrations, and initiator concentrations were obtained from an averaging procedure for the phases in equilibrium. Simulations were continued until initiator is exhausted or until the conversion–time behavior reached a practical asymptote.

Simulations were performed for critical conversions corresponding to points in the reaction trajectory that were close to the binodal compositions for two initial monomer concentrations: (a) $[M]_o$=1.13463 mol/l or initial monomer weight fraction of 0.10 and (b) $[M]_o$=0.41423 mol/l or initial monomer weight fraction of 0.0365. As for starting initiator concentrations, they were (a) 0.00261 mol/l for $[M]_o$=0.41423 mol/l and (b) 0.00741 mol/l for $[M]_o$=1.13463 mol/l.

Figure 2.4.3 shows conversion–time comparison for the polystyrene–styrene–ether reactive system between experimental data and computer simulation results at

Table 2.4.3 Parameters and results for rate coefficient calculations based on the Achilias and Kiparissides model at T = 80°C and 90°C (Dar, 1999; Dar and Caneba, 2002; with permission)

Parameter	Value @ 80°C	Value @ 90°C
T	353 K	363 K
P	0.584 MPa	0.584 MPa
N	76	76
a	3.11×10^{-10} m	3.11×10^{-10} m
X_{co}	385	385
R	1.91×10^{-9} m	1.91×10^{-9} m
R_h, r_b	5.1984×10^{-10}	5.1984×10^{-10}
$k_{to}(T)$	$1.022 \times 10^{11} e^{(-2268/RT)} =$ 4.029×10^{9} l/mol min	$1.022 \times 10^{11} e^{(-2268/RT)} =$ 4.404×10^{9} l/mol min
$k_{po}(T)$	$6.54 \times 10^{8} e^{(-7051/RT)} =$ 2.817×10^{4} l/mol min	$6.54 \times 10^{8} e^{(-7051/RT)} =$ 3.716×10^{4} l/mol min
λ_o	2.7344×10^{-3}mol/l For $\omega_{polystyrene}$=0.5457	2.7344×10^{-3}mol/l For $\omega_{polystyrene}$=0.625
k_t/k_{to}	0.0021	0.0012
k_t	8.461×10^{6} l/mol min	52.848 l/mol min
k_p/k_{po}	0.9996	0.9994
k_p	2.817×10^{4} l/mol min	3.714×10^{9} l/mol min
$k_{po}/(k_{to})^{0.5}$	0.0573 (l/mol s)$^{0.5}$	0.0723 (l/mol s)$^{0.5}$
$k_p/(k_t)^{0.5}$	1.258 (l/mol s)$^{0.5}$	2.0546 (l/mol s)$^{0.5}$
For $\omega_{polystyrene}$=0.98		
k_t/k_{to}	2.7267×10^{-15}	4.9837×10^{-13}
k_t	1.0986×10^{-5} l/mol min	2.195×10^{-3} l/mol min
k_p/k_{po}	4.7668×10^{-4}	0.0081
k_p	13.428 l/mol min	301 l/mol min
$k_p/(k_t)^{0.5}$	4,051 (l/mol s)$^{0.5}$	6,425 (l/mol s)$^{0.5}$

80°C and 90°C for the two initial monomer and initiator concentrations. It is clear that for $[I]_o$=0.00741 mol/l and $[M]_o$=1.13463 mol/l, a critical conversion between 20 and 40% is appropriate. For $[I]_o$ =0.00261 mol/l and $[M]_o$=0.41423 mol/l, it seems to be between 10 and 25%. In Fig. 2.4.4, number-average molecular weight comparisons are shown, which can be used to narrow down critical conversions for the two sets of initial monomer and initiator concentrations. For the reactor fluid temperature of 80ºC, the following appropriate values of critical conversions are (a) 30% for $[I]_o$=0.00741 mol/l and $[M]_o$=1.13463 mol/l and (b) 23% for $[I]_o$ =0.00261 mol/l and $[M]_o$=0.41423 mol/l.

In Fig. 2.4.5, simulations results for polydispersity indices are seen to be greater than those from experimental values, but they are reasonably accurate. In Fig. 2.4.6, polymer radical concentrations from the simulations exhibited a jump behavior, which occurred at the critical conversion values.

The transition to the polymer-rich phase resulted in radical trapping. However, compared to experimental data in Fig. 2.3.16, polymer radical concentrations from the simulations slowly drifted down rather than staying at asymptotic values. What this means is that in the FRRPP process, there seems to be this enhanced radical

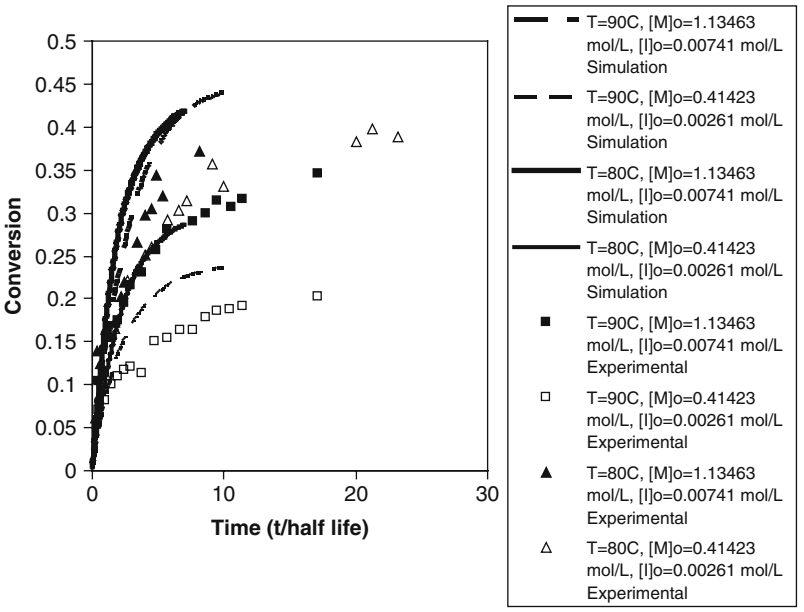

Fig. 2.4.3 Conversion–time comparison for the polystyrene/styrene/ether reactive system between experimental data and computer simulation results at 80°C for the two initial monomer and initiator concentrations (Replotted from Dar, 1999; Dar and Caneba, 2002; with permission)

trapping mechanism that also keeps molecular sizes in control as the polymerization reaction proceeds. If one were to refer to Section 2.2, a relatively large thermal effect can explain this discrepancy.

In the next section, a probe into the extent of the thermal effect within reactive phase separated polymer-rich particulates will be made, based on experimental data.

2.4.4 Thermal Analysis

Based on the kinetic results from the previous subsections, Dar (1999) estimated interior particle temperatures for FRRPP of styrene in ether. He used the same approach as the quasi-steady-state approximation in Section 2.2, which resulted in the use of the same differential equation and boundary conditions (Eqs. 2.2.1 and 2.2.2). The difference is that he employed a temperature-independent energy source term wherein the rate of reaction was based on the calculated derivative of monomer concentration with respect to time within a certain population of polymer-rich particles; thus,

$$\dot{q} = (-\Delta H_{\mathrm{P}}) \left[-\frac{d\,[M]}{dt} \right]. \tag{2.4.20}$$

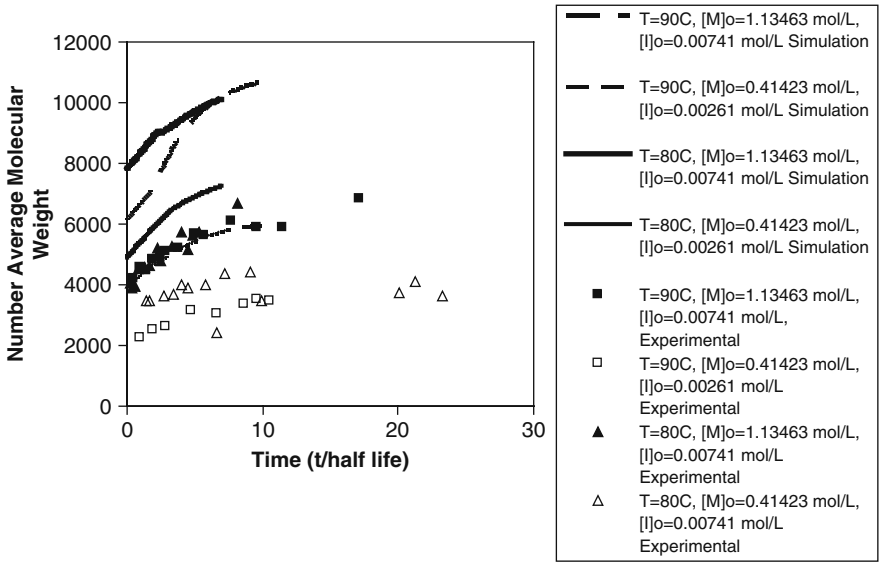

Fig. 2.4.4 Comparison of number-average molecular weights for the polystyrene/styrene/ether reactive system between experimental data and computer simulation results at 80°C (Replotted from Dar, 1999; Dar and Caneba, 2002; with permission)

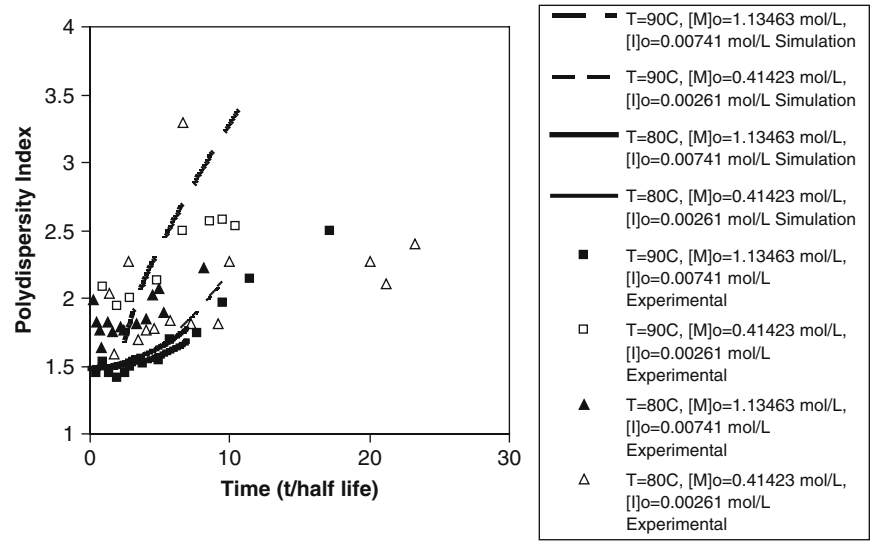

Fig. 2.4.5 Comparison of polydispersity indices for the polystyrene/styrene/ether reactive system between experimental data and computer simulation results at 80°C (Replotted from Dar, 1999; Dar and Caneba, 2002; with permission)

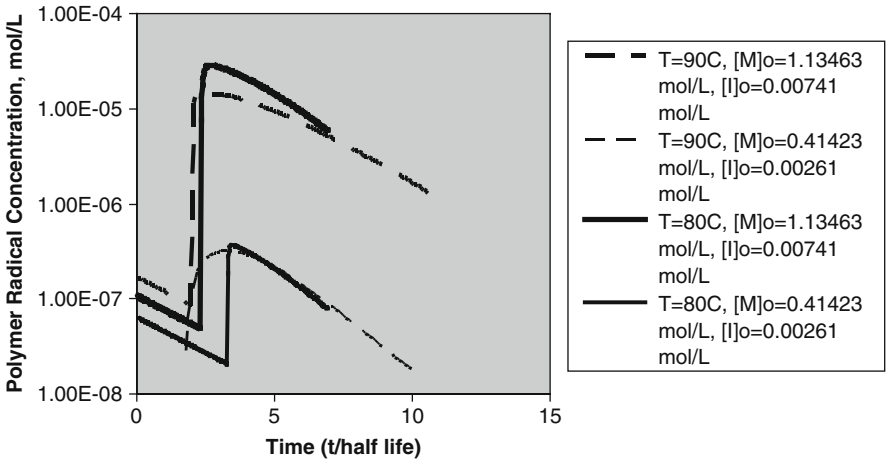

Fig. 2.4.6 Result of simulation of polymer radical concentration vs time for the polystyrene/styrene/ether reactive system at 80°C (Replotted from Dar, 1999; Dar and Caneba, 2002; with permission)

The fact that LCST or even UCST behavior was not taken into account ($\alpha = 0$ in Section 2.2) means that the maximum interior temperature obtained from this calculation is an overestimation.

Polymerization reactions were occurring in the coils within the polymer-lean phase, in small particle globules, and in large particle agglomerated globules. Thus,

$$\frac{d[M]}{dt}_{\text{total}} = \left(\varphi \frac{d[M]}{dt}\right)_{\text{polymer lean}} + \left(\varphi \frac{d[M]}{dt}\right)_{\text{large particles}} + \left(\varphi \frac{d[M]}{dt}\right)_{\text{small particles}}, \tag{2.4.21}$$

where ϕ is the volume fraction. The total rate of change of the monomer concentration can be estimated from experimental conversion–time data as

$$\frac{d[M]}{dt}_{\text{total}} = \frac{([M]_0 V_0(1+\beta) + [M]V_0)}{V_0(1-\varepsilon x+\beta)} \frac{dx}{dt}, \tag{2.4.22}$$

where $[M]_0$ is the initial monomer concentration, V_0 is the initial total volume, and x is fractional conversion. The parameter ϵ accounted for the change in density of the system, and β is a parameter which took the presence of solvent into account. Mathematically

$$\varepsilon = 1 - \frac{\rho_{\text{monomer}}}{\rho_{\text{polymer}}} \tag{2.4.23}$$

and

$$\beta = \frac{f_s}{1 - f_s}. \tag{2.4.24}$$

A similar expression to Eq. (2.4.22) was used to calculate the rate of monomer consumption for the small particles, which were the collapsed globules. The difference is that model kinetic coefficients were used to calculate the derivative of the fractional conversion with time (*dx/dt*), which ended up to be

$$\left(\frac{dx}{dt}\right)_{\text{small particles}} = \left(\frac{k_p f^{\frac{1}{2}}}{k_t^{\frac{1}{2}}}\right)\left(k_d[I_0]e^{-k_d t}\right)^{\frac{1}{2}}(1 - x) \tag{2.4.25}$$

For the rate of monomer consumption in the polymer-lean phase, the assumption is made that these are low molecular weight coils up to 30 monomer units long. Thus,

$$\frac{d[M]}{dt}_{\text{polymer lean}} \approx 30\frac{d[I]}{dt}. \tag{2.4.26}$$

Finally, Eq. (2.4.21) was used to determine the rate of monomer consumption in the large particles, which were also agglomerated globules.

$$\frac{d[M]}{dt}_{\text{large particle}} = \frac{\frac{d[M]}{dt}_{\text{total}} - \left(\frac{d[M]}{dt}\varphi\right)_{\text{polymer lean}} - \left(\frac{d[M]}{dt}\varphi\right)_{\text{small particles}}}{f_{\text{Active}}\varphi_{\text{large particles}}}. \tag{2.4.27}$$

Further assumptions included the following:

1. Volume fraction of large particles ($\phi_{\text{large particles}}$) compared to sum of small and large particles was equal to 0.1.
2. Volume fraction of active large particles (f_{active}) was set to 0.25.
3. Average thermal conductivity of the system was based on weighted average of those of the system components.

Parameters used for the calculations of temperature profiles of large particles for the polystyrene/styrene/ether system are shown in Table 2.4.4.

Based on the above method, Fig. 2.4.7 indicates a maximum temperature for the large particles of 0.1 cm (1 mm), the maximum temperature is 328 K or 135°C, at the center of the reactive large particle (Dar, 1999). Using the same simulation program it will take large reacting particles to have radii less than 0.01 cm for its center temperature to be only 1°C above the reactor fluid temperature. While this is nowhere close to the carbonization temperatures observed in low monomer charge formulation of the same system, it is consistent with the picture presented in Section 2.1. It will be shown that reactive particles from the S/PS/ether system can be as much as 0.35 mm in diameter. Also, it should be noted that Fig. 2.4.7 is based

Table 2.4.4 Physical properties and parameters used in heat transfer calculations for the styrene/ether system (Dar, 1999; with permission)

Parameter	Value
T	353 (K)
$MW_{styrene}$	104.152 (g/mol)
MW_{ether}	74.123 (g/mol)
$MW_{polystyrene}$	8000 (g/mol)
$k_{styrene}$	30.2×10^{-5} (cal/cm s ^{o}C)
k_{ether}	18.66×10^{-5} (cal/cm s ^{o}C)
$k_{polystyrene}$	37.75×10^{-5} (cal/cm s °C)
$\omega_{polystyrene}$	0.5457
$\omega_{styrene}$	0.0591

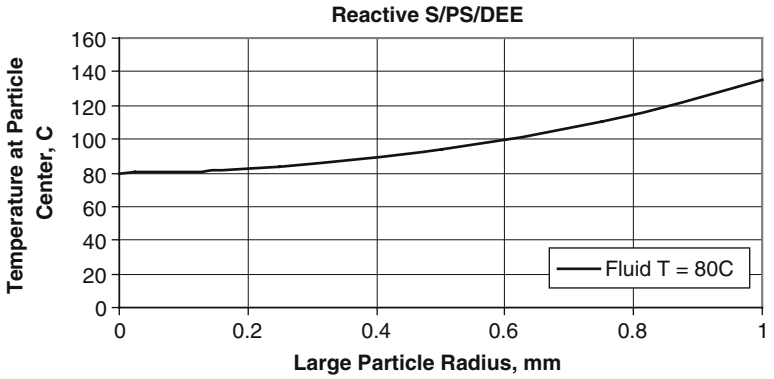

Fig. 2.4.7 Simulation result for the center temperature of large particles from the reactive polystyrene/styrene/ether reactive system at 80°C

on a conventional polymerization model, which does not take into account physico-chemical and thermal effects associated with the FRRPP process.

2.4.5 Nomenclature

2.4.5.1 Alphabets

Upper Case

E – activation energy for a jump per mole, J/mol
N – number of repeat units of the polymer chain
R– universal gas constant, J/mol K
P – pessure, MPa
T – absolute temperature, K
V – volume, m^3

Lower Case

a – effective length per unit
s – molecular surface area of contact per segment
t – time, s
x – fractional conversion

2.4.5.2 Subscripts

1– styrene component
2– ether component
i – component label
0 – initial
p – polymer

2.4.5.3 Superscripts

None

2.4.5.4 Greek Symbols

β –defined in Eq. (2.4.24)
χ –Flory–Huggins interaction parameter
δ – average root mean square end-to-end distance for a polymer chain per square root of the chain length, m
γ – overlap factor
ε – defined in Eq. (2.4.23)
ξ– ratio of molar volumes for solvent and polymer jumping units
τ– defined in Eq. (2.4.3)
ϕ – volume fraction
θ – defined in Eq. (2.4.5)
ω_i – weight fraction

2.4.5.5 Other Symbols

c_1–constant defined in Eq. (2.4.2)
ΔH_P – heat of polymerization, J/mol
D_{pe} – effective polymer self-diffusivity, m^2/s
D_m – monomer self-diffusivity, m^2/s
D_1 – self-diffusivity of monomer–solvent mixture, m^2/s
D_{01} – constant pre-exponential factor, m^2/s
D_2 – self-diffusivity of the polymer, m^2/s
$(D_2)_{\omega 1 \to 1}$ – self-diffusion coefficient at zero polymer concentration, m^2/s

D'_{02} – constant pre-exponential factor, m^2/s
f_s – volume fraction solvent in reactor
K_1 – free-volume parameter 1
K_2 – free-volume parameter 2
k_B – Boltzmann constant
k_d – initiator decomposition rate coefficient, s^{-1}
k_t – termination rate coefficient, mol/l s
k_{to} – intrinsic termination rate coefficient, l/mol s
k_p – propagation rate coefficient, l/mol s
k_{po} – intrinsic propagation rate coefficient, l/mol s
λ_0 – concentration of polymer radicals, l/mol
$[I]$ – concentration of initiator, mol/l
j_c- entanglement spacing between polymer chains
M_n – number-average molecular weight, g/mol
M_W – weight-average molecular weight, g/mol
N_A – Avogadro's number, 6.023×10^{23} molecules/mol
η_S – solvent viscosity, Pa s
$[M]$ – concentration of monomer, mol/l
$\tilde{v}_1$ – reduced volume of styrene
P^* – reference pressure, bar
$\dot{q}$ – energy source term, W/m^3
r_t – minimum distance of approach for a termination reaction to take place, m
r_m – minimum distance of approach for a propagation reaction to take place, m
R_G – radius of gyration of the coil/globule of an individual polymer chain within the polymer domains, m
$R_{G\theta}$ – radius of gyration at theta condition of the coil/globule of an individual polymer chain within the polymer domains, m
R_H – hydraulic radius of the polymer molecule, m
V^* – reference volume, m^3/mol
T^* – reference temperature, K
T^*_{ms} – reference temperature for the mixed styrene(1)–ether(2)
$T^*_{polymer}$ – reference temperature for polystyrene
T_g – glass transition temperature
X_{co} – critical degree of polymerization for the entanglement of polymer chains
X_{12} – defined in Eq. (2.4.5)
$\hat{V}^*_i$ – specific critical hole-free volume of component i required for a jump

2.5 Physicochemical Quantitative Description of FRRPP

The occurrence of the LCST has been established as a necessary condition for the FRRPP phenomenon in free-radical polymerization systems. In Section 2.2, an initial attempt was made to advance a mathematical model that incorporates not only the LCST behavior but also the reaction-transport aspects of the FRRPP process. In

this section, this initial quantitative characterization will be elaborated and generalized from findings in Section 2.2.

A closer look at Eqs. (2.2.5–2.6.7) and resulting Table 2.2.2 establishes a hint of a more complete quantitative description of the FRRPP process. This was done through simulation results with a wider set of parameters and results are shown in Table 2.5.1.

From the table, it is evident that the dimensionless energy source term

Table 2.5.1 Results with wider set of parameters from the method used to generate Table 2.2.2

α	β	γ	θ @ η=0	$d\theta/d\eta$ @ η=1	Φ_0=[$\alpha\theta(0)+\beta$] exp(-$\gamma/\theta(0)$)	$C\tilde{n}=\alpha\beta/\Phi_o$
−0.1	0.5	0.5	1.0407	−0.0812	0.245	−0.2042
−0.1	0.5	2.0	1.009	−0.0182	0.055	−0.90934
−0.1	2.5	0.5	1.26	−0.5055	1.60	−0.1566
−0.1	2.5	2.0	1.058	−0.1131	0.362	−0.6914
0.2	0.5	1.0	1.0446	−0.0878	0.272	0.3674
0.2	0.5	2.0	1.0162	−0.032	0.0983	1.0177
0.4	0.5	0.5	1.0967	−0.1885	0.595	0.3361
0.4	0.5	2.0	1.021	−0.0414	0.128	1.561
0.5	−1	0.5	0.9488	0.1021	−0.31033	1.611
0.5	−1	1	0.9693	0.0613	−0.18368	2.722
0.6	−0.5	0.5	1.0106	−0.0208	0.06485	−4.626
0.6	−1	1	0.9752	0.0493	−0.14879	4.032
0.6	−1	2	0.991	0.018	−0.05388	11.14
0.6	0.5	0.5	1.121	−0.2334	0.750657	0.3997
0.6	3	2.5	1.0544	−0.1042	0.339237	5.3060
−0.2	1	1	1.0504	−0.0995	0.304879	−0.656
−0.2	2.5	2	1.0559	−0.1081	0.344355	−1.4520
0.1	0.1	0.1	1.0307	−0.0608	0.184293	0.05426
−9	10	8	1	−0.0001	0.000335	−268286
−8	10	8	1	−0.0002	0.000671	−119238
−7	10	8	1	−0.0003	0.001006	−69556
−6	10	8	1	−0.0004	0.001342	−44714
−5	10	8	1	−0.0006	0.001677	−29810
7	−5	3	1.0409	−0.0812	0.111683	−312.4
−5	7	3	1.0168	−0.0333	0.100239	−349.2
8	−7	3	1.009	−0.0173	0.054819	−1021
−2	2.5	3	1.0041	−0.0083	0.024787	−201.7
−2	5	3	1.0259	−0.0051	0.158331	−62.16
5	−2	3	1.0271	−0.0523	0.168966	−59.18
2.5	−2	3	1.0042	−0.0084	0.025737	−194.3
4	−3	5	1.0011	−0.0023	0.006805	−1,762
1	−0.8	10	1.0002	0	9.11×10^{-06}	−87,842
2	−1.8	10	1.0002	0	9.12×10^{-06}	−394,895
1	−0.8	9	1.0002	0	2.48×10^{-05}	−32,322
2	−1.8	8	1.0002	0	6.73×10^{-05}	−53,465
2	−0.8	7	1.0003	−0.0004	0.001097	−1,458
0.03	−0.02	10	1.0001	0	4.54×10^{-7}	−1,762
0.04	−0.03	10	1.0001	0	4.54×10^{-7}	−2,643

$$\Phi = (\alpha\theta + \beta)\exp\left(-\frac{\gamma}{\theta}\right) \tag{2.5.1}$$

should be positive in order to have an exothermic reaction. For the expectation of a flat temperature profile, $\theta = 1$ for $\eta = 0$; thus, the dimensionless source term is symbolized as Φ_o and Eq. (2.5.1) becomes

$$\Phi_0 = (\alpha + \beta)\exp(-\gamma)\,. \tag{2.5.2}$$

It was also noted from Tables 2.2.2 and 2.5.1 that $\alpha < 0$ and $\beta > 0$ for FRRPP behavior. This made α and β counteract each other while there was a need to increase the effect of the exotherm. It was also possible for α and β to counteract each other by having $\alpha > 0$ and $\beta < 0$. For now, a combined dimensionless quantity is introduced to incorporate the opposite signs of α and β, as well as the strong effect of the reaction exotherm while keeping the result of a flat temperature profile ($\theta < 1.01$ at $\eta = 0$) in the system. This quantity is symbolized by $C\tilde{n}$ (pronounced see-enye) and defined as

$$C\tilde{n} = \frac{\alpha\beta}{\Phi_0} = \left[\frac{1}{\alpha} + \frac{1}{\beta}\right]^{-1}\exp(\gamma)\,. \tag{2.5.3}$$

Values of $C\tilde{n}$ shown in Table 2.5.1 indicate that for the FRRPP process, it should be below around $-1{,}000$.

A look into values of $C\tilde{n}$ from previously presented experimental data for the FRRPP of styrene in ether was made. If the polymerization rate is solely based on propagation reaction between the monomer and the live polymer radicals, then from Table 2.4.3, the effective activation energy for k' in Eq. (2.2.3) is the same as the propagation activation energy of 7,051 cal/mol K. With a reactor operating temperature of 80ºC, this results in a dimensionless activation energy of $\gamma = 10$. Table 2.5.1 shows that this value of γ provides results within the cutoff of $C\tilde{n} < -1{,}000$ for FRRPP to occur.

What about the values of α and β? These values are obtained from Eq. (2.2.7) if the quasi-steady-state kinetics is assumed (Eq. 2.2.5). Alternately, polymerization rate could be assumed to be solely based on the propagation reaction. In both approaches, the start of the calculation is the determination of the temperature–polymer weight fraction relationship from the phase diagram. An approximate picture of this is shown in Fig. 2.5.1 (basal ternary diagram in Fig. 2.1.11), which follows the reaction trajectory in a representative ternary phase diagram.

Even though it was already established in Section 1.1 that the tie lines for PS/S/DEE system are horizontal, a more general analysis will be made here compared to that in Section 2.2, in which the polymerization rate is solely based on the propagation reaction ($R_P = -k_p[M][P]$). It should also be noted now that the binodal is used as the marker for Point B, when the collapsed globules (unagglomerated and agglomerated) start to phase separate, since it was already been previously established in Section 2.3 that the IPPC or spinodal has not been reached even during

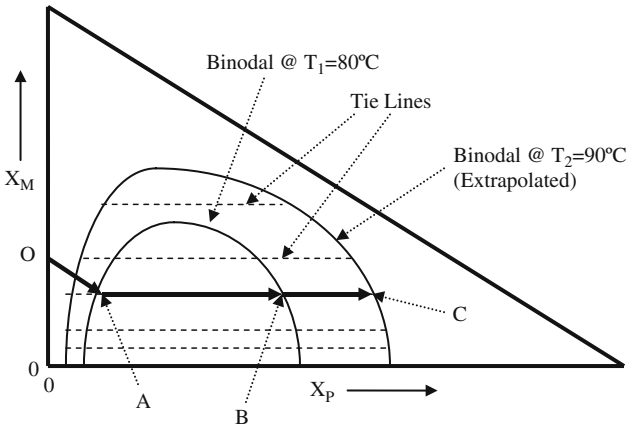

Fig. 2.5.1 Representation of the reaction trajectory (OABC) for the quantitative analysis of FRRPP from the S/PS/DEE system for reactor operating temperature of 80ºC

asymptotic conversion and that the coil–globule picture implies that the globule is in effect a phase separated domain already. Using the phase envelope either in Fig. 1.1.8 or Fig. 2.3.1 for the PS/S/DEE system, values of a and b (Eq. 2.2.4) were obtained, as well as those of α and β. Based on the labeling in Fig. 2.5.1, the quantities a and b are obtained from the following equations:

$$a = \frac{X_{\mathrm{M,C}} X_{\mathrm{P,C}} - X_{\mathrm{M,B}} X_{\mathrm{P,B}}}{T_2 - T_1}, \tag{2.5.4}$$

$$b = X_{\mathrm{M,C}} X_{\mathrm{P,C}} - aT_2 = X_{\mathrm{M,B}} X_{\mathrm{P,B}} - aT_1. \tag{2.5.5}$$

Note that

$$X_{\mathrm{M}} X_{\mathrm{P}} = aT + b \tag{2.5.6}$$

in place of Eq. (2.2.4) because it is the polymer composition that is actually varying between phases, due to the horizontal tie lines. We therefore obtained the following values of a and b as

$$\begin{aligned} a &= 0.00018\mathrm{K}^{-1} \\ b &= -0.041895 \end{aligned} \tag{2.5.7}$$

In order to obtain the values of α and β, the following experimental values are used (Dar, 1999):

Molecular weight of styrene monomer = 104 g/mol
Molecular weight of polystyrene polymer = 5,000 g/mol
Temperature of the reactor fluid = 80ºC
Starting monomer composition = 10 wt%

Ether composition = 90 wt%
Thermal conductivity of styrene monomer = 0.000302 cal/cm s ºC
Thermal conductivity of polystyrene polymer = 0.000375 cal/cm s ºC
Thermal conductivity of ether = 0.000187 cal/cm s ºC
Thermal conductivity of collapsed globules (based on 67 wt% ether, 9 wt% styrene, and 24 wt% styrene) = 0.0002425 cal/cm s ºC
Heat of polymerization = 160.335 cal/g
Density of styrene = 0.906 g/cm^3
Density of polystyrene = 1.04 g/cm^3
Density of ether = 0.7138 g/cm^3
Average density of collapsed globules (based on 67 wt% ether, 9 wt% styrene, and 24 wt% styrene) = 0.809 g/cm^3
Propagation rate coefficient (see Table 2.4.3):

Value for collapsed globules ($\omega_{\text{polystyrene}} = 0.5457$) = 2.817×10^4 l/mol min
Value for dense globules ($\omega_{\text{polystyrene}} = 0.98$) = 13.428 l/mol min
Activation energy = −7,051 cal/mol K

(2.5.8)

Since both α and β are both proportional to the square of the particle radius, r_0, constant values of α_0 and β_0 for collapsed globules are obtained based on

$$\alpha = \alpha_0 r_0^2, \tag{2.5.9}$$

$$\beta = \beta_0 r_0^2, \tag{2.5.10}$$

wherein the following are obtained for $\alpha_0 = 107101273$ cm^{-2} and $\beta_0 = -70617058$ cm^{-2}. Figure 2.5.2 shows the plot of $C\tilde{n}$ for different values of particle radius of collapsed globules from FRRPP of styrene in ether at 80ºC. These values are determined from the equations established in Section 2.2 for α and β, and experimental data for Φ_0. The plot indicates that particles smaller than 100–200 nm would not probably have a flat temperature profile, while larger ones would, based on the cutoff for $C\tilde{n}<-1{,}000$. This would qualitatively agree with conversion rate, MW, and MWD data, whereby molecular weight control was not found to occur until a certain critical conversion was reached for a stirred fluid reactor. It should be noted that particle domains of 350 μm were obtained here based on the work of Tirumala et al. (2003a). This also means that for particle sizes in the order of 10 nm (see Section 2.1), temperature profiles will not be considered flat. For comparison in Fig. 2.5.2, the plot is also obtained for a dense globule at 98 wt% polymer. In this case, the following are obtained for $\alpha_0 = 5.11 \times 10^4$ cm^{-2} and $\beta_0 = -3.37 \times 10^4$ cm^{-2} and that the cutoff particle radius for FRRPP is 6–8 μm. In both cases, values of α, β, and γ are 0.03–0.04, –0.02 to –0.03, and 10, respectively, which are shown to have almost totally flat temperature profiles in Table 2.5.1.

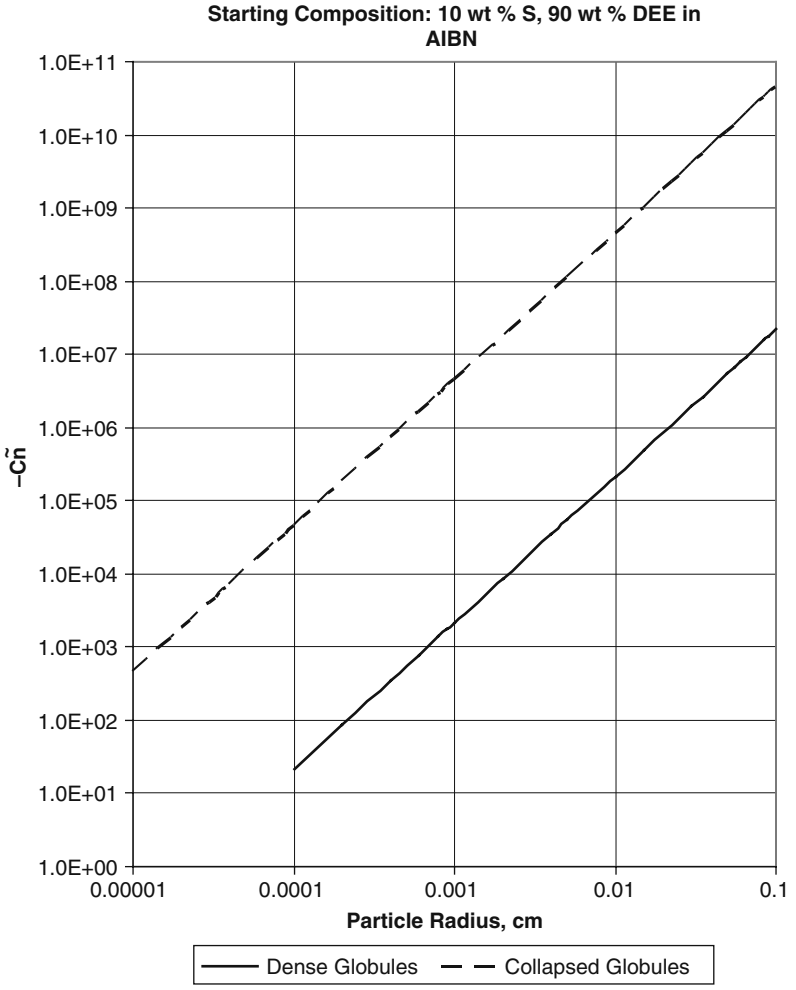

Fig. 2.5.2 Predicted values of $C\tilde{n}$ at different particle radii for FRRPP of styrene in ether at 80ºC for collapsed and dense globules (agglomerated and unagglomerated)

It seems to be evident that the cutoff value of −1,000 for $C\tilde{n}$ is supported experimentally and could then be used to quantitatively characterize the necessary and sufficient condition for the occurrence of the FRRPP process. A final note here is that this criterion corresponds to strict FRRPP process, wherein all aspects of polymerization control occur with a flat temperature profile. If the flat temperature profile is to be relaxed, then the cutoff value of $C\tilde{n}$ will have to be less than −1,000 but below zero. This will reach even smaller polymer-rich domain particle sizes in Fig. 2.5.2.

2.5.1 Nomenclature

2.5.1.1 Alphabets

Upper Case

T – absolute temperature, K

Lower Case

a, b– constants for Eq. (2.2.4)

2.5.1.2 Subscripts

P–polymer
A –Point A in Fig. 2.5.1
B –Point B in Fig. 2.5.1
1 – same as Point B in Fig. 2.5.1
2 – same as Point C in Fig. 2.5.1

2.5.1.3 Superscripts

None

2.5.1.4 Greek Symbols

α –dimensionless version of a from Eq. (2.2.4)
β –dimensionless version of b from Eq. (2.2.4)
γ – dimensionless activation energy, defined in Eq. (2.2.7)
η– dimensionless radius, defined in Eq. (2.2.7)
θ –dimensionless temperature, defined in Eq. (2.2.7)

2.5.1.5 Other Symbols

α_0–defined in Eq. (2.5.9)
β_0–defined in Eq. (2.5.10)
$C\tilde{n}$ – defined in Table 2.5.1 and Eq. (2.5.3), dimensionless
Φ – dimensionless energy source term, defined in Eq. (2.5.1)
Φ_0 – dimensionless energy source term at the center of the particle, defined in Eq. (2.5.2)
r_0–particle radius, m

References

Abe, A., and Flory, P. J., 1965. *J. Am. Chem. Soc., 87*, 1838–1846.

Achilias, D. S., and Kiparissides, C., 1992. *Macromolecules, 25*, 3739–3750.

Aggarwal, A., 1993. M.S. Thesis, Michigan Technological University.

Aggarwal, A., Saxena, R., Wang, B., and Caneba, G. T., 1996. *J. Appl. Polym. Sci., 62*, 2039–2051.

Balke, S. T. and Hamielec, A. E., 1973. *J. Appl. Polym. Sci., 17*, 905.

Bird, R. B., Stewart, W. E., and Lightfoot, E. N., 1960. Transport Phenomena, John Wiley and Sons, New York, p. 350.

Cahen, G., and Treille, P., 1961. Nuclear Engineering, Allyn and Bacon, Boston.

Caneba, G. T., and Soong, D. S., 1985a. *Macromolecules, 18*, 2538.

Caneba, G. T., and Soong, D. S., 1985b. *Macromolecules, 18*, 2545.

Caneba, G. T., 1992a. *Adv. Polym. Technol., 11*, 277.

Caneba, G. T., 1992b. U.S. Patent No. 5,173,551, December 22.

Caneba, G. T., 2007a. "Formation of Radicalized Vinylidene Chloride Copolymer Particulates and Related Materials", Provisional U.S. Patent Application, June.

Caneba, G. T., 2007b. "Multifunctional Multipolymeric Surfactants for Oil-Bitumen Recovery", U.S. Patent and PCT Applications, February 9.

Caneba, G. T., and Dar, Y., 2005. "Free-Radical Retrograde-Precipitation Copolymers and Process of Making the Same", U.S. Patent Application 10/045,725, and Divisional Patent Application, 11/181,481, Filed July 14.

Caneba, G. T., and Saxena, R., 1992. *Proceedings of the A.I.Ch.E. Annual Meeting*, Miami, FL, November 1–6.

Caneba, G. T., Zhao, Y., and Dar, Y., 2003. *J. Appl. Polym. Sci.*, *89*(2), 426.

Chiu, W. Y., Carratt, G. M., and Soong, D. S., 1983. *Macromolecules, 16*, 348–357.

Dar, Y., 1999. Ph.D. Dissertation, Michigan Technological University.

Dar, Y., and Caneba, G. T., 2002. *Chem. Eng. Commun., 189*, 571.

Dar, Y., and Caneba, G. T., 2004. *Chem. Eng. Commun., 191*, 1634.

Dar, Y. L., Wang, B., Simmons, J., Champnella, D., and Caneba, G. T., 2005. "Studies of a Free-Radical Retrograde-Precipitation Polymerization (FRRPP)", poster presented at the A.I.Ch.E. Annual Meeting, Miami, FL, November.

De Gennes, P., 1979. Scaling Concepts in Polymer Physics, Cornell University Press, New York.

Dean, J. A., 1985. Lange's Handbook of Chemistry, 13th Ed., McGraw-Hill Book Co., New York.

Doi, M., 1996. Introduction to Polymer Physics, Clarendon Press, Oxford.

Fried, J. R., 1995. Polymer Science and Technology, Prentice-Hall, Englewood Cliffs, NJ, , ISBN 0-13-685561-X, p. 134.

Hiroaki, K., Suzuki, H., and Matsumura, S., 2008. U.S. Patent No. 7,338,997.

Howell, P. J., Skillerne de Bristowe, B. J., and Stubley, D., 1971. *J. Chem. Soc., (A)*, 397–400

Immergut, E. H., and Brandrup, J., 1989. Polymer Handbook, 3rd ed., John Wiley and Sons, New York.

Kholodenko, A. L., and Freed, K. F. 1984. *J. Phys. A: Math. Gen.*, *17*, 2703–2727

Louie, B. M., 1984. M.S. Thesis, University of California-Berkeley, CA.

McMaster, L. P., 1975, *Adv. Chem. Ser.*, No. 142, N. A. Platzer (Ed.), pp. 43–65.

Nierlich, M., Cotton, J. P., and Farnoux, B., 1978. *J. Chem. Phys.,* 69, 1379–1383.

Nishio, I., Swislow, G., Sun, S., and Tanaka, T., 1982. *Nature, 300*(18), 243.

Odian, G., 1991. Principles of Polymerization, John Wiley and Sons, New York.

Olabisi, O., Robenson, L. M., and Shaw, M. T., 1979. Polymer-Polymer Miscibility, Academic Press, New York, Chapter 2, pp. 75–104.

Oh, J., and Rey, A. D., 2002. "Computer simulation of functional polymeric materials formation via polymerization-induced phase separation under a temperature gradient", in: Phase Separation in Polymer Solutions and Blends, P. K. Chan (Ed.), Research Signpost, Trivandrum, India.

Raos, G., and Allegra, G. 1996. *J. Chem. Phys., 104*, 1626–1645.

Rodriguez, F., Cohen, C., Ober, C., and Archer, L. A., 2003. Principles of Polymer Systems, Taylor and Francis, New York, p. 178.

Sanchez, I. C., 1979. *Macromolecules, 12*(5), 980–988.
Shi, L., 1997. M.S. Thesis, Michigan Technological University.
Soh, S. K., and Sundberg, D. C., 1982. *J. Polym. Sci.: Polym. Chem. Ed., 20*, 315–1329.
Strobl, G., 1996. The Physics of Polymers, Springer Verlag, Berlin.
Tirumala, V. R., 2003a. Ph.D. dissertation, Michigan Technological University.
Tirumala, V., Dar, Y., Wang, H.-H., Mancini, D., and Caneba, G. T., 2003b. *Adv. Polym. Technol., 22*, 126.
Tirumala, V., Divan, R., Mancini, D., and Caneba, 2003c. "Lithographically-Assisted Synthesis of High Aspect-Ratio Hydrogel Microstructures", this paper was partly presented at the Fifth International Workshop on High Aspect Ratio Microstructure Technology (HARMST), Monterey, CA, June 15–17.
Tirumala, V., Mancini, D., and Caneba, G. T., 2004a. "Synthesis of ultrafast response microgels for MEMS applications", *Smart Structures and Materials*, SPIE Conference, *5389*, 221–228.
Tirumala, V., Mancini, D., and Caneba, G. T., 2004b. "*In Situ* Fabrication of Thermoreversible Microgels", *Proceedings of the IEEE International Conference on Intelligent Sensing and Information Processing*, M. Palaniswami, C. Chandrasekhar, G. K. Vengayamoorthy, S. Mohan, and M. K. Ghantasala (Eds.), January 4–7, Chennai, India, pp. 196–200.
Tirumala, V., Guo, L., Caneba, G. T., Mancini, D., Thiyagarajan, P., and Barker, J. G., 2004c. "USANS Investigation of Poly(N-isopropylacrylamide) Gels prepared from Synchrotron-Radiation-Induced Polymerization on a Retrograde-Precipitation Environment", *Proceedings of the American Conference on Neutron Scattering*, June 6–10, College Park, Maryland.
Tirumala, V., Divan, R., Mancini, D. C., and Caneba, G. T., 2005a. *Microsystems Technol. J., 11* (4–5), 347–352.
Tirumala, V., Caneba, G. T., Mancini, D. C., and Wang, H. -H., 2005b. U.S. Patent No. 6,869,983, March 22.
Vrentas, J. S., and J. L. Duda, 1977. *J. Polym. Sci.: Polym Phys. Ed.*, *15*, 417–439.
Wang, B., 1997. Ph.D. Dissertation, Michigan Technological University.
Wang, B., Dar, Y., Shi, L., and Caneba, G. T., 1999. *J. Appl. Polym. Sci., 71*, 761–774.

Chapter 3
Polymerization Processes

In this chapter, implications of the FRRPP phenomenon are presented in terms of unique polymerization production system systems. Control over the rate of polymerization has been exploited, resulting in the formation of new types of statistical and block multipolymers.

3.1 Statistical Polymerizations (Homopolymerizations and Multipolymerizations)

3.1.1 Introduction

Homopolymerizations via FRRPP process normally starts from solution, i.e., the monomer is in a soluble environment. When free radicals are formed from initiator compounds at a high enough temperature, propagation reactions occur and polymer chains are formed. As the polymer radicals attain a high enough chain length, it enters the LCST-based phase envelope and phase separates to form a polymer-rich material. This is where the reaction mechanism of the FRRPP process deviates from conventional solution or dispersion polymerization processes.

The FRRPP can also be implemented in suspension and emulsion polymerization processes. Its analysis in suspension system has turned out to be straightforward, because the suspension size scale (mm sizes) does not interfere with the reaction mechanism, even if one includes mass and thermal transport effects. In emulsion polymerization systems, the submicron size scale of emulsion particles interfere with thermal and probably mass transport effects in the system. Also, the hydrophobic portions of surfactant molecules could affect the phase equilibrium aspects of the FRRPP system.

In random copolymerizations, and certainly multipolymerizations, the FRRPP process can result in products that do not seem to contain random segmental monomer distributions. When polymerizing chains are not prematurely terminated in the FRRPP process, the product distribution can adhere to the predictions of monomer reactivity and monomer concentration ratios. With the incorporation of

G. Caneba, in: *Free-Radical Retrograde-Precipitation Polymerization (FRRPP)*,
Chapter DOI 10.1007/978-3-642-03025-3_3,

local thermal effects in FRRPP systems, block copolymer formation can actually be enhanced from what seems to be a random copolymerization process.

3.1.2 Theory

3.1.2.1 Statistical Effects of Reactivity Ratios

The mechanism of free-radical multipolymerization generally follows a consistent pattern. Monomer sequences within growing chains are dictated by the relative reactivity ratios of various monomers with various radical ends (Odian, 1981). Specifically, the reactivity ratio of monomer 1, r_1, is defined as the ratio of the rate coefficient of the reaction of monomer 1 with the polymer radical ending in monomer 1 to the rate coefficient of the reaction of monomer 1 with the polymer radical ending in monomer 2. Thus, a high value of r_1 means that a segment from monomer 1 in the copolymer chain will more likely be linked to another segment from the same monomer. A value of r_1 close to zero means that the copolymer chain will more likely have alternating segments of monomers 1 and 2. This is not the entire story, because one has to look at the reactivity ratio for the other monomer, i.e., monomer 2. Finally, this assumes that concentrations of monomers are equal. If not, at least it is well known that reaction rates are linear with monomer concentrations. If one looks at acrylic acid (1)–methyl methacrylate (2) copolymerization, $r_1 = 0.33$ and $r_2 = 2.17$. This means that acrylic acid is three times more likely to alternate with methyl methacrylate in the growing copolymer chain, while methyl methacrylate is 2.17 more likely to link up with another methyl methacrylate segment in the growing copolymer chain. Taking both conflicting tendencies into account, there is $(0.33)(2.17) = 0.72$ (or 72%) likelihood for alternating segments of the two monomers, if there is equal concentration of the two monomers. If the ratio of acrylic acid monomer to methyl methacrylate is 0.71, then there is equal likelihood that an alternating and nonalternating sequence will be obtained. However, to assure that 7.2% of the time the series will be a block of methyl methacrylate, a ten-to-one methyl methacrylate-to-acrylic acid monomer charge is desirable.

According to the literature (Brandrup et al., 1999), reactivity ratios for AA (1)/VA (2) copolymerization are $r_1 = 2.0$ and $r_2 = 0.1$. This means that from a reactivity standpoint, AA-radical ends will want to react with AA monomer, while VA-radical ends will also want to react with AA monomer. Thus, if there exists a 50/50 mole ratio of AA to VA in the reactor fluid, AA will tend to add into a growing copolymer chain at 20 times faster than VA; the reactivity of AA monomer would normally result in AA-rich and AA-poor chains, due to chain termination. This implies a very active AA monomer, which is the reason why it was well known that VA/AA copolymers with AA contents greater than 10 wt% cannot be produced efficiently. If the introduction of AA in the reactor is controlled, then the reaction of VA will allow the overall control of the propagation rate while keeping polymer radicals live. This will result in the possibility of producing relatively high AA-content copolymers, as opposed to mixtures of AA- and VA-rich polymers with

relatively low incorporation of comonomers into each set. Further, if a significant proportion of AA is added to the reactor while initiation is taking place so it can be incorporated into most initiated chains until all initiator molecules are exhausted, the longevity of the polymer radicals makes it possible to continue propagation with VA monomer to produce tapered block copolymers.

For the styrene (S)/acrylic acid (AA) system, the average reactivity ratios for AA (1) and S (2) are $r_1 = 0.21$ and $r_2 = 0.33$ (Brandrup et al., 1999). This means that both S and AA do not want to react with copolymer radicals of the same moiety. The extent at which this happens is pretty much the same for both monomers; thus, with almost equal charges of S and AA, alternating copolymers will be formed. However, if S outnumbers AA in the initial charge, more S will be added into the copolymer chain.

3.1.2.2 Effects of Phase Behavior

So far, the above-mentioned statistical analysis of monomer addition to copolymer radicals involves no premature termination reactions, such as what might happen in FRRPP systems. If the reactor fluid were a true solution environment, premature termination reactions would be considered, and certain polymer radicals would terminate faster than others. As best, there would be a larger population of copolymer types. In the S/AA system with excess S charge, a statistical copolymer might be formed early in the propagation reaction that can dissolve in water especially if the AA is neutralized with a suitable base. However, before chain extension can occur with mostly remaining S in the system, a large population of the copolymer chains would be terminated. If chain termination were avoided, an amphiphilic copolymer would have been formed. Such a reaction would have been possible if homopolymers of the monomers comprising the copolymers or multipolymers are simultaneously under FRRPP environment in the reactor fluid. However, we note from Section 3.3 that the reaction control aspect of the FRRPP process could be very aggressive, resulting in relatively low conversion rates. Thus, reactor conditions would have to be altered to speed up chain extension once one of the copolymers has almost been exhausted. It should be noted that we did try different means to effecting chain extension from trapped radical sites via FRRPP mechanism, and the formation of collapsed polymer-rich domains seems to exert uneven transport effects in the system to assure uniform product distribution under prevailing reactor conditions. This will discussed more extensively in the next section.

It so happens that there is a way to exert FRRPP-based control over statistical copolymerizations/multipolymerizations early in the propagation reaction, and then continue chain extension after one of the monomers has been exhausted without having to alter reactor conditions. This is very attractive, because alteration of reactor conditions requires additional reaction time and steps and may even involve the use of extra equipment. For the S/AA copolymerization with excess S in the monomer charge, ether is used as solvent/precipitant to facilitate FRRPP homopolymerization of styrene. However, we have established that poly(acrylic acid) precipitates in ether

below the upper critical solution temperature (UCST) at the reaction conditions. Thus, there is conventional-precipitation-enhanced reaction of AA to S-radical ends and S to AA-radical ends. At the same time, the inclusion of acrylic acid would not enhance the solubility of the polymer radicals. Meanwhile, the presence of significant amounts of styrene in the polymer chains should result in the reduction of bimolecular termination rates due to the FRRPP mechanism. When a large fraction of acrylic acid has reacted, continued addition of styrene in the chains can lead to a tapered poly(styrene-*co*-acrylic acid)-*block*-polystyrene copolymer.

3.1.3 Experimental

3.1.3.1 S/AA System

Since diethyl ether is the solvent/precipitant mostly used in this system, the same pressurized Parr reactor in Fig. 2.3.4 was employed as the polymerization apparatus. The 2,2'-azobis (2,4-dimethylvaleronitrile) (V65) was used as initiator and obtained from Wako Chemical Co. The operating temperature is 80°C, and pressure at around 60 psig. Note that at this temperature, PS phase separates above the LCST and PAA phase separates below the UCST. As a comparison, copolymerization runs were done using cyclohexane as solvent, which dissolves PS at 80°C. The same apparatus was used to verify that pyridine and cyclohexane dissolve polystyrene at the operating temperature range (60–80°C), while poly(acrylic acid) phase precipitates below the UCST in ether and cyclohexane.

Recipes for the formation of the S–AA copolymer include 100 g solvent (ether, pyridine, or cyclohexane), 27 g S, 1–3 g AA, and 0.3 g V-65.

The general experimental procedure for the use of these recipes is described below:

1. A 200-ml quantity of solvent was bubbled with nitrogen for about 15 min.
2. The reactor and all the pipelines were purged with N_2 to displace O_2 from dissolved air.
3. About 80 ml quantity of the solvent was pumped into the reactor.
4. The reactor stirrer was set at 50% of its maximum speed, at around 230 RPM.
5. The temperature controller was programmed to heat the reactor to its operating temperature in 30 min and then maintained at that level.
6. The monomer mixture was prepared by mixing the monomer(s), solvent, and the initiator.
7. The monomer(s)–initiator–solvent mixture was bubbled with nitrogen, for about 15 min.
8. Once the reactor temperature reached the steady state temperature, the monomer(s)–initiator–solvent mixture was pumped into the reactor (using an Eldex metering pump) for 28–35 min.

9. A small amount of solvent was then pumped into the reactor (<5 ml), in order to flush the lines.
10. Nitrogen gas was pushed through the lines to clear any of the material left behind in the liquid lines. Then, the liquid inlet valve was closed.
11. Samples and reactor product were collected into a sealed bottle that is immersed in an ice-water bath, and then the sample bottle was stored in a refrigerator or air-dried followed by vacuum drying.

Conversion values were obtained by gravimetric means, i.e., by obtaining the weight % polymer from weights of reactor fluid samples and dry solid weights. Polymer compositions obtained from ^{13}C-NMR studies (Varian 400 MHz spectrometer using Pyridine-d5 as solvent) were compared with the % monomer charge, in order to calculate monomer conversion to polymer. In order to determine molecular weight distribution of polymer samples, a size exclusion chromatograph was used (Waters 150 CV.) with mixed bed columns (Styragel, Waters Associates). The mobile phase used was THF, and molecular weights were obtained based on narrow molecular weight distribution polystyrene standards. Data were analyzed using Waters *Millennium* software.

3.1.3.2 VA/AA System

The choice of solvents for PVA-based FRRPP synthesis has been narrowed by looking into the various chain transfer constants (Brandrup and Immergut, 1999). High rates of chain transfer are detrimental to polymerization control as they can lead to radical delocalization and relatively quick termination.

There is a need to minimize the occurrence of chain transfer, in order to maintain the radical ends of the polymer. At about 10–20 wt% monomer charge, it was shown that chain transfer to solvent can dominate in the system using EtOH or *n*-buOH as solvent (Caneba et al., 2009).

Azeotropic *t*-buOH/water was used as the solvent for VA/AA copolymerization at an operating temperature of 65°C, because of the relatively low chain transfer constants to both VA and AA. Also, reactor runs verify that the reactor fluid turned a little cloudy from the early stages of reaction to almost the end of the run.

Polymerization experiments were conducted using a 1-l glass reactor that was operated at a slightly positive pressure with a nitrogen gas blanket. Such a device was similar to one described in an earlier publication (Wang et al., 1997), with the additional feature that the glass reactor used can be pressurized to about 40 psig (as specified by the manufacturer, Ace Glass Ltd.). Formation of VA/AA copolymer was accomplished with the reactor containing all the monomers and then starting the reaction by adding the initiator solution. The idea is that most of the AA will react at the early stage and subsequent chain extension will occur with VA addition. The solvent was azeotropic *t*-butanol/water and initiator was VA-043.

Two separate polymerizations were performed to produce a tapered block copolymer with 6 wt% AA (B6-1 and B6-2) in a 1-l glass reactor system. The

reactor was initially charged with the following reagents: 310.7 g azeotropic *t*-butanol/water, 2 g AA, and 72.4 g VA. Then, the temperature was raised to 65°C in 30 min while slowly purging the reactor with nitrogen gas. After the operating temperature was reached, the reactor was sealed and the following was added into the reactor fluid for a period of 20 min: 0.129 g VA-044 dissolved in 10 g distilled water, 43.3 g azeotropic *t*-butanol/water. If higher proportions of AA were needed in the product, more AA were initially charged in the reactor and/or some AA were included with the initiator charge. Normally, this produces a significant amount of random copolymers as well. When AA was added into the reactor after chain extension (when almost all initiator molecules have been exhausted), tapered triblocks were obtained. Random copolymers were produced when AA was almost continuously added into the reactor during the period when initiator molecules are being decomposed into radicals. A summary of reactant sequence addition and the corresponding products are shown elsewhere (Caneba et al., 2009).

The naming convention used for the polymer samples was based on their proposed architecture of the polymers. Solid products that were believed to contain block as well as random chains have been named with the "BR" designation, such as a BR11-1 which was the first product that contains 11 wt% AA. Tapered triblock copolymers were assigned designations such as B9B-1 or BR17B-1. If the product was believed to be mostly random copolymer material, then an "R" designation is used, such as the R20-1 product which contained 20 wt% AA.

Samples were taken at various stages of the experiments. Conversion, MWD, and wt% AA data were obtained using the same methods to analyze above-mentioned S–AA products. Thermal properties were evaluated using differential scanning calorimetry (DSC) and thermogravimetric analysis (TGA). DSC was performed on air-dried sample using TA Instruments DSC 2920. TGA was performed using TA instruments TGA 2950. Data were analyzed using TA *Universal Analysis* software.

Emulsification was done by heating the reactor fluid and replacing vaporized volatile organics with ammonia–water up to pH 7. Usually, sludge formed on the walls of the evaporating vessel. It was found that all the samples formed an emulsion while hot but separated into supernatant and precipitate layers upon cooling to room temperature. On an overall basis, mixtures have 5–10 wt% solids.

In order to determine AA compositions of polymer samples and products, a 400-MHz Varian NMR spectrometer was used. Particle size distributions of the ammonia-neutralized VA/AA self-emulsions were measured using a Leed & Northrop Microtrac Particle Size Analyzer.

Solubilities of products were also investigated using various solvents. Solids from supernatant and residues were collected and dried on aluminum weighing pans.

Fractionation was done by preparing 1 wt% dried solid samples in 100 g THF. The precipitant, cyclohexane, was then added into the solutions at the rate of 1 drop/s while continuously being mixed with a magnetic stirrer bar. After a specific amount of precipitant was admixed into the solution, the precipitate was separated out using a centrifuge (<1,000 RPM).

3.1.4 Results and Discussion

3.1.4.1 S/AA System

Styrene and acrylic acid were copolymerized in ether (FRRPP) and pyridine (solution polymerization) using the following basic recipe: 100 g solvent, 0.3 g V-65, 30 g monomers. At the outset, 80 g ether and 1 g AA were in the reactor at 80°C. Then, 0.5 g AA, 28.5 g S, and 0.3 g V65 were pumped into the 300-ml Parr reactor in 28–35 min to start the polymerization. Figure 3.1.1 shows conversion–time behavior after the reactive mixture was pumped in.

In both solution and FRRPP systems, conversions never reached 100%. The solution system reached an asymptote after four initiator half-lives, indicating the termination of radicals. The FRRPP system still had its conversion increasing almost linearly in the log–log plot with a slope less than 1. Note that this slope in the log–log scale is the so-called autoacceleration index, which would have values less than 1 for a well-controlled system. For future reference, the FRRPP system was named SAA1 and the solution system was named SAA2.

In Table 3.1.2, one can see that after five V65 half-lives UV-based number-average molecular weight remained steady for the FRRPP system (SAA1), while the value is still increasing for the solution system (SAA2). At the same time, RI-based number-average molecular weight was increasing for both FRRPP and solution systems. This means that indeed styrene polymerization was under good control in SAA1, while AA polymerization was not well controlled.

In Fig. 3.1.2, conversion–time data are shown for runs similar to SAA1 and SAA2, only that addition of initiator-containing fluid occurred within 5 min. The FRRPP run was ether based. The other runs involved the use of cyclohexane as solvent instead of pyridine. Cyclohexane precipitates PAA below the UCST, while it is a solvent to PS at the operating temperature.

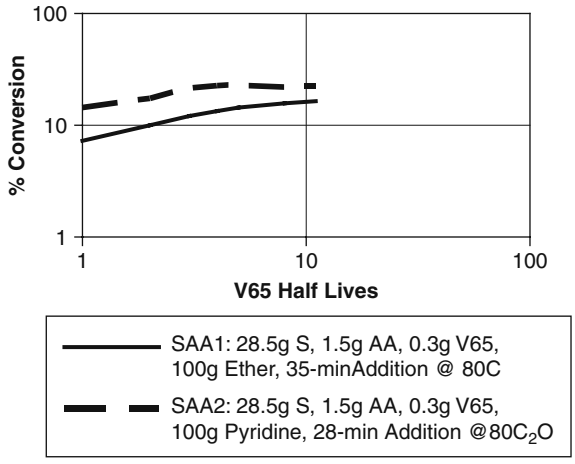

Fig. 3.1.1 Kinetic data on the copolymerization of styrene and acrylic acid via FRRPP and solution polymerization processes (Replotted with permission from Caneba et al., 2003)

Table 3.1.2 Molecular weight information for the SAA1 and SAA2 runs (Caneba et al., 2003)

	SAA1				SAA2			
V65 half-lives	M_n (RI), Da	M_n (UV), Da	PDI (RI)	PDI (UV)	M_n (RI) Da	M_n (UV) Da	PDI (RI)	PDI (UV)
1	2.20	1.07	2.4	3.9	3.68	3.44	1.2	2.0
2	1.99	1.34	2.9	3.5	5.01	3.13	2.1	2.9
5	2.79	1.64	3.2	3.4	5.73	3.62	2.3	3.1
11	3.77	1.59	3.1	6.0	5.72	4.08	2.4	2.9

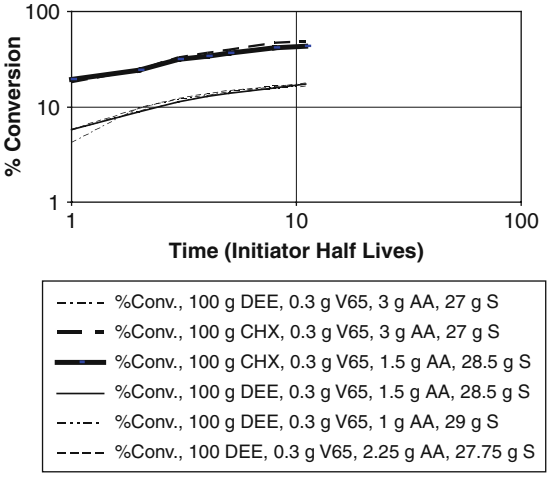

Fig. 3.1.2 Conversion–time plots for S/AA formation from FRRPP (ether) and cyclohexane systems (Replotted with permission from Caneba et al., 2003)

It is clear from Fig. 3.1.2 that the cyclohexane-based runs resulted in much higher conversion values than the ether-based runs. Also, after four times V-65 half-lives, conversion values of the cyclohexane-based runs started to reach a true asymptote, while the ether-based runs seem to keep on going up linearly in the log–log scale. Note that in the cyclohexane-based runs, PAA precipitates below the UCST in cyclohexane while PS dissolves in cyclohexane at the operating temperature of 80°C.

In Fig. 3.1.3, AA contents of product samples from the conversion–time runs in Fig. 3.1.2 are shown. We note from Section 3.1.2 that for equal monomer charges of S and AA, there is almost equal likelihood of incorporation of S and AA monomers onto growing radical chains. For the runs wherein the AA charge is 6.7–10 wt% of the monomers, Fig. 3.1.3 shows AA contents to be in the order of 30–50 wt%. Even the runs wherein AA charge was as low as 5 wt% relative to the monomers, copolymer samples have at least 10 wt% AA contents. It should be noted that PAA exhibits UCST behavior for both diethyl ether (DEE) and cyclohexane (CHX) solvents used. Based on the discussion in Section 3.1.2, this will result in the incorporation of more AA in the copolymer chain compared to what intrinsic reactivities will predict; and this has been observed. In the runs with 6.7–10 wt% AA charge relative to the monomers, AA contents in the copolymer decreased with time at almost the level of 28–36 wt% AA. However, from Fig. 3.1.2, conversions of the CHX-based system are at least twice those of the DEE-based FRRPP systems. This means that longer-time propagation in the FRRPP system is more due to S addition than in the CHX-based system. Thus, FRRPP-based S-AA products were more amphiphilic, as shown by emulsification and solubilization studies (Caneba et al., 2003).

3.1.4.2 VA/AA System

Polymerization of VA in azeotropic EtOH and *t*-buOH seemed to show the effects of chain transfer in these systems. For the EtOH-based system, a bimodal MWD was

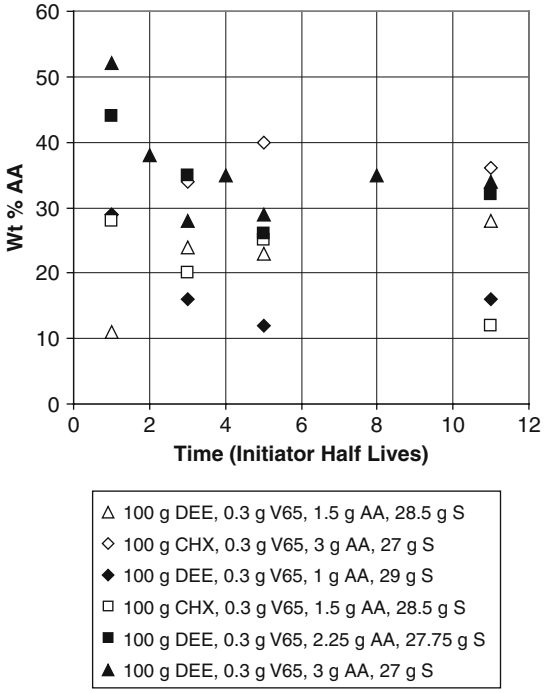

Fig. 3.1.3 Evolution of AA contents in S/AA copolymer samples from FRRPP (using DEE as solvent) and solution polymerization systems (using cyclohexane, CHX, as solvent) for PS portion of copolymer products (Replotted with permission from Caneba et al., 2003)

obtained with a low MW peak at 2–3 kD. For the *t*-buOH-based systems, unimodal peaks were obtained with a slight lower MW shoulder at about 30 kD. Therefore, if the average molecular weight can be targeted to around this value, negative effects of chain transfer can be minimized.

For the formation of VA/AA copolymer, the effort was concentrated in trying to produce blocky polymers (i.e., tapered block copolymers functioning as true block copolymers) by starting with a reactor containing all the monomers and kicking off the reaction by adding the initiator solution. The idea is that most of the AA will react at the early stage and subsequent chain extension will occur with VA addition. The solvent was azeotropic *t*-butanol/water and initiator was VA-044. These runs were done at reduced amounts of initiator in order to minimize premature termination of AA-containing chains; thus, minimizing the formation of random copolymer. The following kinetic data were obtained. Time zero corresponds to the time when all initiator was added in.

VA/AA copolymerizations have been found to produce materials with unimodal MWDs. Also, number-average molecular weights were in the order of 30 kD. Some of the runs produced materials with relatively high AA contents (up to 32 wt%). Conversion–time data (Fig. 3.1.4) also indicate some adherence to a linear log–log plot.

It is worth noting that after 120 min (four times VA-044 half-life), the conversion–time plot reached an asymptote. This may be due to termination of the

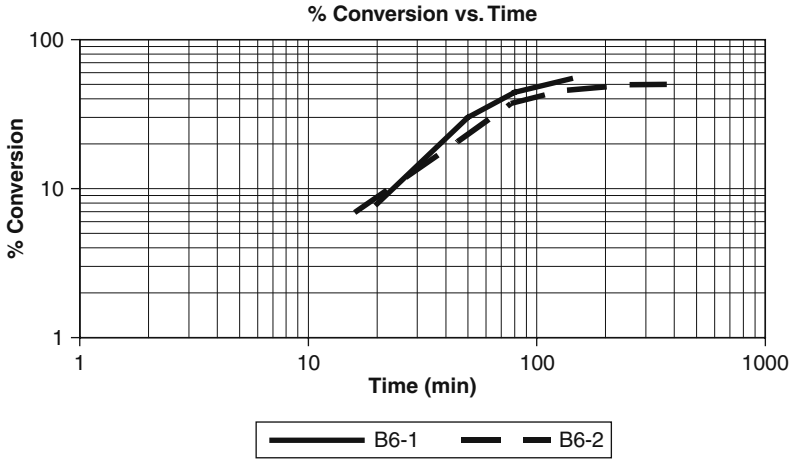

Fig. 3.1.4 Conversion–time plots for VA/AA blocky polymer products with 6 wt% AA content. Note that the initiator (VA-044) has a half-life of 30 min at the operating temperature of 65°C (Replotted with permission from Caneba et al., 2009)

chains or existence of relatively unreactive live radicals. The latter possibility is valid because of the relatively high final conversion values of up to 65%. GPC analysis of the B6-1 product indicates a unimodal peak with number-average M_W of 42 kD and PDI of 2.76 (Fig. 3.1.5(a)). Upon emulsification, GPC analysis of the solid polymer from the emulsion resulted in a number-average molecular weight of 44 kD and a polydispersity index of 3.30 (Fig. 3.1.5(b)). It should be noted that residue from emulsification was observed to be less than 1 wt% in the solids (Caneba et al., 2009).

DSC analysis of the B6-1 material indicated glass transition temperatures of 39.5–44.5 and 80.7–90.1°C (Fig. 3.1.6). They correspond to 64–77 wt% AA in the AA-rich block and 5–11.4 wt% AA in the VA-rich block. TGA analysis showed that this material retained 96% of its weight up to 218.75°C.

A higher percentage VA blocky material, BR11-1, was found to have glass transition temperatures of 42 and 94°C. This translated to about 83 wt% AA in the AA-rich phase and 8.6 wt% AA in the VA-rich phase. For products that were understood to be almost truly random copolymers, a single glass transition between those of PVA (at 36°C) and PAA (at 106°C) was obtained. Thus, thermal analysis supports the result of the formation of either blocky materials or random copolymers.

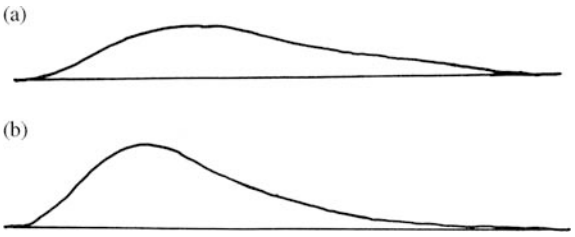

Fig. 3.1.5 GPC traces of the B6-1 raw product (**a**) and emulsified product (**b**). Traces are rescaled to reflect equal axes ranges

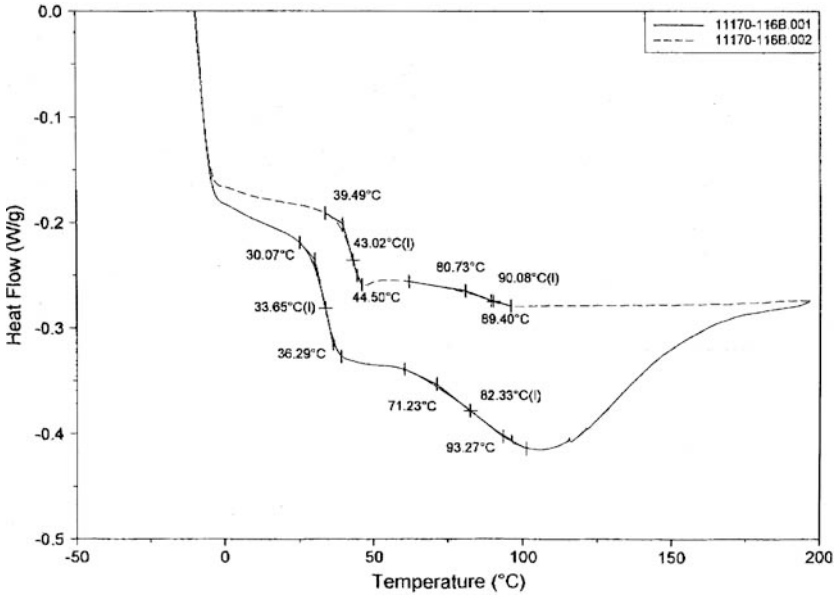

Fig. 3.1.6 DSC traces of the B6-1 product. The *solid curve* is the first heat, while the *dashed curve* is the second heat, which show glass transition temperatures of 39.5–44.5 and 80.7–90.1°C

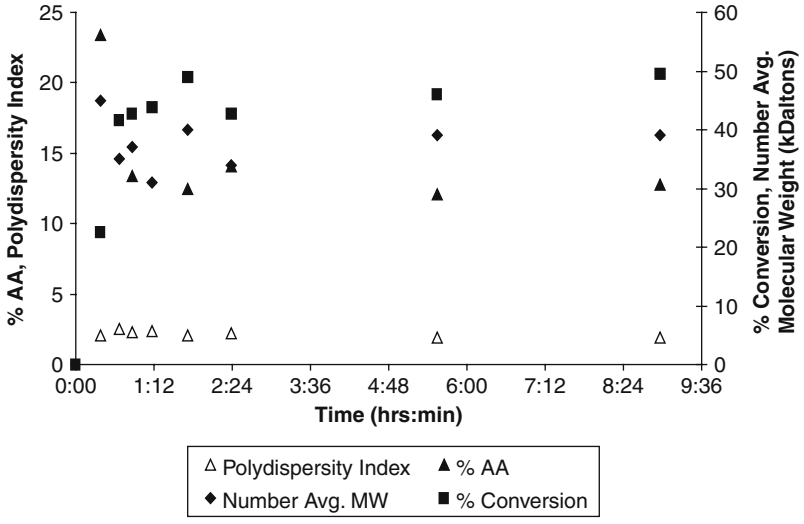

Fig. 3.1.7 Kinetic data for the R10-1 experiment

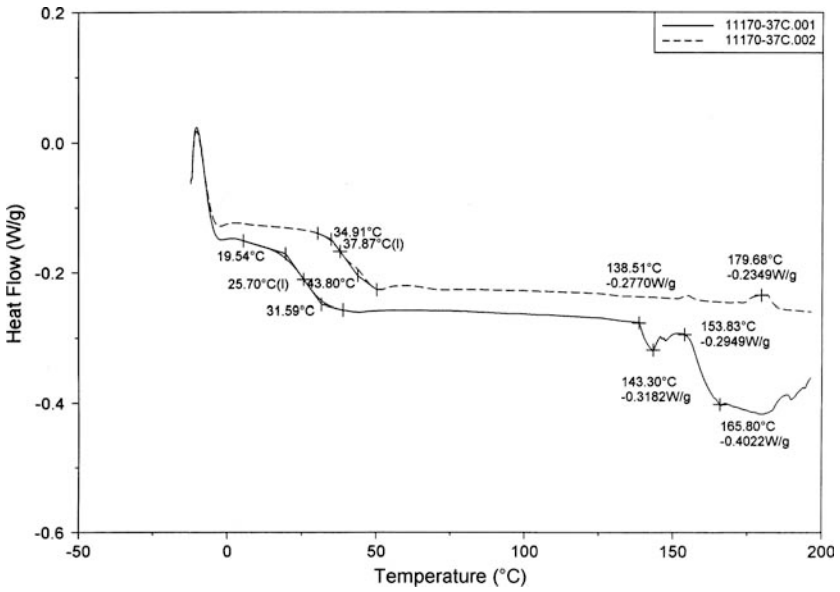

Fig. 3.1.8 DSC traces of the R10-1 product. The *solid curve* is the first heat, while the *dashed curve* is the second heat, which shows a single distinct glass transition temperature between 35 and 44ºC

Kinetic data from an R10-1 experiment are shown in Fig. 3.1.7. The experiment was designed to produce a large proportion of random copolymer, by continuous addition of AA/VA-044 initiator for 2 h. The GPC traces for each sample were unimodal and the polydispersity index varied from 2.4 (in the beginning) to 1.9 (at the end). The data shown in the figure suggest that this experiment resulted in about 10–15% AA (using ^{13}C-NMR) being incorporated in the VA chains. The AA content in the product translated to a random copolymer with a glass transition temperature of about 42°C. This is consistent with the $T_g$values obtained using DSC of 35–44°C (Fig. 3.1.8).

It is clear from Fig. 3.1.7 that after all the initiator (VA-044) has been added at the 2 h and 24 min mark, the reaction was well controlled. In fact, both conversion and number-average molecular weight seem to increase in an almost linear fashion.

Random copolymer (R20-1) and block copolymer (B6-1) products have been fractionated for comparison. The results are shown in Fig. 3.1.9, and GPC results are also shown in Figs. 3.1.10 and 3.1.11. It is evident that fractionally precipitated material from the random copolymer is much more distributed than that from the block copolymer. Curves for two samples (BR36-1 and BR20-1) are also shown in order to get an idea of random copolymer formation at a higher AA content. The two samples were taken at different times in the same reaction with B36-1 coming first just after the addition of the initiator in the reactor. As shown in Fig. 3.1.9, the random copolymer part of BR36-1 was reduced in BR20-1, based on the reduction of the peak at lower % cyclohexane precipitant. This indicates that the pre-made polymer in BR36-1 has helped in the formation of blockier BR20-1.

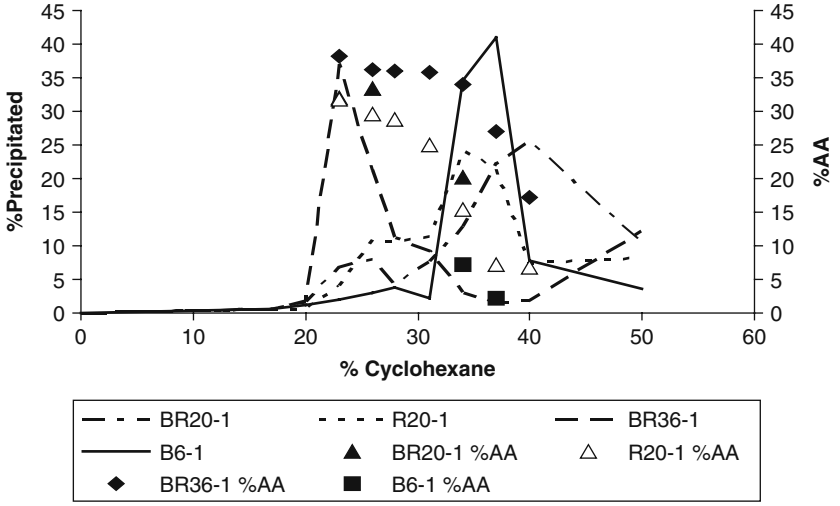

Fig. 3.1.9 Fractionation results for the vinyl acetate/acrylic acid copolymers (Replotted with permission from Caneba et al., 2009)

It is therefore evident that statistical multipolymerizations from the FRRPP process can result in high proportions of unique products not efficiently obtainable from conventional free-radical multipolymerizations. This was demonstrated in the cases involving S and AA as well as VA and AA, wherein self-assembly of monomers into copolymer segments have been observed in the formation of blocky copolymers or equal-monomer-chain-distribution statistical copolymers.

3.1.5 Nomenclature

3.1.5.1 Alphabets

Upper Case

C –chain transfer constant

Lower Case

None

3.1.5.2 Subscripts

P–polymer
S – solvent
I – initiator
M – monomer
X – overall

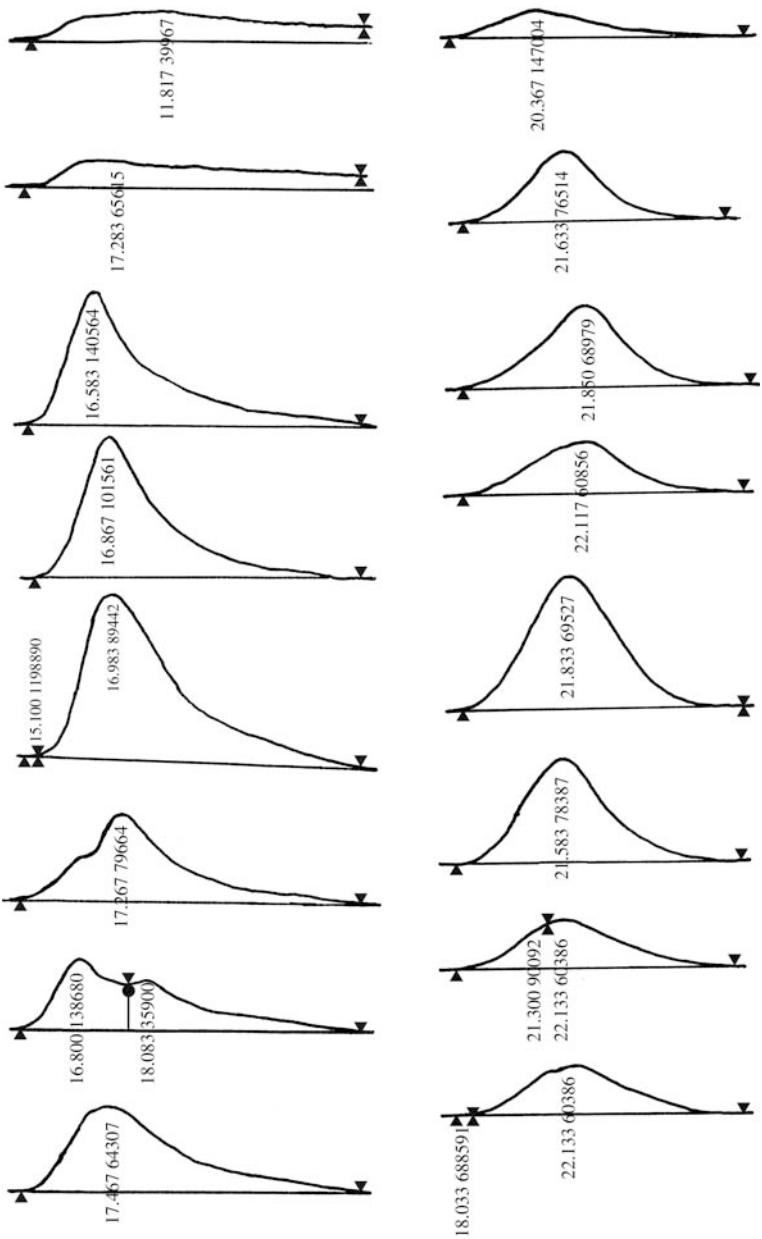

Fig. 3.1.10 GPC traces of fractionated B6-1 and R20-1, based on increasing precipitant levels (going from top to bottom traces). Please refer to Fig. 3.1.9 for levels of precipitated fractions

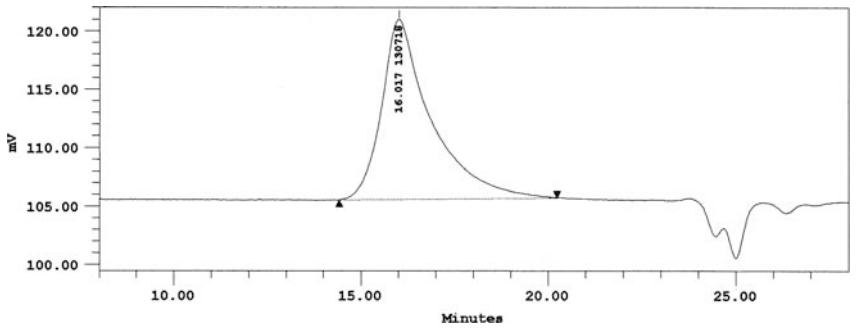

Fig. 3.1.11 GPC trace and results for R20-1 material

3.1.5.3 Superscripts

None

3.1.5.4 Greek Symbols

None

3.1.5.5 Other Symbols

[*I*] – concentration of initiator, mol/l
[*M*] – concentration of monomer, mol/l
[*S*] – concentration of solvent, mol/l
[*P*] – concentration of polymer, mol/l
[*X*] – concentration of a reactive species including solvent, mol/l
P_n – kinetic chain length
P_{n0} – kinetic chain length without chain transfer

3.2 Staged Multipolymerizations

An obvious approach for block copolymer formation is the multistage method, whereby a first-stage polymer radical population is formed. Then, a second set of monomers is added into the reactor in order to continue chain extension to form the next block, and so on. Ideally, unreacted first-stage monomer should be removed from the reactor fluid before the formation of the next block. This is not as easy as it sounds, especially since monomers are normally less volatile than LCST-based solvents/precipitants. An example is the FRRPP of S in ether, wherein ether has a boiling temperature of 32°C, while S boils at 145°C (*CRC Handbook of Chemistry and Physics*). Also, if the PS radicals are trapped within collapsed PS domains, distributing a second set of monomers uniformly within around radical sites without commencement of chain extension is always a challenge. Finally, cooling of the reactor fluid to render the radical sites temporarily dormant will normally terminate

the radicals because as the temperature is lowered, the system traverses the single-phase region in the phase diagram.

For a 350-μm reactive PS particle, an order of magnitude estimate of the diffusion time of 20 min is obtained for an upper limit of mass diffusivity of 10^{-6} cm^2/s. This is based on the following equation for the diffusion time (t_d), size scale (λ), and diffusivity (D):

$$\frac{Dt_d}{\lambda^2} \approx 1. \tag{3.2.1}$$

Thus, in order for continued propagation to occur uniformly within the particles, conditions should be achieved in such a way that the reaction time is much larger than 20 min. As for heat transfer rate within the particles, thermal diffusion times are in the order of 0.2 min only, because thermal diffusivities are in the order of 10^{-4} cm^2/s (Middleman, 1977).

In the following subsections, the author presents some of the methods used to carry out multistaged block multipolymer formation.

3.2.1 Straightforward Addition of Another Monomer(s)

In order for block multipolymer formation to occur uniformly from the first-stage polymer radicals with this method, the second-stage monomer should be able to diffuse fast enough in order to minimize core–shell polymer formation. Also, the second monomer set should form a second block that would have properties that are distinct from the first block. This is not easy if there is substantial first block monomer left in the reactor. However, for certain cases, this is quite feasible.

For first-stage PS radicals formed in reactive S/ether system, the addition of methacrylic acid will result in the formation of S-*block*-(S-*stat*-MAA) copolymer, which could still possess amphiphilic properties. Also, such a block copolymer can be a good intermediate material for the formation of block–graft copolymers (see Section 4.6).

In Fig. 3.2.1, conversion data for the second-stage polymerization from the S/PS/ether FRRPP system are shown (Wang, 1997). For the first two-stage block copolymerization experiment, the pressurized glass tube system used in phase equilibria studies (Fig. 1.1.3) was used. A mixture of 1.5 ml inhibitor-free S, 10 ml ether, and 0.0173 g AIBN was charged into the thick-walled glass tube vessel. Then, the mixture was bubbled with nitrogen gas to displace dissolved air. Before sealing, a magnetic stirrer was dropped into the tube vessel. Reaction started when the sealed tube reactor was placed in the water bath at 80°C. After 10 h of reaction, the tube vessel was quickly cooled in an ice-water bath for 30 min. Then, 1.5 ml nitrogen-purged MAA was added in before the tube-vessel reactor was placed back into the 80°C bath for an additional 8 h. Samples were taken for conversion data.

Another experiment was done in the 300-ml Parr reactor system shown in Fig. 2.3.4. The mixture of 15 ml S, 135 ml ether, and 0.2 g V-501 was pumped into

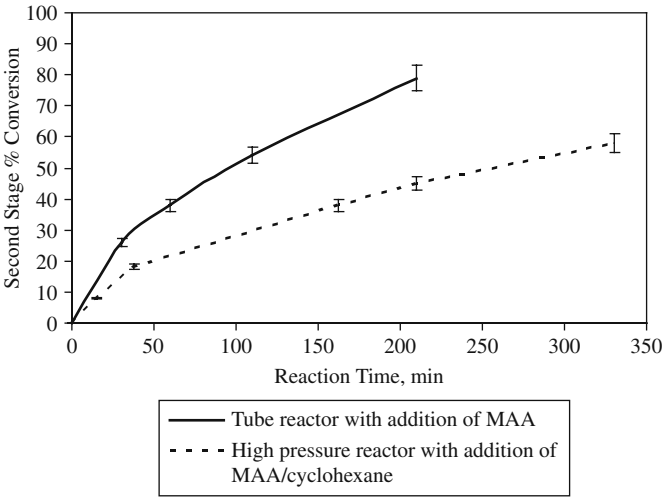

Fig. 3.2.1 The second-stage polymerization conversion–time data with addition of MAA in the intermediate solution of styrene polymerization in ether at 4 h into reaction

the reactor and reacted at 80°C for 5 h. Then, the mixture of nitrogen-purged 15 ml MAA and 50 ml cyclohexane was charged into the reactor. Samples were taken for conversion data, all of which are based on additional second-stage monomer charged into the reactor.

Since cyclohexane is a solvent for PS at the operating temperature of 80ºC, the conversion is more moderate than the system that only had MAA as second-stage monomer charge. The final product from the 300-ml Parr reactor system was dried out and a dry sample was dissolved in THF. Water was added in as precipitant for the purified block copolymer. The unprecipitated block copolymer was called the raw product. In Fig. 3.2.2, size exclusion chromatography data are shown for the intermediate PS, raw block copolymer product, and purified copolymer product.

These curves show definite formation of the S-*block*-(S-*stat*-AA) material. The intermediate PS product has a peak MW of 10,000 Da, while the block copolymer has a peak MW of 300,000–400,000 Da.

3.2.2 Interstage Rapid Cooling Method

First-stage polymerization of styrene in ether (33.4 g styrene, 0.200 g ether, 0.34 g V-65, or AIBN in a 300-ml Parr reactor system) was carried out at 80°C up to five times initiator half-life. Then, the reactor fluid was withdrawn through a 1/8-in. copper tube that is immersed in ice-water bath. The cold reactor fluid was collected into a 1000-ml glass reactor that contains 400 ml distilled water and 12 g acrylic acid (AA). The mixture was continuously mixed at room temperature for at least 2 h in order to soak-in the AA monomer into the polymer-rich domains. Then, the

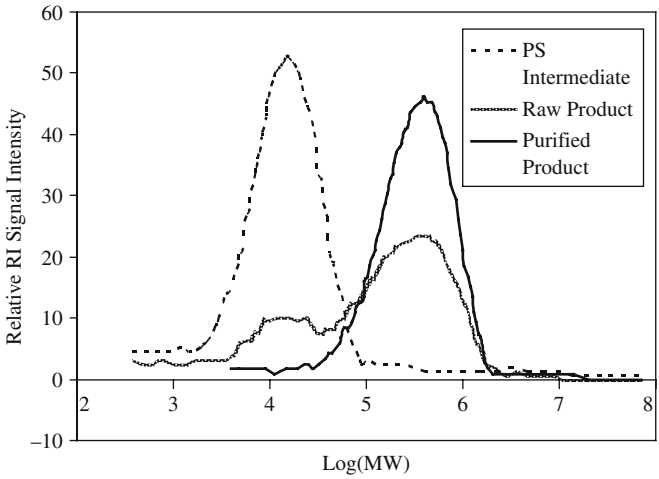

Fig. 3.2.2 Refractive index signal from a size exclusion chromatography system for the polystyrene material that was taken from the reactor just before addition of MAA, as well as raw and purified copolymers (Replotted with permission from Wang, 1997)

reactor was heated to 60°C linearly for 4 h and maintained at this temperature to drive off the ether and continue the reaction. Aside from conversion and molecular weight data, the products were dried and emulsified in hot water with the addition of ammonia (up to pH = 9–10). Upon cooling, the result was a top coagulum, a middle emulsion, and a bottom sludge. The middle emulsion was the material of interest, which should contain mostly PS–P(S–AA) copolymer. Thus, Table 3.2.1 shows the results of analysis of the products (SAA1 and SAA2). The results are contrasted with those of the equivalent run where the second-stage AA monomer was added in the hot reactor fluid with pyridine (no interstage rapid cooling to yield the SAA3 product).

It is evident that the use of V-65 resulted in an improvement in the amount of middle emulsion layer formed. Also, the interstage cooling seems to improve further the amount of the middle emulsion layer. Since we found that about 20 wt% of the bottom sludge to be emulsifiable in hot water, we can assume that the sludge is mostly polystyrene homopolymer. The top layer could be surmised to be relatively low molecular weight homopolystyrene.

Table 3.2.1 Properties of PS–P(S–AA) products

Product	Initiator	Interstage rapid cooling?	% Conversion	Top:middle emulsion:sludge wt/wt/wt
SAA1	AIBN	Yes	58	2.3:74:23.7
SAA2	V-65	Yes	78	2:82:16
SAA3	AIBN	No	53	0:56:44

The above results also point to the relatively high proportion of PS radicals that are available for second-stage reaction from styrene polymerization in ether. This high proportion is pegged at the level of about 80%, based on the fact that 82 wt% of solid product was found in the middle emulsion from Table 3.2.1. Here, polymer radicals have been made accessible to the second-stage monomer with minimal reaction. This was demonstrated to occur when the first-stage fluid was rapidly cooled before exposure to the second-stage monomer. The fact that a very high amount of emulsifiable material was formed means that the PS radicals were preserved by the rapid cooling and exposure to monomers even at room temperature for up to 2 h.

3.2.3 Emulsion FRRPP

A redox system is normally used for emulsion FRRPP. For first-stage polymerization of S in ether, three mixtures were prepared.

Mixture 1: Prepared as emulsion
Distilled water = 67 ml
Sodium dodecyl sulfate (SDS) = 0.5 g
Styrene (inhibitor-free) = 41 ml
t-Butyl hydroperoxide = 0.365 g

Mixture 2: 56 ml ether

Mixture 3:
Distilled water = 83.5 ml
Versenol = 0.021 g
Ferrous sulfate = 0.006 g
FSB = 0.265 g

All fluids were bubbled with nitrogen gas for at least 15 min. Mixture 3 was first charged into the 300-ml Parr reactor (Fig. 3.3.4) and heated to reactor operating conditions: 80°C and 70 psig (N_2 blanket). Then, Mixture 2 was added in and allowed to emulsify in the reactor. Finally, Mixture 3 was pumped in for 11 min plus 5 ml ether flush; the end of pumping is time zero. Conversion data, shown in Fig. 3.2.3, indicate an initial slowdown period followed by a faster approach to 100% conversion.

From the above first-stage PS radicals in emulsions, viable block copolymers were formed, especially PS–PBA block copolymer.

3.2.4 Emulsification of First-Stage Radicals

In this method, FRRPP of S in ether was implemented in a Stage 1 reactor system. This would be the usual procedure and apparatus indicated in Section 2.3. When the conversion reached a practical asymptote, the water and surfactant were added

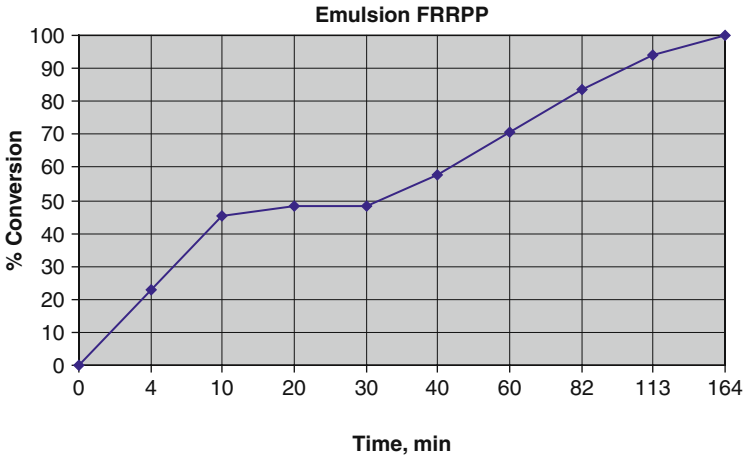

Fig. 3.2.3 Conversion–time plot for emulsion FRRPP of S in ether at 80°C and 70 psig

in order to produce an emulsion. The emulsion produced organic domains that are smaller than the 350-μm domains from the reactive S/PS/ether FRRPP system. This increase in the surface-area-to-volume ratio of the organic phase improved heat dissipation, and further chain extension to higher molecular weight PS radicals. This does not bring the S conversion to polymer close enough to 100%, unless the ether was stripped from the emulsion. Once this was done, the second monomer can be added in order to continue chain extension to form the next block. Then, a third monomer can be added, especially if it preferentially reacts with the polymer radicals.

In a typical experiment, the reactor system in Fig. 2.3.4 was used and pre-loaded with nitrogen-bubbled inhibitor-free S (50 ml) and ether (100 ml). Then, the reactor was heated to 80°C with 70 psig nitrogen gas blanket. At time t=0, the nitrogen-bubbled mixture of ether (100 ml) and Lauroyl peroxide (0.4 g) was pumped into the reactor for 12–13 min with 10 ml ether flush at the end. At t = 12 h and 10 min, the reactor contents were emptied through a 1/8-in. copper tube transfer line immersed into an ice-water bath and into a glass reactor system (1-l glass reactor version of Fig. 3.3.4) that contained nitrogen-bubbled distilled water (250 ml) and Rhodapex CO-436 surfactant. The ether from the first-stage reactor system was then stripped off by slowly heating the 1-l glass reactor system to 40°C in 1 h, while nitrogen-bubbled distilled water (50 ml) was slowly added to replace some of the ether. Then, nitrogen-bubbled BA (87.5 ml) and more nitrogen-bubbled distilled water (100 ml) were charged into the 1-l glass reactor. The reactor was then slowly heated to 60°C for 2 h and maintained at that temperature for 6 more h, in order to react the BA with the PS radicals in the emulsion particles. Finally, the reactor was cooled to room temperature for 1 h, and a block copolymer product was obtained.

Solid product from this second-stage reactor was already elastic, self-tacking, and translucent white. Still, a third-stage reaction was employed with addition of

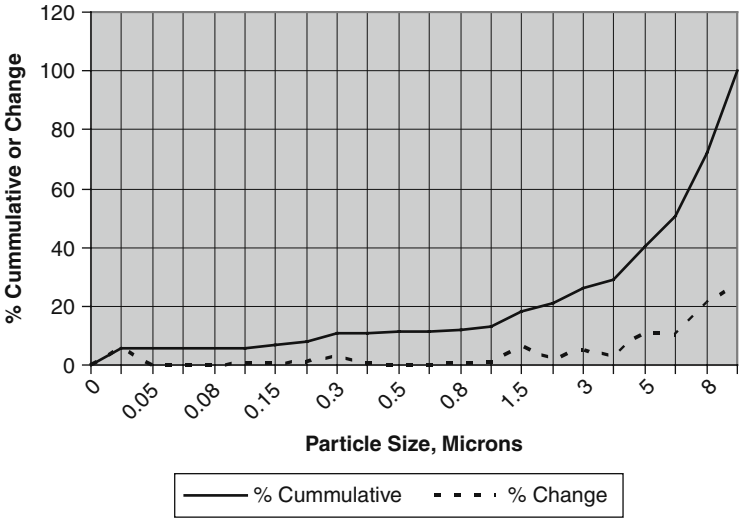

Fig. 3.2.4 Particle size distribution of PS–PBA block copolymer made from a multistage FRRPP process with emulsification of the first-stage product

some S (20 ml) into the reactor at room temperature. Then, the reactor temperature was raised for the last time to 60°C in 1 h. Finally, the reactor was cooled to room temperature in 2.5 h.

The final product was elastic and self-tacking white solid. Upon dissolution in THF and drying, the solid was translucent, indicating a block copolymer structure. Particle size analysis of the latex is shown in Fig. 3.2.4 to have a multimodal distribution, ranging from submicron to 10 μm or greater, but still a stable enough emulsion. In fact, all of our latex products made from this type of emulsion FRRPP

Fig. 3.2.5 Picture of a PS–PBA block copolymer emulsion and solid product made from a multistage FRRPP process with emulsification of the first-stage product

have size distributions with a submicron peak. A picture of a typical emulsion liquid and solid product is shown in Fig. 3.2.5.

3.2.5 Radicalized Polymer Particulates

In a more recent work (Caneba, 2007a), the FRRPP process was shown to be capable of producing dispersions of VDC copolymer radicals that we were able to maintain their activity prior to reaction with a new set of monomers to form block copolymers. Note that in Table 1.1.2, the LCST of VDC copolymers have been found to be of reasonable values.

The first stage of block copolymerization was implemented in a pressurized reactor (about 45–100 psig) at 100–120°C, and even scaled up from 300 ml to 5 gallons. The product is in the form of micron-sized dispersion of VDC copolymer radical particles in the solvent/precipitant, in which both radical population and dispersibility properties were kept intact on storage under nitrogen atmosphere for a matter of days. Also, this first-stage polymerization could result in 100% polymer reaction yield at polymer content in the order of 10 wt% in the fluid. Upon allowing the dispersion to settle, the solvent/precipitant can be decanted off, leaving a dispersible mud material made up of the VDC copolymer radicals. Dried PVDC and VDC copolymer particulates have been determined to be highly crystalline, based on the surface structural features revealed through a scanning electron microscope (Fig. 3.2.6).

With radicalized VDC copolymer particulates, we found that a dispersion from the reactor can last for at least 5 days and still maintain full radical activity. This might be due to the semi-crystalline nature of the copolymers, which makes it difficult for oxygen from the air to penetrate. Note that oxygen forms stable peroxy radicals with polymer radical sites.

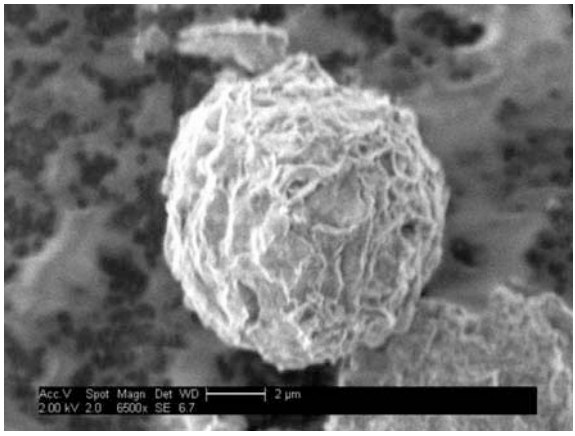

Fig. 3.2.6 Primary particulate structure of a PVDC radicalized material from scanning electron microscopy, showing evidence of crystallinity based on surface features. The scale bar is 2 µm

Radicalized particulates from dispersion FRRPP have been found to be viable intermediates for block copolymer formation. An example recipe and procedure for the formation of an RB1-200 A–B block copolymer is shown in Table 4.2.1, which will be a starting point for the development of other A–B block copolymer procedures. We studied the feasibility of second-stage block copolymer formation from radicalized particulates in the following environments: (a) solution, (b) dispersion, and (c) in situ polymerization. The formation of RB1-200 is believed to involve a second-stage solution polymerization process, due to its single peak in the fractional precipitation plot (similar to Fig. 3.2.7).

In order to form the block copolymer, we took the first-stage reactor suspension and charged it into the second-stage near-atmospheric reactor along with solvent and a new set of monomers. Upon heating, the block copolymer started to form. Various tests were done to show block copolymer formation, amidst the difficulty in dissolving the first-stage VDC copolymer for analysis. These tests include DSC/TGA, ^{13}C NMR, solubility, coagulation, and fractional precipitation methods.

Post-processing mainly involved purification of product and sample copolymers from the reactor runs. If the reactor fluid was a solution or a soft dispersion, the first step was to precipitate the polymer material with a coagulant, such as water or an alcohol. Then, the precipitant dough was dried either in air and/or in a vacuum oven. For reasonably volatile solvents and monomers used in the reactor runs, air and vacuum drying resulted in complete drying. However, for relatively nonvolatile monomers, such as some of the Zonyl® fluoromonomers or vinyl silicones, an extraction process was normally needed after partial drying. It was found that the best way to validate extraction from swollen polymer dough was through supercritical-fluid (SCF) CO_2 extraction. Once an idea of the maximum amount extractables was obtained from a particular starting material through the SCF-CO_2 extraction procedure, the use of more conventional extracting fluids, such as

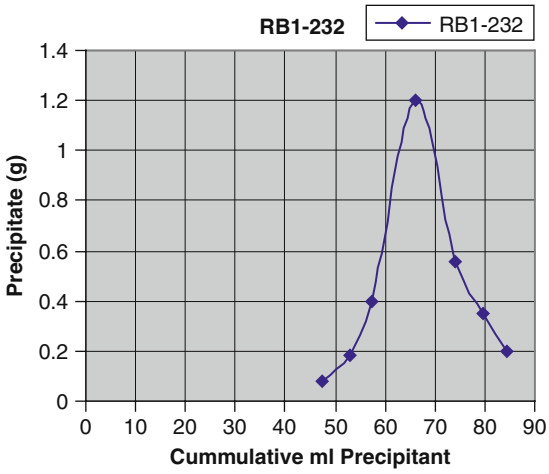

Fig. 3.2.7 Fractionation data for block copolymer of VDC statistical copolymer (96% VDC) with butyl acrylate-*stat*-glycidyl methacrylate

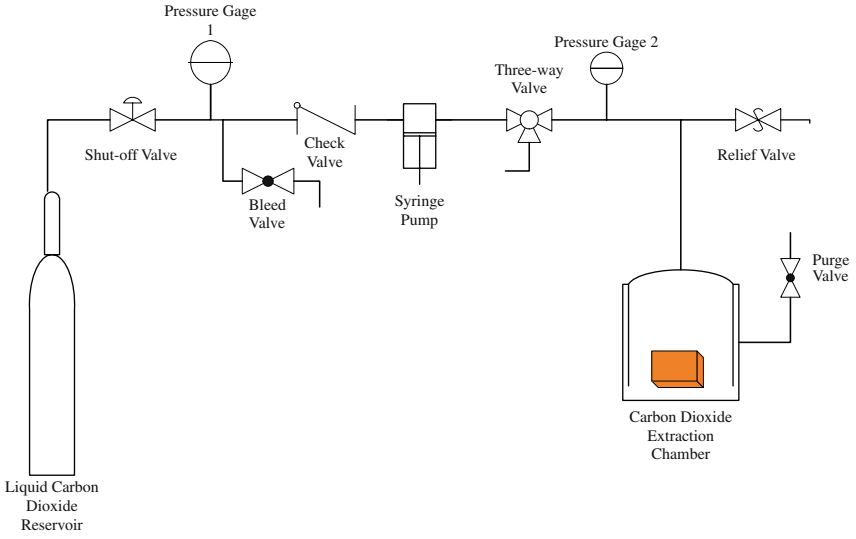

Fig. 3.2.8 Supercritical CO_2 extraction system for purifying polymer samples. The system was also used in microcellular foaming experiments (Section 4.5)

methanol, became reliable. Fig. 3.2.8 shows a schematic diagram of the SCF-CO_2 extraction system used for this purpose, which was also used for microcellular foaming experiments (Section 4.5).

An example product was a diblock made of a VDC copolymer (96% VDC) block with a butyl acrylate-*stat*-glycidyl methacrylate block. The reactor product solution was fractionally precipitated, and the fractogram (Fig. 3.2.7) indicated minimal VDC copolymer contamination due to the single fractionation peak for the block copolymer. It was noted that VDC copolymer contamination would represent dead copolymer radicals after the first-stage reaction, and such material would be precipitated almost immediately. Of course, apparent mechanical properties (such as the transition from the hard VDC copolymer material to soft and/or elastic materials) indicated the formation of block copolymers. Comparison work was done with commercial VDC copolymers, which included solubilization, film spin casting, drying, annealing, and tensile testing.

As an example, the DSC/TGA plots of RB1-200 product in Fig. 3.2.9 confirmed the proposed A–B block copolymer structure. Still, the VDC segments seemed to be on block arrangement within the first-stage A block along with the Zonyl® methacrylate segments, with the Zonyl® melting point showing in the DSC curve (Fig. 3.2.9). The DSC plot of just the A-block also showed distinct melting transitions of VDC and Zonyl® methacrylate segments; thus, these high-performance polymers can accentuate individual segmental component crystallinity even in statistical copolymers.

In Fig. 3.2.9, the strong effect of the curing reaction of the GMA was evident from the rise in the DSC curve between 75 and 270°C (as also verified by melt processing experiments), which indicated good segregation of the B-domain rich

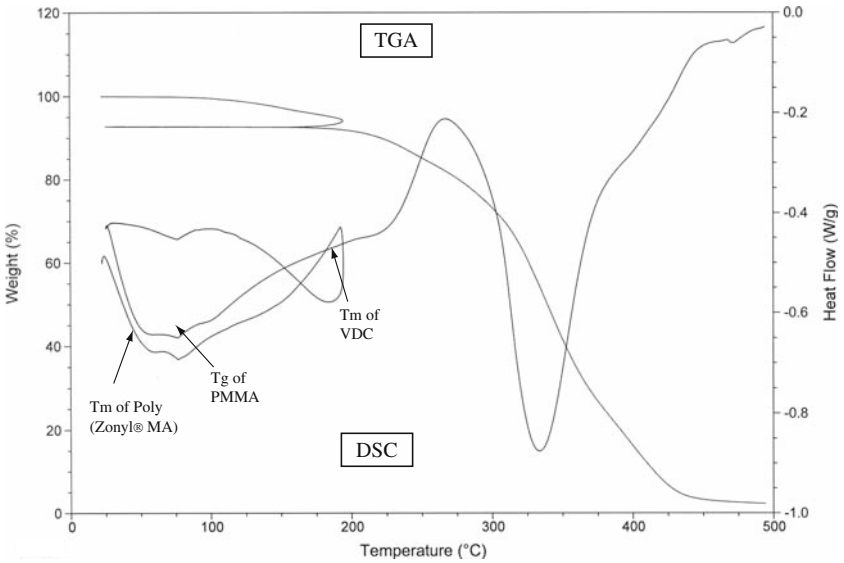

Fig. 3.2.9 DSC/TGA of the RB1-200 product, which contains segments from VDC, Zonyl® methacrylate, methyl methacrylate (MMA), and glycidyl methacrylate(GMA). The run includes a heat-up step to 200°C, then a cool-down step to room temperature, followed by a final heat-up step. Both heat-up and cool-down steps are at 10°C/min rate. Note that exotherm is up in the vertical axis

in GMA segments. Underneath this rise were inflection points corresponding to T_g of PMMA at 105°C and T_m of VDC at 180–220°C, which again indicated good segregation of these segments into their respective domains. The dip at 50–80°C in the DSC curve corresponded to the T_m of the Zonyl® segments.

When properly done, it is therefore possible to implement multistage block multipolymer formation from the FRRPP process. This is especially true if the main first-stage monomer material is a gas or a volatile liquid, such as VDC.

References

Brandrup, J., Immergut, E. H., and Grulke, E., 1999. Polymer Handbook, John Wiley and Sons, New York.

Caneba, G. T., 2007a. "Formation of Radicalized Vinylidene Chloride Copolymer Particulates and Related Materials", Provisional U.S. Patent Application, June.

Caneba, G. T., 2007b. "Multifunctional Multipolymeric Surfactants for Oil-Bitumen Recovery", U.S. Patent and PCT Applications, February 9.

Caneba, G. T., Xu, Z., and Dar, Y. L., 2009. *J. Appl. Polym. Sci. 113*, 3872–3882.

Caneba, G. T., Zhao, Y., and Dar, Y., 2003. *J. Appl. Polym. Sci.*, *89*(2), 426.

Middleman, S., 1977. Fundamentals of Polymer Processing, McGraw-Hill Book Co., New York, p. 360.

Odian, G., 1981. Principles of Polymerization, John Wiley and Sons, New York.

Wang, B., 1997. Ph.D. Dissertation, Michigan Technological University.

Chapter 4
Product Materials

This chapter pertains to the various polymeric product materials that have been generated in the laboratory through the FRRPP process.

4.1 Homopolymers and Statistical Multipolymers

4.1.1 Homopolymers

Narrow and relatively narrow molecular weight distribution (MWD) homopolymers comprise an obvious group of products that can be produced from the FRRPP process. These materials would be used mainly for R&D purposes. PS and PMAA homopolymers would be good examples of relatively narrow MWD homopolymers that can be produced in large scale through the FRRPP process. Recently, poly(vinylidene chloride) (PVDC) has been produced through the FRRPP process, including various related copolymers.

4.1.1.1 Polystyrene (PS)

Based on prior material in Chapters 2 and 3, it should be noted that PS products from FRRPP of styrene in ether would be useful as secondary standards with polydispersity indices between 1.5 and 2.0. However, these products have average molecular weights up to around 10,000 Da only.

Higher average molecular weight PS from FRRPP with acetone as solvent/ precipitant have been produced (Wang, 1997). It should be noted that the LSCT of PS in acetone is at 67°C (Caneba, 1992a, 1992b). Figures 4.1.1 – 4.1.3 show conversion, molecular weight, and polydispersity data for styrene FRRPP with acetone at 80°C.

It is evident from Fig. 4.1.1 that the higher the starting monomer concentration the higher the conversion values. Also, for the same starting monomer concentration, higher conversions are obtained at higher initiator values. Finally, conversion values up to 80% are attainable with this type of system.

G. Caneba, in: *Free-Radical Retrograde-Precipitation Polymerization (FRRPP)*,
Chapter DOI 10.1007/978-3-642-03025-3_4,

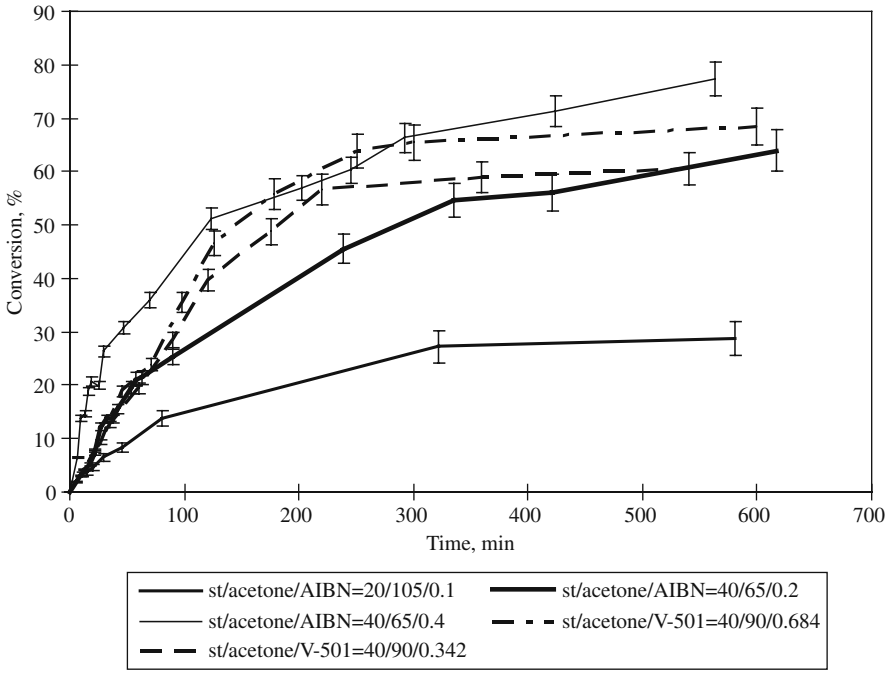

Fig. 4.1.1 Conversion–time plots for batch polymerization of styrene in acetone with AIBN and V-501 initiators at 80°C and 70 psig. Starting compositions (weight basis) are indicated in the legend (Replotted with permission from Wang, 1997)

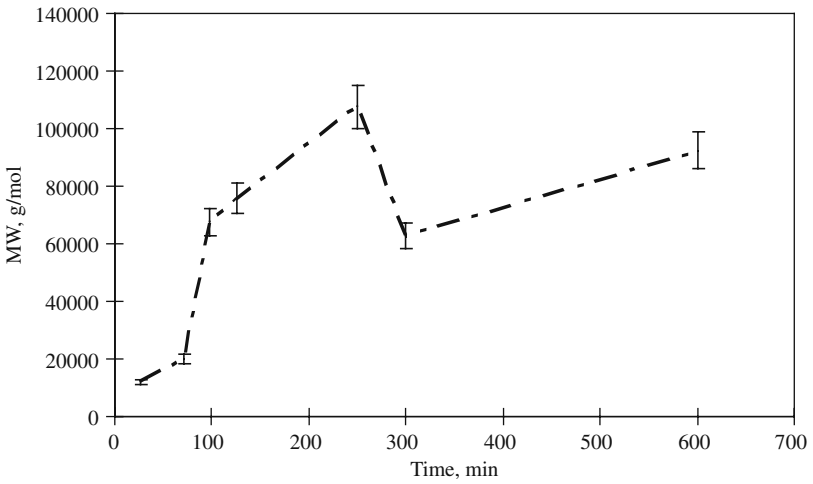

Fig. 4.1.2 Number average molecular weight vs time for PS samples taken from a reaction system which has the following initial composition: styrene/acetone/V-501 = 40/90/0.684 g/g/g. Reaction conditions are 80°C and 70 psig (Replotted with permission from Wang, 1997)

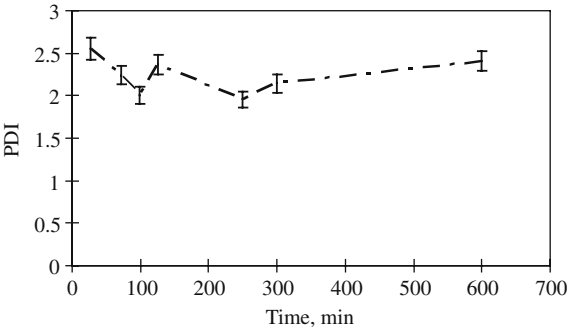

Fig. 4.1.3 Polydispersity index vs time for PS samples taken from a reaction system which has the following initial composition: styrene/acetone/V-501 = 40/90/0.684 g/g/g. Reaction conditions are 80°C and 70 psig (Replotted with permission from Wang, 1997)

Figure 4.1.2 shows that number average molecular weights above 100,000 g/mol are obtainable with FRRPP of S in acetone. In Fig. 4.1.3, polydispersity indices of 2 are also feasible.

In order to show that this type of system still follows the FRRPP mechanism, plots of $k_p/k_t^{1/2}$ vs conversion also show drop in values when corresponding conversion rates are dropping at high conversions (Fig. 4.1.4).

One thing that should be noted is the fact that acetone is a good enough chain transfer agent, which limits the PS molecular weight that can be attained. Also, since new chains are started from acetone-based radicals at the expense of the formation of dead polymer, the use of acetone for FRRPP of styrene is not expected to yield a high percentage of polymer radical species. Still, MWDs for Figs. 4.1.1–4.1.3 indicate a unimodal distribution, with only a slight shoulder to indicate the effect of chain transfer.

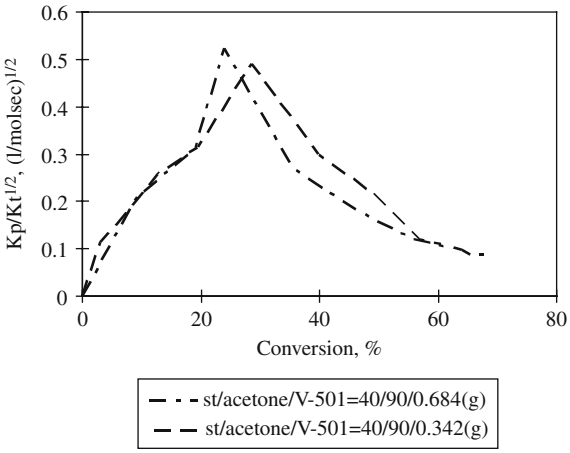

Fig. 4.1.4 Plots of $k_p/k_t^{1/2}$ vs conversion for batch polymerization of styrene through FRRPP process in acetone with V-501 initiator at 800°C and 70 psig, assuming $f = 0.58$. Starting compositions are given in the legend (Replotted with permission from Wang, 1997)

4.1.1.2 Poly(methacrylic acid) (PMAA)

Section 2.3.2 also shows data for the FRRPP formation of PMAA with water as solvent/precipitant. Characterization of the results were painstakingly done by Aggarwal (1993) and resulted in the validity of producing samples of this material as secondary and even primary standards. As shown in Fig. 2.3.20, relatively high molecular weights were obtained, reaching beyond 100,000 Da.

4.1.1.3 Poly(vinylidene chloride) (PVDC)

Reactor conditions for the FRRPP of VDC were deduced from Table 1.1.2 for azeotropic *t*-butanol/MEK as a suitable solvent/precipitant. Section 3.2.5 presented the reactor procedure for the formation of the PVDC material. The range of starting concentration of VDC was 31–83%. After polymerization for 5 h with AIBN as initiator, percent conversion values fell on a range of 1–13% at 120°C. Such a result is similar to conversion results for FRRPP of S in ether. The difference in the FRRPP of VDC was that the PVDC is a fine brown solid dispersion when it was removed from the reactor.

Figure 4.1.5 shows that the PVDC produced from the FRRPP process has a melting transition at 180°C. It also retains most of its original weight up to 200°C, and it retains 60% of its original weight at 250°C.

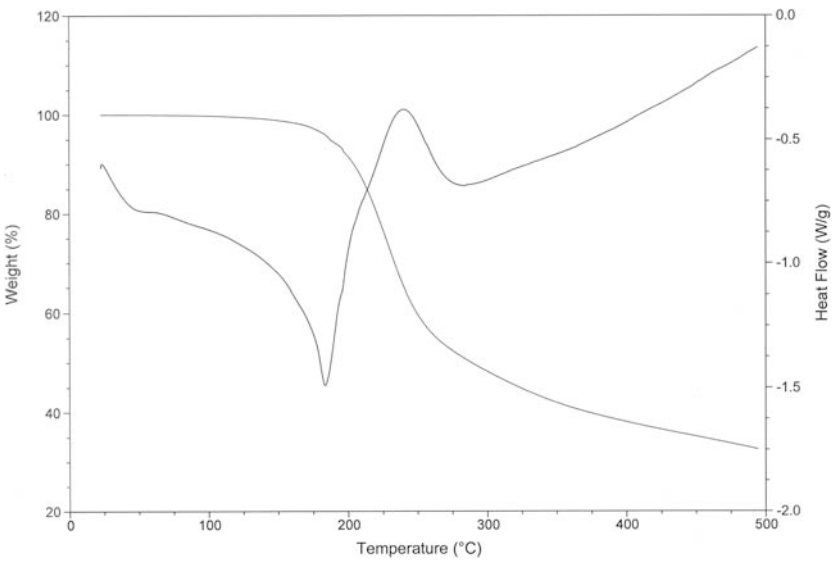

Fig. 4.1.5 DSC/TGA heating curves for a PVDC generated via the FRRPP process. Since the exotherm is up, the melting transition is minimum at 180°C in the DSC curve

4.1.2 Statistical Multipolymers

4.1.2.1 PS-Based Statistical Multipolymers

To supplement the kinetic data in Fig. 3.1.3, Tables 4.1.1 and 4.1.2, wt%AA data are shown below using ^{1}H-NMR methods with pyridine-d5 as solvent. Copolymer spectra were obtained using a Varian-400 MHz spectrometer. Solid copolymer samples were dissolved in a 5 mm NMR test tube with a concentration of 0.1 g/ml. The ^{1}H-NMR was performed at 50°C and the measurement parameters were as follows: acquisition time of 2.502 s, spectral width of 5,000 Hz, pulse width of 4.5 s, and number of scans equal to 16. The ^{13}C-NMR analysis was done at room temperature using the following acquisition parameters: acquisition time of 0.640 s, spectral width of 25,000 Hz, pulse width of 4.5 s, and number of scans between 2,000 and 8,000.

Table 4.1.1 GPC and other kinetic results of PS/PAA samples from the 100 g DEE or cyclohexane, 0.3 g V65, 3 g AA, 27 g S recipe

	Solvent – DEE				Solvent – CHX			
Number of initiator half-lives	Number average MW from RI (kDa)	PDI from RI	Number average MW from UV (kDa)	PDI from UV	Number average MW from RI (kDa)	PDI from RI	Number average MW from UV (kDa)	PDI from UV
1	2.63	2.3			9.45	2.0	8.74	2.1
3			2.16	3.0	11.0	2.0		
5	3.37	2.4	2.33	3.1	14.0	1.9	8.68	2.9
11	4.31	2.7	2.37	4.0	13.9	2.2	7.73	3.7

Table 4.1.2 GPC and other kinetic results of PS/PAA samples from the 100 g DEE or cyclohexane, 0.3 g V65, 1.5 g AA, 28.l5 g S recipe

	Solvent – DEE				Solvent – CHX			
Number of initiator half-lives	Number average MW from RI (kDa)	PDI from RI	Number average MW from UV (kDa)	PDI from UV	Number average MW from RI (kDa)	PDI from RI	Number average MW from UV (kDa)	PDI from UV
1	2.35	2.0	0.95	3.8	9.10	1.9	8.54	2.0
2					10.2	1.9	6.98	2.7
3	2.95	2.2	1.80	2.8	11.3	1.9	7.13	2.9
5	3.37	2.3	2.13	3.1	13.3	2.0	10.2	2.4
11	4.01	2.9	2.34	3.9	14.8	2.1	10.0	2.9

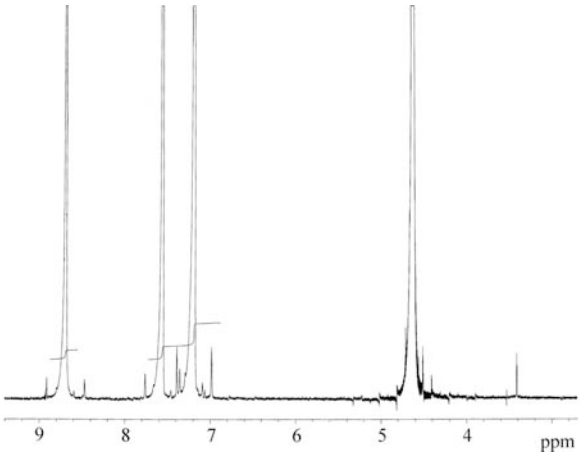

Fig. 4.1.6 ^{1}H-NMR spectrum of pure pyridine-d5 (50°C)

Proton and ^{13}C-NMR plots for pyridine and a typical S/AA copolymer are shown in Figs. 4.1.6–4.1.8.

Figure 4.1.9 shows the molecular structure of the deuterated pyridine-d5 and S/AA statistical copolymer along with carbon position labels.

Results of measurements of S/AA copolymer compositions via ^{1}H- and ^{13}C-NMR are shown in Fig. 3.1.3. In addition, summary of GPC results is presented in Tables 4.1.1 and 4.1.2.

All the GPC results in Tables 4.1.1 and 4.1.2 show unimodal peaks. This could indicate relative absence of random S/AA copolymer species. Also, molecular weights from the RI detector measurements are consistently larger than those from UV detector measurements. This indicates the disproportionate presence of AA in

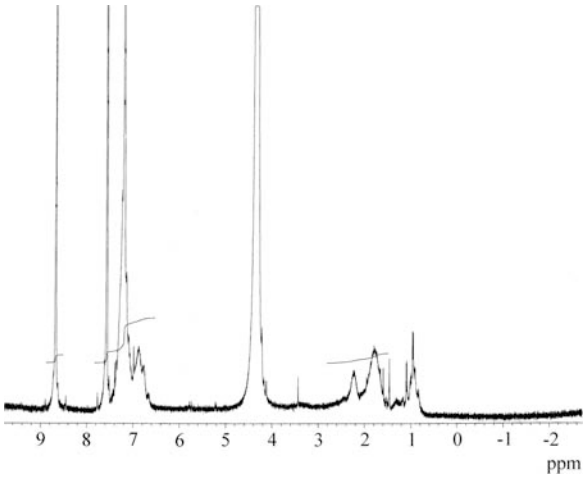

Fig. 4.1.7 ^{1}H-NMR spectrum of S/AA copolymer in pyridine-d5 (50°C)

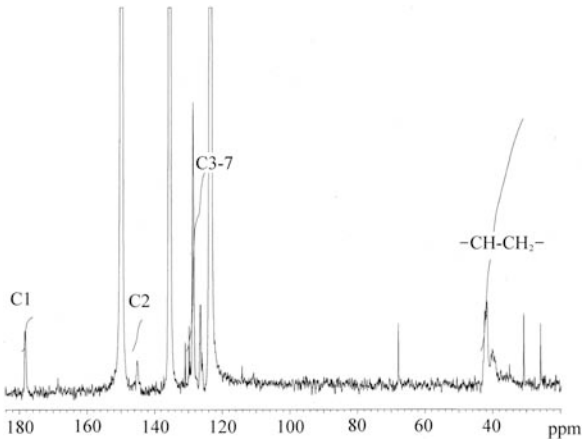

Fig. 4.1.8 ^{13}C-NMR spectrum of S/AA copolymer in pyridine-d5 (25°C)

the polymer chains. Finally, the use of cyclohexane resulted in higher molecular weight with less broad MWD than samples from ether-based runs.

For the products in Fig. 3.1.3, solubilities in toluene as well as % solids in emulsion were obtained. Emulsification was generally done by dissolving the product in THF and then adding ammonia-water. Finally, the THF was stripped off with heat combined with addition of makeup water.

It is evident that the FRRPP products (using DEE as solvent) were mostly soluble in toluene. Equivalent solution products seemed to be less soluble in toluene. This indicates the formation of significant random copolymer and/or homopolymers. As far as emulsifying capability is concerned, the higher the AA content of the FRRPP product, the more emulsifiable it is in water. Finally, it is worth noting the potential of products made from cyclohexane (see Tables 4.1.1–4.1.2), due to relatively high molecular weight products with relatively narrow MWDs. However, based on Table 4.1.3, these cyclohexane-based runs form less amphiphilic materials compared to those from the ether-based runs (Caneba et al., 2003).

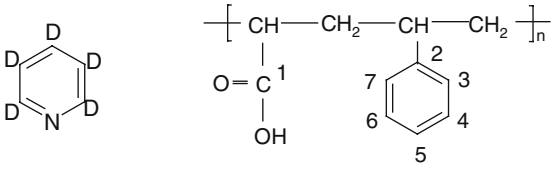

(a) Pyridine-d5 (b) S-AA copolymer

Fig. 4.1.9 Formulas for deuterated pyridine (**a**) and S/AA copolymer (**b**). In (b), "1" refers to the carbon element in carboxyl group and "2-7" stands for the carbon elements in benzene ring, which is linked to the backbone of copolymer chain

Table 4.1.3 Results of solubility and emulsification of S/AA copolymer products

Reactor charge used to generate product	% Solids from supernatant of toluene extraction	% Solid from emulsification in water
100 g DEE, 0.3 g V65, 1 g AA, 27 g S	100	17
100 g DEE, 0.3 g V65, 1.5 g AA, 28.5 g S	100	32
100 g DEE, 0.3 g V65, 3 g AA, 29 g S	90	98
100 g CHX, 0.3 g V65, 3 g AA, 27 g S	52	100
100 g CHX, 0.3 g V65, 1.5 g AA, 27 g S	100	15

Toluene solubility and emulsification studies were also done with the SAA1 and SAA2 products (described in Section 3.1.4.1). The SAA1 product (ether-based run) completely dissolved in toluene and no residue was obtained during emulsification. This means that SAA1 is a true amphiphilic material. The SAA2 product completely dissolved in toluene, but almost none of it formed a self-emulsion even in ammonia-water.

The above data provide the kinetics, solubility, and emulsification results for three solvents: ether, pyridine, and cyclohexane. Note that S polymerization in ether occurs via FRRPP, but AA polymerization in ether occurs via conventional precipitation polymerization (CPP). Pyridine is a solvent for both PS and PAA; thus, copolymerization of AA and S in pyridine is via solution polymerization. Finally, AA polymerization in cyclohexane is via CPP and PS formation in cyclohexane is via solution polymerization.

4.1.2.2 VDC-Based Statistical Multipolymers

The FRRPP polymerization of VDC–Zonyl® TA-N was carried out in parallel pressure tubes and in a Stage 1 stirred-tank reactor system. The reaction process was done at 120°C for about 8 h; reaction yield was about ~80%. A high-throughput polymerization reaction using a robotic dispensing system containing VDC and Zonyl® TA-N was undertaken by varying the amounts of VDC and Zonyl® TA-N for 24 samples.

The second high-throughput polymerization reaction was the use of VDC, Zonyl® TA-N, Zonyl® TM, and Zonyl® PFBE. The Zonyl® concentration for the three reactions was higher than the VDC concentration ranging from 62 to 83% Zonyl®. No polymers were formed in the reaction possibly due to low reactivities of the Zonyl® monomers. An FRRPP recipe of 36 g VDC, 3.6 g Zonyl® TA-N, AIBN 1 wt% initiator in the solvent mixture (methyl ethyl ketone 66%, *t*-butanol 34%) at 110°C was commenced for our first-stage reaction with a 9% conversion. Sometimes during the first-stage reaction additional Zonyl® TA-N was added 3.6 g after the initial monomer, AIBN, and solvent injection. PolyZonyl® TA-N was synthesized with a 15 wt% solution in *t*-butanol, methyl ethyl ketone, and 0.5 wt%

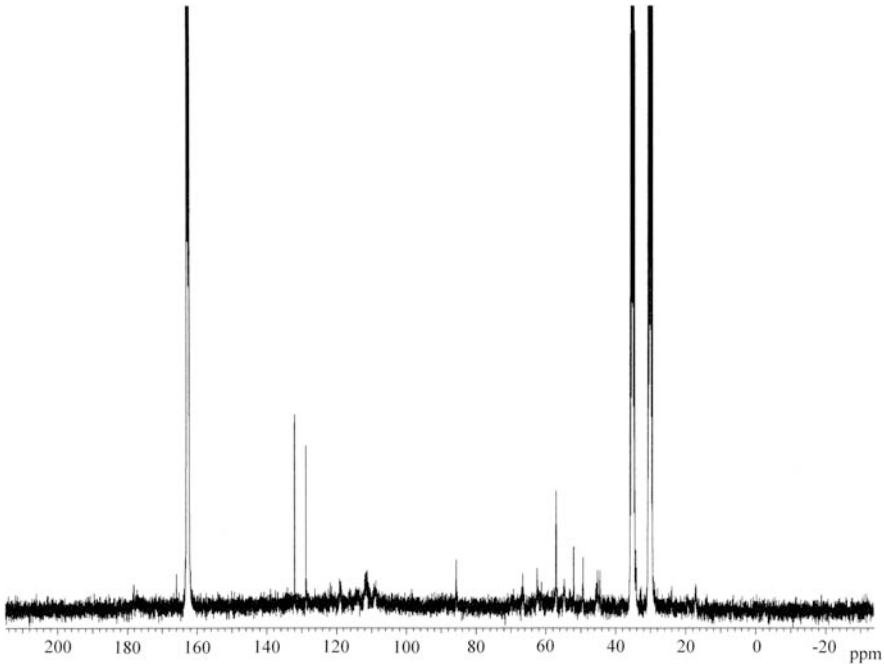

Fig. 4.1.10 ^{13}C-NMR of Zonyl® TA-N in deuterated DMF

AIBN relative to monomer content. The melting temperature of PolyZonyl® TA-N was 80 and 175°C and thermally stable up to 350°C.

In Fig. 4.1.10, the ^{13}C-NMR of Zonyl® TA-N is shown, in comparison to that of the VDC-Zonyl® TA-N spectrum in Fig. 4.1.11. Another verification of the formation of the copolymer (Fig. 4.1.12) is its DSC/TGA plot, which shows transitions pertaining to the VDC (Fig. 4.1.5) and Zonyl® TA-N (Fig. 4.1.13).

Product VDC–Zonyl® TA-N copolymers are in the form of fine particulate (Fig. 3.2.6), which were removed from the reactor through a 1/8 in. copper or stainless steel line that is immersed in ice-water bath. This kept the polymer radicals active for block multipolymer formation.

4.1.2.3 Poly(vinyl acetate)-Based Statistical Multipolymers

During the FRRPP copolymerization of VA and AA when reactor fluid composition was maintained at around 10 wt% AA relative to the monomers, a statistical copolymer with almost equal spacing of VA segments was obtained. AA was added into the reactor fluid for a longer period of time during the reaction run. The reactor initially contained the following: 323.7 g azeotropic *t*-butanol/water, 3 g AA, and 71.2 g VA. The reactor fluid was heated to the operating temperature of 65°C for 30 min

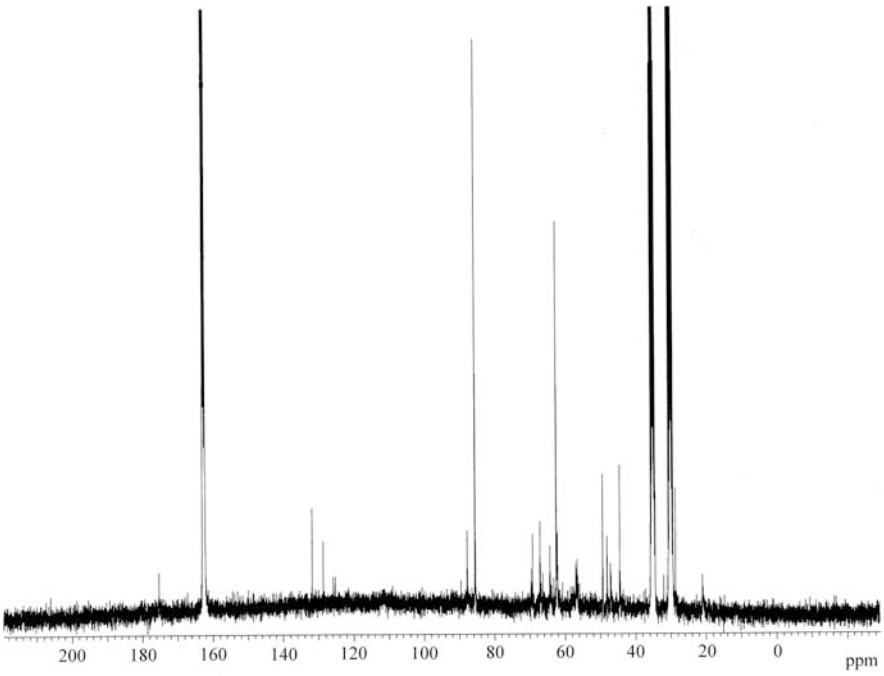

Fig. 4.1.11 ^{13}C-NMR of VDC-*stat*-Zonyl® TA-N copolymer in hot deuterated DMF

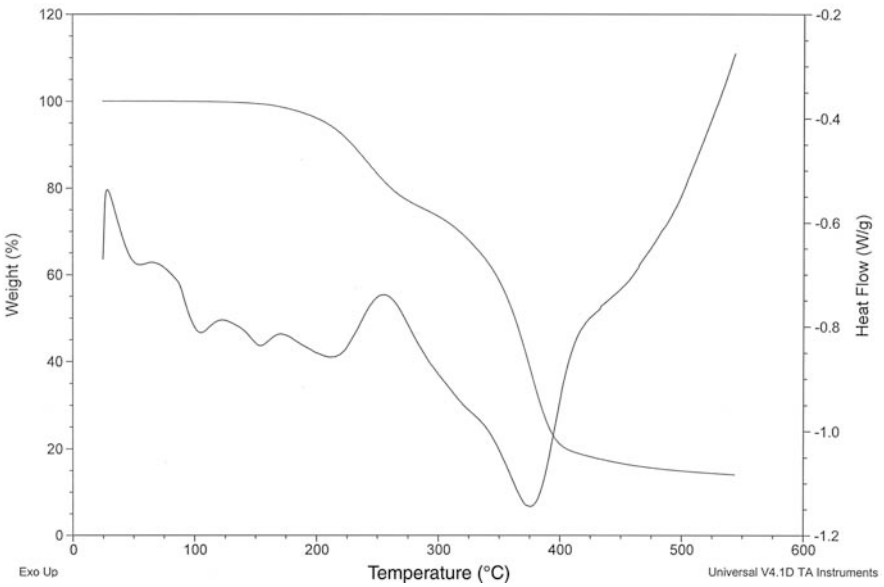

Fig. 4.1.12 DSC/TGA heating curves for a VDC–Zonyl® copolymer generated via the FRRPP process. Since the exotherm is up, the melting transitions are minima at 100, 150, and 200°C in the DSC curve

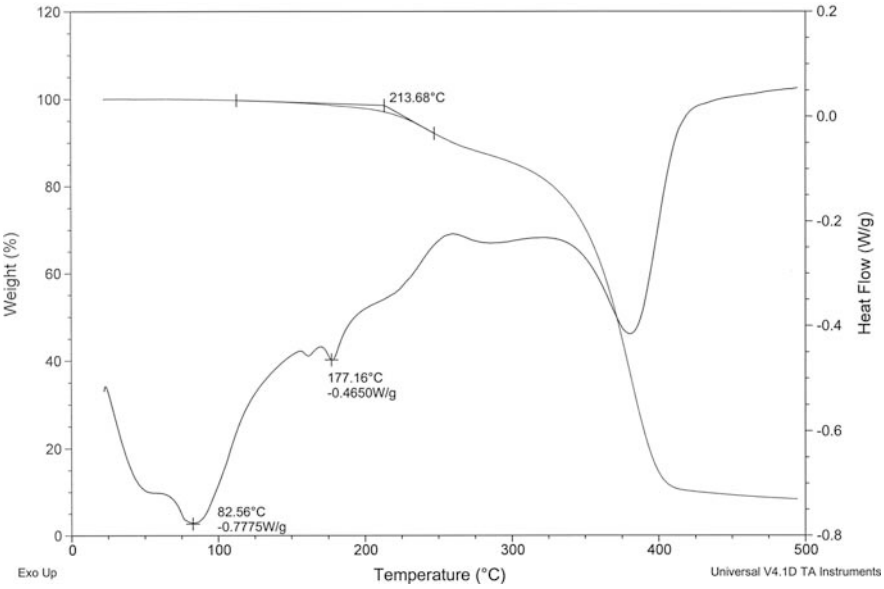

Fig. 4.1.13 DSC/TGA heating curves for a Zonyl® TA-N polymer generated at MTU. Since the exotherm is up, the melting transition is minimum at 60–70°C in the DSC curve

along with a slow nitrogen sweep. When the operating temperature was reached, the reactor was sealed at time zero and the following was added till time $t = 23$ min: 0.3046 g VA-044, 10.3 g distilled water, and 44.7 g azeotropic *t*-butanol/water. At $t = 31$ min, the following solution was introduced up to $t = 2$ h and 23 min: 3.1 g AA, 37.9 g VA, and 82.9 g azeotropic *t*-butanol/water. The reaction was allowed to continue up to $t = 8$ h and 58 min. After this time, an air sweep was used to render the reactor fluid nonreactive before the steam heater was turned off while cooling water was used to bring the reactor fluid to room temperature.

The kinetic data from this experiment is shown in Fig. 3.1.7, resulting in the R10-1 product (Section 3.1.4.2). Its GPC trace is shown in Fig. 3.1.11, which indicates a material with a relatively high molecular weight and a reasonable PDI of 1.97. When the reactor product was coagulated in water with KOH, the coagulum can be drawn into a fibrous material. This is probably due to the development of microcrystalline domains of potassium acrylate in the polymer, as evidenced by a melting transition at 47°C.

4.2 Block Multipolymers

Aside from the PS-PBA type of emulsion FRRPP product introduced in Section 3.2, it is worth mentioning the promise of the formation of other emulsion FRRPP block copolymer products, such as PMMA-PBA.

Fig. 4.2.1 First-stage stirred-tank reactor system (4,500 psig Parr reactor systems on the right) and second-stage 45-psig pressurized 1-l glass reactor on the left used to generate block multipolymers from radicalized VDC copolymer particulates (With permission from Caneba et al., 2008)

In a recent work, formation of block multipolymers from radicalized VDC copolymer particulates has been demonstrated (Caneba et al., 2008). Using the two-stage stirred-tank reactor system (Fig. 4.2.1), recipes and conditions were generated using high-throughput experimentation methods. From cloudpoint experiments (Table 1.1.3), it has already been established that the solvent for the VDC polymerization via FRRPP process is azeotropic MEK/*t*-butanol.

Stage 1 formation of the VDC–Zonyl® TA-N radicalized particulates has been described in Section 4.1. In order to form the block multipolymer, the first-stage reactor dispersion was charged into the second-stage reactor along with solvent and a new set of monomers. Early stages of this work were carried out in high-throughput experimentation format as shown in Fig. 4.2.2. Upon heating, the block copolymer started to form. Various tests were done to show block copolymer formation, amidst the difficulty in dissolving the first-stage VDC copolymer for analysis. These tests included DSC/TGA, ^{13}C-NMR, solubility, coagulation, and fractional precipitation methods. Once the procedure was established, second-stage reaction was carried out in the 1-l near-atmospheric glass reactor system shown in Fig. 4.2.1.

An example product is a diblock called RB1-232 made of a VDC copolymer (96 wt% VDC, 6 wt% Zonyl® TA-N) block with a butyl acrylate-*stat*-glycidyl methacrylate block. The reactor product solution was fractionally precipitated, and

Fig. 4.2.2 High-throughput experimentation 10-atm glass tube reactors used in the early stage block multipolymer formation

the fractogram (previously shown in Fig. 3.2.7) indicates minimal VDC copolymer contamination due to the single fractionation peak for the block copolymer. It was noted that VDC copolymer contamination would represent dead copolymer radicals after the first-stage reaction, and such material would be precipitated almost immediately. Of course, apparent mechanical properties (such as the transition from the hard VDC copolymer material to soft and/or elastic materials) indicate the formation of block copolymers. Comparison work was done with commercial VDC copolymers, which included solubilization, film spincasting, drying, annealing, and tensile testing uniaxially and biaxially.

A related product called RB1-200 was made; its detailed recipe and procedure are presented in Table 4.2.1.

DSC/TGA analysis of RB1-200 (Fig. 4.2.3) indicates a strong effect of the curing reaction of the GMA, based on the rise in the DSC curve between 75 and 270°C (as also verified by melt processing experiments), which shows good segregation of the second block containing the GMA segments. Underneath this rise are inflection points corresponding to T_g of PMMA at 105°C and T_m of VDC at 180–220°C, which again indicates good segregation of these segments into their respective domains. The dip at 50–80°C in the DSC curve corresponds to the T_m of the Zonyl® segments.

Other products from the VDC-based block copolymers will be described in latter sections of this chapter.

Table 4.2.1 Recipe and procedure for the formation of RB1-200 A-B block copolymer

Recipe name: RB1-200						
Stage 1						
Temperature	110 °C		Pressure:	100 psig		
Initial charge:						
50 ml 66:34 wt/wt MEK:*t*-butanol						
Reactant charge:						
3.6 g ® TM in 50 ml 64:36 wt/wt MEK:*t*-butanol						
50 ml VDC stock solution (from 30 ml VDC with 100 ml 66:34 wt/wt MEK:*t*-butanol)						
30 ml 1 wt% AIBN in 66:34 wt/wt MEK:*t*-butanol						
Line purge:						
20 ml 66:34 wt/wt MEK:*t*-butanol						
Stage 2						
Start temp.	Room temp.			Pressure:	10 psig	
Substage 1						
Charge to reactor:						
All of Stage 1 product, 50 g MMA, 50 g GMA, 300 g NMP						
Temp. ramp to 60 °C		Ramp time: 4 h		Soak: 4 h		Cool to RT: 1 h

Table 4.2.1 (Continued)

Substage 2					
Charge to reactor:					
All of Stage 2/Substage 1 reactor product, 200 ml NMP					
Temp. ramp to 60°C		Ramp: 4 h	Soak: 5 h		Cool to RT: 1 h
Substage 3					
Charge to reactor: Stage 2/Substage 2 product					
Temp. ramp to 60°C		Ramp: 1 h	Soak: 5 h		Cool to RT: 1 h

4.3 Reactive Polymer Intermediates

4.3.1 PS-Based Intermediates

An obvious approach to PS-based intermediates via the FRRPP process is through live PS radicals that can be used for chain extension with another set of monomers. Formation of live PS radicals at room temperature has been quite tricky, because chains terminate through conventional free-radical polymerization at relatively low polymer concentration as the temperature was being lowered slowly. Either high polymer concentration was achieved or polymer radicals had to be rapidly cooled to drastically reduce their reactivity. Both approaches were employed successfully and introduced in Chapter 3.

Another approach to PS intermediates was made through the use of functional initiators, which provide the polymer certain functional end groups. For example, the use of V-501 initiator from Wako Chemical Co. provides carboxylic acid end groups to the polystyrene chains, which can be reacted with a basic functionality from another polymer. In order for this reaction to occur cleanly, initiator fragments as well as undecomposed initiator molecules have to be extracted

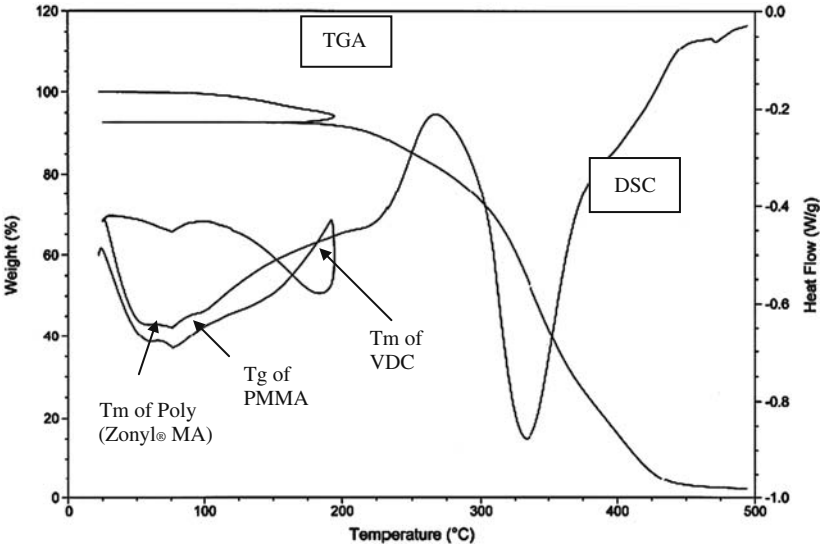

Fig. 4.2.3 DSC/TGA of the RB1-200 product, which contains segments from VDC, Zonyl® methacrylate, methyl methacrylate (MMA), and glycidyl methacrylate(GMA). The run is made up of a heat-up step to 200°C, then a cooldown step to room temperature, followed by a final heat-up step. Both heat-up and cooldown steps are at 10°C/min rate. Note that exotherm is up in the vertical axis

from the polymer. This has been done through dissolution–precipitation cycles (Wang, 1997).

Block copolymer based on PS and either PMAA or PAA (S-*block*-(S-*stat*-MAA) or S-*block*-(S-*stat*-AA) copolymers) that were presented in Section 3.2 have been found to be good reactive intermediates. The acid groups can react with base-functional polymers in order to produce PS blocks with grafted chains on the other block.

4.3.2 VDC Copolymer-Based Intermediates

Radicalized VDC statistical copolymer with Zonyl® has been shown to be capable of formation of various block copolymers, which in turn can also be reactive intermediates. This is true with the RB1-200 and RB1-232 products described in Section 4.2, in which the second block contains epoxide groups from glycidyl methacrylate. Another product, called RB1-201, was similar to RB1-200 but contained Zonyl® TM segments in the second block (see synthesis procedure in Table 4.3.1).

Infrared analysis of RB1-201-3 showed two C=O peaks at 1726 and 1684 cm^{-1} from the acrylate group and one epoxide peak at 907 cm^{-1}. Some epoxide groups were converted into OH groups (10%), based on the 3,440 cm^{-1} OH band.

The DSC/TGA data for RB1-201, shown in Fig. 4.3.1, indicates the presence of various segmental units reflected in the recipe shown in Table 4.3.1. Specifically,

Table 4.3.1 Polymerization recipe and procedure for the formation of RB1-201 samples and products

Recipe name:	RB1-201					
Stage 1						
Temperature:	110°C		Pressure:	100 psig		
Start time:			End time:			
Initial charge:						
50 ml 66:34 MEK:*t*-butanol						
Reactant charge:						
3.6 g Zonyl® TM in 50 ml 64:36 MEK:*t*-butanol						
50 ml VDC stock solution (from 30 ml VDC with 100 ml 66:34 MEK:*t*-butanol)						
30 ml 1 wt% AIBN in 66:34 MEK:*t*-butanol						
Purge charge:						
20 ml 66:34 MEK:*t*-butanol						
Stage 2						
				Pressure:	10 psig	
Cycle 1						
T=60°C		Ramp: 4 h		Soak: 1 h		Cool: 1 h
Charge to Stage 2 reactor:						
1/2 volume of 10/11/06 Stage 1 product						
30 g Zonyl® TM						
21.2 g GMA						
34.4 g MMA						
400 ml NMP						

Table 4.3.1 (Continued)

RB1-201-1: 1/2 Stage 2/Cycle 1 reactor product						
Cycle 2			Operator:			
T=60°C		Ramp: 1 h		Soak: 7 h		Cool: 1 h
Charge to Stage 2 reactor:						
1/2 of Stage 2/Cycle 1 reactor product						
10 g GMA						
15 g MMA						
163 g NMP						
RB1-201-2: 1/2 of Stage 2/Cycle 2 reactor product						
Cycle 3			Operator:			
T=60°C		Ramp: 1 h		Soak: 5 h		Cool: 1 h
Charge to Stage 2 reactor:						
1/2 of Stage 2/Cycle 2 reactor product						
0.4 g V65-B						
RB1-201-3: all of Stage 2/Cycle 3 reactor product						

the presence of the GMA segment was shown based on its self-curing capabilities at 100–200°C.

Still another reactive block copolymer product, called RB1-215, contained butyl acrylate (BA) in the second block (B-block) (Caneba et al., 2008). The same Stage 1 (formation of A-block) was used as in RB1-200 and RB1-201. Typically, there were three cycles to the Stage 2 reaction. Cycle 1 contained 340 ml NMP, 34 g MMA, 42.5 g GMA, 8.5 g BA and Cycle 2 contained 16 g MMA, 16 g Zonyl® TA-N. Cycle 3 was a heating cycle only without addition of any new monomers. Figure 4.3.2 depicts the overall procedure used to produce the reactive RB1-215 ABC triblock multipolymer. Detailed recipe and procedure are also presented in Table 4.3.2.

Some GC-MS analysis of the Stage 2 product RB1-219-221 (same run as that for formation of RB1-215) solutions provided the amounts left over of acrylic

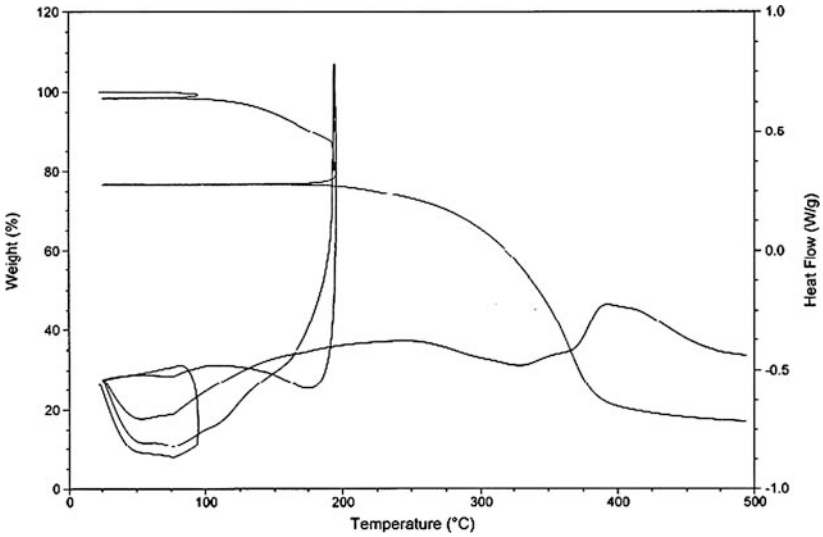

Fig. 4.3.1 DSC/TGA heating/cooling curves for the pure RB1-201. Three heating heating/cooling cycles were used. The first one is heating to 100°C and cooling to room temperature. The second cycle is heating to 200°C and cooling to room temperature. The third cycle is just heating up to 500°C

monomers relative to the *N*-methyl pyrrolidinone solvent amount. Based on the data (Table 4.3.3), it appears that the GMA is more incorporated into the polymer than the MMA, followed by BA. This makes sense because the resulting solid product had relatively strong BA odor.

After the Stage 1 and Stage 2 polymerization runs, products were separated from the reactor solvents (*t*-butanol, MEK, and NMP), unreacted monomers (VDC, Zonyl®-TAN, Zonyl®-TM, MMA, GMA, and BA), and unreacted initiator (AIBN

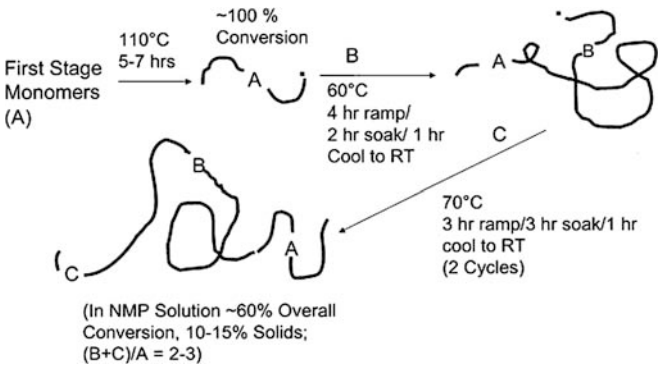

Fig. 4.3.2 Procedure for the formation of RB1-215 (With permission from Caneba et al., 2008)

Table 4.3.2 Polymerization recipe and procedure for the formation of RB1-215 samples and products

Recipe Name: RB1-215						
Stage 1						
Temperature:	110°C		Pressure:	100 psig		
Initial Charge:						
50 mL 66:34 MEK:t-butanol						
Reactant Charge:						
3.6 g Zonyl® TM in 50 mL 64:36 MEK:t-butanol						
50 mL VDC stock solution (from 30mL VDC with 100 mL 66:34 MEK:t-butanol)						
30 mL 1 wt% AIBN in 66:34 MEK:t-butanol						
Purge Charge:						
20 mL 66:34 MEK:t-butanol						
Stage 2						
			Pressure:	10 psig		
Cycle 1						
T=60 C		Ramp: 4hr	Soak: 4hr		Cool: 1hr	
Charge to stage 2 reactor:						
1/2 volume of 11/14/06 Stage 1 product (2nd half)						
20 g MMA						
25 g GMA						
250 mL NMP						
5 g BA						
Cycle 2						
T=70 C		Ramp: 2hr	Soak: 6hr		Cool: 1hr	
Charge to stage 2 reactor:						
All Stage2/Cycle 1 Reactor Product						
10.4 g Zonyl® TM						
10.3 g MMA						
100 ml NMP						
10.1 g GMA						
Cycle 3						
T=70 C		Ramp: 2hr	Soak: 2hr		Cool: 1hr	
Charge to stage 2 reactor: None						
RB1-215: All of Stage 2/Cycle 3 Reactor Product						

and V-65B). First, the polymer was coagulated with excess water (3:1 v/v or more) out of the reactor fluid into a gel or dough (Fig. 4.3.3).

Second, solvents and unreacted reactants were extracted from the dough. Third, the dough was dried into a purified and safe-to-handle product, and then melt-blended with other components, if needed (Fig. 4.3.4).

Table 4.3.3 GC-MS analysis of Stage 2 product of RB1-219–221 (also RB1-215)

RB1-	GMAinit (%)	GMAfinal (%)	MMAinit (%)	MMAfinal (%)	BAinit (%)	BAfinal (%)
219	17.2	1.80	14.7	2.44	—	—
220	17.2	4.07	14.7	4.08	2.50	1.31
221	17.2	1.26	14.7	1.82	—	—

Init=initial concentration
Final=final concentration

Fig. 4.3.3 Coagulated RB1-215 product on a Petri dish (With permission from Caneba et al., 2008)

Coagulation is the process in which the dissolved polymer in the Stage 2 polymerization reactor fluid is precipitated out of solution. By adding water to the reactor fluid product, the chemical environment is altered such that the polymer–solvent interactions become less favorable compared to the polymer–polymer, which results in the polymer precipitating out of solution. The reactor fluid (250 ml) was placed

Fig. 4.3.4 Dried and melt-blended RB1-215 product on a Petri dish (With permission from Caneba et al., 2008)

in a glass pan and at least 750 ml water was added. The solvent-laden polymer precipitate (around 50:50 polymer:solvent v/v) was then removed from the reactor fluid.

Residual solvent and reactants were removed from the "dough." Initial attempts to purify the polymer included one vacuum oven drying step (4 h at 80°C), used to drive off the residual solvent, followed by up to three supercritical CO_2 extraction steps (8-h soak at room temperature and 2,000 psig), used to remove unreacted monomers, oligomers, and residual solvent.

This process was later replaced by a more efficient process that involved extracting the solvent and unreacted monomers and oligomers, with methanol; and once extracted, evaporating the methanol from the purified polymer powder. A 500-g quantity of solvent-laden "dough" was vigorously mixed with 4-l quantities of methanol. The resulting suspension was then allowed to sit for 1–2 h until the polymer settled to the bottom, at which time the methanol with extracted solvent and reactants was decanted off. This process was performed a total of 10 times, ensuring a purified polymer. The methanol-saturated polymer was then allowed to air dry in the fume hood and the purified polymer was collected.

DSC/TGA analysis of RB1-215 product has been shown to be even more thermally stable than the Stage 1 VDC-Zonyl® intermediate product (Fig. 4.1.5). As shown in Fig. 4.3.5, the weight of the RB1-215 material decreased to only 80% of its original value at 300°C, even after two heating cycles. Curing of the GMA segments is also evident at 100–275°C.

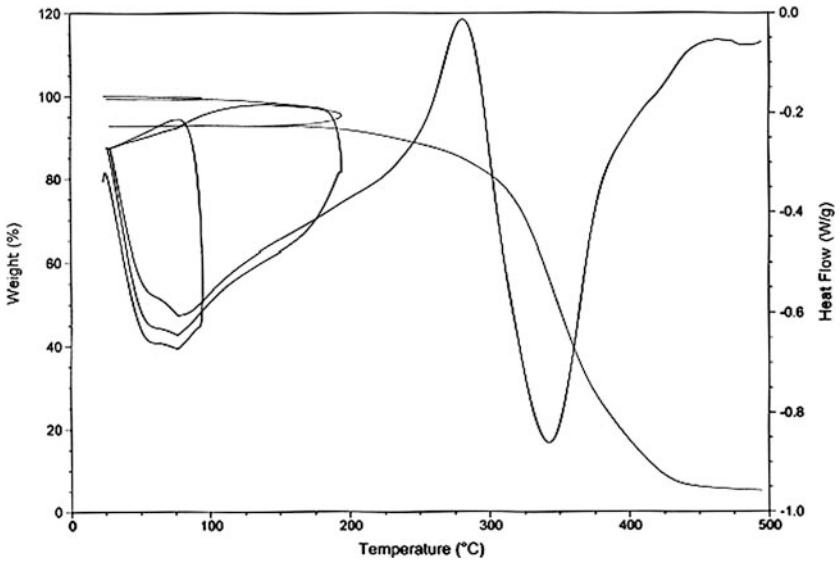

Fig. 4.3.5 DSC/TGA heating/cooling curves for the RB1-215 copolymer generated via the FRRPP process. Three heating heating/cooling cycles were used. The first one is heating to 100°C and cooling to room temperature. The second cycle is heating to 200°C and cooling to room temperature. The third cycle is just heating up to 500°C.

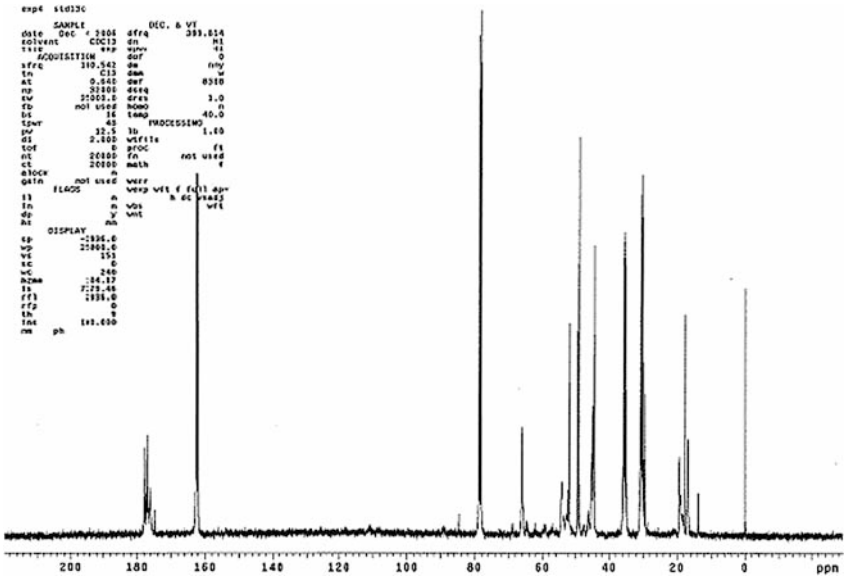

Fig. 4.3.6 ^{13}C-NMR spectrograph of RB1-215

Attempts were made to carry out ^{13}C-NMR spectroscopy of monomeric components, intermediate, and final copolymer products. Problems include long NMR runs (8–12 h per sample) and the difficulty in completely dissolving the VDC segments of the copolymer samples. Still, it was possible to conclude that the second-stage monomers were incorporated into the intermediate copolymer radicals from the Stage 1 reactor (Fig. 4.3.6).

The polymer RB1-222 (same as RB1-215, except Zonyl® TA-N was instead of Zonyl® TM) was fractionated with 50% ethanol/water solution. The polymer solution was diluted either 10:1 or 5:1 v/v with NMP solvent. Based on the fractogram (Fig. 4.3.7), there is very little intermediate VDC–Zonyl® Stage 1 precipitate at 0–15 ml precipitant added. A quantitative analysis indicates that the unreacted Stage 1 contamination amounts to less than 1 wt% of the product copolymer. This result of relatively insignificant unreacted Stage 1 contamination seems to be generally the case. Finally, the two fractogram peaks indicate the formation of both reactive AB and ABC multipolymers. This is due more to the difficulty of achieving more chain extension from the AB multipolymer radical than premature chain termination by recombination, because of the relative ease of processability of the RB1-215 product before curing. Either a less concentrated reactive polymer solution or more monomers need to exist in the reactor during the third stage of polymerization.

Based on the above-mentioned analytical data and reaction kinetic results for RB1-215, its morphological structure can be depicted in Fig. 4.3.8 (Caneba et al., 2008).

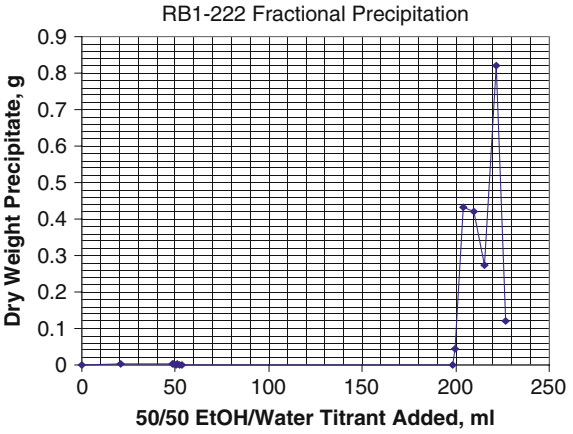

Fig. 4.3.7 Fractional precipitation data for RB1-222 (same as RB1-215, except Zonyl® TA-N was used instead of Zonyl® TM) copolymer product (With permission from Caneba et al., 2008)

The A-block contains the VDC segments, while its B and C blocks contain both GMA and MMA segments. The B-block also contains BA segments. What makes the C-block unique is the presence of the Zonyl® TA-N or Zonyl® TM segments, which have a melting transition of 50–80°C (Caneba et al., 2008).

4.3.3 VA/AA-Based Intermediates

AA segments of tapered VA/AA copolymer (discussed in Section 3.1) can also be used as reactive functional groups for formation of other types of copolymers and multipolymers. These acid segments are also capable of reacting or interacting with solid surfaces, thereby resulting in well-anchored PVA coatings or interfacial agents (see also Section 4.6).

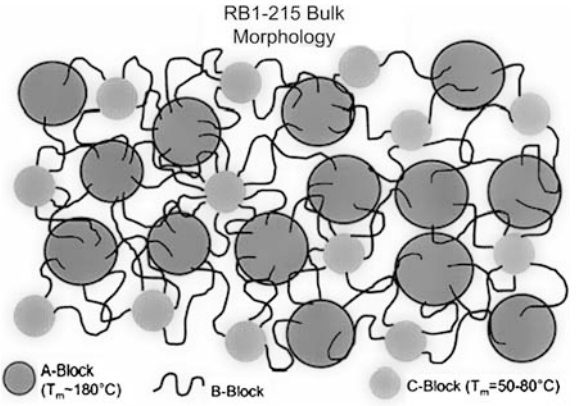

Fig. 4.3.8 Depicted bulk morphology of RB1-215 copolymer (Caneba et al., 2008) (With permission from Caneba et al., 2008)

4.4 Polymer Surfactants

Polymer surfactants are a class of materials that the FRRPP process is able to produce efficiently, either though single-stage or two-stage block copolymerization methodologies. In a conventional sense, surfactants are compounds that comprise a hydrophilic head and a hydrophobic tail (Fig. 4.4.1).

The most popular classification of surfactants is based on its ionic characteristics; they are either anionic, cationic, or nonionic. Since ions are normally found in aqueous fluids, ionic characteristics of surfactants are found in the hydrophilic head; thus, an anionic surfactant would have negatively charged species in the hydrophilic heads. Because of the requirement of charge neutrality in an overall fluid system, an anionic surfactant would have its positive counterion within its vicinity. This counterion is subject to various ion-exchange mechanisms either with other types of counterions in the fluid or on solid surfaces. It is possible for nonionic species to be hydrophilic, because of their polar and hydrogen-bonding interactions with water molecules.

Early types of industrial surfactants were based on alkylbenzene sulfonates (ABS), whereby aromatic compounds were first alkylated followed by the reaction of the aromatic ring with sulfuric acid. Upon neutralization with a convenient base, the result is an anionic ABS surfactant material. Later, cationic and nonionic types were introduced in the market. Even so, one should realize that these and most of the modern surfactants are oligomeric in size (see Fig. 4.4.2 for examples of anionic and nonionic surfactants).

While an entire book can be occupied by a catalog of oligomeric-based surfactants, polymeric-based surfactant types in the market cannot be counted with fingers of both hands. The most recognizable one is the nonionic ethylene oxide-propylene oxide (EO-PPO) segmented block copolymer, manufactured by BASF with the Pluronic® tradename. Surface-active behavior of polymeric surfactants is a new area of research and it seems to be poised for new discoveries. The biggest hurdle to having more polymeric surfactants in the market is their manufacturing cost.

Surfactants are popularly known for their detergency properties. Their appeal is based on the observation that while they are dispersible in water, they can remove efficiently oily contaminants from various surfaces, such as apparel, building materials, and appliances. This was found to be due to the capability of surfactants to form mesoscopic structures called micelles, in which surfactant molecules self-organized into spherical, cylindrical, and even lamellar domains. In these domains surfactant molecules arrange themselves like infantry soldiers of a Roman legion in defensive positions, wherein the hydrophilic heads of each molecule are facing the wide

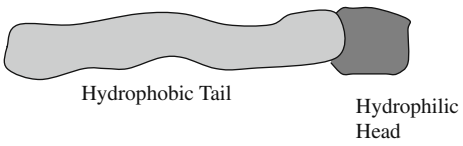

Fig. 4.4.1 Representation of a surfactant molecule, which comprises a hydrophobic (oil-loving) tail and a hydrophilic (water-loving) head

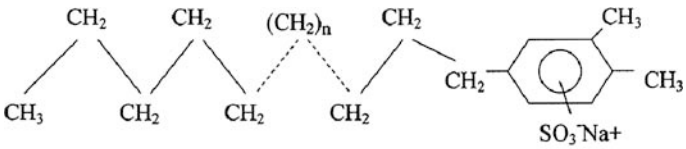

SODIUM ALKYL-ORTHOXYLENE SULFONATE
(n = from 2 to 10)

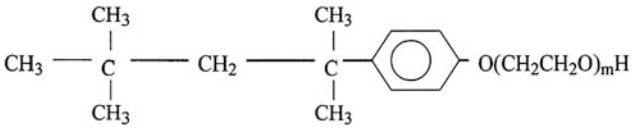

ETHOXYLATED OCTYLPHENOL (NONIONIC)
(m = from 2 to 100 – average value)

Fig. 4.4.2 Examples of anionic (*top*) and nonionic (*bottom*) surfactants

expanse of the aqueous phase while the hydrophobic tails that harbor oily material are facing inward amongst other hydrophobic tails of other molecules. In a fluid system under constant Brownian motion, one would expect that when there are not enough surfactant molecules per volume, micelles would not form. What was observed was the existence of a threshold concentration of surfactant as the lower limit before micelle formation can occur. This is called the critical micelle concentration (CMC). As a general rule, the lower the CMC, the more effective a surfactant is, because less surfactant material is needed to form micelles. The CMC is also associated with the change in slope of the surface tension of the fluid with concentration, again due to the transition in structural assembly of the molecular system (Fig. 4.4.3).

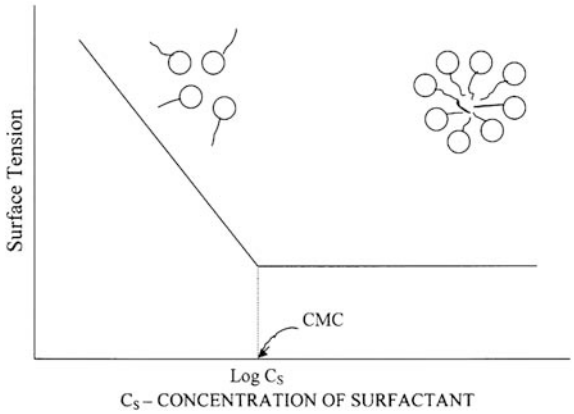

Fig. 4.4.3 Determination of the critical micelle concentration (CMC) based on a change in the slope of the surface tension vs surfactant concentration

Table 4.4.1 HLB numbers of various surfactants (*McCutcheon's Volume 1: Emulsifiers and Detergents*, 1998)

HLB No.	Trade name	Chemical description
1.0	Pluronic® L101	Block copolymers of propylene oxide and ethylene oxide
1.8	Span® 85	Sorbitan trioleate
3.3	Tegin® O	Glycerol oleate
4.0	Glycomul® S	Sorbitan monostearate
7.0	Plurafac® RA-40	Modified oxyethylated straight chain alcohol
9.0	Rhodameen® T-5	Tertiary amines; ethoxylates of primary tallow amines
11.0	Tween® 85	POE (20) sorbitan trioleate (polysorbate 85)
13.0	Brij® 56	Polyoxyethylene (10) cetyl ether
14.0	Pluronic® P105	Block copolymers of propylene oxide and ethylene oxide
17.0	Nonionic E-20	Ethoxylated nonyl phenol
19.0	Varonic® Ll-420	Ethoxylated mono and diglyceride
24.0	Tetronic® 1107	Block copolymers of propylene oxide and ethylene oxide
30.0	Atlas G-263	*N*-cetyl, *N*-ethyl morpholinium ethosulfate (aqueous solution)
40.0	Rhodapon® SB	Sodium lauryl sulfate
71.7	Dow corning Q2-5220 surfactant	Silicone glycol copolymer

Another property of surfactants has to do with their tendency to form oil-in-water (O/W) or water-in-oil (W/O) emulsions, through the so-called hydrophile–lipophile balance (HLB) number. The HLB number is defined in such a way that a value of 7 is the boundary, and below that the surfactant tends to form W/O emulsions. In Table 4.4.1, HLB numbers are indicated for a number of surfactants.

Polymeric surfactants seem to behave differently from their oligomeric counterparts. For example, polymeric surfactants seem to have the tendency to form structures between those of O/W and W/O types, such as bicontinuous structures. If an O/W structure is called a Type I Winsor structure and W/O structure is called the Type II Winsor structure, then polymeric surfactants readily form the Type III Winsor structure (Fig. 4.4.4) (Pope and Baviere, 1991). This structural tendency for polymeric surfactants may be a disadvantage because Type III Winsor structures would result in higher fluid viscosities or even non-Newtonian behavior (such as Bingham plastic behavior) for the same volume fraction surfactant. At low enough surfactant concentration, even polymeric surfactants can form either Type I or Type II Winsor structures, depending on its HLB number. The difference compared to its oligomeric counterpart seems to be in the domain size; polymeric surfactants are much larger and this indicates the tendency to form vesicular (or layered) arrangements. Thus, polymeric vesicles can be seen through optical microscopy and look more turbid in the naked eye (Fig. 4.4.5).

Polymeric surfactants from multipolymers seem to be possible from blocky (tapered- or step-block) and segmental block structures. It has also been possible

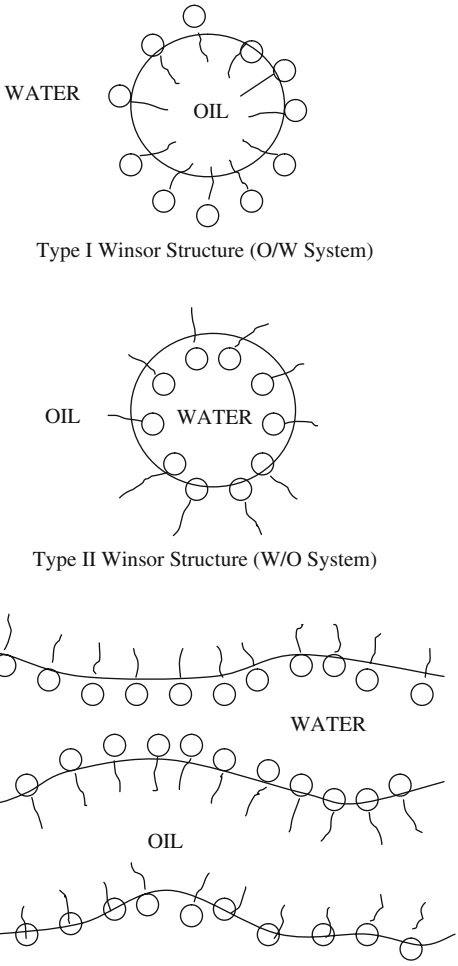

Fig. 4.4.4 Winsor structures for surfactants in oil and water

for an extreme case of segmental block structure, such as equally spaced random copolymer, to exhibit surfactancy behavior.

As shown in Fig. 4.4.2, it takes a relatively small amount (at least 10%) of ionic component in a molecule for it to exhibit surfactancy. This is achievable with the FRRPP process, because one can always add an acid monomer to react with a hydrophobic polymer radical even in the presence of unreacted hydrophobic monomer. The example is when methacrylic acid was added to polystyrene radicals even at 30% styrene conversion to produce an amphiphilic S-*block*-(S-*stat*-MAA) amphiphilic material (see Section 4.2). Methacrylic and acrylic acid monomers are normally reactive to polymer radicals in general, as it can be seen from their reactivity ratios. When amine–PDMS was reacted with the acid groups of the

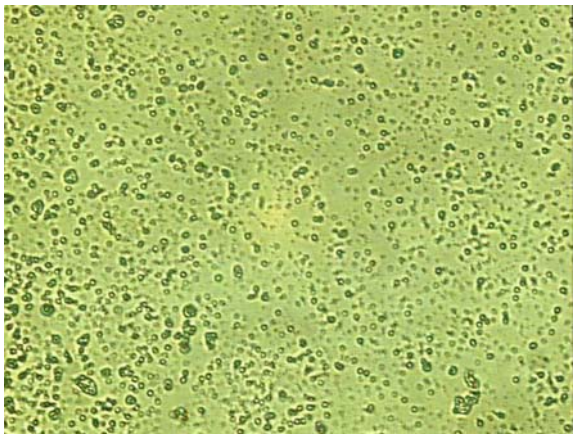

Fig. 4.4.5 Optical micrograph of a surface of a tapered blocky VA/AA-based polymeric surfactant with 6 wt% AA content in diluted emulsion form (from 6.6 wt% solids) at 400X magnification, showing about 10 μm spherical domains and aggregates up to about 60 μm in size (With permission from Caneba and Axland, 2002b)

S-*block*-(S-*stat*-MAA) material, a PS–PDMS block copolymer was formed (see Section 4.6), which was shown to possess good surfactancy properties.

As it was later discovered, it has been more convenient to carry out tapered block copolymer formation with the acid monomer reacting first followed by the hydrophobic monomer in a single-stage FRRPP copolymerization method (see Section 4.1). The result was an anionic polymer surfactant after neutralization of the acid segments with a base (Caneba and Dar, 2005).

VA/AA-based surfactant copolymers and multipolymers are good example cases that can be produced from the single-stage block copolymerization FRRPP process (see Section 4.1). The single-stage copolymerization FRRPP method was employed to produce VA/AA tapered block copolymers. Specifically, the B6-1 VA/AA tapered block copolymer has the following CAS registry:

- CAS # [903900-50-5]
- Type of polymer: a reduced regulatory requirement (RRR) polymer
- CAS name of polymer: 2-propenoic acid with ethenyl acetate, hydrolyzed
- Common name: partially hydrolyzed vinyl acetate-ammonium acrylate copolymer
- Molecular structure:

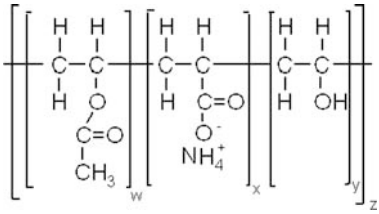

Surface tension measurements for this surfactant indicate a range of CMC values between 0.1 and 1 wt%. This is reasonable because of the distribution of molecular

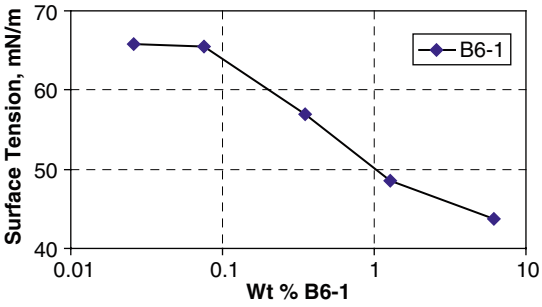

Fig. 4.4.6 Surface tension vs wt% solid for B6-1 surfactant in water, wherein AA segments were neutralized with ammonia

sizes and hydrophilic segment numbers across all the polymer chains that make up the surfactant (Fig. 4.4.6).

It was also discovered that surfactancy can exist from the equally spaced VA/AA statistical copolymer (R10-1) with one AA segment per 10 VA segment, which was found to be that of a water-in-oil surfactant or Winsor Type II structure.

4.5 Polymer Foams from the FRRPP Process

4.5.1 Vinyl Acetate-Acrylic Acid Copolymer Foams

Tapered block vinyl acetate-acrylic acid copolymer materials made from the FRRPP process (see Section 4.1) have been shown to blow into conventional foams with relatively high expansion ratios (in the order of 50). An example foam material is shown in Fig. 6.1.1, which was obtained during drying of THF solvent from the polymer. Similar foams were obtained when acetone was used as solvent/blowing agent. Finally, neutralized B6-1 VA/AA copolymers have been shown to be good foaming surfactants and introduced as suitable foamflooding enhanced oil recovery agents (Section 5.2).

4.5.2 Vinylidene Chloride Copolymer-Based Foams

Conventional foams (with void sizes >1 mm in diameter) can be used as a lightweight alternative to solid materials used in the construction industry. However, for conventional foams, the effect of reducing the overall mass of the system comes at the expense of mechanical strength of the material. One way to minimize the loss of mechanical strength is to generate microcellular foams, which have void diameters on the order of tens to hundreds of micrometers only. This creates a void size that tends to be less than the critical flaw length, usually on the order of 1–10 mm, which is the minimal length for a flaw to propagate and crack the material along shear planes. This crucial difference between microcellular and conventional foams

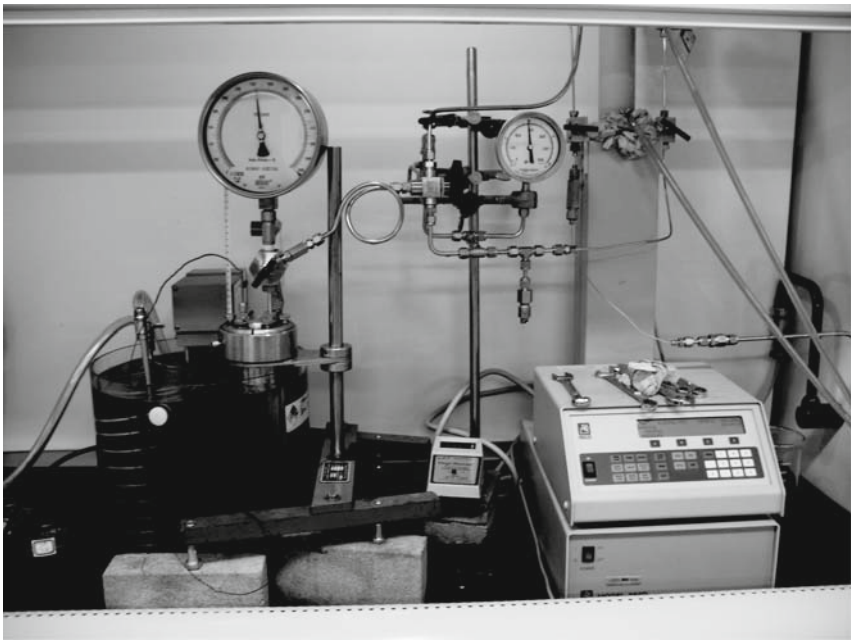

Fig. 4.5.1 Apparatus used to produce microcellular foams

has led to an increase in the use of microcellular foams over conventional foams in weight and strength critical applications. Figure 4.5.1 shows a picture of the apparatus used to generate monolithic VDC-based copolymer microcellular foam samples which is schematically represented in Fig. 3.2.8.

Literature reviews and experimental efforts were carried out in order to determine the best free-radical monomer candidates to incorporate into the VDC-based copolymer in order to promote microcellular foam formation utilizing carbon dioxide as a "green" blowing agent. The saturation concentration and mass diffusion rate of carbon dioxide, the final foam density and stability, and effects of plasticizing agents were studied for multiple polymers at various conditions (including saturation temperature, saturation pressure, soak time, foaming temperature, and foaming time) in order to help determine the monomer make-up of the polymer. Table 4.5.1 shows preliminary foam factorial design used to determine the optimal polymer with CO_2 as blowing agent. However, due to expected delivery system limitations, the majority of the work was limited to using room temperature (23°C), various indicated saturation and foaming temperatures, and a saturation pressure of 1,000 psig.

The copolymer samples went through five steps in order to generate the microcellular foam. First, the samples were brought up to the desired saturation temperature and pressure inside the vessel using the syringe pump and water bath. Second, the polymer samples were allowed to "soak" at this pressure and temperature for the duration of the desired soak time. Third, the vessel was isolated from the syringe

pump and a vent valve was used to depressurize the vessel over the duration specified by the foaming time; polymer at temperatures above their T_g would foam at this step, however, glassy polymers would have to go through two further steps. Fourth, for glassy polymers, polymer below their respective T_gs, an additional hot water bath was implemented to foam these polymer samples at a foaming temperature above their T_g. Finally, the foam samples were quenched in a cold water bath in order to prevent foam collapse (the foam was quenched at a temperature well below the polymer's T_g). For glassy polymers, the weight percent of carbon dioxide in the sample could be determined since the carbon dioxide did not expand the polymer until placed in the hot water bath and a mass could be recorded from a scale.

Of critical importance, analysis of poly(methyl methacrylate) (PMMA) showed that at a saturation temperature, T_s, of 40°C, a saturation pressure, P_s, of 1,500 psig (at these conditions, carbon dioxide is considered a supercritical fluid), and a saturation time, t_s, of 24 h, a 1 mm thick disk absorbed 16.4 wt% carbon dioxide. Additionally, at a foaming temperature, T_f, of 120°C and a foaming time, t_f, of 1 min, PMMA had a stable volumetric expansion ratio of 20. Other polymers also absorbed significant quantities of carbon dioxide, such as polystyrene (PS) and poly(vinylidene chloride-co-acrylonitrile) (P(VDC-AN)), which absorbed 8.9 and 2 wt% carbon dioxide, respectively, yet the stable foams that were formed had expansion ratios of less than 2 at the same conditions used to form the PMMA samples. Another polymer poly(vinyl methyl ketone) (PVMK) achieved an expansion ratio of 20. However, the foams were unstable, readily collapsed, and exhibited large voids (~5 mm diameter), which are inconsistent with microcellular foams. The fact that PVMK readily collapsed after the foaming process made it difficult to determine the concentration of carbon dioxide in the sample. These results led to the eventual incorporation of the MMA monomer into the polymer formulation from the standpoint of carbon dioxide-induced microcellular foamability.

Plasticizer studies were conducted in order to improve the foamability of the other monomeric constituents of the VDC-based copolymers. Table 4.5.2 shows the classes and formulations of the Scientific Polymer Products plasticizers used in this study. Also, water and *N*-methyl-2-pyrolidinone (NMP) were considered in the plasticizer studies. Studies of P(VDC-AN), poly(vinylidene chloride-co-vinyl chloride) (PVDC-VC), and poly(vinylidene chloride-co-acrylontirile-co methyl methacry-

Table 4.5.1 Preliminary microcellular foam factorial design

Polymer	Saturation temperature, T_s, °C	Saturation pressure, P_s, psig	Saturation time, t_s, h	Foaming temperature, T_f, °C	Foaming time, t_f, min
P(VDC-AN)	40	1,500	8	40	2
P(VDC-AN-MMA)	80	2,000	16	80	5
PMMA		2,500	24	120	
P(VDC-VC)	RT(23)	1,000	4	RT (23)	0.5
PS	80		32		

Table 4.5.2 Scientific polymer products (SP^2) plasticizers

SP^2 #	Derivative	Plasticizer
1	Adipic acid	Dicapryl adipate
8	Aazelaic acid	Di(2-ethyl hexyl) azelate
20	Dimer acid	Bis(2-hydroxyethyl) dimerate
24	Fumaric acid	Dibutyl fumarate
29	Lauric acid	Methyl laurate
44	Palmitic acid	Isopropyl palmitate
88	Succinic acid	Diethyl succinate

late) (P(VDC-AN-MMA)) were performed in order to determine the best suitable plasticizer system for creating microcellular foams with the VDC-based polymer.

A plasticizer is used to effectively reduce the polymer's glass transition temperature, T_g, and enhance carbon dioxide absorption of the polymer/plasticizer system. This should promote the growth of foam constructed from a rigid glassy polymer, such as PS or P(VDC-VC). The plasticizer is believed to promote foam growth during the foaming process by making the polymer pliable and compliant to the growth of the nucleated carbon dioxide cells. Simultaneously, the plasticizer is thought to be extracted from the polymer by the escaping carbon dioxide, returning the polymer to its pre-plasticizer rigid state, effectively "freezing" the foam in place, and preventing structure collapse.

Initial plasticizer tests showed that plasticizers #24, dibutyl fumerate, and #88, diethyl succinate, had the most promise when considering the foamability of VDC-based copolymers. These tests were carried out at 12.5, 25, and 50 wt% plasticizer mixed with powdered VDC copolymers (P(VDC-AN), P(VDC-VC), and P(VDC-AN-MMA)), with only the 50 wt% plasticizer samples displaying a significant increase in foamability compared to the non-plasticizer study results. However, at a 50 wt% plasticizer concentration, the carbon dioxide did not sufficiently extract the plasticizer from the polymer and only an expansion factor of 2 was achieved. Another effect the plasticizer had was to agglomerate the powder together into a monolithic form, suggesting that the plasticizer relaxed the individual polymeric strands and allowed entanglements to form between individual powder particles. Other attempts were made to expand VDC-based copolymers with water and NMP, leading to similar results with an expansion factor of 2–3 and retaining significant amounts of water and NMP in the final polymer foam.

The use of NMP and/or plasticizers as well as varying foaming conditions was incorporated in a high-throughput experimental methodology during the downselection for the polymer. For the premade VDC-based copolymer from the polymerization track, an RB1-201 VDC-based copolymer product described in Section 4.3.2 resulted in microcellular structures (Fig. 4.5.2).

Parallel foaming experiments were carried out for RB1-201-2 and RB1-212 samples (see Section 4.3.2) at 45°C and 1,500 psig for at least 8 h in vials approximately

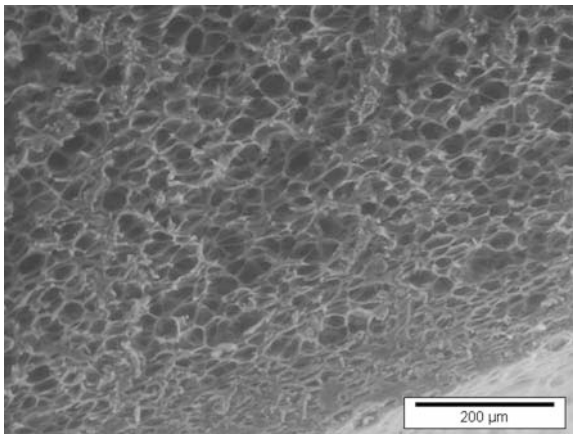

Fig. 4.5.2 Microcellular foam structure obtained from RB1-201 VDC-based copolymer

1.3 cm in inside diameter. Plasticizers used include NMP, #8 Plasticizer, and RB1-212 extract from a previous foaming operation. After foaming, heights in the bottle were observed and recorded. Table 4.5.3 shows that the best result is an expansion factor of only 3 (Sample #10). For higher expansion factors, higher temperatures and/or CO_2 pressures are required.

These tests demonstrated that using supercritical carbon dioxide to produce monolithic microcellular polymeric foams would achieve expansion ratios of 2–3 at room temperature and 1,000 psig of CO_2.

The RB1-215 VDC-based copolymer, an A-B-C triblock copolymer type introduced in Section 4.3.2 was also developed for microcellular and conventional foam

Table 4.5.3 Foaming results of 0.5 g polymer samples at 45°C and 1,500 psig CO2 for at least 8 h

#	Polymer	Plasticizer/solvent, g			Height, cm	Monolith (M) or particulate (P)	Expansion factor
		RB1-212 extract	NMP	#8 Plasticizer			
1	RB1-201-2	0.05	0	0	1	M	2
2	RB1-201-2	0	0.05	0	1	M	2
3	RB1-201-2	0	0	0.05	0.5	P	
4	RB1-212	0.05	0	0	0.7	M	
5	RB1-212	0	0.05	0	0.8	M	
6	RB1-212	0	0	0.05	0.7	M	
7	RB1-212	0.10	0	0	0.8	M	
8	RB1-212	0	0.10	0	1.2	M	2.5
9	RB1-212	0	0	0.10	0.7	P	
10	RB1-201-2	0.10	0	0	1.5	M	3
11	RB1-201-2	0	0.10	0	0.8	M	
12	RB1-201-2	0	0	0.10	0.7	M	

formation. Its A-block contains the VDC segments, while its B and C blocks contain both GMA and MMA segments. The B-block also contains BA segments. What makes the C-block unique is the presence of the Zonyl® TA-N or Zonyl® TM segments, which have a melting transition of 50–80°C. The product has been coagulated into a dough, placed in a vacuum oven at 80°C for 1 h, and then melt processed at 100–180°C. Melt processing above 120°C resulted in an insoluble elastic material; thus, the occurrence of self-crosslinking. Attempts were made to foam the copolymer using CO_2 as blowing agent. Three samples were generated with the following recipes and process conditions:

1. Sample #1 – vacuum dried and then heated at 90–100°C, initially weighing 2.4 g, 2.5 cm in diameter, and 0.8 cm thick
2. Sample #2 – airdried then heated at 90–100°C, initially weighing 2.2 g, 2.5 cm in diameter, and 0.9 cm thick
3. Sample #3 – same as Sample #2, except that 3.3 g initial weight was heated with 0.5 g Zonyl® BA, whereby the resulting final weight is 3.2 g only (lost 0.6 g). Pieces of this material did not fuse together, due to the surface active properties of the Zonyl® BA.

All samples were foamed at room temperature with 900–1,000 psig CO_2 for 8 h, using a fast pressure drop (within 30 s to atmospheric pressure). Expansion factors of the samples are 2.5 for Sample #1 (monolith), 2.5–3 for Sample #2 (monolith), and 2.5 for Sample #3 (fused particulates). When NMP (20% relative to initial polymer) was added into Samples #1–#3 and then refoamed (45°C and 1,500 psig CO_2 for 4 h), an expansion factor of 5 was obtained for Sample #1 and 7.5 for Sample #3, respectively (Fig. 4.5.3). Thus, having both NMP and Zonyl® BA seems to result in foams with the highest expansion factor of 7.5.

Fig. 4.5.3 Foam samples from RB1-215 product

DSC/TGA results for RB1-215 indicated promise as thermal resistant foams (Section 4.3.2). It was later concluded that the RB1-215 material could not result

in strong expansive foams (expansion factors greater than 5) at room temperature and 1,000 psig CO_2. Higher temperatures and pressures will be needed for the formation of foams with higher expansion ratios.

4.5.3 VDC Multipolymer Nanocomposites in Polyurethane Foams

An approach was formulated whereby one of the VDC-based copolymers (RB1-201) would be dispersed in a PU foam formulation, and then crosslinked with the base PU. This approach naturally produces CO_2, provides crosslinking of the copolymer, and disperses it in nanoscale as an interpenetrating polymer network (IPN).

Polyurethane (PU) thermosets have been known to possess good mechanical, thermal, and chemical properties. The key to these properties is the level of crosslinking in the final product. As the density of the product foam is brought down, there is the need to improve its mechanical properties. With the VDC-based copolymer, this can be achieved by in situ PU foam formation in the presence of the copolymer with reactive groups. The result is an interpenetrating polymer network (IPN) (Sperling, 1974–75, 1981, Sperling and Amts, 1971; Mishra et al., 1994; Huelck et al., 1972;Donatelli et al., 1976). ABS (acrylonitrile-butadiene-styrene) and HIPS (high-impact polystyrene) are two commodity polymers that have been produced using poly(butadiene) as the pre-existing polymer, resulting in material properties that exploit excellent characteristics of component polymers.

The implementation of IPN formation using the RB1-201 copolymers is depicted in Fig. 4.5.4.

Variants of the RB1-201 were produced in the laboratory, and chemical company was contracted for toll manufacturing. In the toll manufacturing site, the first-stage reactor was a pressurized 5-gallon system, while the second-stage reactor was a glass-lined 100-psig 50-gallon reactor system.

We proceeded in using the toll manufactured RB1-201 material in hybrid PU/RB1-201 polymer foam formulation, and details of the foaming procedure is shown in Fig. 4.5.5. We noted that this toll manufactured RB1-201 was readily dispersed in THF and it can be reasonably dispersed in the polyol of the PU formulation. Thus, foam samples were made from the flow hybrid foaming process as well. The PU formulation employed was the so-called Tigerfoam® system.

The polyurethane flow foaming apparatus was then assembled and has been operated in order to produce a variety of Tigerfoam® based foams with varying concentrations of toll manufactured RB1-201 polymer and to determine the effects of alternate blowing agents, aside from R-245fa. The foam was expanded into 2 and 3 in. packaging tubes for mechanical, chemical, and flame testing. The toll manufactured RB1-201 polymer was added to the polyol side at total concentrations of 0, 2.5, 5, 10, and 20 wt%, resulting in final toll manufactured RB1-201 polymer

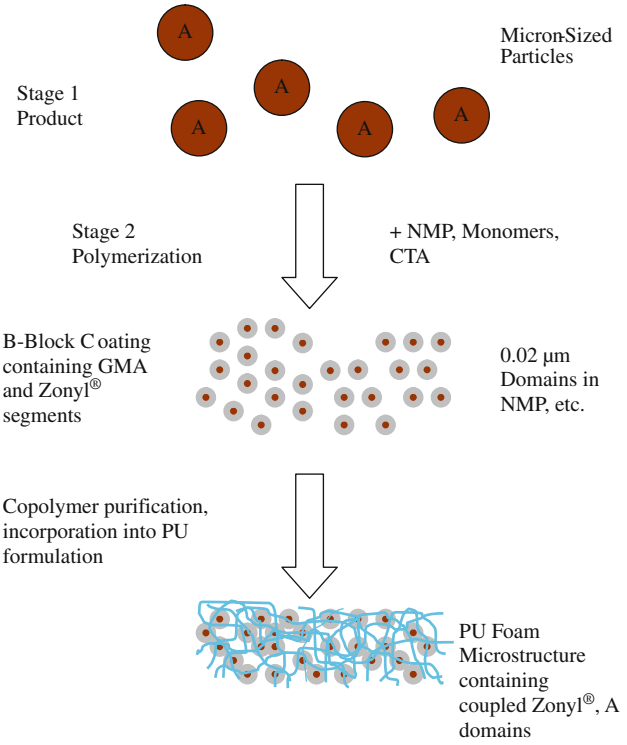

Fig. 4.5.4 Outline of the steps and expected morphologies for IPN formation using the RB1-201 copolymer (as pre-existing polymer) and conventional PU formulation

concentration in the polyurethane foam of 0, 1.25, 2.5, and 5 wt%. Additionally, the refrigerant R-134a was replaced in the polyol component with R-245fa for 0, 2.5, 5, and 10 wt% RB1-201 polymer in polyurethane foams in order to determine the effect of a R-134a/R-245fa blowing agent system. These in-house produced hybrid samples from Tigerfoam® components as well as Tigerfoam® reference samples were tested. The tests showed no significant deterioration in mechanical properties compared to Tigerfoam®, while improvements were obtained in thermal analysis tests (please see Figs. 4.5.6 and 4.5.7 and Table 4.5.4). These comparative studies were performed for a foam density around 60 kg/m^3, wherein compressive strengths were found to be in the order of 300 kPa.

In summary, it was found that hybrid 5 wt% RB1-201 in Tigerfoam® is thermally superior over reference constituent materials, which seems to be due to a synergistic effect. Also, addition of the RB1-201 up to 5 wt% in the Tigerfoam® did not result in significant deterioration of foam mechanical properties. Finally, foam samples contain 20–23 wt% volatiles.

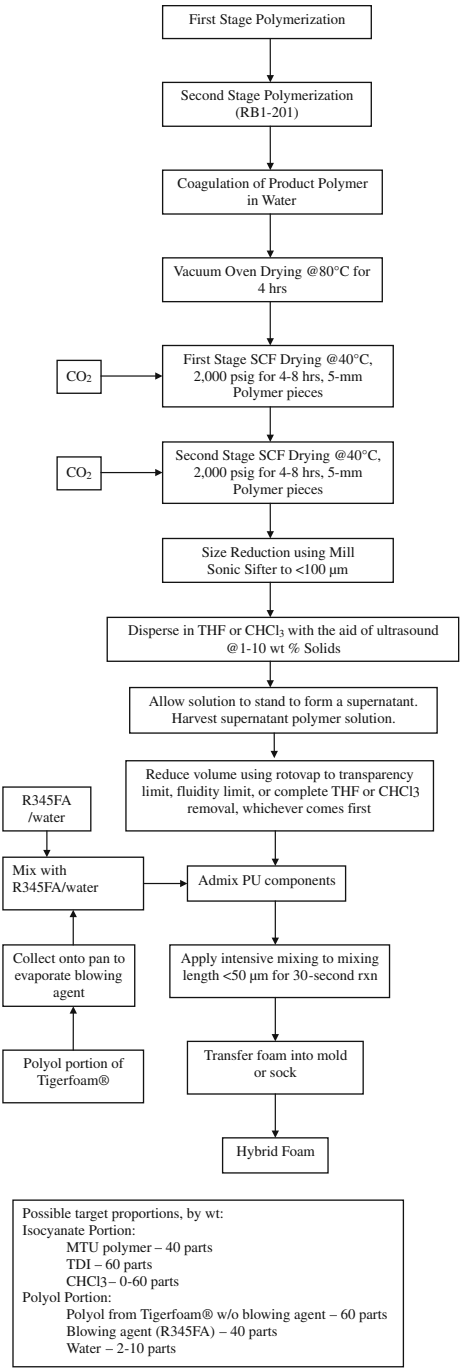

Fig. 4.5.5 DSC/TGA heating/cooling curves for the toll manufactured RB1-201/Tigerfoam® material. Three heating heating/cooling cycles were used. The first one is heating to 100°C and cooling to room temperature. The second cycle is heating to 200°C and cooling to room temperature. The third cycle is just heating up to 500°C

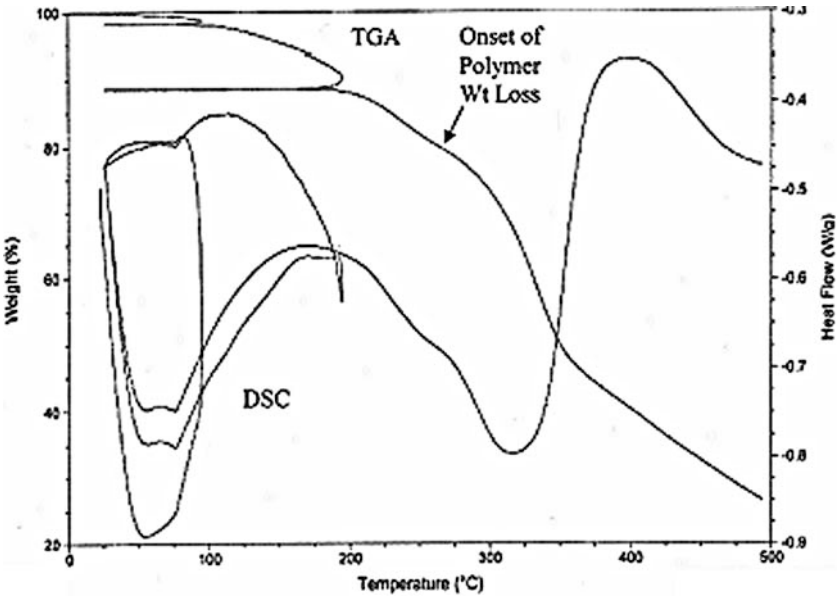

Fig. 4.5.6 DSC/TGA heating/cooling curves for the pure Tigerfoam®. Three heating heating/cooling cycles were used. The first one is heating to 100°C and cooling to room temperature. The second cycle is heating to 200°C and cooling to room temperature. The third cycle is just heating up to 500°C

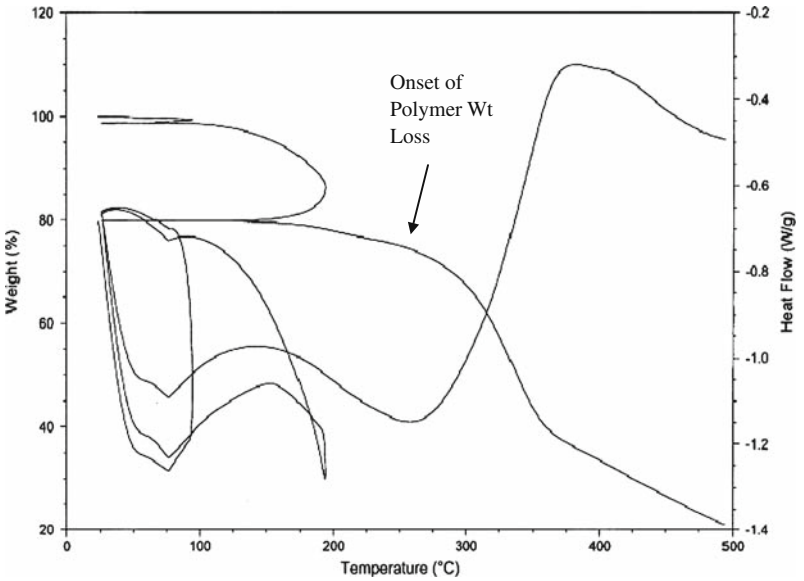

Fig. 4.5.7 Operational details of the batch procedure used in the preparation of the hybrid RB1-201/Tigerfoam®

Table 4.5.4 Quantitative determination of improvements in thermal properties of the hybrid foam material relative to various references, based on DSC/TGA analysis

Polymer	Residual volatiles present (wt%)	Onset of polymer wt loss (°C)	%wt loss after first heat to 100°C	%wt loss after second heat to 200 °C	Normalized polymer % wt retention @ 300°C	Normalized polymer %wt retention @ 350°C
Tigerfoam®	22	220	2	18	86	54
Hybrid (5 wt% Toll manufactured RB1-201 in Tiger-foam™)	20	260	4	10	91	63
Toll Manufactured RB1-201	23	220	2	20	84	58

4.6 Coatings

Aside from the coatings that can be produced from emulsion FRRPP (Section 3.2.3), this section contains other materials that were developed for more specialized coatings.

4.6.1 Polystyrene-Poly(Dimethyl Siloxane) (PS–PDMS) Coatings

PS–PDMS coatings were produced from intermediate S-*block*-(S-*stat*-MAA) copolymers presented in Section 3.2.1. The idea is to blend the S-*block*-(S-*stat*-MAA) intermediate with amine-functional PDMS, in order to form ionic or covalent bonds between the acid and amine groups. The result is a material in which the PS was covalently attached to a block containing PDMS grafts (Fig. 4.6.1). When this PS–PDMS material was blended with a PS substrate, the PDMS preferentially concentrated on the surface, while it is well anchored by its PS block.

It can be noted from Fig. 4.6.1 that the amine–PDMS used in this work had 95% of dimethyl siloxane units and 5% of amine-containing branches.

The number-average molecular weight, M_n, in Daltons of PDMS was obtained from an empirical relationship with its kinematic viscosity, ν, in centistokes (CSt).

$$Ln(M_n) = 0.00115801(Ln\nu)^3 - 0.05101102(Ln\nu)^2 - 0.97300151(Ln\nu) + 5.03104572 \quad (4.6.1)$$

Since the amine–PDMS used in the experiments had kinematic viscosities of 130 and 1,500 CSt, Equation 4.6.1 predicted their number average molecular weights to be equal to 19,300 and 5,955 Da, respectively.

Procedures used for the formation of the PS–PDMS samples (I, II and III) in the 300-ml Parr reactor system (Fig. 2.3.4) are as follows (Cai, 1997).

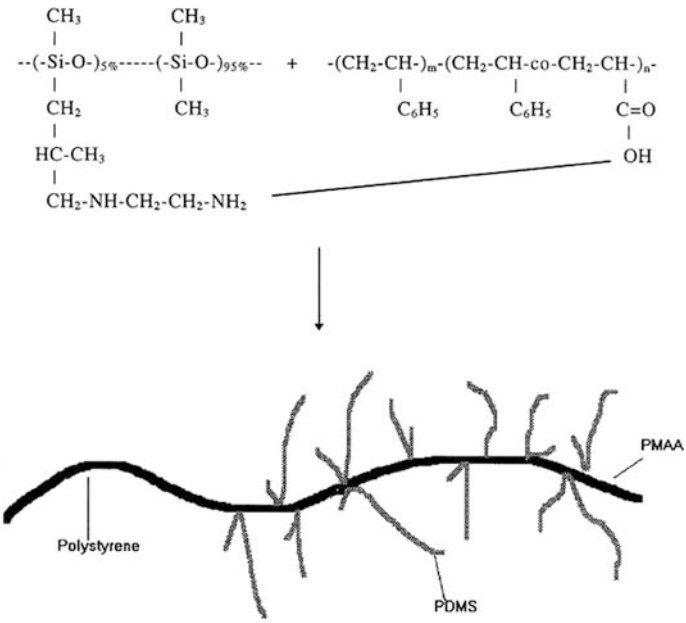

Fig. 4.6.1 Reaction scheme used to produce PDMS grafted onto intermediate S-*block*-(S-*stat*-MAA) copolymers

Formation of the 1:1 S-*block*-(S-*stat*-MAA) material started by passing nitrogen gas (>200 ml/min.) into the reactor for 5 min to effectively displace oxygen from the reactor. After the reactor was sealed, 50 ml ethyl ether bubbled with nitrogen gas (with less than 2 ppm oxygen content) for 15 min was pumped into the reactor. The reactor was then preheated to operating conditions of 80°C with a blanket of 70 psig nitrogen gas. The reaction is started by pumping in the monomer (30 ml inhibitor-free styrene bubbled with nitrogen for at least 15 min) and solvent-initiator (0.2533 g AIBN initiator in 70 ml ethyl ether, bubbled with nitrogen gas for at least 15 min) solutions into the reactor within 15 min. After 10 h of reaction (styrene conversion at this time was 45%), 10 ml inhibitor-free monomer methacrylic acid(MAA) (bubbled with nitrogen gas for at least 15 min) was pumped into the reactor, and the reaction was continued for another 12 h. Finally, the reactor was cooled to room temperature in 15 min to stop the reaction. Solid polymer was extracted from the product reactor fluid and purified (procedure indicated below). Proton NMR analysis of the purified solid S-*block*-(S-*stat*-MAA) material indicated an S-to-MAA segmental ratio of 0.93. That is why this S-*block*-(S-*stat*-MAA) material was nominally called the 1:1 intermediate product.

Formation of the 1:2 S-*block*-(S-*stat*-MAA) material started by passing nitrogen gas (>200 ml/min) into the reactor for 5 min to effectively displace all the oxygen in the reactor. After the reactor was sealed, 50 ml ethyl ether bubbled with nitrogen gas (with less than 2 ppm oxygen content) for 15 min was pumped into the reactor. The

reactor was then preheated to operating conditions of 80°C with a blanket of 70 psig nitrogen gas. The reaction is started by pumping in the monomer (15 ml inhibitor-free styrene bubbled with nitrogen for at least 15 min) and solvent-initiator (0.20 g V-501 initiator from Wako Chemical Corp. in 135 ml ethyl ether, bubbled with nitrogen gas for at least 15 min) solutions into the reactor within 15 min. After 6.5 h of reaction, 15 ml inhibitor-free monomer methacrylic acid (MAA) in 50 ml cyclohexane (bubbled with nitrogen gas for at least 15 min) was pumped into the reactor, and the reaction was continued for another 5.5 h. Finally, the reactor was cooled to room temperature in 15 min to stop the reaction. Solid polymer was extracted from the product reactor fluid and purified (procedure indicated below). Proton NMR analysis of the purified solid S-*block*-(S-*stat*-MAA) material indicated an S-to-MAA segmental ratio of 0.50. That is why this S-*block*-(S-*stat*-MAA) material was nominally called the 1:2 intermediate product.

Purification of the reactor fluid containing the intermediate S-*block*-(S-*stat*-MAA) material (Sample I) involved the following steps. Around 0.70 g of S-*block*-(S-*stat*-MAA) raw product (white solid) was dissolved in 28 g THF. Then, 16 g of methylene chloride was added to precipitate S-*block*-(S-*stat*-MAA) material and polymethacrylic acid, while polystyrene remained in the supernatant solution. After removal of the supernatant, the precipitate was redissolved in THF and precipitation procedure was repeated two more times. The final precipitated solid weighed 0.14 g, and it was dissolved in THF. Subsequently, 20 g distilled water was added into the solution, and the intermediate S-*block*-(S-*stat*-MAA) material precipitated out while polymethacrylic acid will remained in solution. The supernatant was removed, and the precipitate was redissolved in THF again to repeat this procedure two more times. The S-*block*-(S-*stat*-MAA) solid remaining in the final precipitate weighed 0.07 g.

For the formation of the PS–PDMS block copolymer, 0.3–0.5 g S-*block*-(S-*stat*-MAA) material was first dissolved in 50 ml THF. Also, 8–20 g amine–PDMS (from Dow Corning Co.) was dissolved in 30 ml THF. Then, the two solutions were mixed with 2 g of molecular sieve (to remove water) for 8–20 h under nitrogen gas at 70°C. Other reaction runs were done at room temperature. After the reaction, the solution became slightly cloudy with a slight increase in viscosity. In order to separate the fluid from the remnants of the molecular sieve, centrifugation was used. The upper liquid supernatant solution was transparent, and some brown solid precipitated out at the bottom. Upper drying of the supernatant, an elastic, sticky, rubbery product was obtained. Physical properties of the product depend on the ratio of the amine–PDMS and the S-*block*-(S-*stat*-MAA) material used in the reaction. Experiments were also done without using molecular sieve and obtained the same product, but no residues left in the centrifuge tubes after centrifugation. Therefore, it seemed that molecular sieves were not needed.

Table 4.6.1 shows various PS–PDMS products, depending on the ratio of the two reactant polymers.

We also ran some samples with the same ratio of S-*block*-(S-*stat*-MAA) to amine–PDMS copolymers at room temperature, but after IR, acid (water) extraction, TGA, DSC, and surface tension tests, we did not notice significant product

Table 4.6.1 PS–PDMS products from recipes and reaction conditions

#	S-*block*-(S-*stat*-MAA) (S:MAA)	(g)	Amine–PDMS (CSt)	(*g*)	S-*block*-(S-*stat*- MAA): amine–PDMS	Rxn time @ RT (h)	Apparent product description
Ia	1:2	0.56	1,500	7.80	1:13.9	10	Transparent gel
Ib	1:2	0.37	1,500	10.11	1:23.7	12	Transparent gel, softer than Ia
Ic	1:2	0.20	1,500	12.04	1:60.2	20	Viscous transparent liquid
IIa	1:1	0.36	1,500	8.80	1:24.4	15	Viscous white liquid
IIb	1:1	0.40	1,500	8.40	1:16.8	8	Viscous white liquid
IIc	1:1	0.40	1,500	21.0	1:52.5	12	Viscous white liquid, but more sticky
IIIa	1:1	0.49	130	11.71	1:23.9	12	Viscous white liquid
IIIb	1:1	0.43	130	7.80	1:18.1	8	Viscous white liquid
IIIc	1:1	0.41	130	19.58	1:47.7	10	Less viscous (compared to IIIa) white liquid

differences. We also ran some reactions for 2 h and got the same products as those that were run for 8–20 h.

Thermal analysis was done with reactant, intermediate product, and final PS–PDMS products. For the PS–PDMS products, TGA traces show stability of Products Ia, IIa, and IIb up to 360°C with almost 100% weight retention (see Fig. 4.6.2 for TGA trace of Ia PS–PDMS product). Intermediate S-*block*-(S-*stat*-MAA) materials show similar behavior, except that the 1:2 material had a 5% weight loss at 220–240°C. DSC analysis of Ia, Ib and IIa PS–PDMS products show crystalline transitions at –50°C and 170°C (typically shown in Fig. 4.6.3 for Ia PS–PDMS product). Further DSC analysis of S-*block*-(S-*stat*-MAA) and amine–PDMS indicates that the low temperature crystalline transition is attributed to the amine–PDMS, while the high temperature crystalline transition is attributed to the S-*block*-(S-*stat*-MAA) material. In order to verify some kind of chemical bonding between the amine–PDMS and the S-*block*-(S-*stat*-MAA), a TGA analysis of a physical mixture of the two shows a relatively less stable material, in which a gradual weight drop started at 60°C with a weight plateau starting at 220°C and 90% weight retention. Then, at 360°C, a more dramatic weight drop occurred just like that for the reacted amine–PDMS and S-*block*-(S-*stat*-MAA) material.

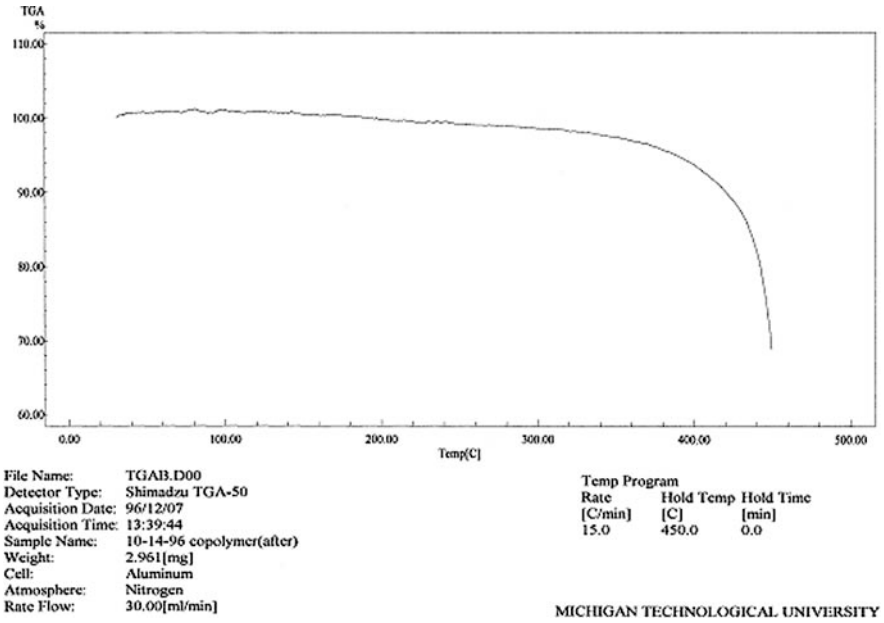

Fig. 4.6.2 TGA trace for product Ia PS–PDMS material

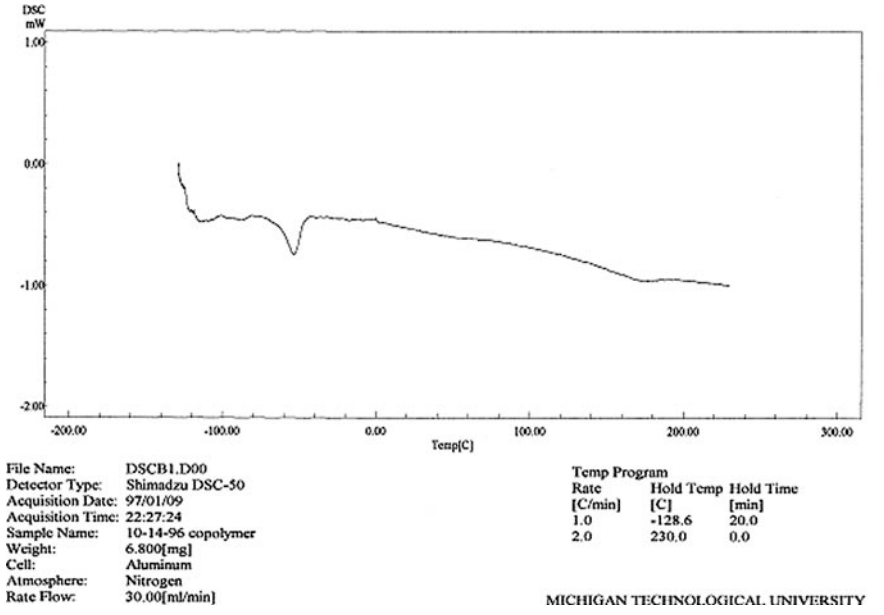

Fig. 4.6.3 DSC trace of product Ia PS–PDMS material

Finally, infrared (IR) analysis was obtained from the PS–PDMS product materials to try to detect the nature of the chemical reaction between the amine group in amine–PDMS and the acid group in the S-*block*-(S-*stat*-MAA) material. Based on IR reference samples (Pouchert, 1981, 1989), if the carboxyl unit and amine unit have reacted to form covalent bonds with the liberation of water to form a CONH– group, the C=O band should appear at 1,640 cm^{-1}. If no water was produced and carboxyl units and amine units were ionically bonded as $(COO)^-((NH_3)+$, the stretching vibration of the C=O in the ionic bond should appear at 1,550 cm^{-1}. IR results of the Ia PS–PDMS product show an absorption at 1,545 cm^{-1}, which looks like the band in pure PDMS that appears at 1,594 cm^{-1}. The 1,594 cm^{-1} absorption for PDMS is the bending vibration of the N–H of the amine unit, which shifted to 1,545 cm^{-1} in the PS–PDMS product because of the formation of ionic bonds. Also the IR result of the S-*block*-(S-*stat*-MAA) material showed a big absorption at 1,700 cm^{-1}, which represents the C=O stretch of the carboxyl unit.

In the PS–PDMS IR trace, only a small absorption at 1,702 cm^{-1} appeared. This is because of the small amount of S-*block*-(S-*stat*-MAA) material in the PS–PDMS product as well as the consumption of the carboxyl unit to ionic bonding. On the other hand, there were still some unreacted carboxyl units in the S-*block*-(S-*stat*-MAA) material according to the 1,702 cm^{-1} absorption. There was no absorption near 1,640 cm^{-1} in the PS–PDMS graph, which means that no covalent bonds have been formed between the carboxyl and amine unit.

These IR results are in confirmation with thermal analysis data, because in the DSC traces, there was no evidence of covalent bond formation or the liberation of water. Also, there was also evidence of residual acid functionality in the PS–PDMS products, based on the persistence of the 170°C crystalline transition (Fig. 5.4.4). The persistence of this ionic bonding was tested and confirmed through solubility analysis of reactant, intermediate, and final polymer products. Finally, PDMS extraction with various fluids were tried, and only a strong acid (HCl) was found to be capable of PDMS extraction from the PS–PDMS products.

Application of the PS–PDMS coating onto the PS base polymer was carried out by solution-blending base PS with small amounts of PS–PDMS products in THF. Solutions were cast onto glass slides for surface energy (contact angle) measurements. These measurements were done in order to calculate surface free energy quantities, based on various model equations (Cai, 1997). Static contact angles were obtained from video capture methods with the aid of software for pixel-based calculations. Results of these measurements have been qualitatively consistent, and typically shown in Fig. 4.6.4.

It is evident that water shows contact angles greater than 90° even below 1 wt% PS–PDMS content. In fact, contact angle data reach asymptotic values between 1 and 2 wt% PS–PDMS in base PS, and this has been consistently observed for all PS–PDMS product samples. This confirms the assumption that PDMS from the PS–PDMS products tend to concentrate on outer surfaces of the solid PS/PS–PDMS mixtures. The apparent result is a well-anchored PDMS coating, in which PS–PDMS can function as internal mold release agent for PS. Also, the

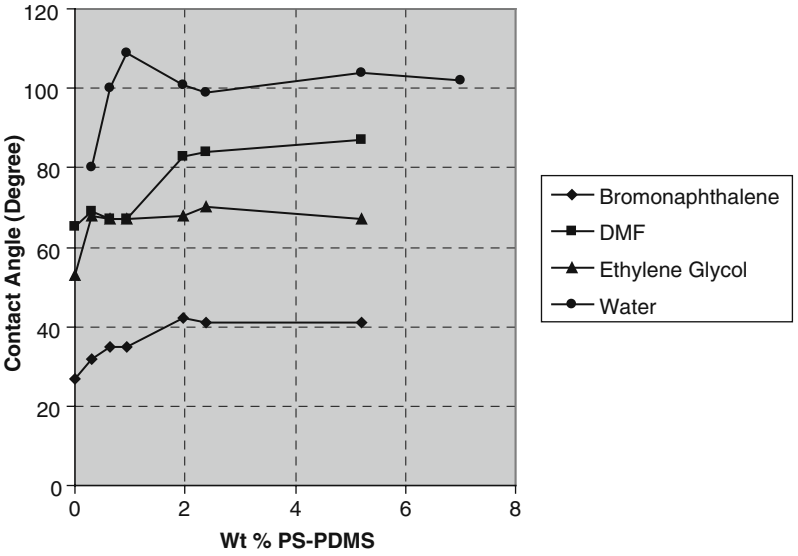

Fig. 4.6.4 Contact angle data for various liquids on surfaces from Ib PS–PDMS product in PS base material

surface PDMS layer could provide the PS material with inherent water repellancy properties.

Washing of the PDMS from the PS/PS–PDMS surfaces was done using various liquids, such as acids, bases, and organic fluids. After washing of the surfaces, their contact angles were measured. Results indicate no significant changes in contact angle values after washing, which confirms the anchoring capabilities of the PS–PDMS products on base PS surfaces.

4.6.2 VA/AA with SWCNTs

Polymer composite coatings with carbon nanotubes (CNTs) are normally difficult to produce, because CNTs do not mix well with polymers in the melt. Even from solution, dispersion of CNTs within a polymer matrix is not straightforward. The theoretical reason behind this difficulty was analyzed (Caneba and Axland, 2004), and it was due to the need for strong polar and/or hydrogen-bonding functionalities in the polymer. This made the use of block copolymers with acid segments suitable for such an application.

Exposure alone of carbon nanotubes to thermodynamically favored compounds does not necessarily result in a dispersed carbon nanotube system. What happens is that dispersing agent molecules will interact with the outer fibers of the nanotube bundles, and no further dispersion can occur. The fibers have to be separated from one another even for a short period of time, allowing the dispersing agent molecules

to form a superstructure around the fibers. Sonication has been shown to provide this kind of mechanical action at such a small area between carbon nanotube fibers (Islam et al., 2003).

Sonication involves the use of sound waves in the frequency range of 20 kHz – 10 MHz (http://www.fb-chemie.uni-rostock.de/ess/sonochem_intro.html). It causes the fluid to cavitate locally, followed by the collapse of cavitated bubbles. Energies involved in this phenomenon are so high that they have been found to be equivalent to a 2,000–5,000 K rise in local fluid temperatures and pressures up to 1,800 atm inside collapsing cavities. What might be significant for nanotube dispersion is the observation that when cavitated bubbles collapse from a solid surface, a supersonic jet of fluid from the opposite side of the bubble impinges onto the surface. If the solid surface is made up of nanotube bundles, then this jet can force fluid molecules, additives, and nanotubes themselves to lodge between the fibers. For small molecules with weak intermolecular forces, the effect is should be marginal at best. Alternately, the same thing happens if the solvent molecules do not interact with the nanotube surface. However, if solvent molecules have strong interactions from hydrogen bonding sites and they interact with the nanotube surface, then the fluid jet forms a strong wedge between fibers to separate them. If the fluid contains polymers that are strongly interacting with its segments, with other polymeric molecules, and with the nanotube surface, then an even more stable wedge is formed. If fluid cavitation occurs behind the polymeric wedge, then the leading edge of the polymer wedge will be pulled back or around the fibers either in a clockwise or a counterclockwise direction. This is probably the reason why people find polymers wrapped around nanotubes and/or nanotube bundles.

If the above-mentioned effects of highly interacting polymers with the aid of sonication in nanotube bundles are believed to be true, then polymeric wrapping can be understood more clearly. First of all, complete polymeric wrapping of single nanotube fibers can be possible if the fibers are separated in the first place. This might happen if the fiber concentration is very dilute (in the 1 mg/l level). If the fibers are bundled up in a more concentrated solution, then, the chain length of the polymer also plays a significant role. If the polymer is relatively long compared to the nanotube diameter, then it will wrap around entire bundles. At least the wrapped bundles are going to be separated from the main bundles and wrapped bundles can be suspended in the fluid. If the polymer size is optimized to wrap around only a single fiber, then it is possible to separate out single fibers from solution if fiber entanglements are nonexistent.

Blocky VA/AA copolymer (Fig. 4.6.5) was sonicated with high-pressure carbon monoxide based single-walled carbon nanotubes (HiPco SWCNT) in THF (Caneba

Fig. 4.6.5 Linear bead model of the vinyl acetate (*open beads*) and acrylic acid (*filled beads*) segments that make up the tapered B6-1 VA/AA block copolymer (see Sections 3.1 and 4.4). Bead numbers are drawn to scale to approximate molecular make-up of the blocky VA/AA material with 6 wt% AA segments

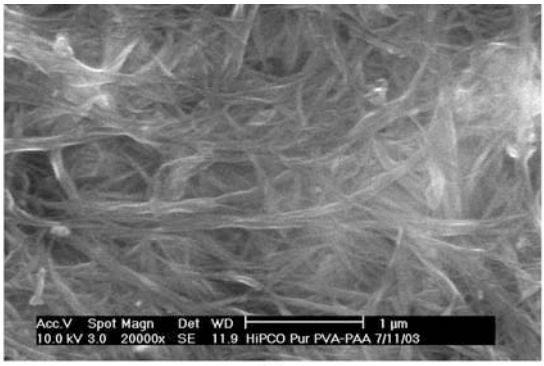

(a)

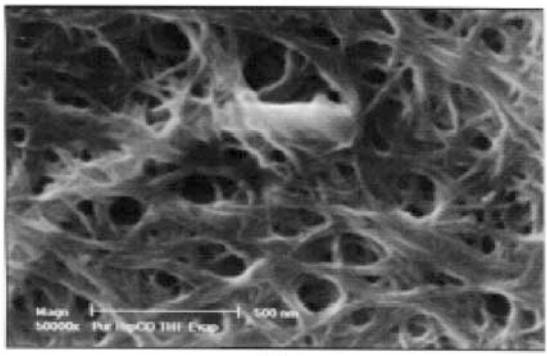

(b)

Fig. 4.6.6 Scanning electron micrographs of surfaces of HiPco coatings dispersed in THF with: (**a**) the aid of a VA/AA copolymer dispersing agent at 1:1 VA/AA-to-HiPco wt/wt ratio and (**b**) without the aid of a polymer dispersing agent/binder. The better definition of the rope structure in (**a**) indicates a higher electrical conductivity on the nanotube surface (With permission from Caneba and Axland, 2004)

and Axland, 2004). With this type of dispersant, up to 50 wt% HiPco can be dispersed in the blocky VA/AA material, other types of organic polymers can effectively disperse CNTs up to around 1 wt% only. Films were cast from the mixture, and CNT dispersion level was characterized.

Figure 4.6.6 shows scanning electron micrographs of HiPco coating surfaces: (a) with and (b) without the blocky VA/AA copolymer dispersing agent. More defined CNT fibers are seen for the coatings with the VA/AA material, which indicates better CNT dispersion.

Surface resistivity performance tests were done for the HiPco SWCNT that was dispersed with blocky VA/AA material at 1:1 VA/AA/HiPco wt/wt ratio. Results indicate that proper dispersion maintained electrical properties of HiPco, because surface resistivities range from 2.17 to 3.50 k Ohms/sq from HiPco loadings of 0.059–0.557 mg/cm^2 (Caneba and Axland, 2004). Note that electrically conductive surfaces require surface resistivities below 100 k-Ohm/sq.

Another coating property that was investigated for the VA/AA/HiPco system was its capability of thermoelectric effect, in which the coating was heated when DC electricity was applied across it (Caneba and Axland, 2004). Finally, the same type of coating was found to function as a high emissivity material, due to its capability of dispersing the CNT in the polymer coating.

4.7 Bottom-Up Micropatterning of Polymers

The idea of control over polymerization rate in a stirred-vessel FRRPP system has been extended to dimensional control of a quiescent polymerization film material. Polymerization was initiated in certain specific regions by directed radiation, similar to methods used in microlithography in microsystems. In a number of efforts, synchrotron X-ray was used as the radiation source and a 500-μm thick photomask made of gold was employed (Tirumala 2003; Tirumala et al., 2003, 2004a,b,c, 2005a,b, 2006). Liquid reactive material containing monomer(s) and solvent/precipitant were sandwiched between two standard 8-in. Silicon wafers with a thin spacer material (Fig. 4.7.1). Heat is applied on the backside of the wafer system through a heater block of controlled temperature.

Specific types of polymer micropatterns were made of crosslinked and uncrosslinked poly(methacrylic acid) and poly(*N*-isopropyl acrylamide) or polyNIPAM. Also, the spacer material between the Si wafers was adjusted to hundreds of micrometers, allowing for a single-exposure high aspect ratio microlithography of theses polymers. Also, since these polymers under go LCST behavior during polymerization conditions, they are suitable as thermoreversible gels during application.

The synthesis method started with the preparation of the reactive solution in a separate container, making sure that it was reasonably devoid of atmospheric oxygen through a 15-min nitrogen gas purge. In this case, there was no need to add the initiator, since the hard synchrotron X-rays provide the necessary electromagnetic excitation to initiate polymerization. Thus, only monomer(s) and solvent/precipitant were needed in the reactive mixture. Then, the Si wafer system was filled with the reactive mixture, and it was mounted in order to preheat to the operating temperature. At time $t = 0$, reactive mixture at its operating temperature was exposed to the X-ray source. For the methacrylic acid-water system, operating temperatures were typically at 60 and 80°C. For the NIPAM-water system, it was at typically at 45°C. Note that the LCST of polyNIPAM-water system was cited at 32°C (Tirumala, 2003a). After around 15–30 min, the wafer system was removed from its mount and quickly cooled in an ice-water bath. Then, the wafer assembly was

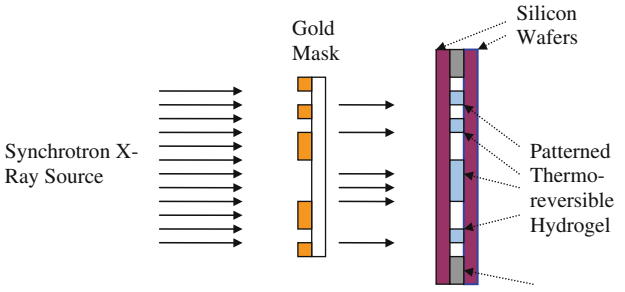

Fig. 4.7.1 Schematic diagram of the synchrotron X-ray microlithography system for the formation of patterned hydrogels from the FRRPP process

opened to expose the polymer micropatterns for air drying. No wet development was needed.

Various micropatterns produced from synchrotron X-ray induced FRRPP are shown in the literature (Tirumala, 2003; Tirumala et al., 2003, 2004a,b,c, 2005a,b, 2006). Patterns included lines, squares, rectangles, ovals, star-type objects, small filled circles, etc. Figure 4.7.2 shows an optical micrograph of a micropattern from dry polyNIPAM. In order to obtain an idea of the size scale, the width of the light colored polymer domain is in the order of a few hundred micrometers only.

In Fig. 4.7.3, an optical micrograph of the wet version of Fig. 4.7.2 material is shown at the same magnification. The expansion of the polymer domains is seen as well as the surface features. Channels between the polymer domains have gotten

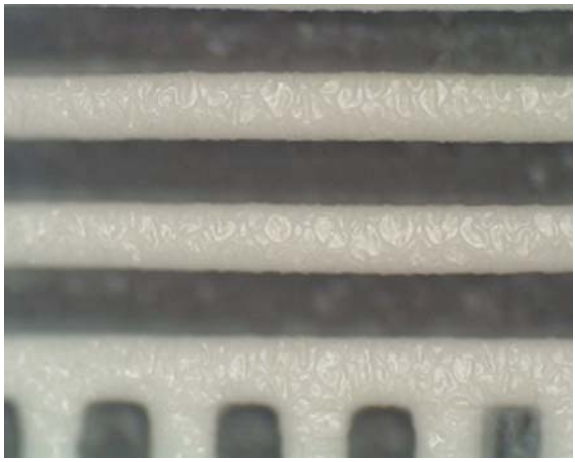

Fig. 4.7.2 Optical micrograph of a polyNIPAM dry pattern

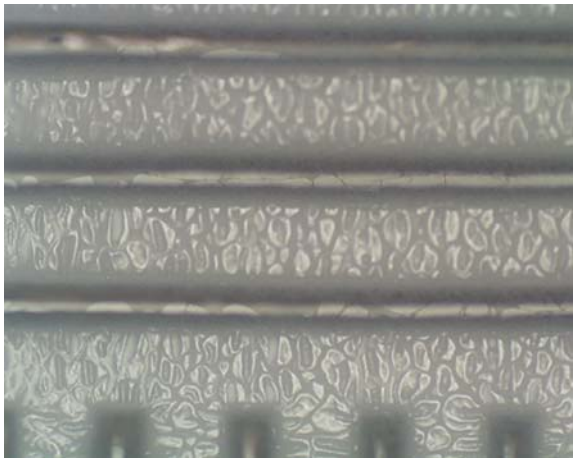

Fig. 4.7.3 Optical micrograph of the wet polyNIPAM version of the pattern in Fig. 4.7.2

more narrower. Thus, these domains can be used to control flow of fluids between the channels by various means, such as temperature, pH, salt type and content, and even by electric field. Patterns on the surfaces of the polymeric films are portions of the polymer that are in contact with the Si wafer during polymerization.

In Fig. 4.7.4, optical micrographs of square-line micropatterns made of poly(methacrylic acid) are shown. The left side is a square micropattern of the polymer, while the right side is a checkered-line micropattern of the same polymer.

In Fig. 4.7.5, a micro-"star" of polyNIPAM material is shown, which has been harvested from the above-mentioned micropatterning operation. This result suggests the possibility of producing other types of two-dimensional micron-shaped polymers, including thermoreversible hydrogels.

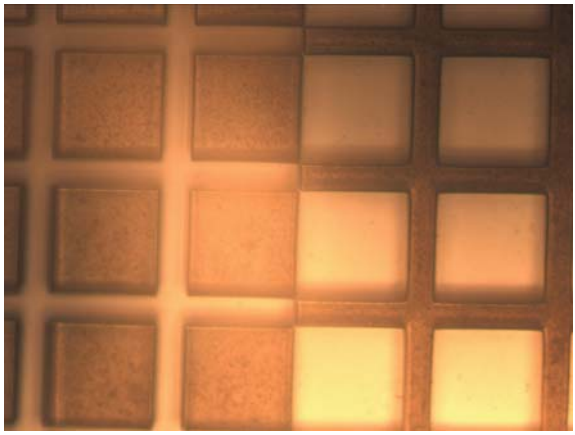

Fig. 4.7.4 Optical micrographs of poly(methacrylic acid) micropatterns. The left side is a square micropattern, while the right side is a checkered line micropattern of the same polymer

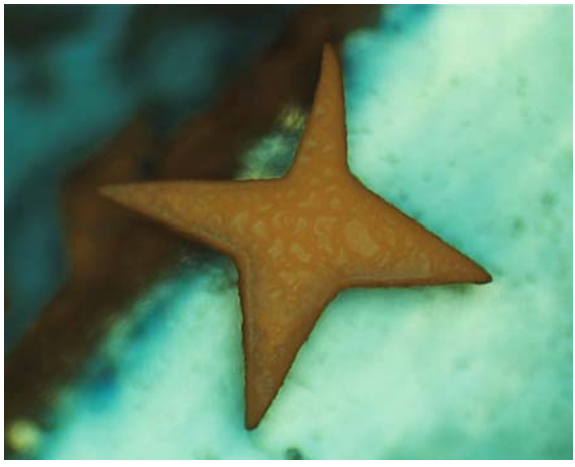

Fig. 4.7.5 Star-shaped polyNIPAM detached from the Si wafer after the FRRPP-based micropatterning operation using synchrotron X-rays

We note from the above patterns and those that were published in the literature that shapes and sizes of these patterned polymers closely resemble exposure areas of the X-ray masks (Fig. 4.7.1).

Therefore, the FRRPP process has been demonstrated to be capable of being translated from reaction control in mixed fluid systems to quiescent film systems.

References

Aggarwal, A., 1993. M.S. Thesis, Michigan Technological University.

Cai, Y., 1997. M.S. Thesis, Michigan Technological University.

Caneba, G. T., 1992a. *Adv. Polym. Technol., 11*, 277.

Caneba, G. T., 1992b. U.S. Patent No. 5,173,551, December 22.

Caneba, G. T., 2007a. "Formation of Radicalized Vinylidene Chloride Copolymer Particulates and Related Materials", Provisional U.S. Patent Application, June.

Caneba, G. T., 2007b. "Multifunctional Multipolymeric Surfactants for Oil-Bitumen Recovery", U.S. Patent and PCT Applications, February 9.

Caneba, G. T., and Axland, J. E., 2002. *J. Miner. Mater. Charact. Eng.*, *1*(2), 97.

Caneba, G. T., and Axland, J. E., 2004. *J. Miner. Mater. Charact. Eng., 3*(2), 73.

Caneba, G. T., and Dar, Y., 2005. "Free-Radical Retrograde-Precipitation Copolymers and Process of Making the Same", U.S. Patent Application 10/045,725, and Divisional Patent Application, 11/181,481, Filed July 14.

Caneba, G. T., Zhao, Y., and Dar, Y., 2003. *J. Appl. Polym. Sci.*, *89*(2), 426.

Caneba, G. T., Renier, M., and Ott, B., 2008. *J. Miner. Mater. Charact. Eng., 7*(2), 175.

Donatelli, A. A., Sperling, L. H., and Thomas, D. A., 1976. *Macromolecules, 9*(4), 671, 676.

Huelck, V., Thomas, D. A., and Sperling, L. H., 1972. *Macromolecules, 5*(4), 340–348.

Islam, M. F., Rojas, E., Bergey, D. M., Johnson, A. T., and Yodh, A. G., 2003. *Nano Lett., 3*(2), 269.

Mishra, V., Murphy, C. J., and Sperling, L. H., 1994. *J. Appl. Polym. Sci., 53*, 1425–1434

Pope, G. A., Baviere, M., 1991. "Reduction of capillary forces by surfactants", in: Basic Concepts in Enhanced Oil Recovery Processes, M. Baviere (Ed.), Critical Reports on Applied Chemistry, Elsevier Applied Science, London and New York, Vol. 33.

Pouchert, C. J., 1981. The Aldrich Library of Infrared Spectra, 3rd ed., Aldrich Chemical Company, Inc., Milwaukee, Wisconsin.

Pouchert, C. J., 1989. The Aldrich Library of FT-IR Spectra, 1st ed., Aldrich Chemical Company, Inc., Milwaukee, Wisconsin, Vol. 2.

Sperling, L. H., 1974–75. Encyclopedia of Polymer Science and Technology, 1st ed., John Wiley and Sons, Inc., New York.

Sperling, L. H., 1981. Interpenetrating Polymer Networks and Related Materials, Plenum Press, New York.

Sperling, L. H., and Amts, R. R., 1971. *J. Appl. Polym. Sci., 15*(9), 2317–19.

Tirumala, V. R., 2003. Ph.D. dissertation, Michigan Technological University.

Tirumala, V., Dar, Y., Wang, H.-H., Mancini, D., and Caneba, G. T., 2003b. *Adv. Polym. Technol., 22*, 126.

Tirumala, V., Mancini, D., and Caneba, G. T., 2004a. "Synthesis of ultrafast response microgels for MEMS applications", *Smart Structures and Materials*, SPIE Conference, *5389*, 221–228.

Tirumala, V., Mancini, D., and Caneba, G. T., 2004b. "*In Situ* Fabrication of Thermoreversible Microgels", *Proceedings of the IEEE International Conference on Intelligent Sensing and Information Processing*, M. Palaniswami, C. Chandrasekhar, G. K. Vengayamoorthy, S. Mohan, and M. K. Ghantasala (Eds.), January 4–7, Chennai, India, pp. 196–200.

Tirumala, V., Guo, L., Caneba, G. T., Mancini, D., Thiyagarajan, P., and Barker, J. G., 2004c. "USANS Investigation of Poly(N-isopropylacrylamide) Gels prepared from Synchrotron-

Radiation-Induced Polymerization on a Retrograde-Precipitation Environment", *Proceedings of the American Conference on Neutron Scattering*, June 6–10, College Park, Maryland.

Tirumala, V., Divan, R., Mancini, D. C., and Caneba, G. T., 2005a. *Microsystems Technol. J., 11* (4–5), 347–352.

Tirumala, V., Caneba, G. T., Mancini, D. C., and Wang, H. -H., 2005b. U.S. Patent No. 6,869,983, March 22.

Tirumala, V. R., Caneba, G. T., Mancini, D. C., and Wang, H. H., 2006. *J. Appl. Polym. Sci., 102*(1), 429.

Wang, B., 1997. Ph.D. Dissertation, Michigan Technological University.

Chapter 5
Related Energy Application of FRRPP Products

5.1 Surfactant-Based Waterflooding for Subterranean Oil Recovery

5.1.1 Introduction

Multifunctional multipolymeric surfactant mixtures which can be produced from the FRRPP process are capable of efficiently recovering trapped oil from subterranean sources. A typical oil reservoir, shown in Figure 5.1.1, is an anticline (inverted-dome) rock formation wherein the oil is trapped within the open-pore rock formation from sandstone or carbonate material bound by impermeable rock on top and brine in porous rock at the bottom. Immediately above the oil bank could be a layer of natural gas at high pressure, since this formation is originally underground where the pressures could at least be that of the ground overbearing material. Other oil bank formations cited in the literature include salt formations, reefs, etc.

During oil exploration, the presence of the oil bank is determined and holes are drilled through the rock in order to access the oil. When this happens, the inherent

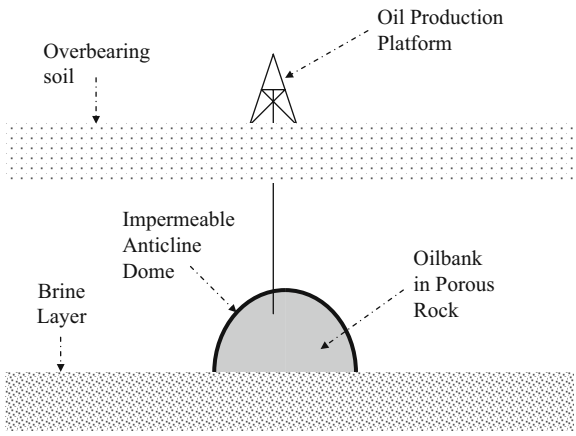

Fig. 5.1.1 Anticline dome oil formation, in which oil in porous rock is trapped between a brine layer at the bottom and the impermeable dome on top

G. Caneba, in: *Free-Radical Retrograde-Precipitation Polymerization (FRRPP)*,
Chapter DOI 10.1007/978-3-642-03025-3_5, © Springer-Verlag Berlin Heidelberg 2010

pressure of the oil and gas forces some of the oil from the reservoir. Production from this inherent pressure is called primary oil recovery and is normally capable of expelling 5–20% of the oil-originally-in-place (OOIP). Beyond primary production are methods that are called secondary, tertiary, quaternary, etc., techniques, which can be anything that involves forcing and/or stimulating the oil toward the surface. A list of these post-primary techniques includes (Mohanty and Caneba, 2005)

1. Waterflooding – injection of water or brine
2. Alkaline flooding
3. Polymer flooding
4. Thermal methods
5. Gasflooding
6. Surfactant flooding
7. Microbial methods

Waterflooding offers a simple method of post-primary production from an oilfield. A typical approach is to use a five-spot pattern of wells, in which the outer wells (injection wells) are used for pumping in water/brine, while the middle well (production well) is used for collecting the oil (Fig. 5.1.2).

The product stream from the production well is a mixture of oil and water/brine, and the oil can easily be separated by gravity. Note that oil has a specific gravity of about 0.9, while water/brine at or slightly above 1.0. Thus, even if one allows the mixture to stand in a holding tank, the oil will naturally accumulate as a top layer of fluid. The bottom aqueous layer can be reused typically by pumping it back through the injection wells, for a closed-loop operation with some additional make-up water to replace the oil removed from the reservoir.

In order to improve production from waterflooding operations, various water-soluble thickening polymers are incorporated into the injection fluid (Mohanty and Caneba, 2005). The idea is that there is a need for a relatively high capillary number, N_c, in order to realize more efficient oil displacement from solid surfaces. Note that the capillary number is related to the displacing fluid viscosity, μ, interstitial velocity, V, and interfacial tension (IFT), γ, (Pope and Baviere, 1991)

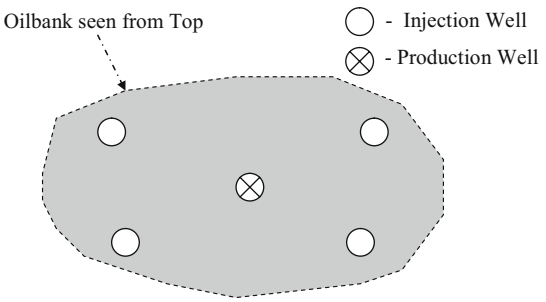

Fig. 5.1.2 Five-spot pattern of injection and production wells typically used in post-primary oil recovery operations

$$N_c = \frac{\mu V}{\gamma}, \tag{5.1.1}$$

i.e., one needs relatively high aqueous phase viscosity for a more efficient oil displacement.

Thickening polymers have been added into the surfactant-based oil recovery fluid in order to facilitate mobility control (Evani, U.S. Patent No. 4,184,096; Boudreau, U.S. Patent No. 6,776,234; Boudreau, U.S. Patent Application 20040224854). Materials that are popularly used are based on ionic polyacrylamides (PAM) and xanthan. Ionic PAM is obtained either by free-radical polymerization of acrylamide monomer with subsequent hydrolysis or by free-radical copolymerization of acrylamide and acrylic acid monomers followed by neutralization of the acrylic acid segments with sodium hydroxide. The degree of hydrolysis or fraction of ionizable groups ranges from 15 to 35%. Weight-average molecular weights are in the order of 10^7 Da, and polydispersity indices are in the 2–3 range. Xanthan, a biopolymer, is produced by fermentation of the bacterium *Xanthomonas campestris*. Weight-average molecular weights are in the 4–5 $\times$ 10^6 Da range, and they are monodisperse with polydispersity indices between 1.3 and 1.5. In water or brine solution, xanthan attains a double-stranded conformation stabilized by hydrogen bonds. An obvious drawback of using conventional thickeners such as polyacrylamides or xanthan gum is the added cost to the oil recovery operation, which is equivalent to \$5–10 per barrel of oil produced (Mohanty and Caneba, 2005).

Equation (5.1.1) also indicates that the use of surfactants to lower the interfacial tension is advantageous in providing more efficient oil displacement from the porous rock formation. This is the essence of surfactant waterflooding, wherein the surfactant is usually mixed with the injection water.

Surfactants normally contain predominantly hydrophilic groups and hydrophobic groups in two regions of the same molecule. They have been proposed to facilitate recovery of crude oil from subterranean deposits (Gale et al., U.S. Patent No. 3,946,812), even right after primary oil recovery operation. Improvements of surfactant-based oil recovery operations have been proposed and new ones are being discovered. Usually, surfactants are produced from natural materials (fatty acids, lignin, etc.) or by coupling small-molecule reagents into oligomers along with modification reactions. An example of the latter is the formation of alkylaryl sulfonates, whereby a benzene–toluene–xylene (BTX) stream is functionalized with an alpha-olefin stream followed by the sulfonation of the benzene ring.

Early surfactant formulations proposed for oil recovery were based on conventional detergent materials in conjunction with waterflooding (Gale et al., U.S. Patent No. 3,946,812; Farmer III et al., U.S. Patent No. 3,943,160) and steam-flooding methods(Isaacs and Prowse, U.S. Patent No. 4,458,759). Other materials were proposed in order to improve the performance of surfactant flooding, such as alkali, co-surfactants, polymers, and other chemicals (Gupta, U.S. Patent No. 4,467,869; Chen and Williams, U.S. Patent No. 4,577,000; Dardis, U.S. Patent No. 4,509,597; Stapp, U.S. Patent No. 4,470,461; Cooke, U.S. Patent No. 4,460,791). Other embodiments involve the application of these performance-enhancing agents,

particularly the alkali and polymer materials, in separate injection slugs from the surfactant-bearing solution (Gupta, U.S. Patent 4,467,869). This is culminated with the so-called ASP technology, signifying the use of an alkali slug, followed by the surfactant slug, and then the relatively viscous aqueous polymer solution slug (Hsu and Hsu, U.S. Patent No. 6,022,834). Even though these surfactant-based methods can be very effective in experimentally recovering up to about 80% of tertiary OIP, they involve heavy use of a variety of chemicals, some of them VOCs, which can lead to economic, environmental, and material compatibility problems. The use of multifunctional multipolymeric material surfactant mixture in this invention can also eliminate several processing steps because it is the only chemical that needs to be introduced. It can also be biodegradable and can recover up to 90% of tertiary OIP.

Conventional fatty acids-based alkylbenzene sulfonate (ABS) detergents proposed in oil recovery applications are strictly categorized as oligomers, since their molecular weights are lower than the so-called entanglement molecular weight, M_e (Fried, 1995). These materials normally have 18–26 alkyl groups, while polystyrene has an entanglement molecular weight of about 18,100 Da, corresponding to around 181 monomer segments.

Broad molecular weight distribution (MWD) alkylaryl sulfonate surfactant macromolecules have been recently cited by Berger (Berger, P.D., U.S. Patent Application 20050199395) to result in the lowering of the interfacial tension (IFT) between oil and water compared to their equivalent narrow MWD counterparts. From a performance standpoint, this means that surfactant macromolecules of various sizes can form along interfaces of various radii of curvature, allowing the removal of large and smaller oil domains from a solid surface. Surfactant macromolecules usually have narrow molecular weight distributions, and there is a need to mix a number of surfactants from different reactor runs to enhance the performance of the mixture. If a polymerized multifunctional surfactant with broad molecular weight distribution can be produced in a single reactor run, then the blending step of various surfactants can be eliminated.

In any of proposed surfactant-thickener combinations, none of them take advantage of cost savings from having the appropriate anionic surfactant also function as a thickener or having the thickener closely related chemically to the surfactant that the combination can be produced from the same reactor or processing equipment. A recent prior art (Moss, U.S. Patent No. 7,125,825) wherein the surfactant was also a thickener involved an oligomer formulation, and the hydrophobic portion of the surfactant is a branched or straight-chained saturated or unsaturated aliphatic hydrocarbon, with the possibility of having hydroxyalkyl groups. Moreover, this prior art cited disadvantages of polymer-based thickening to include compatibility problems with components resulting in chemical precipitation. Finally, thickeners of this prior art were claimed to be pseudoplastic, i.e., the type that reduces its viscosity under shear while the viscosity increases when the shear is removed. Still another prior art(Shpakoff and Raney, 2006a, b, U.S. Patent Nos. 7,137,447 and 7,055,602) involves the mixture of an anionic aliphatic surfactant with an aliphatic nonionic additive for enhanced oil recovery performance.

The understanding of the action of surfactants as demulsifier can be established from an analogy with industrial cleaning operations, as described in a US Environmental Protection Agency web site (http://es.epa.gov/technifo/facts/florida/aque-fs.html). Here, a surfactant/water solution is used to remove soil coated with machining oil from the surface of a metal part. A desirable surfactant is cited to be one that subverts the soil with oil from the part, rather than one that aggressively emulsifies them. This surfactant should have more affinity to the metal part than the soil covered with oil. From a processing standpoint, this weak surfactant system lifts the soil with oil and suspends them while the fluid mixture is being agitated. When the agitation is stopped, the oil separates from the surfactant–water solution and rises to the top, while the soil settles to the bottom; thus, facilitating the reuse of the aqueous fluid. If an emulsifying surfactant is used, the oil and a portion of the soil will be suspended in the aqueous phase, resulting in a dirty fluid. To recycle the aqueous phase will require a separate operation involving the addition of a demulsifier. In terms of subterranean oilfield operation, the analogy calls for the use of surfactant molecules that contain polar hydrophobic portions which will have more affinity to the rock surface than to the oil. Unfortunately, conventional surfactants contain only aliphatic and aromatic hydrophobic groups which have very good affinity to the oil; thus they act as emulsifying surfactants. That is why a separate and costly demulsification operation is done to separate and recover the oil from the surfactant (Arnaud, U.S. Patent No. 6,875,351; Van Den Berg et al., U.S. Patent No. 6,787,027). Otherwise, the surfactant can be totally incorporated in the oil and never recovered at all.

Demulsification is an operation that is used in conjunction with conventional surfactant-based oil recoveries. Oil is normally well dispersed within surfactant domains, and addition of a demulsifier is needed to free the oil from the surfactant. Examples of commercial demulsifiers are polyol, amine, and resin products by Clearwater (Houston, Texas), ALKEN® product line by Alken-Murray Corp., and Kemelix™ line by Uniqema. Other approaches to demulsification have been cited in the literature (Presley and Harrison, 1642824 Aug., 1972 DE 252/330; Deng et al., 2004; Newcombe, U.S. Patent No. 4,216,079; Balzer, U.S. Patent No. 4,842,067). In order to facilitate the reuse of surfactant for oil recovery, it would have to be separated from the demulsifier, which is normally a very difficult procedure, comprising of liquid–liquid or solid–liquid extraction followed by distillation or vacuum stripping. If the surfactant has demulsification characteristics, then this separation may not be necessary, and surfactant reuse can become a possibility. This has been illustrated in the oligomeric sense in a prior art (Guymon, U.S. Patent No. 5,252,138), which used a surfactant from the group consisting of a linear alcohol having carbon atoms within the range on the order of about 8–15 carbon atoms and ethylene oxide units on carbon atoms within the range on the order of about 2–8 ethylene oxide units.

The FRRPP process has been shown to produce oil recovery compositions comprising of multifunctional multipolymeric surfactants that contain monomeric, oligomeric, and/or polymeric units containing functional groups that are chemically and functionally similar to various small-molecule, oligomeric, and polymeric additives found in various stages of oil/bitumen recovery operations. In various prior

art compositions and applications, added effectiveness in oil recovery operations is imparted through additive materials or through separate steps in an overall oil recovery operation. Through the FRRPP process, a collection of monomers, oligomers, and/or polymers possessing various chemical groups are incorporated within a set of polymer chains that make up the main component of the composition. These functional groups may be naturally present in the raw materials used to produce the multifunctional multipolymer or may be purposely or naturally altered by modifying reactions. A subpolymer (equivalent to a number of monomer segments) representation of these chemical functionalities in a portion of the entire polymer is shown in Fig. 5.1.3, which is depicted by the A, B, C, D, . . .-functionalities (Table 5.1.1) emanating from various subpolymers (Caneba et al., 2008).

Note that the above table shows both functionality classes that will impart hydrophobicity and hydrophilicity in the overall polymer, and the collection of various multipolymeric macromolecules should at least have both hydrophobic and hydrophilic functionalities either in the same macromolecules or bridged with highly compatible groups of functionalities from different macromolecules.

The FRRPP process also involves related polymeric materials to the multifunctional multipolymeric surfactants, which are produced in the same mixture with the surfactant; normally these related macromolecules have slightly deviated chemical features and/or compositions compared to the surfactant macromolecules in such a way that the whole mixture would be compatible in water.

Possible features in multipolymers that can involve macromolecules with deviated structures/compositions include, but are not limited to

1. vinyl chain backbone for affinity to crude oil, which is mostly made up of chemically similar hydrocarbons;
2. carboxylic acid or amine/amide functionalities for neutralization with various bases/acids, to impart salt tolerance and various degrees of hydrophilicity and acid–base characteristics;
3. ester and/or alcohol functionalities to impart co-surfactant characteristics, foam stability, long-term biodegradability, and demulsification characteristics;
4. relatively broad molecular weight distribution of the multipolymer macromolecule for enhanced lowering of the interfacial tension (IFT);

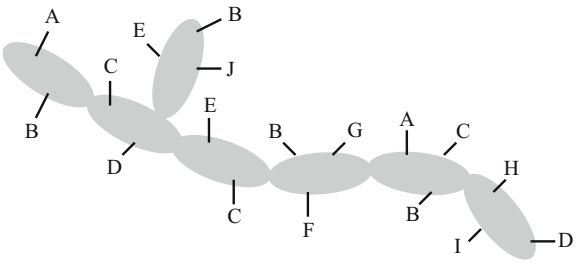

Fig. 5.1.3 Subpolymer representation of the multifunctional multipolymeric surfactant with various functional groups (A, B, C, D, . . .) (With permission from Caneba et al., 2008)

Table 5.1.1 Possible functionalities (A, B, C, D, . . .) for the above structural representation of the multifunctional multipolymeric surfactant. Examples of commercial polymers with various functionality classes as well as their corresponding small-molecule counterparts are given. These small-molecule counterparts could be proposed to be injected into oilfields to facilitate oil extraction (With permission from Caneba et al., 2008)

A, B, C, D, . . .-functionality class	Examples of A, B, C, D,. . .-functionality found in commercial polymers	Examples of A, B, C, D, . . . functionality found in small-molecule compounds
Hydroxyl	Poly(vinyl alcohol)	Methyl alcohol, ethyl alcohol, isopropyl alcohol
Ketone	Poly(methyl vinyl ketone), poly(isopropyl vinyl ketone), ethylene–carbon monoxide copolymers	Acetone, methyl ethyl ketone, methyl isobutyl ketone
Ester	Poly(vinyl acetate), poly(methyl acrylate), poly(ethyl acrylate), poly(methyl methacrylate), poly(butyl acrylate), ethylene–vinyl acetate copolymers	Methyl acetate, ethyl acetate, propyl acetate, butyl acetate
Carboxylic acid	Poly(acrylic acid), poly(methacrylic acid), ethylene–acrylic acid copolymers, ethylene–methacrylic acid copolymers	Acetic acid, citric acid
Amine	Poly(acrylamide), poly(isopropyl acrylamide)	Ethanolamine, ethylamines, propylamines
Salts	Neutralized poly(acrylic acid), such as poly(ammonium acrylate), poly(sodium acrylate), poly(potassium acrylate); corresponding neutralized poly(methacrylic acid)	Ammonium acetate, sodium acetate
Aromatic hydrocarbon	Polystyrene	Benzene, toluene, xylene
Aliphatic hydrocarbon	Polyolefins	Pentane, hexanes, heptane, octane
Mixed hydrocarbons	Hydrogenated styrene–butadiene copolymers	Naphtha, gasoline, kerosene

5. high molecular weight polymer with alcohol functionalities to impart sterically hindered colloidal properties;
6. ester functionality possessing reduced hydrophilicity as a compatible high molecular weight component, which serves as a viscosifier for enhanced mobility control in subterranean oil recovery operations;

7. functionalities that can be derived from products of free-radical polymerization chemistry using monomers, such as olefins, styrenic, vinyls, vinylidenes, acrylics, methacrylics, ketones, ethers, halogens, bases, esters, and alcohols from esters;
8. functionalities that can be derived from products of ionic polymerization chemistry using monomers, such as olefins, styrenic, acrylics, and methacrylics;
9. functionalities that can be derived from products of polycondensation or step-growth chemistry containing, but not limited to, ester, carbonate, amide, phenolic, formaldehyde, urethane, urea, melamine, and epoxide segments; and
10. functionalities that can be derived from products of ring-opening polymerization chemistry using ringed molecules, such as silicones, ethers, lactones, lactides, anhydrides, lactams, cycloalkenes, ethyleneimines, and oxazolines.

The reference situation is one in which the multipolymer has surfactancy properties; thus, the chains contain both hydrophilic and hydrophobic groups. At a surfactant concentration below the so-called critical micelle concentration (or CMC), the surfactant molecules are present in solution as isolated polymeric surfactant molecules (Fig. 4.4.3). Above the CMC, the surfactant molecules arrange themselves into aggregates called micelles, which can result in three mesoscale (between microscopic and macroscopic scales) Winsor types I, II, and III structures (Fig. 4.4.4), wherein the hydrophilic groups find themselves in the water side of the interface, while the hydrophobic groups are in the oil side of the interface. In type I mesoscale Winsor (or oil-in-water, O/W) structures, the water phase completely covers the oil phase with the hydrophilic end of the surfactant molecules aggregating outwardly along the interfacial region (Fig. 4.4.4(a)). In type II mesoscale Winsor (or water-in-oil, W/O) structures, the oil phase completely covers the water phase with the hydrophobic end of the surfactant molecules aggregating outwardly along the interfacial region (Fig. 4.4.4(b)). In type III mesoscale Winsor structures, both water and oil phases exist as a co-continuous domain structure with the surfactant molecules aggregated along the interfacial region (Fig. 4.4.4(c)). In oil recovery applications, type III structure is preferred because it is associated with very low interfacial tensions (Pope and Baviere, 1991). In terms of surfactant molecular properties, the following features were also cited by Pope and Baviere to promote type III behavior:

1. increase molecular weight (or branching) of surfactant-hydrophobic part, in the context of conventional surfactants which are oligomeric rather than polymeric in size;
2. decrease polarity of surfactant-hydrophilic part;
3. increase in long-chain alcohol concentration within the surfactant oligomer macromolecule; and
4. decrease in short-chain alcohol concentration within the surfactant oligomer macromolecule.

However, in the context of polymeric surfactants, type III behavior is promoted by decrease in the polarity of the hydrophilic part of the surfactant relative to that of the hydrophobic part. While the polarity level of the hydrophobic part could be much higher than that of a hydrocarbon, the relatively large size of the hydrophilic part promotes type III behavior. Therefore, the relatively high polarity of the hydrophobic part is crucial to the effectiveness of these multifunctional multipolymeric surfactants, as long as the hydrophilic part is either ionic or has a high enough polarity if it is nonionic.

5.1.2 Theory

Promoting compatibility between polymeric surfactants and related polymers is not straightforward. The reason is that when one looks into the Gibbs energy change for a polymeric-based mixture, ΔG, which is thermodynamically derived as

$$\Delta G = \Delta H - T\Delta S, \tag{5.1.2}$$

it should have a combination of an enthalpy change ΔH and entropy change ΔS that makes it a negative quantity for compatibility of components in a mixture. Due to the so-called combinatorial entropy for polymer mixtures, the entropy change is always negative and rapidly increasing in magnitude with the number of polymer segments. Thus, the enthalpy change should be a relatively large negative number for the Gibbs energy change to be negative (Mohanty and Caneba, 2005). This can only mean that for compatible polymer mixtures, there is a need for relatively strong specific interactions, such as strong dipole forces, hydrogen bonding, Lewis acid–Lewis base interactions. These strong interactions cannot be satisfied by hydrocarbon types of segments in the hydrophobic portions of the polymeric surfactants. In fact, one needs large numbers per macromolecule of some of the multifunctionalities in order for the surfactant–thickener mixtures to be compatible.

A macromolecular picture of the effectiveness of polymeric surfactants in oil displacement from porous rock can be understood from the fact that polymers normally assume the coiled Gaussian chain configuration (Rodriguez et al., 2003). Under the shear field of a flow situation within the pores, the polymeric macromolecules assume an elongated configuration and would tend to lodge themselves onto the oil adjacent to the rock surfaces.

5.1.3 Experimental

5.1.3.1 Sandpack Oil Recovery Studies

A particular type of sand (MI 2NS) was selected and dried by direct heat from a hot plate surface: The dried MI 2NS sand was passed through a 20-mesh screen for final sizing and air-tight storage. Before use, the stored sand was placed on a plastic

pan up to ½-in. in height and redried using a microwave oven for about 2 min with mechanical mixing every 30 s.

Flow displacement of oil through a sandpack or sand column is relevant to enhanced oil recovery in subterranean sources. An experimental apparatus setup shown in Fig. 5.1.4 was used to experimentally simulate the displacement of oil from an oilfield, in accordance with accepted procedure. Pressure drop between the top of the fluid on the sand column at atmospheric pressure and the partial vacuum at the bottom of the column was the driving force for fluid motion.

About 60 ml of 20-mesh passed MI 2NS sand was packed into a cylindrical column that was mounted on a Buckner funnel. A coarse filter paper was used to hold the sandpack onto the Buckner funnel. To fill the pores with water, the vacuum was turned on and 48-ml water was placed on the top of the sandpack. Just before all the water level drops down to the top surface of the sandpack, 48 ml of Fuel Oil #2 was poured slowly on the water. The filtrate flow rate of about one drop per second was maintained by controlling the power from the vacuum. When the oil level dropped down to the top of the sandpack, the 250-ml Erlenmeyer flask was replaced by an empty one and 48 ml of secondary recovery water was slowly poured onto the sandpack. After this primary plus secondary recovery water level dropped down to the top of the sandpack, the oil recovered inside the Erlenmeyer flask was measured.

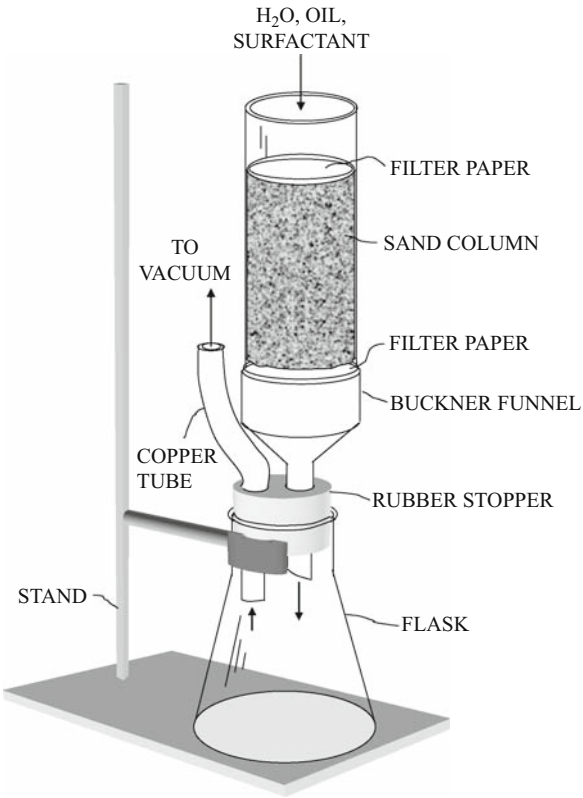

Fig. 5.1.4 Sandpack oil recovery apparatus used to simulate waterflooding and surfactantflooding EOR

At this point, the water-to-oil ratio (WOR) was found to be equal to about 50. Then, tertiary recovery fluid was slowly poured onto the top surface of the sandpack. Once again, the oil recovered from the collector container was measured. Recovered Fuel Oil #2 was measured gravimetrically or volumetrically. For small amounts recovered, an ethylene–propylene–diene monomer (EPDM) absorbent foam was used, which was found to preferentially absorb the Fuel Oil #2 completely from water or water–surfactant within the margin of error of the weighing device of $\pm$0.1 g.

5.1.3.2 Core Rock Study

A 1-in. diameter 2-in. long cylinder of porous Berea rock (9$\pm$1 ml pore volume and porosity of 100–200 mD) was used to simulate displacement of oil from a subterranean source. The core was held by a Temco (Temco, Inc., Tulsa, OK) RCHR-Series Hassler-type core holder with an overbearing pressure of 130–150 psig of a hydraulic fluid. The operation was done at room temperature of 16°C and fluids were introduced through the core using a high-pressure syringe pump (Cole-Parmer, Inc.). For a pump setting of 5.5 ml/min, 40 ml of tap water was passed injected into the core, i.e., sweep of at least 3$\times$ pore volume. Then, for a pump setting of 0.34 ml/min, 2 pore volumes (18 ml) of Citgo light crude oil was passed through the core and the core pressure went up to 65–60 psig. Subsequently, waterflooding was done to simulate secondary recovery at a water flow rate of 0.34 ml/min for 2 pore volume passes of water (18 ml). After this secondary recovery, 9.99 g of oil was obtained in the collector. Then, tertiary waterflooding was done by passing 3 pore volumes of water (27 ml) and the pressure went up to 50–65 psig only. At the end of this waterflooding tertiary recovery mode, only 0.165 g of oil was obtained in the collector. To recover more of the oil still trapped in the core, 1 pore volume (9 ml) slug of a 0.5 wt% B6-1 VA-*t*-AA multifunctional surfactant in water was used for enhanced tertiary recovery followed by 2 pore volume slugs of water.

5.1.4 Results and Discussion

Results of the sandpack oil recovery experiments are shown in Table 5.1.2.

It is evident from Table 5.1.2 that some tertiary oil can be recovered using a multifunctional multipolymeric surfactant solution of the present invention. Thickened surfactant has been found to recover the greatest amount of tertiary oil based on OOIP levels (runs #3 and #4) at 0.39 and 0.41% OOIP, respectively. Also, unthickened surfactant (run #2) showed marginal increase in performance compared to that of water (run #1) in the tertiary recovery. Results of run #6 demonstrate that reused surfactant/thickener mixtures from runs #3 and #4 showed expected performance considering that its concentration dropped to almost 0.2 wt% in water.

In oilfield situations, the height of the sandpack represents the distance between the injection and production wells. The pressure drop between the top surface of the sandpack and the vacuum pressure in the receiving flask corresponds to the pressure drop between the injection and production wells. About 2 pore volumes of thickened NH_3-neutralized B6-1 surfactant in water or brine at 0.5 wt% solid surfactant slug would be pumped into the injection well at constant pressure followed by driving

Table 5.1.2 Improvement of surfactant/water displacement of Fuel Oil #2 from oil-originally-in-place (OOIP) in a sandpack

Run No.	Tertiary surfactant used				Ratio of primary + secondary oil to OOIP (g/g)	Ratio of tertiary oil to OOIP (g/g)
	Type	Wt% in water	Vol. used (ml)	Vol. (ml) water after surfactant		
1	None (water)	0	48	0	0.41	0.15
2	NH_3-neutr. B6-1	0.5	48	0	0.54	0.17
3	Thickened NH_3-neutr. B6-1	0.5	20	28	0.41	0.41
4	Thickened NH_3-neutr. B6-1	0.5	20	28	0.57	0.39
3	Thickened NH_3-neutr. B6-1	0.1	48	0	0.58	0.08
4	Thickened NH_3-neutr. B6-1	0.5	10	38	0.41	0.21
5	Thickened NH_3-neutr. B6-1	0.5	10	38	0.53	0.17
6	Reused from runs #3 and #4	$\cong 0.2$	48	0	0.68	0.14

water or brine slug. This operation can be implemented in either secondary, tertiary, or quaternary phases of oil recovery. Produced oil, surfactant, thickener in brine can be separated using a gravity or centrifugal separator, or a similar device. If rate of recovery of surfactant in brine should be relatively fast, then either a hydrocyclone or a continuous centrifuge is recommended. Otherwise, clarifiers or gravity settlers will suffice. Recycle surfactant in brine can be re-thickened by the addition of make-up extra-thickened NH_3-neutralized B6-1 in water or brine at about 2.5 wt% solid polymer content. Extra thickening properties can also be imparted in regularly thickened versions by the addition of some NH_3-neutralized VA/AA random copolymer into the mixer. The addition of streams into the mixer is monitored based on attainment of a particular value of the interfacial tension of the fluid that is pumped into the injection well. A spinning drop apparatus can be used to determine the interfacial tension, while a Brookefield, Fann, or a capillary viscometer could be used to determine the viscosity. Alternately or in conjunction with this operation, similar sandpack oil and/or core displacement experiments can be performed. Part of the aqueous phase that is recovered from the gravity or centrifugal separator can be recycled, while the rest can be desalted by evaporation or precipitation in order

to produce processed brine, which will likely be almost free of surfactant/thickener. The processed brine can be fed back into the mixer before injection into the well, if needed.

During the enhanced recovery using the core rock, 0.45 g of oil was collected and the produced water phase was still cloudy with the presence of the surfactant. For the oil specific gravity of 0.83, 1 pore volume corresponds to 8.3 $\pm$0.8 g of oil. For a total recovery of 10.45 g of oil, this means that the surfactant was able to recover the last remaining oil in the core holder; additional volume of recovered oil came from the flow lines which amounted to 2 ml (1.9 g) at most. Also, from this example run, the multifunctional multipolymeric surfactant was capable of delivering about three times the amount of oil compared to that of tertiary recovery waterflooding.

From a process standpoint, waterflooding with a surfactant is a relatively simple operation if secondary and/or tertiary waterflooding had been implemented in the oilfield operation. One merely incorporates surfactants into the aqueous phase in pump in the needed amount followed by a water slug. Even if two types of multifunctional multipolymeric surfactants have to be used (unthickened followed by thickened type), such an approach is very different from foamflooding, wherein a gas has to be introduced after the surfactant–water slug followed by a water-based slug of either pure water or viscous polymer in water. The latter operation requires a carbon dioxide or nitrogen gas source as well as the necessary infrastructure. As seen from the total oil recovered in this example, the use of the multifunctional multipolymeric surfactant alone was able to recover most of the remaining oil at a rate several times that of tertiary waterflooding. Therefore, a case can be made that rules out the use of foamflooding or even gas flooding in place of the use of multifunctional multipolymeric surfactants.

Thus, multifunctional multipolymeric surfactant–thickener mixtures generated from the FRRPP process are proposed to be used in the recovery of oil from subterranean sources from waterflooding operations. The idea is to simply add the surfactant into the water in the injection well and enhanced production of oil (at least three times the rate compared to waterflooding) can be realized in the production wells. Surfactant–thickener mixtures can also be recycled and can function as demulsifiers, which add to the viability of the oil recovery operation.

5.2 Foamflooding Subterranean Enhanced Oil Recovery

5.2.1 Introduction

If a gas slug is applied behind the surfactant–water slug into the subterranean oilfield formation, a foam develops and facilitates oil displacement through the reservoir. An effective method of screening surfactants for foamflooding is the so-called static foaming test, whereby a mixture of surfactant–water and oil is placed in a column container such as a graduated cylinder. Then, a foam is produced by a simple effort of shaking the container vertically. After cessation of the shaking action, the foam

volume is measured as a function of time; the surfactant system that maintains a high foam volume is regarded as the best one for foamflooding EOR (Borchardt et al., 1988).

In this section, we present the potential of using VA/AA-based copolymers from the FRRPP process as foaming surfactants in the recovery of crude oil that is trapped in various rock formations. Aside from the widely positive oil recovery performance characteristics of VA/AA copolymers that will be described below, a review of the raw material cost structure also points to its possibility of being commercially available in the future as shown its relatively simple projected manufacturing operation depicted in Fig. 5.2.1 (Caneba and Axland, 2002).

In foamflooding enhanced oil recovery operations using a suitable gas such as CO_2, VA/AA copolymers have been shown to be good foaming surfactants (Caneba and Axland, 2002). Its polymeric nature results in the capability to form surfaces with relatively large radii of curvature. Since its hydrophobic part is an ester, the interface is relatively stable in the presence of hydrocarbons from the crude oil. After neutralization of the acid, the polymer is stable in brine solutions, since brine acts as a buffering agent. It is worth noting that good foaming surfactants for CO_2 flooding operations have oxygenated hydrophobic groups (Borchardt et al., 1988). The more the oxygenated groups, the better. The drawback is that the cost of the foaming surfactant increases as well. We think that the VA/AA copolymer will be cost-effective because the raw material cost is relatively low, while manufacturing process occurs under mild operating conditions at reasonable yields (currently up to 17 wt% in solution, almost 100 wt% yield in solid). Final product can be in the form of a concentrated self-emulsion (with some alcohol) in water or as a dried solid.

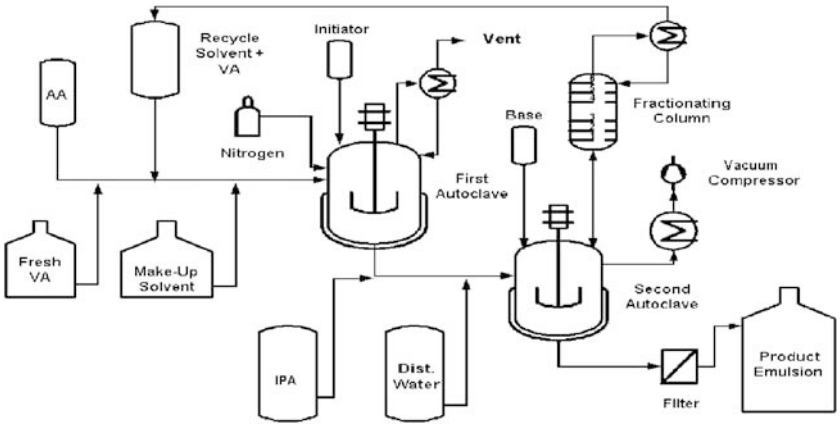

Fig. 5.2.1 Envisioned manufacturing diagram for the production of the B6-1 VA/AA emulsion product for foamflooding EOR. The cycle time in this batch operation is 4 h (With permission from Caneba and Axland, 2002)

5.2.2 Experimental

The atmospheric static foam test method (Borchardt et al., 1988) was used in order to determine comparative performance of the neutralized VA/AA surfactant. In a 25-ml graduated cylinder, 10 ml of 0.5 wt% surfactant in brine (1.5X, which contained 15.57 wt% NaCl and 1.14 wt% $CaCl_2$), and 3 ml crude oil were mixed by vertical shaking, and the foam volume measured vs time. Two kinds of crude oil were used: a heavy one and a light one.

Emulsions from VA/AA copolymers in distilled water were viewed using an optical microscope (Zeiss Axioplan 2 from Zeiss, Thornwood, NY) at 100X and 400X magnifications. A drop of emulsion was placed between glass slides. Frames of i were captured using the Scion ImagePC computer software and stored onto disks as an image files.

5.2.3 Results and Discussion

Table 5.2.1 shows the results of the static foaming test in comparison with literature values.

Table 5.2.1 Comparative foaming performance of VA/AA block copolymer compared with other oxygenated surfactants (With permission from Caneba and Axland, 2002)

Surfactant	Temperature (°C)	Organic material	Foam volume (ml)
VA/AA (B6-1)[a]	67	Bear Lake Crude[b]	4–5
VA/AA (B6-1)	20	Bear Lake Crude	2.3
Tergitol XD[c]	20	Bear Lake Crude	1.6
VA/AA (B6-1)	20	50/50 v/v heptane/toluene	2
Alcohol ethoxysulfate, AES911-2.5S	75	50/50 v/v decane/toluene	1
Alcohol ethoxyethylsulfonate, AEGS1215-12	75	50/50 v/v decane/toluene	0.6
Alcohol ethoxysulfate, AES911-5S	75	50/50 v/v decane/toluene	0.3
Alcohol ethoxyethylsulfonate, AESo1215-16	75	50/50 v/v decane/toluene	0.2
Alcohol ethoxylate, AES1215-18	75	50/50 v/v decane/toluene	0

[a]The Code B6-1 is the neutralized VA/AA block copolymer with 6 wt% AA content.
[b]This is a crude oil condensate from Bear Lake, Michigan.
[c]Tergitol XD is an ethylene oxide/propylene oxide block copolymer that is produced by Union Carbide, which is a relatively expensive nonionic surfactant.

It can be seen from Table 5.2.1 that the neutralized VA/AA block copolymer outperforms (B6-1) other oxygenated surfactants. It is worth noting that the higher the proportion of oxygenated material in the surfactant, the better is its foaming performance.

In another set of experiments, light and heavy crude oil was used in the static foam test column. Here, the foam volume vs time was monitored. VA/AA-based surfactants were compared with commercial alcohol ethoxylates (Brij 78 and 721) and ethoxylated alkylphenols (Triton X-155 and X-705, and Igepal DM-880, DM-970, and CA-890), which are some of the better nonionic foaming surfactants in the market at reasonable prices. The test was conducted at 70°C. Figure 5.2.2 shows that VA/AA (B6-1 and 6/25/02 products) surfactant systems have higher foam volumes compared to other nonionic foaming surfactants in both light and heavy crude oil. It is worth mentioning that the Tergitol XD surfactant used to generate data in Table 5.2.1 resulted in a negligible foam volume at the higher operating temperature of 70°C.

Figure 5.2.3 shows results of comparison of foam volumes vs time between VA/AA-based surfactants and commercially available anionic surfactants. Features of the anionic surfactants used are

1. Triton H55 – phosphate esters, potassium salt
2. Rhodacal DS10 – sodium dodecyl benzene sulfonate
3. Rhodapex CO436 – sulfates and sulfonates of oils and fatty acids

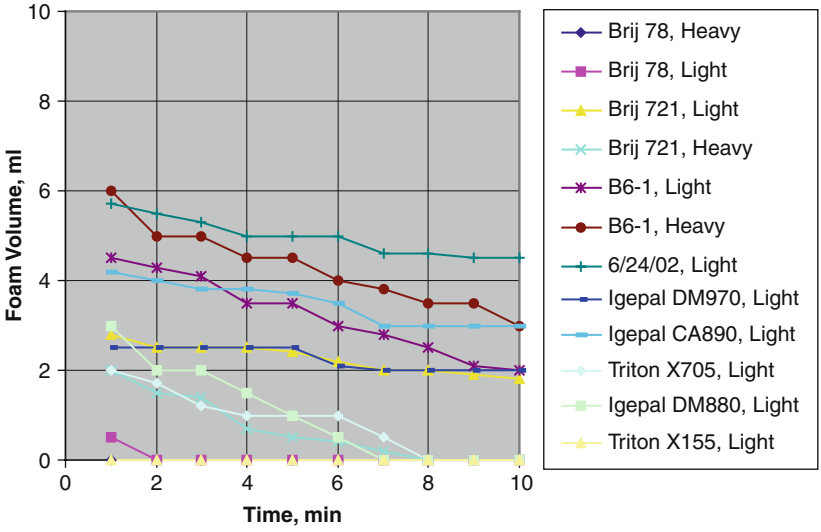

Fig. 5.2.2 Static foam volume vs time for the VA/AA-based copolymers (B6-1 and 6/24/02 emulsions) and commercially available nonionic surfactants (Brij, Triton, and Igepal surfactants) at 70°C. Light and heavy crude oil was used in this test (With permission from Caneba and Axland, 2002)

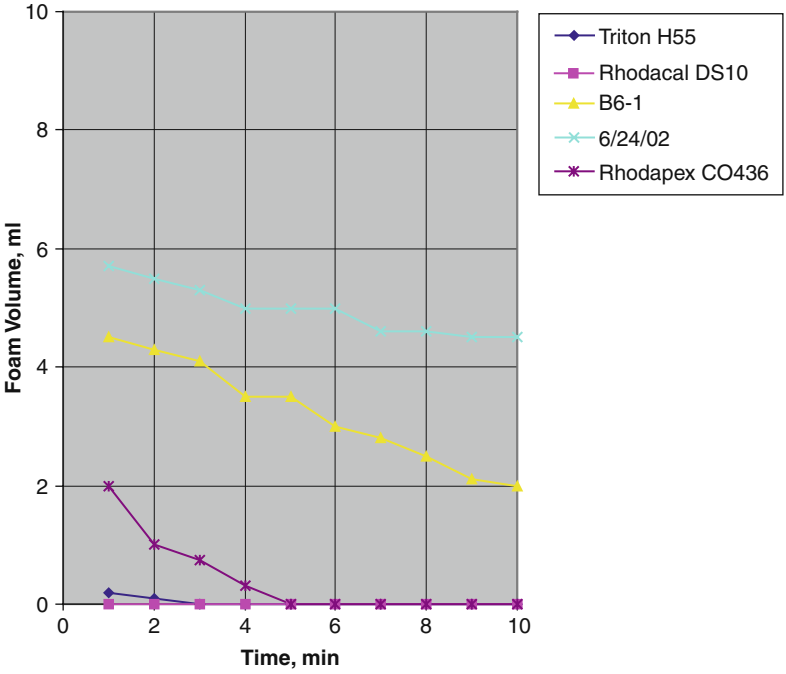

Fig. 5.2.3 Static foam volume vs time for the VA/AA-based copolymers (B6-1 and 6/24/02 emulsions) and commercially available anionic surfactants (Triton, Rhodacal, and Rhodapex surfactants) at 70°C. The Triton H55 is 50% solids. Light crude oil was used in this test (With permission from Caneba and Axland, 2002)

Again, VA/AA-based surfactants outperform some of their anionic counterparts. The difference here and in Fig. 5.2.2 is that nonionic surfactants seem to be better foam formers than anionic types. Also, it is evident that longer chain nonionics

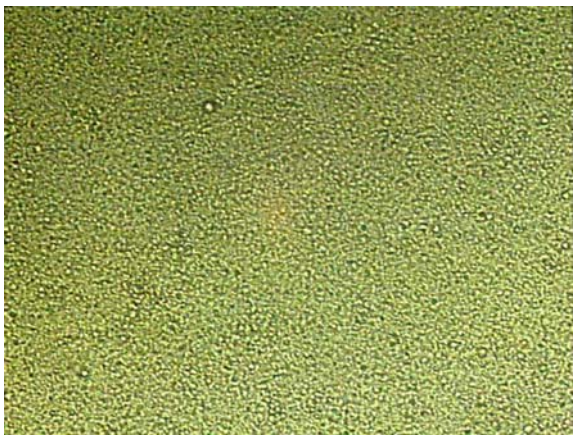

Fig. 5.2.4 Optical micrograph of a surface of a VA/AA-based emulsion (6.6 wt% solids) at 400X magnification, showing a bicontinuous network structure with 5–10 μm open cells (With permission from Caneba and Axland, 2002)

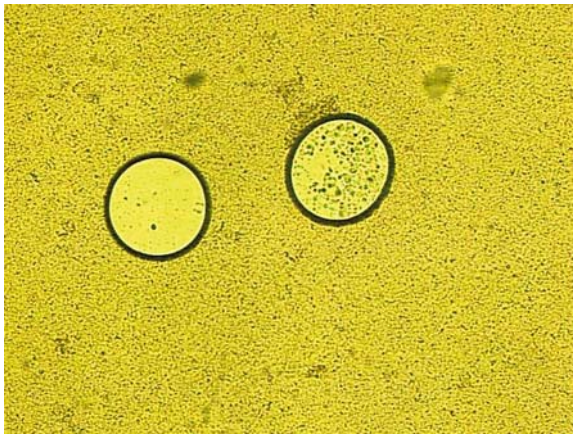

Fig. 5.2.5 Optical micrograph of a surface of a VA/AA-based diluted emulsion (from 6.6 wt% solids) at 100X magnification, showing a surface of a bubble that has a bicontinuous network structure (With permission from Caneba and Axland, 2002)

(higher numbered Brij, Triton, and Igepal) and anionics tend to be better foaming surfactants than their shorter counterparts.

Figure 5.2.4 shows a network surface structure of a VA/AA-based emulsion with 6.6 wt% solids. The repeat unit in the network structure is between 5 and 10 μm. The formation of the network or bicontinuous surfactant structure is well established in relatively high molecular weight ethylene oxide/propylene oxide segmented block copolymer nonionic surfactants, and it has been ascribed to the formation of liquid crystalline macromolecular assemblies. Upon dilution, the emulsion showed 5–10 μm spherical domains that could form aggregates up to about 60 μm in size (Fig. 4.4.5). In Fig. 5.2.5, bubble surfaces are shown with the network surfactant structure, even in the diluted emulsion. Apparently, the surfactant macromolecules tend to concentrate on bubble surfaces and form a more viscous and probably elastic polymer surface layer.

It is clear that surfactants with polar hydrophobic components produce longer lasting foams that are appropriate for foamflooding operations. A quantitative measure of the polarity of a small molecule is through the value of its dipole moment. Symmetric hydrocarbon molecules, such as linear aliphatics and cycloaliphatics, have dipole moments at 0 Debye (Prausnitz et al., 1999). Structurally and electronically asymmetric compounds have dipole moments greater than zero, and values are tabulated. Another quantitative measure of polarity is the hydrogen-bonding number (Hansen, 1999); compounds with a relatively large hydrogen-bonding index are relatively polar. In addition, they tend to be hydrophilic as well. Of course, ionic compounds are classically considered hydrophilic. In order to determine how polarities of small molecules translate to that of a multipolymer, one merely determines polarities of segments or group of segments from a multipolymer compared to the closest small-molecule analog. A more practical way of characterizing polarity of multipolymer segments or group of segments is through the Hansen solubility parameter, δ, which is related to the dispersion or nonpolar (δ_d or δ_n), polar (δ_p), and hydrogen-bonding (δ_h) contributions (Hansen, 1999)

$$\delta^2 = \delta_d^2 + \delta_p^2 + \delta_h^2. \tag{5.2.1}$$

Based on the tabulations for the various contributions to the total solubility parameter of various compounds, polar materials have values of δ_p greater than 0. This would then be the lower limit for the polarity of the hydrophobic portion of the multifunctional multipolymeric surfactant in this invention. For the hydrophilic part, it could either be ionic or be nonionic if the hydrogen-bonding solubility parameter, δ_h, is greater than 1.0. Thus, if one looks into the various functionalities cited in Table 5.1.1, most of them fall within the range of solubility parameters for good foamflooding performance, except for aliphatic and aromatic compounds/functionalities. This is not necessarily a fallacy because as along as these nonpolar groups/functionalities are mixed with polar groups/functionalities, the overall effect is still polar. In fact, a quantitative measure of a combined solubility parameter (or dispersion, polar, hydrogen-bonding portions) for n groups/functionalities is obtained as a volume average

$$\delta = \sum_{i=1}^{n} \Phi_i \delta_i, \tag{5.2.2}$$

where Φ_i is the volume fraction of group/functionality i in the hydrophobic or hydrophilic portion of the multipolymeric surfactant. Volume fractions or various compounds closely representing various functional groups in the surfactant can be obtained from various sources (Prausnitz et al., 1999).

For a basis of 1 barrel of oil recovered, we assume that current micellar technology requires 0.1–0.2 lb of surfactant (Thomas and Farouq Ali, 2001). The lowest figure for energy consumption in the production of alcohol sulfate, linear alkylbenzenesulfonate, alcohol ethoxylate, or alkylphenol ethoxylate surfactants is 61 GJ/1000 kg (Britton, 1998). This is equal to at least 26,300 Btu of manufacturing energy per lb of surfactant. Since the VA/AA copolymer is about four times better than conventional foaming surfactants (based on Table 5.2.1), then 80% of the energy consumed will be saved by the substitution, based on the valid assumption that the energy consumption to manufacture conventional and VA/AA surfactant is almost the same. This amounts to 21,038 Btu/lb. Since there are about 350 billion barrels of oil still recoverable here in the United States,[1] the surfactant substitution should result in at least 735 trillion Btu of energy saved. The energy consumption for the manufacture of VA/AA surfactant from vinyl acetate and acrylic acid should not be greater than that consumed to produce conventional surfactants (26,300 Btu/lb) because reagents come from ethylene (20,000 Btu/lb), propylene (similar energy

[1]Taken from the abstract of DOE funded project announcement in January 2002 under the project entitled, "Development and Optimization of Gas-Assisted Gravity Drainage (GAGD) Process for Improved Light Oil Recovery", of Louisiana State University. It can be seen in http://fossil.energy.gov/oil_gas/res_efficiency/bkg_oil_resefficiency_2002sel.htm

consumption to manufacture as ethylene), and acetic acid (in the same order of 12,000 Btu/lb from ethanol manufacture).[2]

In the oil recovery application, the use of VA/AA-based material could result in a fourfold decrease in future use of foaming surfactants. Also, the VA/AA copolymer could be formulated to have long-term biodegradability. For the basis of 350 billion barrels of recoverable oil here in the United States at 0.1 lb surfactant use per barrel of oil recovered, waste surfactant savings is 80% of current possible use of foaming surfactants. This amounts to 1.4×10^7 tons of surfactant waste saved. In a 60-year period of oil production at the current rate of about 6 billion barrels per year, this could result in 2.33×10^5 tons/year of waste savings.

Thus, this section pertains to the possible use of newly synthesized vinyl acetate/acrylic acid (VA/AA) copolymer to help recover trapped crude oil, an important mineral resource. The proposed approach is to use the copolymer as a foaming surfactant (in water or brine), which will be driven by a gas, such as carbon dioxide or nitrogen. Neutralized forms of the copolymer result in an anionic surfactant, which has been found to have minimal adsorption onto the rock matrix. Neutralized VA/AA copolymers generated from the FRRPP process are found to outperform other anionic surfactants and even more adsorbing nonionic surfactants. Due to the long-chain nature of the hydrophilic groups and polar hydrophobic groups of nonionic surfactants, they are found to produce better foams than anionic ones. Since VA/AA copolymers have long-chain hydrophilic groups and polar hydrophobic groups, it is not surprising that they are good foaming agents as well. Optical microscopy of VA/AA emulsions reveals that they form microscopic network surface structures, which are presumably due to liquid crystalline formation in macromolecular scale.

5.3 Bitumen Recovery from Surface Sources

5.3.1 Introduction

Bitumen recovery from surface sources, such as tar sands, their tailings, shale oil, and surface spills ranges from thermal (Bouck, U.S. Patent No. 4,412,585), steam assisted (Widmyer, U.S. Patent No. 4,34,812; Needham, U.S. Patent No. 4,068,717), chemical (Hardin, U.S. Patent No. 4,110,195; Mitchell, U.S. Patent No. 4,410,551; Miller, U.S. Patent No. 4,470,899; Graham et al., U.S. Patent No. 4,722,782; Taylor, U.S. Patent No. 4,822,481; Graham et al., U.S. Patent No. 5,143,598), and surfactant-based methods (Merchant Jr. and Smith Jr., U.S. Patent No. 4,407,707;

[2]Taken from Fuel or Energy Source Conversion Factors of Metrics Summary in the I&I 2002 Solicitation.

Siefkin and Boesiger, U.S. Patent No. 4,368,111; Thirumalachar and Narasimhan Jr., U.S. Patent No. 4,929,341; Guymon, U.S. Patent No. 5,252,138; Olah, U.S. Patent No. 5,000,872; Schramm and Smith, U.S. Patent No. 5,009,773; Gregoli et al, U.S. Patent No. 5,340,467; Ashrawi, U.S. Patent No. 5,282,984; Catla, U.S. Patent No. 5,746,909). All these methods can be implemented through strip-mining or excavation, while in situ methods have been proposed (Yildirim, U.S. Patent No. 4,406,499). Strip-mining or excavation is being implemented and it has resulted in the alteration of the landscape. Also, it has resulted in enormous man-made lakes, which also contains tailings of the bitumen extraction operation on the lakebed; thus, they are called tailings ponds. In situ extraction, while it hardly disturbs the landscape, is still an inefficient method. One approach here is to use the steam-water-assisted-gravity (SAG) method for in situ recovery of bitumen from buried tar sands. Such an operation is energy intensive, since steam is usually produced using natural gas. With a surfactant that is capable of picking up heavy crude, involving the use of hot water only, is recyclable/reusable; thus, saving enormous amounts of energy. Alternately, with steam-water methods, the use of a reusable surfactant can still result in economical incremental oil production.

5.3.2 Experimental

5.3.2.1 Extraction of Heavy Crude Oil from Standard Sand

To demonstrate the capability of an FRRPP-produced multifunctional polymeric surfactant to remove heavy crude oil from sand, 1 part oil per 10 parts sand by weight was prepared. A particular type of sand (MI 2NS) was selected and dried by direct heat from a hot plate surface: The dried MI 2NS sand was passed through a 20-mesh screen for final sizing and air-tight storage. Before use, the stored sand was placed on a plastic pan up to ½-in. in height and redried using a microwave oven for about 2 min with mechanical mixing every 30 s. A given weight of the microwaved sand was placed in a bottle along with the heavy crude oil (1 part by weight of heavy crude oil for 10 parts by weight of sand). The oil was distributed in the sand using a mechanical mixer for about 5 min at a mixing speed of about 100–500 rpm. Finally, the oil mixed with the sand was sealed in the bottle to be later used for extraction experiments.

Oil extraction was started by placing 10.0 ± 0.1 g of the oil/sand material in a standard 25-ml graduated cylinder. Then, 7.0 ± 0.1 g of extracting aqueous solution was added. The mixture was then agitated using a mixer and mixing blade at constant speed for a given period of time. The extracting solution was made up of an ammonia-neutralized vinyl acetate–acrylic acid tapered block copolymer in water as described in various publications and patent applications (Caneba and Dar, 2005). The tapered block copolymer was called B6-1, which means that it nominally contained 6 wt% acrylic acid and it was synthesized using an almost straight

batch reaction procedure. Its typical number-average molecular is 42,000 Da with a polydispersity index of 2.76. Finally, the B6-1 solid is at least 98 wt% active.

The level and manner of mixing the oil/sand and extracting solution were maintained the same for all samples at different mixing times. After mixing, the mixtures would form three phases if allowed to stand for at least 12 h; a sand pack phase at the bottom, a cloudy aqueous phase above it, and a thin black oily phase on top. In addition, the sand pack contains a black oil/sand layer on its top surface. This top layer was found to come from oily agglomerates that formed during the mixing process, which were nevertheless kept by the surfactant from growing to more than about 1 mm in size. Also, this layer was found to be uniformly spread on top of the sand pack. Thus, the oily/sand layer was transferred into a sealed bottle using a small scoop along with some wash water. Crude oil from the topmost layer, oil/sand scoop, and transfer bottle was harvested using a preweighed oil-soaked soie paintbrush for oil-based paints. Since we found the mixing blade to contain oily material around it after each use, a parallel conditioning run using the same procedure and operating variables was always done in order to establish this amount of oil that was subtracted from the total oil recovered in the actual subsequent run.

Most of the oil that settled with sand on the top of the sand pack was extracted by heating it with water. Also, this oily fraction definitely has a higher density than the rest of the crude oil, indicating the possible presence of heavy metals, such as vanadium, nickel, or sulfur. Also, the oily portion that separated after heating which rose to the water surface could be crude residuum. The heavier oily material indicates a portion that is complexed with heavy metals and sulfur.

5.3.2.2 Tar Sands Studies

Tar sand used in the experiment contained a heavy type of bitumen, which was found to be at 15 wt% bitumen. About 100 g of the tar sand was placed in cylindrical glass bottles. Then, 100 g of either pure tap water or 0.5 wt% ammonia-neutralized B6-1 VA-*t*-AA copolymer in tap water was added. The sand and aqueous fluid inside the bottles were conditioned at their operating temperatures (60 or 80°C) inside a Blue M natural convection oven for at least 1 h. Then, each of the bottles was opened and placed in a sand bath at the operating temperature. The sand was then mixed using a bread dough mixer (lowest setting) for 5 or 15 min. The bitumen that floated to the top of the aqueous layer was harvested using a preweighed soie brush, and excess bitumen was placed in a preweighed cup.

5.3.3 Results and Discussion

The result of the extraction of heavy crude oil from standard sand is shown in Table 5.3.1.

Based on the above results, it is possible to obtain almost 100% recovery using a high enough level of surfactant and mixed for a long enough time. Also, in well-mixed and/or well-dispersed systems, a 50/50 proportion of oil from the top liquid

Table 5.3.1 Result of extraction of heavy oil from standard MI 2NS sand. Error in % recovery was ±5.5%

	% Oil recovery from top liquid layer and from top of sand pack (in parenthesis)	
Mixing time (min:s)	0.25 wt% B6-1 surfactant in water	0.5 wt% B6-1 surfactant in water
2:00±0:05	0 (0)	22 (5.5)
5±0:05	5.5 (22.5)	33 (33)
10±0:05	33 (33)	44 (44)

layer and oil from the top of the sand pack was obtained. This is not surprising since it is well known that half of heavy crude can contain residuum material. The use of a good polymeric surfactant allowed the separation of this heavy oil material, which can be further refined to extract more of the oil from heavy metals and sulfur. To demonstrate the recyclability of the surfactant used, cloudy aqueous solutions were gathered from similar experiments and they were all shown to be almost as cloudy as fresh surfactant–water mixtures.

In order to implement this experiment efficiently in the field (Fig. 5.3.1), a take-up mechanical system is used to transfer contaminated soil or sand (surface oil/bitumen sources) into a mixer system (Mixer 1) whereby contact with surfactant–water occurs. Then, oil from the top of the fluid is skimmed off, while the oil from the rest of the liquid can be purified using a gravity or centrifugal separator, or a similar device. The aqueous surfactant fluid coming out of the separator can be reused by pumping it back into Mixer 1. The top layer of the sand or soil is skimmed off and can be further processed using some heat in order to recover residuum and even heavy metal complexes. The rest of the soil or sand can undergo a final wash in Mixer 2/separator before discharge, and its wash water can be recycled into the system. Finally, the washed sand or soil is dumped on an appropriate place. A way to implement these steps more efficiently is to use augers also as mixers while soil or sand moves in one direction and fluids move in the opposite direction by gravity. Still another approach is to use hot surfactant and water (into Mixer 1 and/or Mixer 2) in order to introduce heat into the mixer(s) for more efficient cleanup. This approach, shown in Fig. 5.3.1, is its portable version, because it involves a relatively small processing time. Figure 5.3.2 shows a relatively long processing time stationary version, which is less energy intensive, since it totally relies on a clarifier or a gravity settler to separate all the component phases.

Another way of using the surfactant system is to take advantage of its foaming capabilities. This is done by blowing air underneath the contaminated soil that is also being contacted with the surfactant–water solution. At the same time the fluid is taken in by a vacuum cleaning tool which filters out soil or sand particles. The fluid removed by the vacuum cleaning tool can be separated using a gravity or centrifugal separator, or an equivalent device. The advantage of this approach is that cleanup

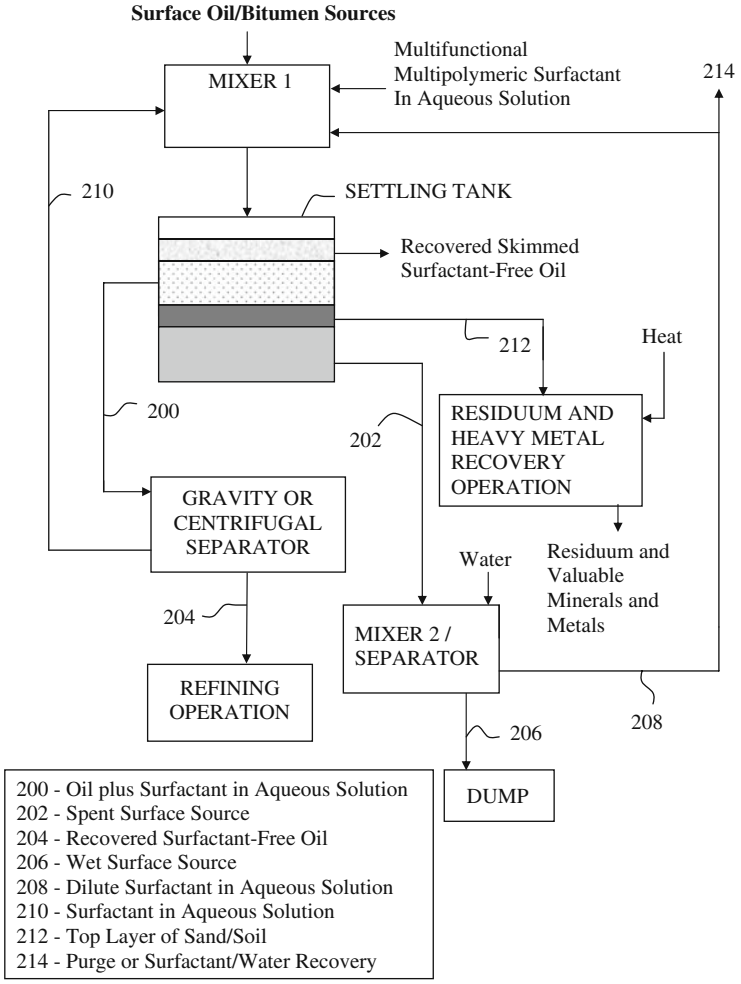

Fig. 5.3.1 Portable process for bitumen removal from surface sources

can be done in situ even though some mechanical action can be used at the same time. This approach can be implemented in both portable and stationary forms.

Results of the tar sands experiment presented in the patent literature (Caneba, 2007) involves a dramatic improvement in the recovery of bitumen from the surfactant–water system to that of using water alone.

The bitumen layer from the experiment at 80°C and 15 min mixing time on top of the tar sand and from the rest of the sand were harvested and extracted with THF. Vanadium contents were also obtained from these two bitumen sources and from the tar sand source. For the tar sand, bitumen was also extracted by repeated washings of THF followed by drying of the THF from the wash fluids. One gram of

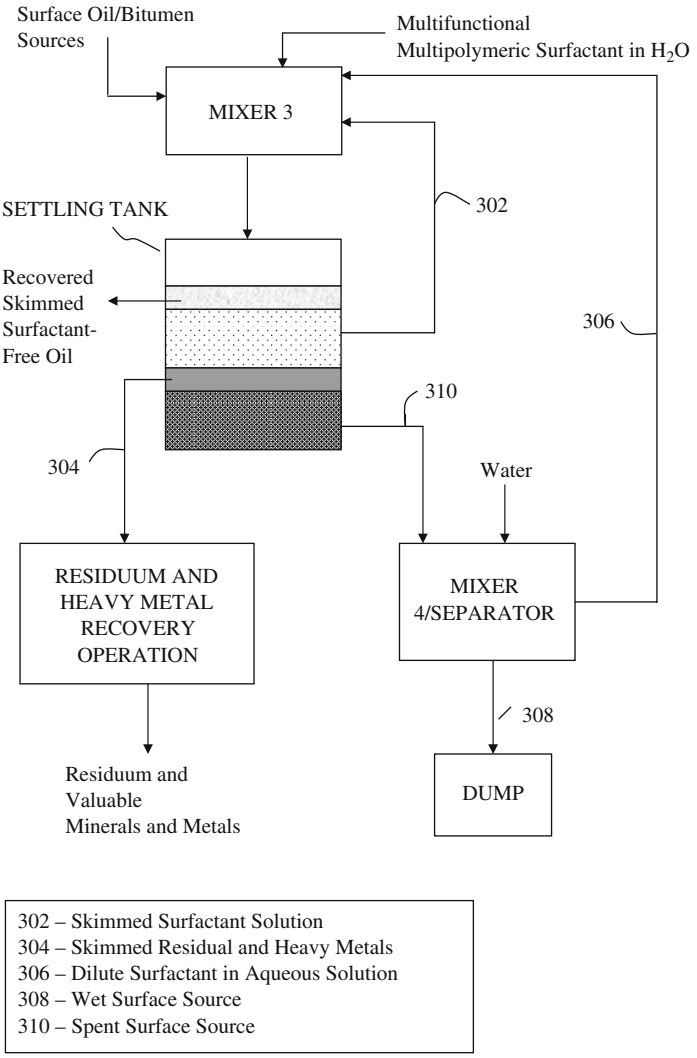

Fig. 5.3.2 Stationary process for bitumen removal from surface sources

bitumen from the three sources was placed into ceramic crucibles. They were gradually heated at 10°C/min to 700°C and the temperature maintained for 1 h. Residues from the crucibles were transferred to a beaker and dissolved in 40–50 ml 60/40 v/v concentrated HCl/HNO_3. Resulting solutions were diluted with deionized water to 250 ml for inductively coupled plasma (ICP) spectrometer analysis. Results indicate that the starting tar sand has 121 ppm vanadium, the top bitumen layer has 255 ppm vanadium, and the rest of the tar sand after mixing has only 171 ppm vanadium. Therefore, the surfactant–water system is capable of concentrating vanadium in the bitumen on top of the sand layer after mixing.

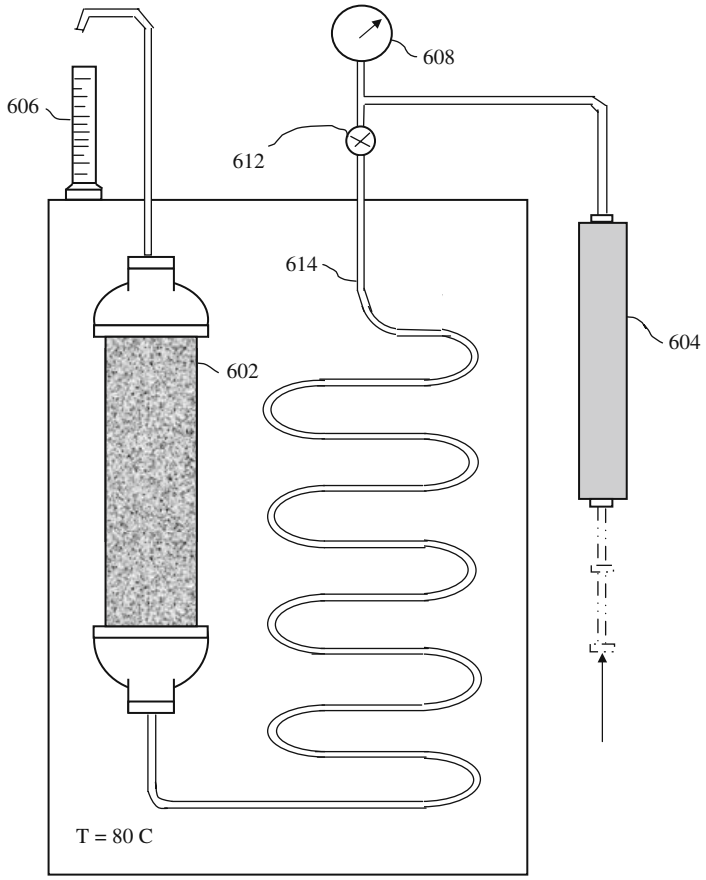

Fig. 5.3.3 In situ bitumen removal apparatus from tar sands

The experimental study to simulate in situ tar sand extraction was done using the apparatus shown in Fig. 5.3.3. A piping with 3/4" diameter × 4" internal dimension (602) was fitted with flanges that end with 1/8" female NPT connections. It was loaded and packed with the tar sand material and closed with screens on both ends. Upstream is a 1/8" copper refrigerant coil (614); since the coil and tar sand packed column were inside the natural convection Blue M oven, the coil had the function of an aqueous phase preheater. Before the fluid entered the oven, it was metered in by a stainless steel 50-ml syringe (604) that was driven by a syringe pump. Inlet pressure was measured using the gage (608), and outlet from the tar sand packed column was obtained at atmospheric pressure using the collector (606). For the tar sand that was found to contain 15 wt% heavy bitumen, around 52–53 g of tar sand was packed into the column, with a pore volume of around 10 ml. With a flow rate of 3.64 ml/min of water, only 0.08 g of bitumen was extracted at an oven temperature of 80°C using 50 ml of water. When 50 ml of thickened B6-1 was used, around 0.49 g of bitumen

was extracted off at the same set of conditions (except the pressure gage read around 10 psig when using the surfactant–water while it read close to zero psig when using pure water). This means that using five pore volumes, the thickened surfactant–water fluid was capable of extracting six times more bitumen than just water. With higher grade tar sand and operated close to 100°C, higher % extraction of the tar sand can be obtained for the in situ operation.

References

Arnaud, J., 2005. U.S. Patent No. 6,875,351, April 5.

Ashrawi, S. S., 1994. U.S. Patent No. 5,282,984, February 1.

Balzer, D. U.S. 1989. Patent No. 4,842,067, June 27.

Berger, P. D., 2004. U.S. Patent Application 20050199395, Filed March 10.

Borchardt, J. K., Bright, D. B., Dickson, M. K., and Wellington, S. L., 1988. "Surfactants for Carbon Dioxide Foam Flooding", in: Surfactant-Based Mobility Control – Progress in Miscible-Flood Enhanced Oil Recovery, D. H. Smith (Ed.), *ACS Symposium Series*, *373*, Washington, DC, Chapter 8.

Bouck, L. S., 1983. U.S. Patent No. 4,412,585, November 1.

Boudreau, E. L., 2004. U.S. Patent No. 6,776,234, August 17.

Boudreau, E. L., 2004. U.S. Patent Application 20040224854, Filed June 9.

Britton, L. N., 1998. *J. Surf. Deter., 1*, 109–117; also available at http://www.cler.com/new/britton.htm.

Caneba, G. T., and Axland, J. E., 2002. *J. Miner. Mater. Charact. Eng.*, *1*(2), 97.

Caneba, G. T., and Dar, Y., 2005. "Free-Radical Retrograde-Precipitation Copolymers and Process of Making the Same", U.S. Patent Application 10/045,725, and Divisional Patent Application, 11/181,481, Filed July 14.

Caneba, G. T., 2007. U.S. Patent Application 11/673, 364 Filed Feb. 9.

Caneba, G. T., Renier, M., and Ott, B., 2008. *J. Miner. Mater. Charact. Eng., 7*(2), 175.

Catla, J. S., 1998. U.S. Patent No. 5,746,909, May 5.

Chen, C. S. H., and Williams, A. L., 1986. U.S. Patent No. 4,577,000, March 18.

Cooke, T. W., 1984. U.S. Patent No. 4,460,791, July 17.

Deng, S., Yu, G., Jiang, Z., Zhang, R., and Ting, Y. P., 2004. *Colloids Surf. A: Physicochem. Eng. Aspects*, *252*, 113–119.

Evani, S., 1989. U.S. Patent No. 4,184,096, March 21.

Farmer III, R., Lawson, J. B., and Sawyer, Jr., W. M., 1976. U.S. Patent No. 3,943,160, March 9.

Fried, J. R., 1995. Polymer Science and Technology, Prentice-Hall, Englewood Cliffs, NJ, , ISBN 0-13-685561-X, p. 134.

Gale, W. W., Ashcraft, Jr., T. L., and Saunders, R. K., 1976. U.S. Patent No. 3,946,812, March 30.

Graham, R. J., Helstrom, J. J., Peck, L. B., and Stone, R. A., 1988. U.S. Patent No. 4,722,782, February 2.

Graham, R. J., Helstrom, J. J., Peck, L. B., Stone, R. A., and Bernier, Jr., E. J., 1992. U.S. Patent No. 5,143,598, September 1.

Gregoli, A. A., Hamshar, 3rd, J. A., Rimmer, D. P., Yildirim, E., and Olah, A. M., 1994. U.S. Patent No. 5,340,467, August 23.

Guymon, E. P., 1993. U.S. Patent No. 5,252,138, October 12.

Hansen, C. M., 1999. Hansen Solubility Parameter, CRC Press, Boca Raton.

Hardin, D. J., 1978. U.S. Patent No. 4,110,195, August 29.

Hsu, O. Y. S., and Hsu, N. S. N., 2000. U.S. Patent No. 6,022,834, February 8.

Isaacs, E. E., Prowse, D. R., 1984. U.S. Patent No. 4,458,759, July 10.

Merchant, Jr., P., and Smith, Jr., D. L., 1983. U.S. Patent No. 4,407,707, October 4.

Miller, J. D., and Hupka, J., 1984. U.S. Patent No. 4,470,899, September 11.

Mitchell, D. S., 1983. U.S. Patent No. 4,410,551, August 30.
Mohanty, K. K., and Caneba, G. T., 2005. "Enhanced oil recovery – a review", *Encyclopedia of Chemical Processing*, Dekker Encyclopedias, November.
Moss, D. K., 2006. U.S. Patent No. 7,125,825, October 24.
Needham, R. B., 1978. U.S. Patent No. 4,068,717, January 17
Newcombe, J., 1980. U.S. Patent No. 4,216,079, August 5.
Olah, A. M., 1991. U.S. Patent No. 5,000,872, March 19.
Pope, G. A., Baviere, M., 1991. "Reduction of capillary forces by surfactants", in: Basic Concepts in Enhanced Oil Recovery Processes, M. Baviere (Ed.), Critical Reports on Applied Chemistry, Elsevier Applied Science, London and New York, Vol. 33.
Prausnitz, J. M., Lichtenthaler, R. N., and Azevedo, E. G. D., 1999. Molecular Thermodynamics of Fluid Phase Equilibria, 3rd ed., Prentice-Hall, Englewood Cliffs, NJ.
Presley, C. T., and Harrison, R. J., 1972. 1642824, August, DE 252/330.
Rodriguez, F., Cohen, C., Ober, C.K., and Archer, L. A., 2003. Principles of Polymer Systems, 5th Edition, Taylor and Francis, New York.
Schramm, L. L., and Smith, R. G., 1991. U.S. Patent No. 5,009,773, April 23
Shpakoff, P. G., and Raney, K. H., 2006a. U.S. Patent No. 7,137,447, November 21.
Shpakoff, P. G., and Raney, K. H., 2006b. U.S. Patent No. 7,055,602, June 6.
Stapp, P. R., 1984. U.S. Patent No. 4,470,461, September 11.
Taylor, A. S., 1989. U.S. Patent No. 4,822,481, April 18.
Thomas, S., and Farouq Ali, S. M., 2001. *J. Canadian Petro. Tech.*, *40*, February, 46–52.
Van Den Berg, Antonius, F. G., Jansen, A., and Stamps, P. A., 2004. U.S. Patent No. 6,787,027, September 7.
Widmyer, R. H., 1977. U.S. Patent No. 4,34,812, July 12

Chapter 6
Outlook

Since the FRRPP process is more of an enabling technology than a means toward a specific product or application, it is not easy to predict how it will be used in the future. The following discussion pertains to some of the ideas that can be exploited using this new technology.

6.1 Polymers for Defense and Homeland Security

6.1.1 Labeled Surfactants

The FRRPP process has been proposed to generate unique materials with certain programmable structures. Some of the unique features involve polymeric surfactants that have the ability to be dispersed in water at relatively low concentrations, and to be environmentally responsible formulations which allow for wide area/volume delivery. They would also have the ability to penetrate low porosity solids, such as soil, cement, rock, masonry with modest pressure drop requirements. If labeled, these surfactants can be applied on various surfaces or within porous structures for subsequent detection of changes in surface/underground structures. These materials can also be transformed into a nonflowing gel, and finally into a hard rubber dry sealant material. Other transformations of interest could be investigated from various possible polymeric surfactants that can be synthesized using the FRRPP process.

Figure 6.1.1 shows that the B6-1 VA/AA-based surfactant precursor solid material can be blown into a low-density foam after drying, and then transformed into a self-emulsion in water upon neutralization with ammonia.

When the vinyl acetate segments were hydrolyzed, a gel material was formed from the surfactant, which was expanded in volume by a factor of about 5. Upon drying, the gel turned into a hard rubber sealant material (Fig. 6.1.2(a)), which has a closed structure (Fig. 6.1.2(b)) and a surface that is very adherent to glass.

The hydrolysis of the vinyl acetate from the material (also called B6-1) was obtained when 0.5 wt% was dispersed in water at 80°C for less than 3 weeks. Acetic acid is a product of the reaction, which also results in the formation of vinyl alcohol

G. Caneba, in: *Free-Radical Retrograde-Precipitation Polymerization (FRRPP)*,
Chapter DOI 10.1007/978-3-642-03025-3_6,

(a) (b)

Fig. 6.1.1 B6-1 VA/AA solid foam material (**a**) and its corresponding self-emulsion at 0.5 wt% in water after neutralization with ammonia (**b**)

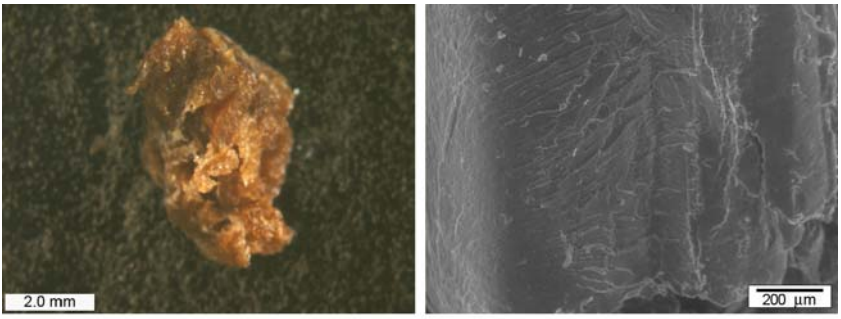

(a) (b)

Fig. 6.1.2 Optical microscope picture of the hard rubber dried solid material (**a**) from the hydrolyzed version of the surfactant solid in Fig. 6.1.1, and SEM micrograph of the surface of the same material (**b**) showing no open pores. Scale bars are (**a**) 2 mm and (**b**) 200 µm

(VOH) segments and an accompanying pH change from 7 to 5. It is well known that the rate of hydrolysis is increased with the addition of catalytic amounts of a strong acid, such as sulfuric or hydrochloric acid. Thus, the small amount of acetic acid produced from the reaction has a catalytic effect as well. Finally, it is well known that the vinyl alcohol polymer is biodegradable in the soil.

It should be noted that these VA/VOH/AA-based multipolymeric surfactants were developed as a displacement fluid for petroleum and tar sands (Caneba, 2007); thus, their permeability properties have been tested as well. If conditions are such that in time the material hydrolyzes to become a sealant in the rock formation, then it could also be investigated for its potential use in carbon sequestration operations.

Surveillance of security perimeters has always been a problem, and various technologies are currently being employed. Most of these technologies are based

on actively deployed devices, which can be identified and disabled. Even when these technologies are working, there is always a problem of identifying intruders, because they can cover their faces if they so choose. As new technologies are deployed, the other side comes up with ways to defeat them. This is a neverending cat-and-mouse game. Thus, there is always a desire for new methods of covert surveillance and that includes identification features. One approach that has not been investigated to its full extent is chemical tagging based on spectral signals, if it can be done in an environmentally responsible fashion.

Various means of chemically tagging perimeter areas of bases could involve any type of imaginable chemicals. However, when one requires it to be undetected by the naked eye, all pigmented materials could be ruled out, except those that are smaller in size compared to the wavelength of light, such as nanoscale materials. Since these materials have to be environmentally responsible and do not pose significant health risks, then a lot of nanoscale materials or materials with heavy metals would have to be ruled out as well. If the tag material has to be dispersed with a carrier fluid, it would normally have to be a liquid carrier, since a gas or vapor carrier will be prone to oversprays and inefficient application, especially in relatively open areas. Among all liquid carriers, water is accepted as the most environmentally responsible and economical. It is therefore evident that tag materials could be salt or surfactant-based materials that could incorporate certain inorganic elements and possess other functions, such as adhesion, long-term biodegradability, weathering. Therefore, the proposed solution is to use tag chemicals made up of multifunctional hydrophilic–hydrophobic multipolymeric surfactants. This will be contingent on the availability of a suitable polymerization method that can allow the production of such material.

The object of a proposed research project is to develop a sprayable surfactant–water solution wherein the surfactant has labeled moieties. The solution is sprayed over a wide area of ground. If the ground surface is disturbed, IR signal changes of the label from the surfactant can be detected, indicating the possibility that intrusion over the perimeter surface. Also, the transfer of the surfactant material onto other surfaces (intruder) will be detectable. Finally, the formulation is going to be environmentally responsible, since it is delivered with water and components can be designed to be mostly biodegradable over a period of 1–2 years.

An approach to formation of labeled monomers could involve lanthanides (e.g., cerium and yttrium) as labels (P.A. Heiden, personal communication). Rare earth salt such as cerium hydroxide can be reacted directly with a polymerizable monomer or a ligand (to shift the absorption) that is reacted with a polymerizable monomer. This route is illustrated below using cerium(III) acetate hydrate.

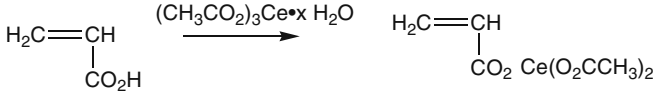

The cerium(III) ion emission is from 5d → 4f transitions. Under UV excitation an emission band is expected between 300 and 350 nm. The spectroscopic properties can be shifted by altering the ligands, such as shown below.

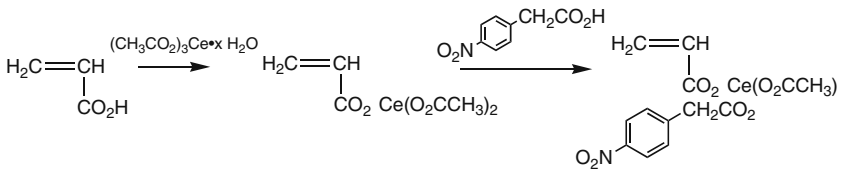

6.1.2 Specialty Surfaces

A proposed concept for the specialty polymer surfaces is the use of phase-inverting block copolymers. A simple example is an AB diblock with a Teflon®-like A-block (based on Zonyl®, TFE, CTFE) and a hydrophilic B-block (based on acrylic acid [AA] or methacrylic acid [MAA] or their salts, with added ethylene [E] and vinyl acetate [VA] comonomers for better adhesion to surfaces, if needed). The diblock will behave like a detergent in water and can be sprayed onto a solid surface. The Teflon®-like A-block will force itself to the air surface due to its lower surface tension. To reverse, water is applied on the coating to expand the hydrophilic B-block and cover the Teflon®-like A-block. When an abrading action is applied, the coating peels off to restore the original coefficient of friction. Another example is an ABC triblock copolymer made of a hard A-block, a relatively soft Teflon®-like B-block, and a hydrophilic C-block. The A-block will provide additional anchor domains in the bulk of the polymer. The Teflon®-like B-block will concentrate on the air surface, due to its low surface tension. In war zones that are relatively dry, a coating of this kind can be anchored by relatively hard hydrophilic groups in the C-block, such as acrylic acid (AA) or methacrylic acid (MAA) or their salts, with added ethylene (E) and vinyl acetate (VA) comonomers for better adhesion to surfaces, if needed. Adhesion to substrates may not be necessary since a cohesive but detached layer can result in surface lubricity; thus, the hydrophilic C-block may not be dominant after the lubricating layer is applied but become phase inverted and abradable when exposed to water. With the Teflon®-like block (coming from a Zonyl® monomer), a good mechanically attached slippery layer can be obtained. The hard A-block can be made from a vinylidene chloride (VDC), which can be partially hydrolyzed into ketone-containing segments for long-term UV-based reversibility. The polymer will be dispersed in water, since it will have surfactant-type behavior, and applied on substrates by spraying, brushing, rolling, etc. After drying, the B-block will concentrate on the air–polymer interface, which will provide its slippery characteristics. In order to remove this slippery surface, one merely sprays or applies water on the surface, in order to swell the C-block and invert the phases to a C-dominant domain structure. When this happens, the surface will no longer be as slippery and could even be rubbed off. Even though at a later time the rest of the coating becomes slippery again, long-term UV-based photodegradation of the A-block will facilitate water-based erosion of the coating, resulting in water-insoluble, nonfloating chunks of polymer (since the polymer will be heavier than water due to the presence of VDC

and Zonyl® segments). Also, surfactants are generally considered environmentally benign materials, since they disperse in water.

Polymeric approaches to impart lubricity to solid substrates normally involve the use of fluorocarbon, silicone, urethane, and hydrophilic segments and functional groups. However, when combined with other above-mentioned features, no currently developed polymer has been shown to be satisfactory**.** Such myriad set of requirements can be addressed with the use of multifunctional block copolymers that are to be produced from the FRRPP process. Numbers for possible surface coverages of polymers and their corresponding relationship to the coefficient of friction are not well established in the literature. Usually, surface lubricity can be correlated with the surface tension of the resulting slip layer. One recent patent (U.S. Patent No. 6,326,131) involves the use of a two-part lubricant (wax and fluorosurfactant) at coverages of 13.5 and 1.78 mg/m^2, respectively, with the resulting coefficient of friction down to 0.10. This result indicates the feasibility of meeting surface coverage and coefficient of friction values of 10 g/m^2 and 0.10, respectively.

For a surface coverage of 10 g/m^2 and a dry polymer specific gravity of 1, the polymer layer thickness results in a value $\delta = 100$ nm. For block copolymer domains in the order of 15 nm (such as PS domains from Kraton® with block molecular weights in the order of 16,000 Da), there are only a few domains along the thickness of the polymer ice layer. For a diffusive process through this layer, an order-of-magnitude estimate relating the diffusivity D with the diffusion time t_d and layer thickness δ is expressed in terms the following equation:

$$\frac{Dt_\mathrm{d}}{\delta^2} \approx 1. \tag{6.1.1}$$

For applicable values of δ and mutual diffusivities in polymer domain/small-molecule systems, resulting order-of-magnitude estimates for the diffusion time are shown in Table 6.1.1.

This means that dispersed hard 15-nm blocks should have diffusivities less than about 10^{-11} cm^2/s and 100-nm soft block matrix layers should have diffusivities in the order of 10^{-9} cm^2/s in order for application and reversible mechanism to occur in less than 1 s. This is reasonable for the soft block, since diffusivities for rubbery polymers can go up to 10^{-6} cm^2/s. However, glassy polymers can have diffusivities as low as 10^{-14} cm^2/s. Thus, for diffusion times less than 1 s, these domains should have sizes less than 1 nm. This can be satisfied by a hydrophilic block made up of a random copolymer of a hydrophilic monomer and a comonomer with a

Table 6.1.1 Practical numerical relationships for layer thicknesses, δ, diffusion time, t_d, and mutual diffusion coefficient, D, for polymer domain/small-molecule systems

D (cm^2/s)	10^{-12}	10^{-11}	10^{-9}	10^{-6}
δ (nm)	15	15	100	100
t_d (s)	2.25	0.225	0.1	0.0001

low glass transition temperature. Also, ionomers with relatively low hydrophilic segment compositions, such as around 15 wt% for acrylic and methacrylic salts, could be employed. In addition, the block copolymer segment-to-segment sequencing could be tapered in order to obtain a diffuse interface between the block copolymer domains. Finally, proper use of solvent(s) can result in a diffuse domain structure, such as one that is more compatible with the dispersed phase compared to the dispersing matrix (Caneba et al., 1983–1984). As for tapering in the block copolymer segment-to-segment sequencing, this has been obtained in the past using the FRRPP process through a unique single-stage polymerization approach while taking advantage of intrinsic reactivity ratios of the various radical ends (Section 4.3.1). Of course, the multistaged FRRPP approach (i.e., one stage per block formation, as presented in Section 4.1.2) is capable of tapered block structures based on scheduled addition of monomer(s) in the reactor.

6.1.3 Other Applications

Other possible military- and homeland security-related uses are as follows:

1. Sprayable surfactant–water solution wherein the surfactant has labeled moieties. The solution is sprayed over a wide area of ground. If the ground surface is disturbed, the absence of the label from the surfactant can be detected, indicating the possibility that mines, IEDs, EFPs, etc., might have been planted on the disturbed ground surface.
2. Carriers for sensor labels to probe underground structures, if a portion of the multipolymeric surfactant is labeled or if the surfactant–water solution is used to displace/carry another fluid containing labeled molecules. Thus, underground structures can be mapped before and after an event.
3. Deliverable penetrating cement material using on-site water, in which the warfighters would need to carry only small amounts of the multipolymer solid and even smaller amounts of whatever catalyst is needed for hydrolysis. The surfactant will be generated using water that is obtained on-site with a little heating if it is too cold. Then, the catalyst is added in or mixed during delivery, by pouring, pumping, vacuuming into a porous material of interest. Gel/cement formation would then occur over time (preferably in minutes) or could be activated with heat, ultrasound, microwave, etc.
4. Reinforcement of fortifications by filling pores of wood, masonry, etc., with protecting gel/cement.
5. Protection from chemical, biological, and nuclear attack, again by filling pores from wood, masonry, dry walls, and even the ground material (soil, masonry, etc.).
6. Isolation of contaminated soil, by injecting the surfactant solution underneath the contamination to turn into the gel/cement.

7. Reduction of water seepage into excavated structures, trenches, etc., which can be uncomfortable for the warfighter. The application of the penetrating environmentally responsible surfactant solution that turns onto a gel/cement could reduce mud formation in these dug-up structures.
8. Environmentally responsible method of hardening soft soil, mud, which would be made more passable by military vehicles.

6.2 Conceptual Connections to Nuclear Material Systems

6.2.1 Energy-Producing Isotopes

It is clear that the FRRPP process has resulted in discovery of new polymeric materials, and more block copolymers will still be discovered from it. The abovementioned thermal effects (Section 2.2) have not been the subject of a more systematic study, and yet understanding it is a key to its application to more energetic systems. If a mere few grams of a monomer can release enough exothermic energy and result in char formation of Teflon®, metal deformation, metal alloy phase separation, the initiation of an intense localized surface combustion that slowly consumes a bath material a few thousand times its weight, then what can more energetic materials do especially around even more energetic materials/systems? Understanding this phenomenon and attempting to lay the groundwork in its application toward controlled and release on demand of energies from extracted/purified radioactive materials is the essence of a proposed project.

The FRRPP method has been shown to control the release of exothermic heat of reaction from a chain polymerization system to the point that its release practically preserves the adiabatic rise temperature. Understanding its underlying concepts would be very beneficial toward its use in other more energetic systems. If one looks into particular isotopes of radioactive elements, it could be possible to design a mixture of these elements (or their compounds) with other materials (metals, metal oxides, etc.) in such a way that a homogeneous solution of these mixtures is radioactively moderated. Upon raising the solution temperature above the LCST, the resulting phase separation phenomena will cause the heterogeneous system to be locally supercritical but macroscopically subcritical. During coarsening of the radioactive domains, the system suddenly could become supercritical especially when phase layering occurs, thereby releasing its full radioactive potential as depicted in Fig. 6.2.1. This is just the notion of what the mechanism might be, and a full understanding of the FRRPP concept and experimental systems is needed. However, if fully understood, the concept is of great potential toward the scale-down of the uses of radioactive energy and radiation sources.

As it was demonstrated for polymerization system where a small amount of a monomer can result in the consumption of a bath material thousands of times its weight (multiplicative effect), envisioned radioactive systems could also be featured to have propagation properties. It is reasonable to expect that a distributed

deployment of the envisioned material at its moderated state can be triggered in one location. The rise in temperature and radiation level in that location can cause adjacent areas to undergo phase changes and become "hot" as well. If this propagation is still macroscopically subcritical, then it is possible to render various locations macroscopically/microscopically subcritical/supercritical, based on the remote trigger and a particular protocol for the harnessing of thermoradiative energies. Alternately, one can look at the possibility of an inherently moderated solution system that could be triggered to possess controlled release and/or catastrophic release of energy on demand. This could result in smaller-sized and safer nuclear systems, which could be safe enough to incorporate in portable devices.

The first and foremost aspect of a proposed work is the understanding of the thermal effects of the FRRPP process. The proposed mechanism in Fig. 6.2.1 is a good start, but it has to be verified. Without this understanding, there is not much basis for future work with other materials systems. This should be done both

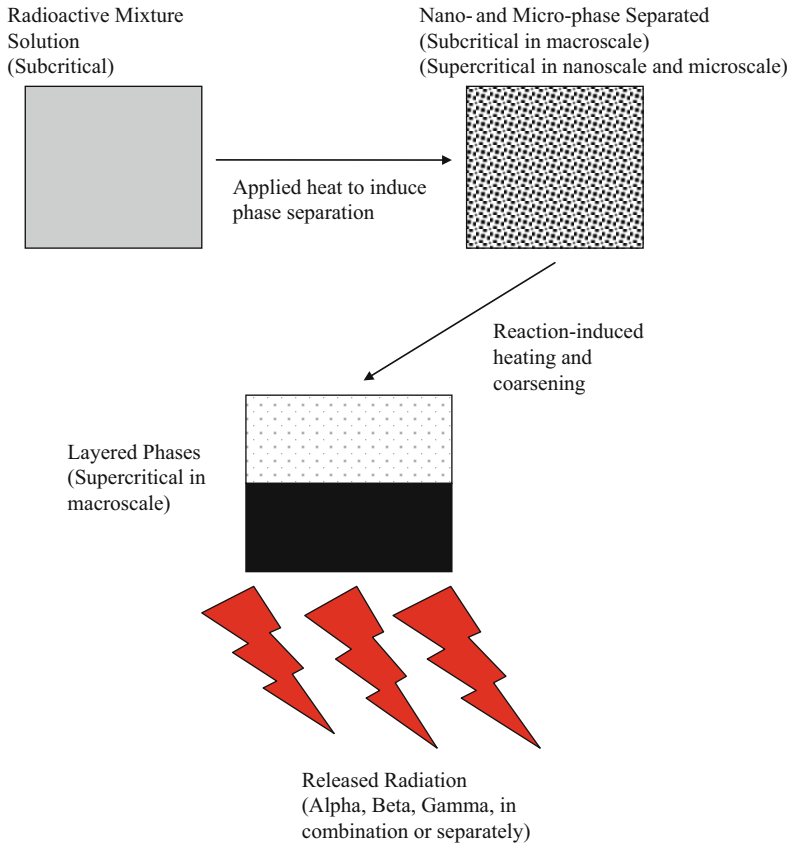

Fig. 6.2.1 Notional relevance of the FRRPP concept to more energetic radioactive material mixture systems

theoretically and experimentally. Then, armed with this understanding from the FRRPP systems, the phenomenon would have to be translated to radioactive decay from natural and induced systems. What feasible purified or even mixed isotopes can be used for eventual systems of interest? The critical property of interest here is the LCST. Conceptually, the LCST is tied with relatively strong specific intermolecular forces in polar and hydrogen-bonded systems (Caneba and Shi, 2002). In nonpolar systems, the LCST was found to be based on differences between thermal expansion coefficients of the components. In liquid metal mixtures, LCSTs have been reported for bismuth-containing alloys (Hurle and Pike, 1966), which makes sense since bismuth has a relatively high thermal expansion coefficient and lower melting temperature compared to other metallic liquids. Mathematical modeling of the phenomenon has been a difficult task, using mean field approaches. Thus, it should be more feasible to use quantum mechanical approaches to make certain quantitative predictions about it, if a dedicated supercomputer is available. Aside from working out the actual reaction mechanism with accompanying radiation emissions, the determination of the combinations of active materials with other materials that undergo phase separation above the LCST would have to be made. This could come from solid, liquid, or even gaseous forms of the radioactive species, as long as the result is a liquid solution that turns heterogeneous at a higher but manageable temperatures and appropriate time scales. Again, stable species in the mixture or containment materials would have to be determined in terms of their properties either as a moderator or as a reflector or varying degrees between the two. Note that there will be a need to look into morphological effects on transition from subcriticality to supercriticality in these systems. Understanding morphological evolution and thermoelectric effects is a key to the ability to design systems with modulated thermal and electric energy outputs. These are considerations for just the active portion of the system that would have to be determined in this project.

The other aspect of the design of systems is the containment package and how it interacts with the active reaction system. Should it be a pure reflector or partially a moderator? These systems can be used for power production from a relatively small-sized devices to larger systems. If it is really possible to store thermal energy and dramatically release it on demand, then this might pave the way into the design of controlled thermal sources of enormous amounts of energy per mass.

We can also turn our attention to the use of this concept to the release of direct electrical energy from beta-electron-releasing isotopes. These isotopes are relatively benign compared to those that release neutron beams, X-rays, or gamma rays. If these isotopes have relatively short half-lives and are converted into useful stable compounds, then they would be nonproliferating. In fact, this is probably the essence of ancient alchemy, since the release of beta electrons will result in an increase in atomic number. It is therefore conceivable that a beta-releasing isotope can be converted into an expensive stable element after it produces direct electricity in a battery-like construction. Nuclear-based batteries harnessing beta electrons have been used already in remote devices and in electromagnetic propulsion of satellites. With the mechanism shown in Fig. 6.2.1, the sudden outburst of beta electrons can

be used as electrical power booster and even in electromagnetic propulsion booster systems.

A good example is the ^{45}Ca isotope, which could be obtained from exposure of natural Ca to neutron beams maybe in a nuclear reactor core (Etherington, 1958). When the isotope releases beta electrons spontaneously as direct electrical power, it is converted to a stable ^{45}Sc, which can be used as an alloying agent with aluminum instead of titanium. In fact, the Sc/Al alloy is tough and strong lightweight alloy that it is used for bike bodies and lacrosse racquets. Also, the ^{45}Ca kinetics involves a half-life of 165 days, which means that five times that period assures more than 99% conversion to Sc. Also, the direct electrical energy release has been calculated to be in the order of 148.73 kWh/g or 148.73 MWh/kg. If we take advantage of the above-mentioned mechanism of storing this energy in nanoscale and then releasing it on demand by causing the nanoscale domains to coarsen by gravity or centrifugal force, then bursts of electricity can be obtained. Such a level of electrical power can be capable of industrial efficient production of useful isotopes, and even in for various electromagnetic levitation vehicles. In fact, the use of isotopes is already being planned for powering small space vehicles, especially in deep-space missions.

Other isotopes of interest that release beta-electrons include ^{35}S and ^{90}Sr. Table 6.2.1 shows the various energetic and kinetic characteristics of these above-mentioned isotopes.

Table 6.2.1 Energetic and kinetic characteristics of candidate isotopes

Isotope	Half-life	Energy density (kW h/g)	Average power in first two half-lives (kW/kg)
^{45}Ca	165 days	148.73	37.56
^{35}S	88 days	122.38	57.95
^{90}Sr	28 yrs	162.41	0.6598

If nuclear power is going to make a comeback, then an isotope engineering program can be established. Isotope engineering does not necessarily have to be emphasized in uranium or plutonium, but in relatively safe isotopes that can be produced from nuclear reactors or extracted from nuclear waste. Some of these isotopes are already being used in medical as well as in tracer applications; so there is already a history in handling them albeit in dilute form. From an intellectual standpoint, isotope engineering opens a new window to materials, since new elements can be formed. If some of these new elements are expensive or useful ones, then that makes it even more desirable.

6.2.2 Nuclear Waste Materials

Understanding thermo-reaction effects in controlling runaway systems would be applicable toward more efficient and safe harvesting of residual energy from nuclear waste forms. An effort could first be the development of the computational capabilities to simulate the solid-state properties of candidate waste form materials under

the range of conditions experienced during synthesis, storage, and disposal. Specifically, candidate waste forms containing short-lived fission products (e.g., ^{137}Cs and ^{90}Sr) that generate substantial amounts of heat, as well as a strong field of ionizing radiation could be the focus (M. Peters, personal communication). Ideally, these waste forms would be capable of high waste loadings and remain stable at high temperatures and in intense radiation fields. For high waste loadings, temperatures well in excess of 800°C have been discussed. Although, there are a number of potential waste forms for ^{137}Cs and ^{90}Sr (e.g., borosilicate glass, CsCl, SrF_2, $SrTiO_3$, hollandite, pollucite, framework silicates/titanates, and apatite), the issue of thermally based phase stability in a high radiation field has not been adequately studied and needs to be fully addressed (Weber et al., 1997, 1998). Another point is that the ^{137}Cs will contain a substantial fraction of ^{135}Cs, which has a half-life of several million years; hence, long-term durability of the waste form may be required.

If an effort will focus on ^{137}Cs and ^{90}Sr, model equations for the following systems can be derived and simulated:

1. ^{137}Cs and its transmuted isobar (^{137}Ba) (http://books.nap.edu/catalog/10684.html)
2. ^{90}Sr and its transmuted isobars (^{90}Y and ^{90}Zr) (http://books.nap.edu/catalog/10684.html)
3. ^{137}Cs, ^{135}Cs, and their transmuted isobars
4. ^{137}Cs, its transmuted isobar (^{137}Ba), in borosilicate glass ceramic
5. ^{137}Cs, ^{135}Cs, their transmuted isobars, in borosilicate glass ceramic
6. Lanthanides in borosilicate glass ceramic
7. ^{90}Sr, its transmuted isobars, lanthanides, in borosilicate glass ceramic
8. ^{137}Cs, ^{135}Cs, ^{90}Sr, their transmuted isobars, lanthanides, in borosilicate glass ceramic

In general, there are a number of valid conservation relations that can be considered:

1. Conservation of mass–energy
2. Conservation of linear momentum
3. Conservation of nucleons
4. Conservation of ionic charges.

It is the first one that will be emphasized, and can be broken into conservation of mass and energy, which are coupled with Einstein's mass–energy equivalence ($E = mc^2$). As such, the accumulation terms of the conservation of mass are not affected. Also, we could neglect forced convection effects in the system. The resulting mass diffusion equation would be similar to that in Eq. (1.5.2), except that a so-called elastic strain energy could be added to the potential function to take into account crystal lattice differences between solid phases (De Fontaine, 1967).

For the conservation of energy, the following nonconvective form will be used (Bird et al., 2007):

$$\rho C_V \left(\frac{\partial T}{\partial t}\right) = -\vec{\nabla} \bullet \vec{q} + S, \tag{6.2.1}$$

where ρ, density of the system; C_V, heat capacity of the system at constant volume; T, absolute temperature; $\vec{q}$, conductive plus radiative heat flux functions; S, energy source term (units of energy/time/volume) from chemical reactions, transmutation reactions, mass conversions to energy, etc.

Half-life and other reaction-based coefficient values can be obtained from the literature for all nuclides of interest, and they will be used in the model equations. It is well known that ^{137}Cs has a half-life of 30.23 yrs to ^{137m}Ba intermediate with a half-life of 2.55 min, which in turn transmutes to the stable ^{137}Ba. This means that for all practical purposes, ^{137}Cs transmutes to ^{137}Ba with a half-life of 30.23 yrs. For ^{90}Sr, it has a half-life of 28.1 yrs to ^{90m}Y with a half-life of 3.1 h, then to ^{90}Y with a half-life of 64 h, and then to ^{90m}Zr with a half-life of 0.81 s, and finally to the stable ^{90}Zr. For ^{135}Cs, it practically transmutes to ^{135}Ba with a half-life of 3×10^6 yrs. As for the lanthanides, their half-lives are also available in the literature (*CRC Handbook of Chemistry and Physics*). If reaction pathways and parameters cannot be obtained from the literature, they could be simulated from open-source or in-house quantum mechanical software packages with the aid of other data available in the literature, such as radiation cross-section values.

Energy source term could have contributions from transmutations and from various chemical reactions. Transmutation energies obtained from the literature (*CRC Handbook of Chemistry and Physics*) could be used along with local concentrations of radioactive and stable species. For materials that are receiving transmutation radiations, their capabilities to absorb radiation as well as their concentrations are also going to be incorporated in the energy source term. Open-source software packages, such as the Ziegler's SRIM/TRIM package (available through the World Wide Web), could be adapted in our material systems to determine energetic effects and fate of the various nuclides, chemical bonds, etc. Otherwise, commercial quantum mechanical or open-source software packages could be used.

Thermal evolution would be the primary processing history for the various systems of interest. The ramp-and-hold thermal history can be incorporated in the model simulation, based on the ratio of the ramp time to the characteristic time of the behavior of the system (such as phase separation). This method has been employed for spinodal decomposition with temperature drop in a polymer/solvent system (Laxminarayan and Caneba, 1991), and a Deborah number (*De*) is used to signify the ratio of the characteristic phase separation time to the temperature ramp characteristic time. Thus, if *De* is infinite, the system would be under sudden quenching. Results of the work for a nonreactive binary polymer/solvent system established bounds for dimensionless interdomain distance (interdomain distance divided by its value during sudden quenching) vs *De*. Also, the dimen-

sionless induction time (onset of accelerated phase separation divided by its value during sudden quenching) was obtained vs the parameter ε' (thermodynamic and mobility effects of quench level, in which a high value signifies deep quench) and $1/De$. The extreme case of sudden quenching ($1/De=0$) behavior was shown to be insensitive to the quench level.

6.3 Fuel Cell Membranes

6.3.1 Proton Exchange Membrane (PEM) Fuel Cells

Fuel cell energy systems have been of longstanding interest in the entire range of transportation and appliance sectors. There is always an interest in improving efficiencies of fuel cell system in order to reduce overall weight and volume, or to provide the capability of running heavier vehicles from these power sources. If higher temperatures can be employed in proton exchange membranes, catalyst activities can be increased, but this increased activity should be matched by appropriate water removal and proton diffusion rates. In methanol fuel cells, the membrane should also function as an effective barrier for methanol crossover. This is the reason why over the past several years there has been a race for the discovery of PEMs that can operate reliably above 100°C.

One can use halogenated block copolymers synthesized by FRPPP to control the ion-containing nanodomain structure of the PEM, thereby enabling properties that are not accessible with randomly functionalized polymers. The utility of this approach has already been demonstrated in model systems where high conductivity has been demonstrated at low relative humidity using sulfonated block copolymers (Kim, et al., 2003; Ding et al., 2002; Park et al., 2007; Elabd et al., 2006). However, these model systems were not robust chemically, nor were they useful for high temperature application. FRPPP will enable halogenated monomers to be polymerized to form the acid- and thermal-resistant anchor of a robust, high temperature block copolymer, in which a portion of the adjacent block can then be functionalized. Such a nanoscale morphological structure is expected to result in a more optimal fuel cell membrane, due to a wider search design space.

A currently popular type of polymer material used in fuel cell applications is Nafion®, which is essentially a perfluorinated polymer with randomly sulfonated hydrophilic segments. The order of substitution by the hydrophilic groups is based on the so-called equivalent weight (EW) and membrane thickness (Mauritz and Moore, 2004); for the Nafion© 117 used in fuel cell applications, the material has 1100 EW (1100 g Nafion© per mole sulfonic acid groups) and 7 mils thickness. With segmental distribution of random copolymers, membrane hydrophilic domains are expected to be relatively tight. This means that in order to effect high ion transport rates, relatively large amounts of water need to be retained in these hydrophilic domains. Note that water retention is found to be a significant impediment in the

design of higher temperature fuel cell membranes. If a block copolymer segmental structure is employed, well-defined hydrophilic nanochannels would be the resulting morphology, due to the proximity of various hydrophilic functional groups from the copolymer chains. Thus, more water can be retained in such a morphological structure to result in high ion transport rates even at higher operating temperatures. Such a proposition has been validated by various model material studies (M. Hickner, personal communication).

A similar result can be concluded from the hydrophilicity of hydrophilic–hydrophobic copolymers. For example, it is well- known that at least 10 % hydrophilic segments is needed to disperse a statistical hydrophilic–hydrophobic copolymer in water. Whereas, in our work with vinyl acetate–neutralized acrylic acid block copolymers, stable dispersion in water was achieved even at 4 wt % acrylic acid content (Caneba and Dar, 2005). Finally, a comparative study of permeabilities has been made between block and random copolymers for sorption and diffusion of cyclohexane in styrene–butadiene copolymers (Caneba et al., 1983–1984). Since the permeability is proportional to the product of the diffusivity and solubility, numerical results for 10 wt % S contents indicate an increase in permeability for the block copolymer membrane compared to the random copolymer membrane.

The idea of a regular morphology can be extended to membranes for direct methanol fuel cells (DMFCs). It is thought that the nature of adsorbed water in the membrane controls the proton conductivity and the methanol permeability (Serpico et al., 2002). In random copolymers, such as Nafion®, the water content, proton conductivity, and methanol permeability are tightly correlated. As previously mentioned, block copolymers have the potential for high proton conductivity without large degrees of water adsorption because of proximity of hydrophilic segmental groups. By lowering the water sorption, the methanol permeability will be decreased without a sacrifice in proton conductivity (M. Hickner, personal communication).

6.3.2 Hydroxide Exchange Membrane Alkali Fuel Cells (HEMFCs)

HEMFCs have been cited to possibly overcome problems associated with DMFCs, such as (a) methanol crossover between electrodes; (b) the use of relatively high loadings of expensive catalysts; (c) electrode weeping resulting in waterflooding; (d) electrode corrosion which precludes the use of ultrathin bipolar metal electrode plates; and, (e) the formation of precipitated metal carbonate crystals in electrolyte-filled pores of electrodes (Varcoe and Slade, 2005). Since current concerns with HEMFCs are rooted from stability of membrane materials, successful efforts in membrane development for HEMFCs could yield enormous dividends. This is especially true with the use of methanol as fuel rather thean hydrogen, because of relative ease of conversion of current petroleum-based fuel distribution networks for methanol, as well as safety concerns with the use of hydrogen. Therefore, HEMFCs are potentially capable of supplanting PEMs as fuel cell membrane systems of choice in the near future (W. Li, personal communication).

The FRRPP process has been proposed to generate multifunctional membranes that can be employed in HEMFCs. The same type of halogenated multifunctional polymer membranes can be used, but tailor-made for this application.

6.4 Medical Applications

6.4.1 Nanoparticle Polymers

6.4.1.1 Homogeneous Polymer Nanoparticles

A natural offshoot of the nanotechnology connection articulated in Section 2.1 is the capability of the FRRPP process in generating nanoscale polymers. It has been mentioned in the literature that size scale of nanoparticles for medical applications have been at least 10 nm in size. Based on the results indicated in Section 2.1, FRRPP-based nanoparticles can go down to 1 nm; thus, these materials can easily find uses in medical applications, especially if they are the multifunctional type. Still, the author will classify this type of nanoparticle morphology as homogeneous. They could be made up of homopolymers, statistical copolymers, and even block copolymers with surface functionalities for attaching or binding with various bioactive agents.

Polymer types that can be formulated into FRRPP-based homogeneous nanospheres for medical applications include thermoreversible hydrogels, such as linear and cross-linked copolymers based in methacrylic acid, *n*-isopropyl acrylamide (NIPAM), vinyl alcohol from vinyl acetate. Nanospheres from more conventional polymers, such as polystyrene, can be used as model materials as well. It should be noted that nanoparticles are of the same size as viruses; thus, they are all capable of generating or becoming viruses themselves. It is important to accompany studies of formation and application of nanoparticles for medical applications with studies based on less complicated model materials.

Due to their relative small sizes, methods of entry of nanoparticles seem to include oral, intravenous, directly onto organs, and even through inhalation (Gelparina et al., 2005). Functions of homogeneous nanoparticles inside body can include (a) drug release, (b) diagnosis/detection, and (c) cell targeting.

In drug release applications (Gupta and Kompella, 2006), nanoparticles are desirable because of high loading capacity of hydrophobic drugs compared to molecular introduction of therapeutic material. They also have high stability and faster drug introduction. They can be also functionalized in order to attach onto cancer cells and become fluorescent (Wang et al., 2002); thereby providing means to detect these cells before they are observed conventionally, and then releasing therapeutic drugs to destroy the cells (Roy et al., 2003).

6.4.1.2 Heterogeneous Nanoparticles

Another approach to medical application of FRRPP is to use its control polymerization properties to grow ultrathin polymer layers onto various nanoparticles. This

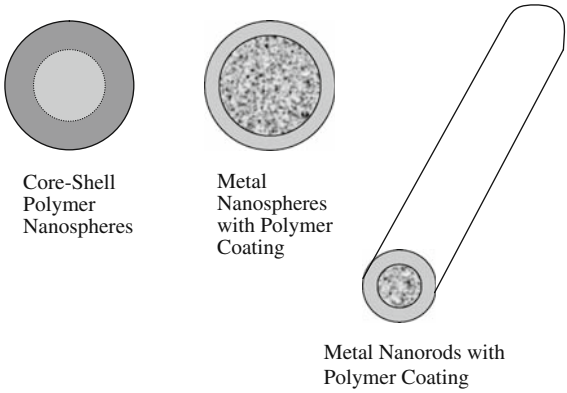

Fig. 6.4.1 Nanoparticle morphologies from the FRRPP process

will result in heterogeneous structures as depicted in Fig. 6.4.1. This is done by initiating FRRPP from surfaces of the nanoparticles in the environment of the reacting solution, especially without chemical initiators, in order to produce the relatively pure ultrathin polymer layer.

These patterned heterogeneous nanospheres or nanorods can contain magnetic materials, which can be guided chemically through surface functionalities, used in hyperthermic therapy, and further guided magnetically (Ito et al., 2005).

6.4.2 Patterned Polymers

Micropatterning of polymers, especially thermoreversible hydrogels, have various possible medical uses. One of them is as media for bioseparation operations, using various driving forces, such as electric field, pressure difference, or even concentration gradient. Another application is the use of these patterned polymers in microfluidic systems. This is especially attractive if patterning is done using UV lithographic exposure from a reactive polymer solution. FRRPP will occur if the patterned polymer phase separates with the original polymer solution above the LCST.

References

Bird, R. B., Stewart, W. E., and Lightfoot, E. N., 2007. Transport Phenomena, 2nd Ed., John Wiley and Sons, New York.

Caneba, G. T., 2007. "Multifunctional Multipolymeric Surfactants for Oil-Bitumen Recovery", U.S. Patent and PCT Applications, February 9.

Caneba, G. T., and Dar, Y., 2005. "Free-Radical Retrograde-Precipitation Copolymers and Process of Making the Same", U.S. Patent Application 10/045,725, and Divisional Patent Application, 11/181,481, Filed July 14.

Caneba, G. T., and Shi, L., 2002. "Lower critical solution temperature of polymer-small molecule systems: a review", in: Phase Separation in Polymer Solutions and Blends, P. K. Chan (Ed.), *Research Signpost*, ISBN #81-7736-097-3, Chapter 4, pp. 63–104.

Caneba, G. T., Soong, D. S., and Prausnitz, J. M., 1983–84. *J. Macromol. Sci. Phys., B22*, 693.
De Fontaine, D., 1967. Ph.D. Dissertation, Materials Science, Northwestern University.
Ding, J., Chuy, C., and Holdcroft, S., 2002. *Macromolecules, 35*, 1348.
Elabd, Y. A., Napadensky, E., Walker, C. W., and Winey, K. I., 2006. *Macromolecules*, 39, 399.
Etherington, H. (Ed.), 1958. Nuclear Engineering Handbook, McGraw-Hill Book Co., New York.
Gelparina, S., Kisich, K., Iseman, M. D., and Heifets, L., 2005. *Am. J. Respir. Crit. Care Med., 172*, 1487–1490.
Gupta, S. P., 1984. U.S. Patent No. 4,467,869, August 28.
Gupta, R. B., and Kompella, U. B. (Eds.), 2006. Nanoparticle Technology for Drug Release, Informa Healthcare, ISBN #9781574448573.
Hurle, D. T. J., and Pike, E. R., 1966. *J. Mater. Sci., 1*, 399.
Ito, A., Shinkai, M., Honda, H., and Kobayashi, T., 2005. *J. Biosci. Bioeng., 100*, 1–11.
Kim, Y. S., Dong, L., Hickner, M., Pivovar, B. S., and McGrath. J. E., 2003. *Polymer, 44*(19), p. 5729.
Laxminarayan, A., and Caneba, G. T., 1991. *Polym. Eng. Sci.*, *31*, p.1597.
Mauritz, K. A., and Moore, R. B., 2004. *Chem. Rev.*, 104, 4535.
Park, M. J., Downing, K. H., Jackson, A., Gomez, E. D., Minor, A. M., Cookson, D., Weber, A. Z., and Balsara. N. P., 2007. *Nano Lett., 7*(11), 3547.
Roy, I., Ohuchansky, T. Y., Pudavar, H. E., Bergey, E. J., Oseroff, A. R., Morgan, J., Dougherty, T. J., and Prasad, P. N., 2003. *J. Am. Chem. Soc.*, *125*, 7860–7865.
Serpico, J. M., Ehrenberg, S. G., Fontanella, J. J., Jiao, X., Perahia, D., McGrady, K. A., Sanders, E. H., Kellogg, G. E., and Wnek, G. E., 2002. *Macromolecules, 35*, 5916–5921
Varcoe, J. R., and Slade, R. C. T., 2005. *Fuel Cells*, 5(2), 187.
Wang, S., Mamedova, N., Kotov, N. A., Chen, W., and Studer, J., 2002. *Nano Lett.*, *2*, 817–822.
Weber, W. J., Ewing, R. C., Angell, C. A., Arnold, G. W., Cormack, A. N., Delaye, J. M., Griscom, D. L., Hobbs, L. W., Navrotsky, A., Price, D. L., Stoneham, A. M., and Weinberg, M. C., 1997. *J. Mater. Res. 12*, 1946.
Weber, W. J., Ewing, R. C., Catlow, C. R. A., Diaz de la Rubia, T., Hobbs, L. W., Kinoshita, C., Matzke, Hj., Motta, A. T., Nasatasi, M., Salje, E. K. H., Vance, E. R., and Zinkle S. J., 1998. *J. Mater. Res., 13*, 1434.

Appendix

A.1 Mathematical Modeling of Spinodal Decomposition

From a theoretical standpoint, the phenomenological approach used is based on the Helmholtz free energy F that is varying with composition and composition gradient (Cahn and Hilliard, 1958; Cahn, 1961, 1965, 1968; De Fontaine, 1967, 1975).

$$F = \int_V U(u_1,u_2,\ldots,u_n,\nabla u_1,\nabla u_2,\ldots,\nabla u_n)d\underline{r}, \tag{A.1}$$

where u_i are relative to the overall mass fraction of component i, c_i^o

$$u_i = c_i - c_i^o \qquad i = 1,2,\ldots n. \tag{A.2}$$

Application of the Taylor series expansion to U relative to the overall composition of the system

$$U = U_o + \left[\sum_{i=1}^{n} \nabla u_i \left(\frac{\partial}{\partial \nabla u_i}\right)\right] U_o + \frac{1}{2}\left[\sum_{i=1}^{n} \nabla u_i \left(\frac{\partial}{\partial \nabla u_i}\right)\right]^2 U_o + \ldots, \tag{A.3}$$

and eliminating all odd-derivative terms if we are dealing strictly with isotropic systems,

$$F = \int_V \left[U_o + \frac{1}{2}\left[\sum_{i=1}^{n} \nabla u_i \left(\frac{\partial}{\partial \nabla u_i}\right)\right]^2 U_o + \ldots\right] d\underline{r}. \tag{A.4}$$

In order to minimize F, the calculus of variations was used with the aid of a Lagrange multiplier. Then, application of the conservation of mass, Onsager reciprocity relation for the mobilities, and neglecting terms beyond the quadratic derivatives in Eq. (A.4) (De Fontaine, 1967), one obtains

G. Caneba, in: *Free-Radical Retrograde-Precipitation Polymerization (FRRPP)*,
Chapter DOI 10.1007/978-3-642-03025-3, © Springer-Verlag Berlin Heidelberg 2010

$$J_k = -\sum_{i=1}^{n-1} M_{ki} \nabla (\varphi_i - \varphi_n), \tag{A.5}$$

where M_{ki} is the mobility coefficient of the *ki* component pair and

$$\varphi_i - \varphi_n = \frac{\partial f}{\partial u_i} - \frac{\partial f}{\partial u_n} - 2\sum_{j=1}^{n-1} \kappa_{ij} \nabla^2 u_j. \tag{A.6}$$

In Eq. (A.5), k (unless specified otherwise) varies from 1 to $n-1$, and n is the number of components. Here, f is the bulk-free energy of mixing per unit volume. u_i $(= u_i(\underline{r},t))$ is the composition variation of component i such that,

$$\sum_{i=1}^{n} u_i = 0. \tag{A.7}$$

From Onsager reciprocity relation we get $M_{ki} = M_{ik}$. Since mass is conserved, we get

$$\sum_{i=1}^{n} M_{ki} = 0. \tag{A.8}$$

The quantity κ is the so-called gradient-energy coefficient. The set of terms in the summation in Eq. (A.6) is the added term to Fick's first law of diffusion (see Section 2.2), which provides the effect of concentration gradient to the diffusional flux of material. For a purely diffusive process, Eq. (A.6) is combined with the differential component balance expression to give

$$\frac{\partial u_i}{\partial t} = \sum_{j=1}^{n-1} \nabla \left[M_{ij} \nabla \left(\varphi_j - \varphi_n \right) \right]. \tag{A.9}$$

For a binary system of constant density, Eq. (A.9) reduces to

$$\frac{\partial u}{\partial t} = \nabla \bullet \left[M(u) \nabla \left[\left(\frac{\partial f}{\partial u} \right) - 2\kappa \nabla^2 u \right] \right]. \tag{A.10}$$

For deep quench systems, and for the early stage of spinodal decomposition, we get the following solution to Eq. (A.10):

$$u = \sum_{q} \exp\left[R(\vec{q})t\right] \left[A(\vec{q}) \cos\left(\vec{q} \bullet \vec{r}\right) + B(\vec{q}) \sin\left(\vec{q} \bullet \vec{r}\right)\right], \tag{A.11}$$

where $\vec{q}$ is the wave number of the sinusoidal composition fluctuations, which is related to the wavelength, λ, by

$$\vec{q} = \frac{2\pi}{\lambda}. \tag{A.12}$$

The quantity $\vec{r}$ is the distance variable from a central position, and $R(\vec{q})$ (which may be thought of as a first-order rate constant describing the phase separation process) is given by

$$R(\vec{q}) = -M\left(\frac{\partial^2 f}{\partial u^2}\right)(\vec{q})^2 - 2M\kappa\,(\vec{q})^4 \tag{A.13}.$$

Equation (A.11) indicates a sinusoidal solution which has an exponential amplitude. If $R(\vec{q})$ within the exponential amplitude is negative, the resulting composition profile will dissipate with time. If $R(\vec{q})$ is positive, the profile will grow exponentially with time. At a critical value of $\vec{q}=\vec{q}_m$ wherein $R(\vec{q}_m) = 0$, the interdomain distance, λ_m, is obtained from Eqs. (A.12) and (A.13) as

$$\vec{q}_m = \frac{2\pi}{\lambda_m} = \left[-\frac{\left(\frac{\partial^2 f}{\partial u^2}\right)}{2\kappa}\right]^{1/2}. \tag{A.14}$$

Reduction of Eq. (A.10) to binary and one-dimensional systems for composition-dependent M and D is found elsewhere (De Fontaine, 1967; Caneba and Soong, 1985). The solution procedure involves expressing both diffusivity and mobility in truncated polynomial form up to the quartic term. Results of all calculations in binary polymer/solvent systems indicate that the interdomain distance and domain size progressively increase with time. Thus, interdomain distances developed in the early stages of spinodal decomposition are the smallest achievable in the system.

In order to analyze ternary systems that are applicable to nonreactive version of the FRRPP process, an extension of the numerical procedure used in binary systems is shown below.

The Eq. (A.9) describes early-stage as well as late-stage behavior of a spinodal decomposition process in any coordinate system. We assume that κ_{ij} independent of concentration. For simplicity, let us consider the case of early stages of spinodal decomposition. Also, both diffusion and mobility coefficients are assumed to be constant at the average composition of the system. We get

$$\frac{\partial u_k}{\partial t} = \sum_{j=1}^{n-1}\left(D_{kj}^{o}\nabla^2 u_j - 2M_{kj}^{o}\kappa_{kj}\nabla^4 u_j\right) \quad k = 1,\ldots,n-1, \tag{A.15}$$

where D_{kj}^{o}, the diffusion coefficient, is

$$D_{kj}^{\mathrm{o}} = M_{kj}^{\mathrm{o}} f_{kj}^{\mathrm{o}}. \tag{A.16}$$

Note that f_{ij}^{o} is actually the second derivative of the free energy of mixing ΔG_{M}, and all along with the diffusion and mobility coefficients are evaluated at the average composition of the system, c_k^{o}.

In one dimension ($\underline{r} \to x$), Eq. (A.15) becomes

$$\frac{\partial u_k}{\partial t} = \sum_{j=1}^{n-1} \left(D_{kj}^{o} \frac{\partial^2 u_j}{\partial x^2} - 2M_{kj}^{o} \kappa_{kj} \frac{\partial^4 u_j}{\partial x^4} \right) \quad k = 1, \ldots, n-1. \tag{A.17}$$

In order to solve numerically, it is advantageous to nondimensionalize Eq. (A.17). This can be done as follows. Let us define

$$\begin{array}{cc} \tau = D_{11}^{\mathrm{o}} t/\lambda_{\mathrm{m}}^2 & \alpha_{kj}^{\mathrm{o}} = D_{kj}^{\mathrm{o}}/D_{11}^{\mathrm{o}} \\ \delta_{kj}^{\mathrm{o}} = 2M_{ki}^{\mathrm{o}} \kappa_{ij}/D_{11}^{\mathrm{o}} \lambda_{\mathrm{m}}^2 & \eta = x/\lambda_{\mathrm{m}} \end{array}. \tag{A.18}$$

Therefore, the dimensionless form of Eq. (A.17) is

$$\frac{\partial u_k}{\partial \tau} = \sum_{j=1}^{n-1} \left(\alpha_{kj}^{\mathrm{o}} \frac{\partial^2 u_j}{\partial \eta^2} - \delta_{kj}^{\mathrm{o}} \frac{\partial^4 u_j}{\partial \eta^4} \right) \quad k = 1, \ldots, n-1. \tag{A.19}$$

Equation (A.19) is the basic equation that can be solved for a multi-component system. It reduces to the following pair of equation for a ternary system ($k = 3$) that must be solved simultaneously:

$$\frac{\partial u_1}{\partial \tau} = \alpha_{11}^{\mathrm{o}} \tilde{\nabla}^2 u_1 + \alpha_{12}^{\mathrm{o}} \tilde{\nabla}^2 u_2 - (\delta_{11}^{\mathrm{o}} \tilde{\nabla}^4 u_1 + \delta_{12}^{\mathrm{o}} \tilde{\nabla}^4 u_2), \tag{A.20}$$

$$\frac{\partial u_2}{\partial \tau} = \alpha_{21}^{\mathrm{o}} \tilde{\nabla}^2 u_1 + \alpha_{22}^{\mathrm{o}} \tilde{\nabla}^2 u_2 - (\delta_{21}^{\mathrm{o}} \tilde{\nabla}^4 u_1 + \delta_{22}^{\mathrm{o}} \tilde{\nabla}^4 u_2), \tag{A.21}$$

where $\tilde{\nabla}(\ldots)$ is the dimensionless form of $\nabla(\ldots)$, or $\tilde{\nabla}(\ldots) = \lambda_m \nabla(\ldots)$.

To set up the numerical solution of Eq. (A.19)–(A.21), we transform it into reciprocal domain. First, we revert to a dimensionless version of Eq. (A.15)

$$\frac{\partial u_k}{\partial \tau} = \sum_{j=1}^{n-1} \left(\alpha_{kj}^{\mathrm{o}} \tilde{\nabla}^2 u_j - \delta_{kj}^{\mathrm{o}} \tilde{\nabla}^4 u_j \right). \tag{A.22}$$

The transformation to reciprocal regime is done by multiplying Eq. (A.22) by $(1/V)\exp(-i\underline{\beta}'.\underline{r}')d\underline{r}'$ and integrating over the domain volume V

$$\frac{1}{V} \int_V \frac{\partial u_k}{\partial \tau} \exp(-i\underline{\beta}'.\underline{r}')d\underline{r}' = \sum_{j=1}^{n-1} \frac{1}{V} \int_V (\alpha_{kj} \tilde{\nabla}^2 u_j - \delta_{kj} \tilde{\nabla}^4 u_j) \exp(-i\underline{\beta}'.\underline{r}')d\underline{r}'. \tag{A.23}$$

Note that in Eq. (A.23), $\underline{\beta}'$ is described as $\underline{\beta}' \to \pi k_n/\lambda_n$ and $\underline{r}'$ is the space vector (in one dimension $\underline{r}' \to x$). Both $\underline{\beta}'$ and $\underline{r}'$ are made dimensionless by defining

$$\underline{\beta} = \underline{\beta}'\lambda_{\mathrm{m}} = \left(\frac{\pi k_i \lambda_{\mathrm{m}}}{\lambda_i}\right) \text{ and } \underline{r} = \frac{\underline{r}'}{\lambda_m}, \tag{A.24}$$

where λ_{m} is the interdomain distance. Note that in one-dimensional form of $\underline{r}$ is given by $\underline{r} = \eta = x/\lambda_{\mathrm{m}}$. Then, the non-dimensionalized form of the product $\underline{\beta}'.\ \underline{r}'$ in Eq. (A.23) is $\underline{\beta}.\underline{r}$. The dimensionless form of Eq. (A.23) is given as

$$\frac{1}{V}\int_V \frac{\partial u_k}{\partial \tau} \exp(-i\underline{\beta}.\underline{r})d\underline{r} = \sum_{j=1}^{n-1} \frac{1}{V}\int_V (\alpha_{kj}\tilde{\nabla}^2 u_j - \delta_{kj}\tilde{\nabla}^4 u_j)\exp(-i\underline{\beta}.\underline{r})d\underline{r}. \tag{A.25}$$

Applying Leibnitz rule to the left side of Eq. (A.23) along with the condition of vanishing surface integral due to periodic boundary conditions, and also applying Green's theorem twice to the first term and four times to the second term on the right side of Eq. (A.25) along with the condition of vanishing surface integral, we get

$$\frac{1}{V}\frac{d}{d\tau}\int_V u_k \exp(-i\underline{\beta}.\underline{r})d\underline{r} = -\underline{\beta}^2 \sum_{j=1}^{n-1}(\alpha_{kj} + \underline{\beta}^2\delta_{kj})\frac{1}{V}\int_V u_j \exp(-i\underline{\beta}.\underline{r})d\underline{r} \tag{A.26}$$

Now let us expand the $(n-1)$ composition variation in three-dimensional Fourier series as follows:

$$u_k(\underline{r},\tau) = \sum_K A_{k,K}(\tau)\exp(i\underline{\beta}.\underline{r})d\underline{r}, \tag{A.27}$$

with coefficients defined by

$$A_{k,K}(\tau) = \frac{1}{V}\int_V u_k(\underline{r},\tau)\exp(-i\underline{\beta}.\underline{r})d\underline{r}. \tag{A.28}$$

Here, K (which varies from $-\infty$ to $+\infty$) is the triplet of integers k_1, k_2, and k_3. Then, from Eqs. (A.26–2.4.28), we obtain

$$\frac{dA_{k,K}}{d\tau} = -\underline{\beta}^2 \sum_{j=1}^{n-1}(\alpha_{kj} + \beta^2\delta_{kj})A_{j,K}. \tag{A.29}$$

The above equation is valid in three dimensions. We can now reduce this equation to one dimension by the substitution

$$\begin{array}{lll} K \to k_1 & where & k_1 = -\infty, \ldots, -1,0,1, \ldots, \infty \\ \underline{r} \to \eta = x/\lambda_m & and & \underline{\beta} \to \pi k_1 \lambda_m / \lambda_1 \end{array} \tag{A.30}$$

Here $2\lambda_1$ denotes the length of the domain. Therefore, the one-dimensional diffusion equation for a multicomponent system is given by

$$\frac{dA_{k,k_1}}{d\tau} = -\underline{\beta}^2 \sum_{j=1}^{n-1} (\alpha_{kj} + \underline{\beta}^2 \delta_{kj}) A_{j,k_1}. \tag{A.31}$$

Let us define

$$\Gamma_{kj,k_1} = -\underline{\beta}^2 (\alpha_{kj} + \underline{\beta}^2 \delta_{kj}). \tag{A.32}$$

Then Eq. (A.31) reduces to

$$\frac{dA_{k,k_1}}{d\tau} = \sum_{j=1}^{n-1} \Gamma_{kj,k_1} A_{j,k_1} \tag{A.33}$$

Equation (A.33) is a system of ordinary differential equations with dimensionless time τ as the only independent variable. In actual computation, it is advantageous to use only positive integers for k_1, up to as large a value as time permits. From the definition of Fourier transform, the negative indices are eliminated by denoting

$$A_{k,-k_1} = A^*_{k,k_1} \text{and} \quad A_{k,0} = 0 + i0. \tag{A.34}$$

In the above equations, the asterisk denotes the complex conjugate.

At any stage, the composition profile may be easily constructed by the inverse Fourier transform

$$u_k(\eta,\tau) = 2 \sum_{k_1=1}^{n} (B_{k,k_1} \cos(\underline{\beta}\eta) - C_{k,k_1} \sin(\underline{\beta}\eta), \tag{A.35}$$

where

$$A_{k,k_1} = B_{k,k_1} + \iota C_{k,k_1} \; or \; |A_{k,k_1}| = \sqrt{B^2_{k,k_1} + C^2_{k,k_1}} \tag{A.36}$$

Our objective is to solve Eq. (2.4.33). In order to do that, we obtain an Euler-type algorithm for the solution of frequency components A_{k,k_1} of wavelength λ_1 as a function of wave index number k_1.

$$A_{k,k_1} = A^{\circ}_{k,k_1} + \Delta\tau \sum_{j=1}^{n-1} \Gamma_{kj,k_1} A^{\circ}_{j,k_1} \; k = 1, \ldots, n-1 \quad k_1 = -\infty, \ldots, -1,0,1, \ldots, \infty. \tag{A.37}$$

Equation (A.37) is the basic equation around which the computer programs are constructed. Here, A^{o}_{k,k_1} is the wave vector of A_{k,k_1} at time τ_o. From Eq. (A.37), a new vector A_{k,k_1} is calculated from an old A^{o}_{k,k_1}. The new vector is then labeled as A^{o}_{k,k_1} and substituted back into Eq. (A.37) to yield the vector A_{k,k_1} at time $\tau_o+\Delta\tau_o$. This operation is repeated m times until a desired later time $\tau_o+m\Delta\tau_o$ is obtained. Γ_{kj,k_1} in Eq. (A.37) can be visualized as the amplification factor.

Since the computer may not be able to handle negative indices for k_1, they can be eliminated using Eq. (A.34) along with Eq. (A.37)

$$A_{k,k_1} = A^{o}_{k,k_1} + \Delta\tau \sum_{j=1}^{n-1} \Gamma_{kj,k_1} A^{o}_{j,k_1} \quad k_1 = 1,\ldots,\infty, \tag{A.38a}$$

$$A^{*}_{k,k_1} = A^{o*}_{k,k_1} + \Delta\tau \sum_{j=1}^{n-1} \Gamma_{kj,k_1} A^{o*}_{j,k_1} \quad k_1 = 1,\ldots,\infty. \tag{A.38b}$$

For binary systems, only a single equation is needed for all of the above (k_1 subscript disappears to give way to k and j as wave number indices); specifically the last two equations reduce to

$$A_k = A^{o}_k + \Delta\tau \sum_{j=1}^{\infty} \Gamma_j A^{o}_j \quad k_1 = 1,\ldots,\infty. \tag{A.39a}$$

$$A^{*}_k = A^{o*}_k + \Delta\tau \sum_{j=1}^{\infty} \Gamma_j A^{o*}_j \quad k = 1,\ldots,\infty. \tag{A.39b}$$

References

Cahn, J. W., and Hilliard, J. E., 1958. *J. Chem. Phys., 28*, 258.

Cahn, J. W., 1961. *Acta Metall., 9*, 795.

Cahn, J. W., 1965. *J. Chem. Phys., 42*, 93.

Cahn, J. W., 1968. *Trans. Met. Soc. A.I.M.E.*, The 1967 Institute of Metals Lecture, *242*, 166.

Caneba, G. T., and Soong, D. S., 1985. *Macromolecules, 18*, 2545.

De Fontaine, D., 1967. Ph.D. Dissertation, Materials Science, Northwestern University.

De Fontaine, D., 1975. "Phase changes", in: Treatise on Solid State Chemistry, N. B. Hannay (Ed.), Plenum Press, New York, Vol. 5, pp. 129–178.

Index